Université de Strasbourg

UNIVERSITÉ DE STRASBOURG

msii ÉCOLE DOCTORALE

ÉCOLE DOCTORALE MSII (ED n°269)

Laboratoire ICUBE – UMR 7357

Département Génie Civil Énergétique (GCE) – INSA

THÈSE présentée par :

Xiang ZHANG

soutenue le : **18 Octobre 2022**

pour obtenir le grade de : **Docteur de l'université de Strasbourg**

Discipline/ Spécialité : Mécanique, Génie Civil

Modélisation de couplage chemo-thermo-hydro-mécanique (CTHM) dans les structures en pisé

THÈSE dirigée par :

[M. NOWAMOOZ Hossein]	Maître de conférences, INSA de Strasbourg

RAPPORTEURS :

[Mme MASROURI Farimah]	Professeur, Université de Lorraine
[M. CUI Yu-jun]	Professeur, Ecole des Ponts ParisTech

AUTRES MEMBRES DU JURY :

[Mme HATTAB Mahdia]	Professeur, Université de Lorraine
[M. FRANCOIS Bertrand]	Assistant Professor, Université de Liège

Modeling the chemo-thermo-hydro-mechanical coupling (CTHM) of rammed earth structures

by

Xiang ZHANG

A thesis submitted in partial fulfillment for
the degree of Doctor of Philosophy

in the

Doctoral School of MSII
University of Strasbourg

October 2022

Dedicated to my mother and my father

Dédié à mon père et à ma mère

"Zwei Dinge erfüllen das Gemüth mit immer neuer und zunehmender Bewunderung und Ehrfurcht, je öfter und anhaltender sich das Nachdenken damit beschäftigt: Der bestirnte Himmel über mir und das moralische Gesetz in mir. Ich sehe sie beide vor mir und verknüpfe sie unmittelbar mit dem Bewusstsein meiner Existenz".

Kritik der praktischen Vernunft - **Immanuel Kant**

Remerciements

Mes amis les plus proches, mes professeurs les plus chers et les membres de ma famille les plus chers ont tous joué un rôle déterminant dans mon développement en tant que jeune adulte et m'ont apporté soutien et encouragement tout au long de mon parcours.

J'aimerais également exprimer ma plus vive reconnaissance au professeur Hossein NOWAMOOZ pour ses conseils avisés, ses encouragements indéfectibles et ses commentaires perspicaces sur mes recherches. Lorsqu'il était mon superviseur, il m'a transmis non seulement des informations mais aussi l'approche académique la plus rigoureuse. C'est un honneur pour moi d'être un étudiant en doctorat dans son laboratoire, et je le ressentirai toujours ainsi. J'ai eu cette chance et je la chérirai toujours.

Je remercie les Professeurs Yu-Jun CUI et Farimah MASROURI d'avoir été les rapporteurs de ma thèse et de m'avoir fait des commentaires perspicaces. Je remercie également le Prof. Mahdia HATTAB, Asst. Prof. Bertrand FRANCOIS, d'avoir accepté de faire partie du jury et d'avoir fourni des suggestions précieuses pour cette thèse.

J'exprime mes remerciements aux professeurs de la division Génie Civil de l'INSA de Strasbourg, le Professeur Cyrille CHAZALLON, le Professeur Associé Georg KOVAL, le Professeur Associé Juan Carlos QUEZADA, et le Professeur Associé Saida MOUHOUBI. Ils sont gentils et toujours prêts à aider.

Je remercie du plus profond de mon cœur tous ceux qui ont été mes amis à travers les hauts et les bas de ma vie. Fujiao TANG et Chong WANG, qui ont été là pour moi tout au long de mes études de doctorat, me prodiguant des mots de soutien et répondant patiemment à mes nombreuses questions. Mes remerciements vont également à Lei MA, Haitao GE, Léo Coulon, Oussama Hammoudmy, Victor Desloges, Marieh Fatahizadeh, Anicet Dansou, et Laura Gaillard, ainsi qu'aux autres étudiants du MIA1 et de l'INSA de Strasbourg, qui m'ont soutenu tout au long de ce projet et avec qui j'ai partagé de nombreux moments agréables.

Je tiens à exprimer ma profonde reconnaissance à tous les membres de ma famille qui m'ont soutenu jusqu'à présent. Je ne saurais exprimer suffisamment ma reconnaissance à mes parents pour m'avoir aidé à réaliser mon plein potentiel et pour leur dévouement indéfectible.

Pour conclure, je voudrais exprimer ma grande reconnaissance au China Scholarship Council qui m'a apporté un soutien financier pour ce travail.

Acknowledgments

My closest friends, my most cherished teachers, and my most cherished family members all played an instrumental role in my development as a young adult and provided me with support and encouragement along the way.

I'd also like to express my warmest appreciation to Prof. Hossein NOWAMOOZ for his thoughtful direction, unwavering encouragement, and insightful feedback on my research. When he was my supervisor, he imparted not only information but also the most stringent academic approach. It is an honor for me to be a Ph.D. student in his Lab, and I will always feel that way. Having had this opportunity is something I will always cherish.

I am grateful to Prof. Yu-Jun CUI and Prof. Farimah MASROURI, for being the rapporteurs of my dissertation and giving me insightful comments. Gratitude also goes to Prof. Mahdia HATTAB, and Asst. Prof. Bertrand FRANCOIS, for accepting to be part of the jury and providing valuable suggestions for this thesis.

I express my acknowledgements to the professors in the division of Civil Engineering at INSA de Strasbourg, Prof. Cyrille CHAZALLON, Assoc. Prof. Georg KOVAL, Assoc. Prof. Juan Carlos QUEZADA, and Assoc. Prof. Saida MOUHOUBI. They are kind and always ready to help.

Thanks go out from the depths of my heart to everyone who has been a friend to me through the ups and downs of my life. Especially Dr. Fujiao TANG and Dr. Chong WANG, who have been there for me throughout my PhD studies, delivering words of support and patiently answering my numerous inquiries. Thanks are also extended to Lei MA, Haitao GE, Léo Coulon, Oussama Hammoudmy, Victor Desloges, Marieh Fatahizadeh, Anicet Dansou, and Laura Gaillard, as well as other students from MIA1 and INSA de Strasbourg, who have supported me throughout this project and with whom I have shared many enjoyable moments.

I would like to show my profound appreciation to all my family members who have supported me thus far. I cannot adequately convey my appreciation to my parents for helping me fulfill my full potential and for their unwavering dedication.

In closing, I would like to express my great appreciation to the China Scholarship Council for providing financial support for this work.

List of publications

Journal papers:

X. Zhang, H. Nowamooz, Effect of rising damp in unstabilized rammed earth (URE) walls, Constr. Build. Mater. 307 (2021) 124989. [Accepted]

X. Zhang, H. Nowamooz, Thermo-hydro-mechanical (THM) behavior of Unstabilized Rammed Earth (URE) wall submitted to environmental and mechanical loadings, Mater. Struct. 54 (2021) 198. [Accepted]

X. Zhang, H. Nowamooz, Factors influencing the Thermo-Hydro-mechanical behaviour of unstabilized rammed earth walls, Materials. 15 (2022) 8821. [Accepted]

X. Zhang, H. Nowamooz, Chemo-thermo-hydro-mechanical behavior of cement stabilized rammed earth wall in interaction with environment and underground soil, Eng. Struct. (2022). [Under review]

X. Zhang, H. Nowamooz, Predicting the Chemo-thermo-hydro-mechanical behaviors of cement stabilized rammed earth materials from the designing stage, Mater. Struct. (2022). [Under review]

X. Zhang, H. Nowamooz, Mechanical degradation of unstabilized rammed earth (URE) wall under salts and rising damp attack effect, Acta Geotech. (2021). [Under review]

Conference papers:

X. Zhang, H. Nowamooz, Effective stress concept for the hydro-mechanical behaviour of Unstabilized Rammed Earth (URE) materials, *First International RILEM Conference on Earthen Construction*. (2022).

X. Zhang, H. Nowamooz, Thermo-hydro-mechanical (THM) behavior of unstabilized rammed earth (URE) wall submitted to environmental and mechanical loadings, *First International RILEM Conference on Earthen Construction*. (2022)

Table of contents

List of tables

List of figures

General introduction

Unstabilised rammed earth (URE) is an ancient construction technique that can be found through many heritage sites spread worldwide. In addition, URE is an eco-friendly building material due to the fact that it is primarily composed of natural soil. Recent years have witnessed a resurgence of interest in URE, fueled by increased environmental concerns.

However, because URE is generated using the local soil, which varies widely from site to site, apparent differences have been discovered between the properties of different URE materials. In addition, when cement is applied to URE to increase its strength and durability, the URE will be transformed into cement stabilized rammed earth (CSRE), however no method has been proposed to depict these transitional changes in the literatures. In addition, the chemical effects of cement hydration on the chemo-thermo-hydro-mechanical (CTHM) properties of CSRE (URE) have not been thoroughly studied from a global perspective, which makes it more difficult to predict the structural behaviors of CSRE (URE) constructions under in-situ conditions.

To comprehend the characteristics of various CSRE (URE) materials, the combined effects of initial water content, initial dry density, initial grain size distribution, initial cement content, curing temperature, curing method, and curing time should be taken into account from the beginning of the design process. However, only a few of the aforementioned factors have been described in the available literature, and other aspects have not been controlled stringently or exhaustively, causing the properties of CSRE (URE) to vary widely between experimental studies. In addition, most studies focus on several characteristics of a particular type of CSRE (URE) material, and the lack of a global perspective on all types of CSRE (URE) materials makes it extremely challenging to create a globally recognized standard for CSRE (URE) materials.

In the **first chapter**, a systematic literature review was conducted with the goal of understanding the time-related chemo-thermo-hydro-mechanical behavior of a typical CSRE (URE) material from the design stage, illustrating the transitional changes from URE to CSRE, and providing a global view for developing the construction standards for different CSRE (URE) materials.

On the basis of the results of the literature review, the **second chapter** proposes a coupled numerical framework that takes into account the combined effects of initial water content, initial dry density, initial grain size distribution, initial cement content, curing temperature, curing

method, and time to explain and predict the CTHM properties from URE to CSRE materials under laboratory and in-situ conditions.

In the **third chapter** of this thesis, the proposed numerical model is validated by comparing the numerical modeling findings to the experimental results. First, the heat transfer, water flow, and drying process in URE, as well as the relevant mechanical characteristics, are modelled and compared to experiments. Afterwards, the cement hydration process and its associated thermo-hydro-mechanical behaviors of CSRE are simulated, and the simulation results are compared with the experimental observations to evaluate the effectiveness of the proposed numerical approach.

In the **fourth chapter**, the numerical model is then extended to study the structural behaviors of CSRE (URE) constructions under in-situ conditions. The long-term structural behaviors of URE walls are first studied by considering the effects of different environment types on the walls. After that, apart from the effects of the environment, the effects of rising damp from the ground are also studied for the long-term characteristics of the URE walls. Eventually, the long-term CTHM characteristics of the CSRE wall under the interactions of the environment and underground soil are studied.

Chapter 1. Literature review

1.1 Background and construction technique

Rammed earth (RE) is an ancient building material that can be found at several historic sites across the globe [1,2]. Approximately one-third of the world's population lives in rammed earth structures [3]. Throughout the history of human civilization, RE has been utilized widely as a fundamental construction method. Recent environmental concerns [4,5] have sparked a revival of interest in the planet Earth. This material is today regarded as a contemporary material that may be used to construct aesthetically beautiful and comfortable structures [6,7]. Due to the low embodied energy [8,9], the inherent moisture buffering capabilities for interior situations, and the high durability [10,11], it may be claimed that RE is a more sustainable alternative to conventional materials.

Figure 1.1. (a) A typical rammed earth construction [12] (b) Areas with tradition of earth construction in a worldwide scale

RE is compacted primarily with the mixture of water and the raw soil such as clay, silt, fine, sand and gravel in a formwork layer by layer by using a pneumatic or manual rammer [13,14] (Fig 1.2). In this study, the particle size limits of 2 µm, 80 µm and 2mm are used to define the clay content (<2 µm), the silt content (2 µm ~80 µm), the sand content (80 µm ~2 mm) and the gravel content (>2mm). The fine content (c_{fi}) is defined by the sum of clay and silt content (particles smaller than 80 µm), and the coarse content is the sum of sand and gravel content (particles larger than 80 µm). When the clay is used as the only binder, it is referred to as unstabilised rammed earth (URE); and when other stabilizers are added during the production

process of URE for the purpose of improving its properties, such as the strength or durability [15], it is referred to as stabilized rammed earth (SRE). Among various stabilizers, for example, cement [16], lime [17], fiber [18], coal ash [19] etc., the cement stabilization has gained popularity due to its higher and faster strength gain, durability, availability and ability to obtain acceptable engineering properties [20]. When the cement is used as the stabilizer, this specific rammed earth is called cement stabilized rammed earth material (CSRE). In this study, we focus on the CSRE material and the URE is considered as a particular case of CSRE with zero cement stabilizer added. It has been observed that a minimum cement content of 0.5% is required to mobilize the shear strength of cemented soil and the formation of cemented bonds [21]. According to the investigation results presented in this study, the commonly used cement content for various CSRE in the literature is in the range of 2% to 15% (Figure 1.4). The increment of additional cement over 15% leads to a higher strength but a higher environmental cost and economic impact [22]. Furthermore, the overuse of cement may transfer CSRE to concrete (without steel, fiber etc.), which disqualifies the original intention of rammed earth as a green construction material.

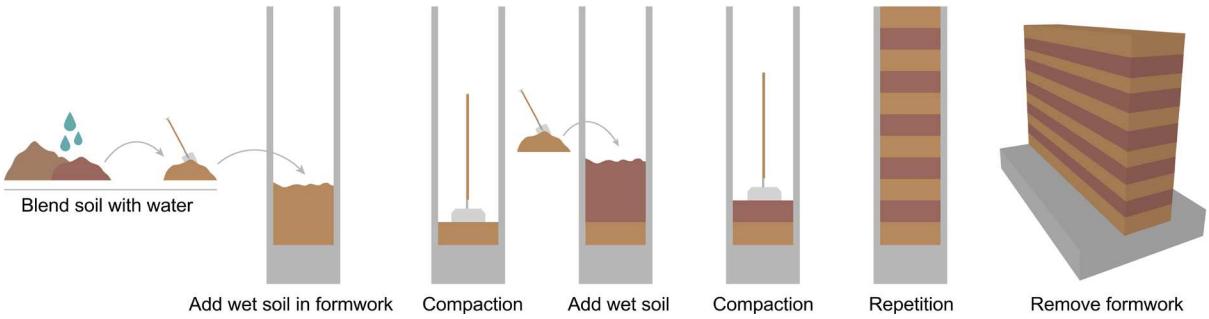

Figure 1.2. A scheme for the construction of a wall with the rammed earth technique

As a building material, RE is expected to have higher compressive strength during its lifetime. Generally, the mechanical resistance of RE increases as the dry density (ρ_d) increases [23–25] with the effect being more dramatic for higher densities [26]. And the dry density (ρ_d) of RE is increased when the compaction energy increases [27,28]. In reality, Due to the economic and environmental benefits, the compression energy cannot always be increased in order to achieve the highest dry density (ρ_d) but fixed at a certain level, for example, the Proctor compaction method described in the official Government documents published by Standards New Zealand (e.g. NZS 4298: 1998 [29]).

When the compaction energy is not changing, the compaction dry density is mainly depended upon material grain size distribution (GSD) and the amount of water added in the soil mixture [14]. The compaction dry density is increased with fine content with fix compaction energy

[30]. When the water content of the soil mixtures is too low during compaction, then the soil cannot achieve the same level of compaction due to the greater degree of friction between the soil particles. If too much water is present, then capillary water occupies the soil pore spaces, reducing the level of achievable compaction and decreasing the level of dry density (ρ_d) when the material has been dried. It has been widely proved that the dry density (ρ_d) first increases and then decreases with water content [31–33]. And the water content (usually gravimetric water content (w)) corresponding to the highest dry density (ρ_d) is called the optimum water content (OWC), and the highest compaction dry density (ρ_d) at this optimum condition is the maximum dry density (MDD) (Figure 1.3). The MDD is influenced by the changings of GSD, for example, the MDD of URE can be decreased [34,35] or increased [36,37] with sand content, and increased [24] or decreased [36,38] with the fine (clay) content. Some author observed that the MDD first increases and then decreases with clay content [39]. When the cement is added to URE, the URE is transferred to CSRE and the GSD of URE is thereby changed by the additional cement content. On one hand, the MDD can be decreased [40,41] or increased [42,43] due to the increase of cement content. On the other hand, it has been observed by some authors [34,44,45] that no detectable variation in MDD attributable to cement or lime stabilizers. The similar uncertain effects of cement (in a global scale) on MDD are found for CSRE through our literature reviews [15,18,20,38,44,46–57] (Figure 1.4).

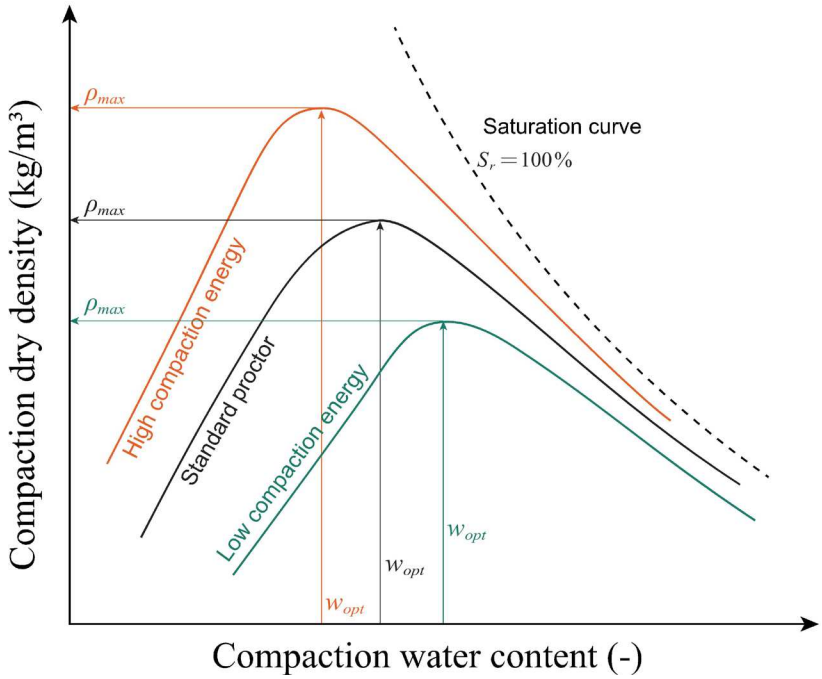

Figure 1.3. Effects of compaction energy on compaction curves of RE materials

Theoretically, while the compaction energy and GSD are constant, the OWC and MDD are proportional to one another (Figure 1.3). It indicates that the variance in MDD for a given OWC is a result of the fluctuating compaction effort and GSD. The effects of GSD (the same compaction energy) on OWC and MDD are introduced in the previous paragraph. The effects of compaction energy (the same GSD) on OWC and MDD are studied by some authors [27,58], and the main conclusion is that the MDD increases but OWC decreases when compaction energy increases (Figure 1.3).

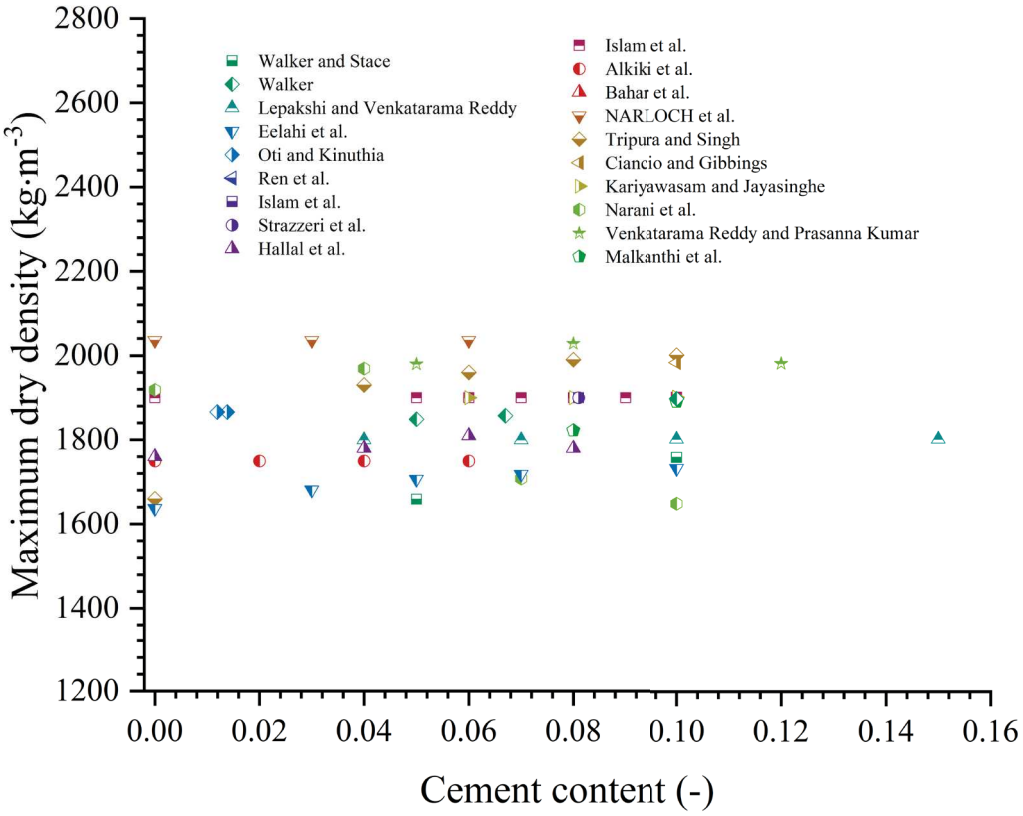

Figure 1.4. Maximum dry density (MDD) according to the initial cement content of CSRE [15,18,20,38,44,46–57]

In conclusion, in order to forecast the optimal compaction condition of CSRE (URE), the mass of water, cement, soil grain size distribution, and compaction energy must be taken into account simultaneously. Only a few of the aforementioned components have been published in the current literature, and other aspects have not been controlled stringently or comprehensively, causing the optimal compaction condition of CSRE (URE) to vary between experimental studies. Figure 1.5 demonstrates that the MDD tends to decrease as the OWC rises, while apparent differences remain between the outcomes of several experimental studies. These variations might be caused by the grain size distribution of the material, compaction techniques, etc.

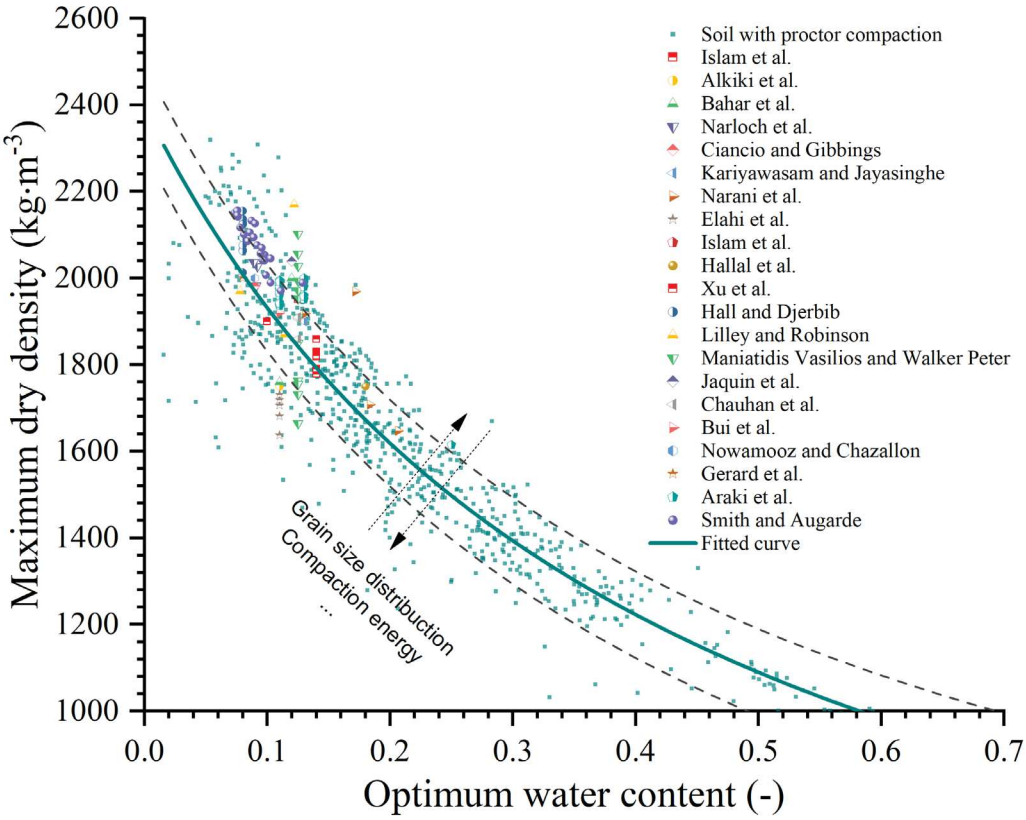

Figure 1.5. Maximum dry density (MDD) according to the optimum water content of CSRE [15,18,20,28,46–49,57,59] and URE [13,31,60–68]

Up to this point, a brief introduction to the building process of CSRE (URE) and the primary elements affecting their initial compaction condition have been provided. As construction materials, engineers are typically concerned with the mechanical strength, water resistance, and thermal isolation characteristics of CSRE (URE). In the subsequent section 1.2, these features are introduced.

1.2 Basic properties from URE to CSRE

The studied materials are regarded as unsaturated porous media [69,70]. And the main factors influencing the thermo-hydro-mechanical behaviors of (CSRE) URE are introduced in the following sections 1.2.1, 1.2.2 and 1.2.3. Since CSRE is created from URE, URE's characteristics are first investigated. And the characteristics of CSRE are introduced after URE.

1.2.1 Mechanical behaviors

In this part, the compressive strength, tensile strength (T_f), elastic modulus and Poisson's ratio of URE are introduced in the section 1.2.1.1.1, 1.2.1.2.1 and 1.2.1.3.1, respectively. As introduced in section 1.1, once the URE is compacted, the dry density (ρ_d), GSD and water content (w) are specified. Apart from the effects of dry density (ρ_d), the influences of GSD, cement and water also need to be considered to better understand the characteristics of URE and CSRE. Instead of water content (w), the suction is used as a state variable **[71]** to describe the effects of water. For a given soil, the suction is normally increased when water content (w) decreases, and the water content (w) is corelated to suction (s) through soil water retention curve (SWRC) **[72]**. Since CSRE is created from URE, URE's characteristics are first investigated. The effects of cement on URE, or the characteristics of CSRE, are then examined.

1.2.1.1 Compressive strength

The compressive strengths of URE and CSRE are introduced in section 1.2.1.1.1 and 1.2.1.1.2, respectively.

1.2.1.1.1 Compressive strength of URE

The MDD and OWC are fixed when a certain type of URE is compressed to the optimal state. Then URE's behavior is mostly influenced by its GSD. Due to the diversity in GSDs, multiple soil water retention curves (SWRC) displaying the relationship between water content (w) or degree of saturation (S_r) and negative pore water pressure or suction (s) are formed [73,74]. Besides, the variation of GSD changes the soil particle contact condition which may lead to different soil particle attraction forces [75], roughness [76] or friction angles [77] of the material. Consequently, according to the Mohr-Coulomb failure criteria and the effective stress theory as described by Bishop [78], the URE may have different strengths due to different GSDs when the dry density (ρ_d) and water content (w) maintain the same. Different GSD may lead to heterogeneous mechanical behaviors on a micro-scale [79]. Some homogenization procedures are applied by Strazzeri et al. [54] to describe the overall macroscopic behavior of earthen mixtures. In this study, the fine content (c_{fi}) is used to show the effects of GSD for its apparent influences on compressive strength (Fig 1.7) and SWRC (Fig 1.27).

Furthermore, in the in-situ situation, rammed earth materials are not necessarily compacted to their optimal conditions, and diverse mechanical behaviors may arise. Therefore, it is necessary to consider the dry density (ρ_d) of earth materials that are not compacted at the optimum

conditions [68,80] as well as the GSD due to different types of rammed earth materials. Some authors observed that there are no apparent effects of dry density (ρ_d) on the strength of rammed earth [60,81,82], while some authors found that the strength of rammed earth will increase with the dry density (ρ_d) [51,83]. This discrepancy is probably caused by the lack of the same control experiment and the combined effects of other factors, such as GSD, water content (w), etc.

When URE holds the same moisture condition (the same relative humidity), its compressive strength increases with fine content (c_{fi}) and dry density (ρ_d) [24,34]. In addition, it has been shown that, with the same dry density (ρ_d) and at saturated conditions, the cohesiveness and confined compressive strength of URE are improved with fine content (c_{fi}) [84]. Furthermore, with the same dry density (ρ_d) and under the same unsaturated (suction) level, the confined and unconfined compressive strength of URE increases when the fine content (c_{fi}) increases [61]. An opposite case has been observed that the fine content (c_{fi}) decreases the strength of URE [85]. It is probably caused by the fact that the increment of fine content (c_{fi}) decreases the MDD and increases OWC under constant compaction energy. For a certain type of URE, the UCS at different imposed suction states are largely reported in literature [14,31,64,86–91], and the results show that UCS of URE increased significantly when the suction (s) increases. Since dry density (ρ_d), suction (s) and fine content (c_{fi}) are all the factors influencing the strength of URE, it is better to control one of them and observe the effects of the other two variables.

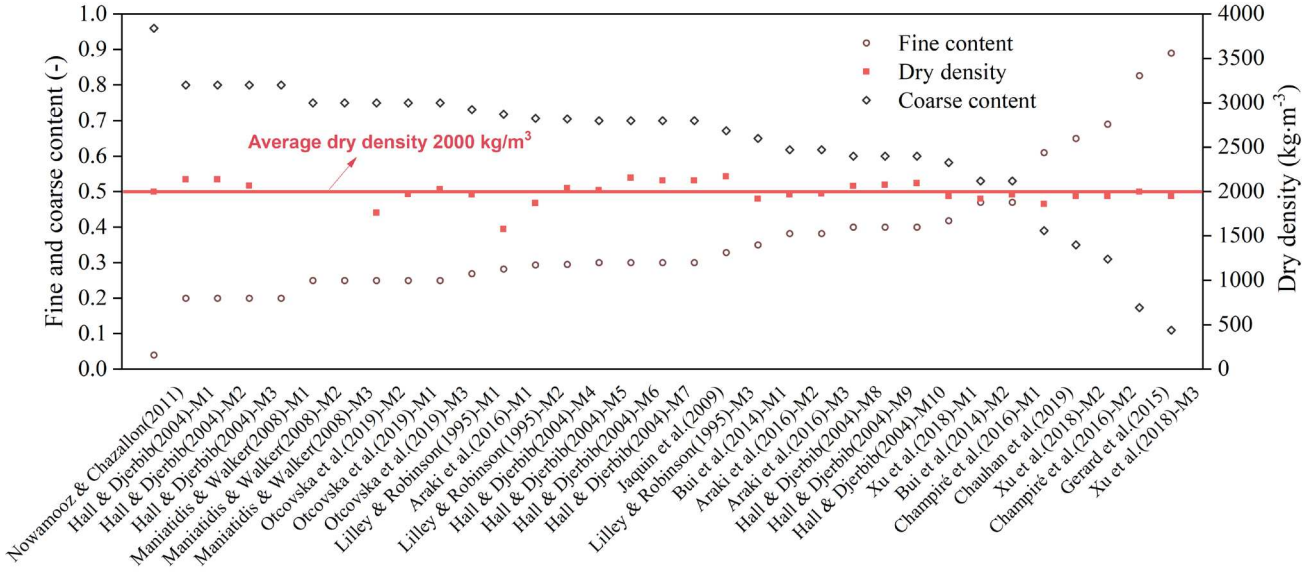

Figure 1.6. Typical URE with various fine contents (80 μm) and the same average dry density of 2000 kg·m-3 [13,14,31,62–64,67,87–90,92]

Author and material	Clay	Silt	Fine	Sand	Gravel	Coarse	Dry density kg·m^{-3}
Araki et al.(2016) [67]-M1	0.28		0.28	0.70	0.02	0.72	1577
Araki et al.(2016) [67]-M2			0.38	0.56	0.06	0.62	1969
Araki et al. (2016) [67]-M3			0.38	0.56	0.06	0.62	1978
Bui et al.(2014) [87]-M1	0.05	0.30	0.35	0.49	0.16	0.65	1920
Bui et al.(2014) [87]-M2	0.09	0.38	0.47	0.50	0.03	0.53	1920
Champiré et al.(2016) [89]-M1	0.17	0.30	0.47	0.51	0.02	0.53	1970
Champiré et al.(2016) [89]-M2	0.17	0.52	0.69	0.31	0.00	0.31	1950
Chauhan et al. (2019) [31]	0.08	0.53	0.61	0.28	0.11	0.39	1860
Gerard et al. (2015) [88]	0.13	0.69	0.83	0.17	0.00	0.17	2000
Hall & Djerbib(2004) [14]-M1	0.06	0.14	0.20	0.39	0.41	0.8	2137
Hall & Djerbib(2004) [14]-M2	0.06	0.14	0.20	0.47	0.33	0.8	2136
Hall & Djerbib(2004) [14]-M3	0.06	0.14	0.20	0.54	0.26	0.8	2066
Hall & Djerbib(2004) [14]-M4	0.10	0.20	0.30	0.31	0.39	0.7	2155
Hall & Djerbib(2004) [14]-M5	0.10	0.20	0.30	0.39	0.31	0.7	2126
Hall & Djerbib(2004) [14]-M6	0.10	0.20	0.30	0.47	0.23	0.7	2124
Hall & Djerbib(2004) [14]-M7	0.10	0.20	0.30	0.52	0.18	0.7	2013
Hall & Djerbib(2004) [14]-M8	0.13	0.27	0.40	0.31	0.29	0.6	2076
Hall & Djerbib(2004) [14]-M9	0.13	0.27	0.40	0.39	0.21	0.6	2093
Hall & Djerbib(2004) [14]-M10	0.13	0.27	0.40	0.45	0.15	0.6	2063
Jaquin et al.(2009) [64]	0.10	0.20	0.30	0.51	0.20	0.71	2039
Lilley & Robinson(1995) [62]-M1	0.11	0.16	0.27	0.49	0.25	0.74	1970
Lilley & Robinson(1995) [62]-M2	0.16	0.13	0.29	0.41	0.29	0.7	1870
Lilley & Robinson(1995) [62]-M3	0.21	0.12	0.33	0.30	0.38	0.68	2170
Maniatidis & Walker(2008) [63]-M1	0.12	0.13	0.25	0.45	0.30	0.75	1971
Maniatidis & Walker(2008) [63]-M2	0.12	0.13	0.25	0.45	0.30	0.75	1763
Maniatidis & Walker(2008) [63]-M3	0.12	0.13	0.25	0.45	0.30	0.75	2027
Nowamooz & Chazallon(2011)[13]	0.01	0.03	0.04	0.67	0.29	0.96	2000
Otcovska et al.(2019) [92]-M1	0.20		0.20	0.80	0.00	0.8	
Otcovska et al.(2019) [92]-M2	0.25		0.25	0.75	0.00	0.75	
Otcovska et al.(2019) [92]-M3	0.25		0.25	0.75	0.00	0.75	
Xu et al.(2018) [90]-M1	0.17	0.25	0.42	0.58	0.00	0.58	1950
Xu et al.(2018) [90]-M2	0.27	0.38	0.65	0.35	0.00	0.35	1950
Xu et al.(2018) [90]-M3	0.35	0.56	0.90	0.10	0.00	0.1	1950

Table 1.1. The different pore size distribution of the studied RE materials reported in the literature

The mechanical strength of URE **[14,31,64,87–90]** with the average dry density (ρ_d) of 2000 kg·m^{-3} but with various fine content (Figure 1.6) and suctions are investigated in order to know the combined effects of suction (s) and fine content (c_{fi}) on UCS. The details about the components of the studied materials are presented in Table 1.1. For the initial control of suction, liquid–vapor equilibrium method was used. The saturated aqueous solution of different salts

are used to control the relative humidity of the air around the samples by liquid–vapor equilibrium. The exchange of water occurs in terms of water vapor based on Kelvin's thermodynamical equilibrium (Equation 14). The UCS is determined when the relative humidity of the URE specimen and the air are in balance. The investigation results are presented in Figure 1.7. It demonstrates that the UCS of a particular URE is continually raised by suction (s). Despite having the same suction (s) value, the material strength might vary when the material types are distinct. Additionally, the impacts of the material components are explored, and the results reveal that fine content (c_{fi}) improves URE strength. Consequently, both the rise in suction (s) and fine content (c_{fi}) contribute to the augmentation of URE's strength.

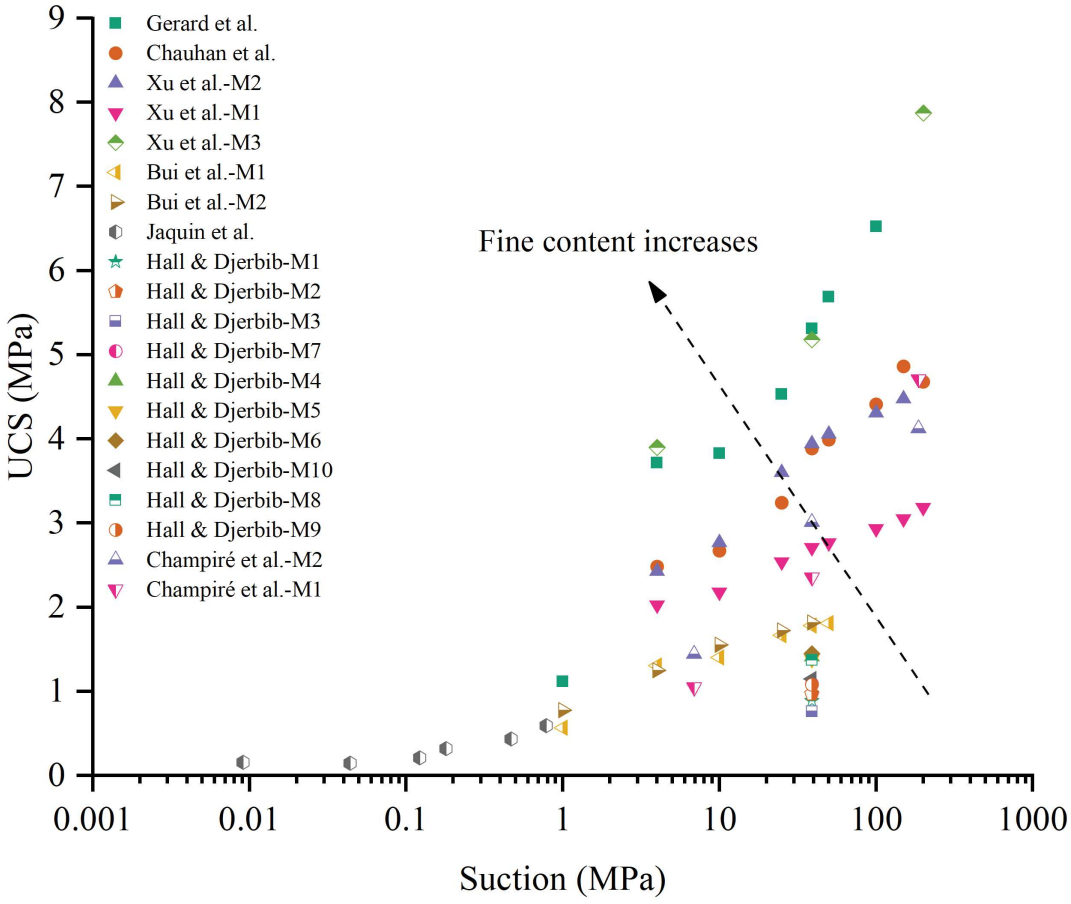

Figure 1.7. Effects of suction and fine content on UCS of URE [14,31,64,87–90]

In reality, the humidity of URE specimens and ambient humidity may not always be in balance. After compaction, the water content (w) of URE is decreased and suction (s) increased with time because the URE materials are normally exposed and dried in the environment. The variations of the material humidity in the drying process for several URE cylindric samples are tested in the controlled environment relative humidity conditions by some authors [31,88]. And the related results are presented in Figure 1.8.

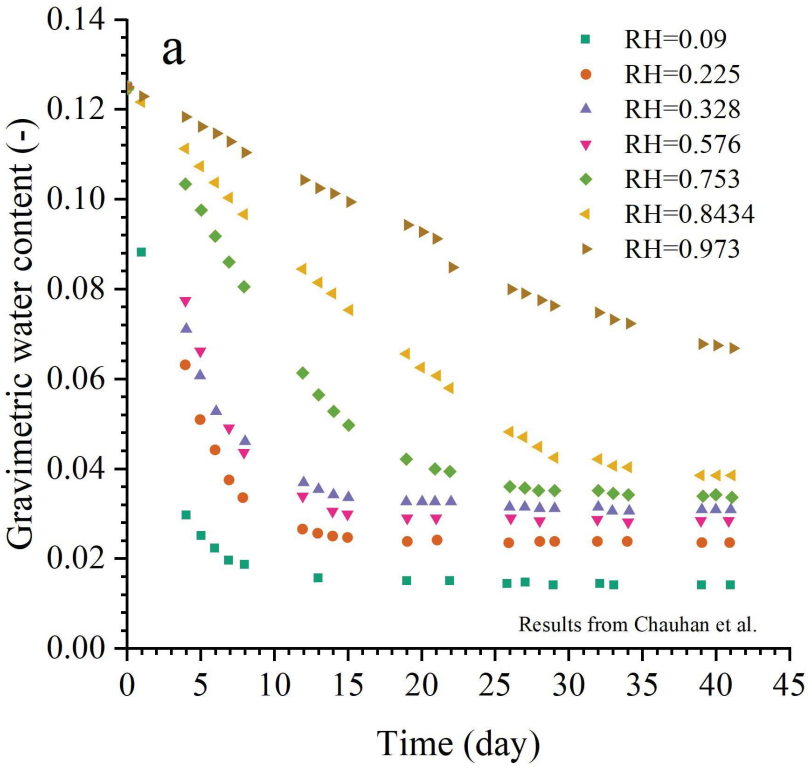

(a)

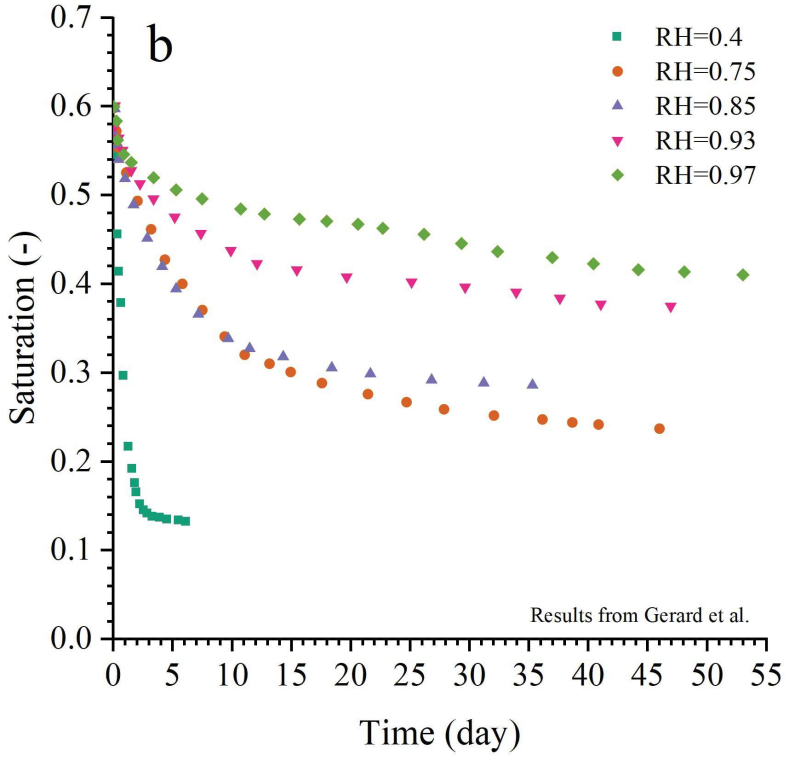

(b)

Fig 1.8. Drying process of URE after compaction in (a) Gravimetric water content (w) scale [31] and (b) Saturation scale [88]

The results show that the humidity of the sample continuously decreases due to a drier environment condition. The drier the ambient air, the faster the sample is dried to the same humidity level as the environment. In addition, the water in URE evaporates quickly at early age and then reaches a level where the sample cannot be dried anymore.

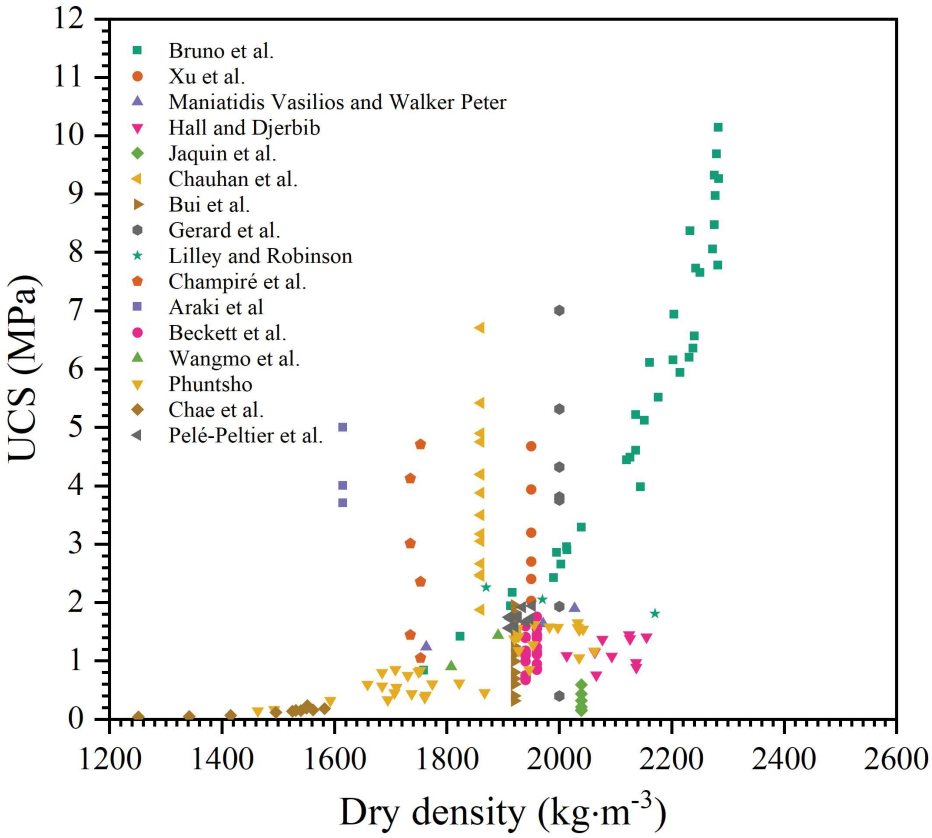

Figure 1.9. UCS of URE according to the dry density [27,31,60–67,69,83,89,93]

Thus, the UCS of URE is increased with fine content (c_{fi}) and the suction (s) when the material keeps the same average dry density of 2000 kg·m^{-3} and then dried in the environment after compaction. On the basis of the experimental results [27,31,60–67,69,83,89,93], the dry densities (ρ_d) of URE are enlarged from the average value of 2000 kg·m^{-3} to a larger range of 1200 to 2400 kg·m^{-3} to demonstrate the impacts of dry density (ρ_d) on UCS of URE. And the related results are presented in Figure 1.9. It can be observed that the UCS of URE has the trend to be increased with the increase of dry density (ρ_d). However, URE material may process different UCS at the same dry density (ρ_d) level, which is probably caused by the changing of fine content (c_{fi}) and suction (s).

1.2.1.1.2 Compressive strength of CSRE

The addition of lower cement content (2%-15%) transforms URE to CSRE, and a higher cement content (>20%) may transfer URE to concrete. The CSRE is located in the transition area between URE and concrete. Therefore, it is necessary to consider both the mechanisms of unsaturated soil and cement hydration process in CSRE. The effects of suction (s), dry density (ρ_d) and fine content (c_{fi}) are introduced in the section 1.2.1.1.1. In this section, the effects of cement on the compressive strength of CSRE are mainly focused and illustrated.

It has been observed that the interaction of cement and fine soil particles [94] exists in cement-based soil materials. Some studies [50,95] have found that the strength improvement of CSRE is prevented by a higher fine (or clay) content of the raw soil, while some authors [96] find the increased fine content (c_{fi}) favors the material strength. These discrepancies may be caused by the changes of dry densities caused by the variations of fine content (c_{fi}) when CSRE is produced at constant compaction energy. Since the fine content (c_{fi}) of the raw soil is used as a factor to reflect the UCS of CSRE in this study, the effects caused by the addition of cement on the GSD of raw soil are not considered.

The UCS of CSRE with no cement under the same wet condition almost does not change after compaction since the suction (s) remains constant and no additional binder is produced [19]. Nevertheless, the existence of cement increases the material strength because of the binders produced by the cement hydration process [28]. In a normal environment condition, the cement in CSRE start reacting with water once compacted (or mixed), and the chemical reaction products act as binder gluing the soil particles together. The cement is consumed quickly due to the adequate supply of water and cement particles at early age. The accumulation of the hydration products resulting in a significant strength increment of CSRE in the first several days after compaction. As time passes, the amount of chemical reactants decreases, resulting in a slower rate of cement hydration. And when the rate of the chemical reaction reduces to zero, the hydration products are not accumulated anymore, and the mechanical strength of CSRE eventually stabilized at a constant value. For cementitious materials, it can take over one year for the cement to be fully hydrated [97]. In addition, UCS tested after 28 days cannot be representative of the actual properties of the CSRE after longer lapses of time [98]. The strength increments of some typical CSRE [15,46,99,100] over time are investigated and the results are presented in Figure 1.10.

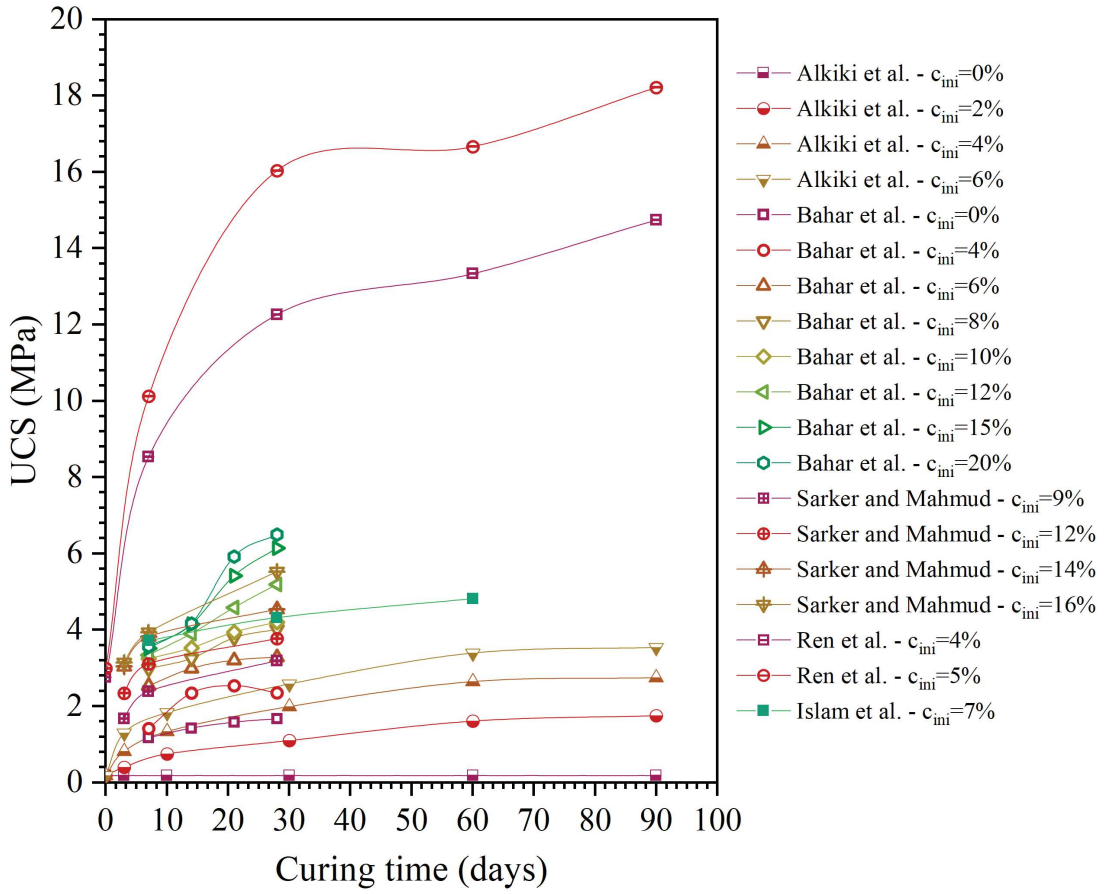

Figure 1.10. UCS of CSRE with various initial cement contents according to curing time [15,46,99,100]

It can be observed that, once the cement is added in the compacted soil, the strength of CSRE will continuously increase with time. Moreover, the compressive strength of CSRE is mainly obtained in the first 28 days and later slowly increases with time. The CSRE with the cement content of 5% from the results of Ren et al. [100] have a higher UCS than the CSRE consists of 20% cement from the results of Bahar et al. [28]. This is caused by a higher compaction dry density (ρ_d) of CSRE (over 2300 kg·m^{-3}) from Ren et al. than that of Bahar et al. (around 1760 kg·m^{-3}). In addition, the results form Alkiki et al. show that the strength of CSRE with no cement (URE) is not change over time under a sealed curing condition, while the strength of CSRE without cement (URE) from Bahar et al. is increased over time when the samples are cured under the laboratory condition allowing water evaporation. It means that the strength of the CSRE comes from two parts when dry density (ρ_d) and fine content (c_{fi}) remain constant, one is the binder effects of hydration products, another is the suction (s).

Since the strength of CSRE will increase over time after compaction, generally, a curing technique is recommended for CSRE to achieve a higher value of strength [62]. CSRE with a

higher initial cement content reaches a higher strength than that of CSRE with a lower initial cement content after the same days of curing [20,22,101]. It means that more quantities of cement react with water and more binders are produced during the hydration process. To better show the effects of cement content on the strength of CSRE, some experimental tests [15,28,44,46,49,51,53,56,57,99,100] after the same period of curing (28 days) are investigated in this work, and the results are presented in Figure 1.11.

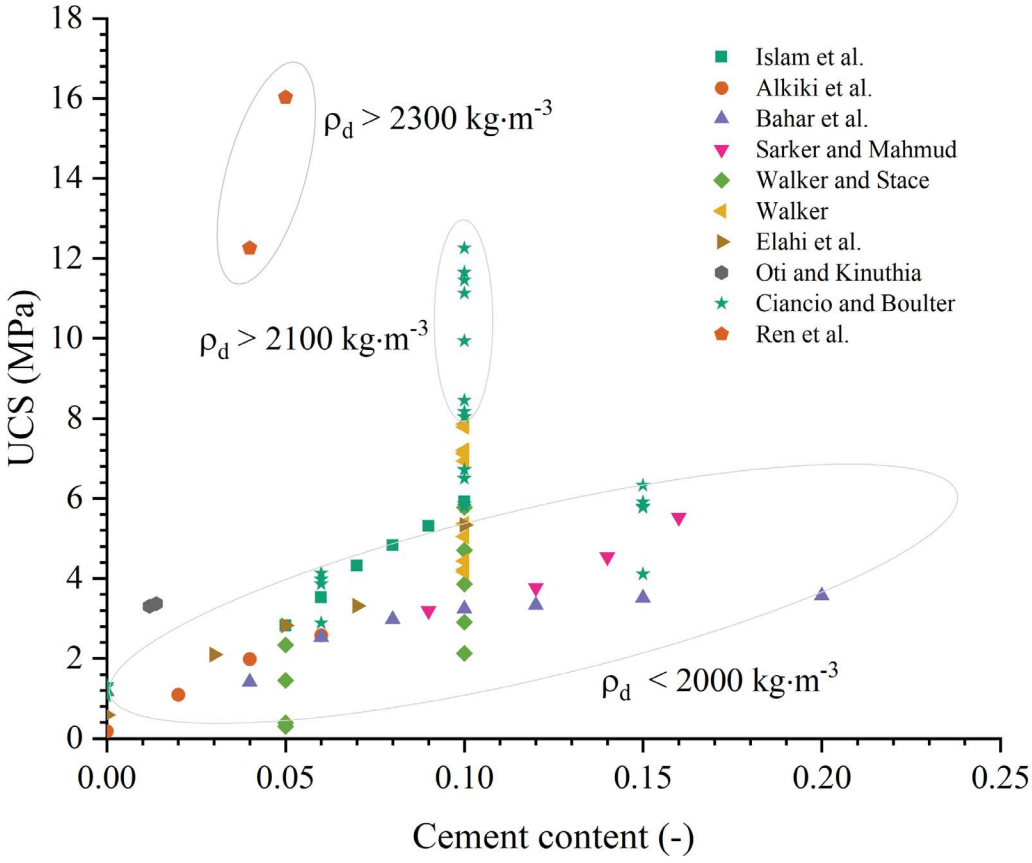

Figure 1.11. UCS of CSRE after 28 days of curing according to cement content [15,28,44,46,49,51,53,56,57,99,100]

It can be observed from Figure 1.11 that the UCS of CSRE has the tendency to be increased when cement content increase. And the continuously added cement (<20%) almost linearly increased the material strength, which means there is no optimum cement content for CSRE from the mechanical perspective of view. In addition, the CSRE specimen with lower cement content may possess high mechanical strength owing to a high compaction dry density (ρ_d). In this work, the effects of dry density (ρ_d) on CSRE with zero cement content (URE), moderate cement content (CSRE) and high cement content (concrete) are investigated and compare together. The results are presented in Figure 1.12.

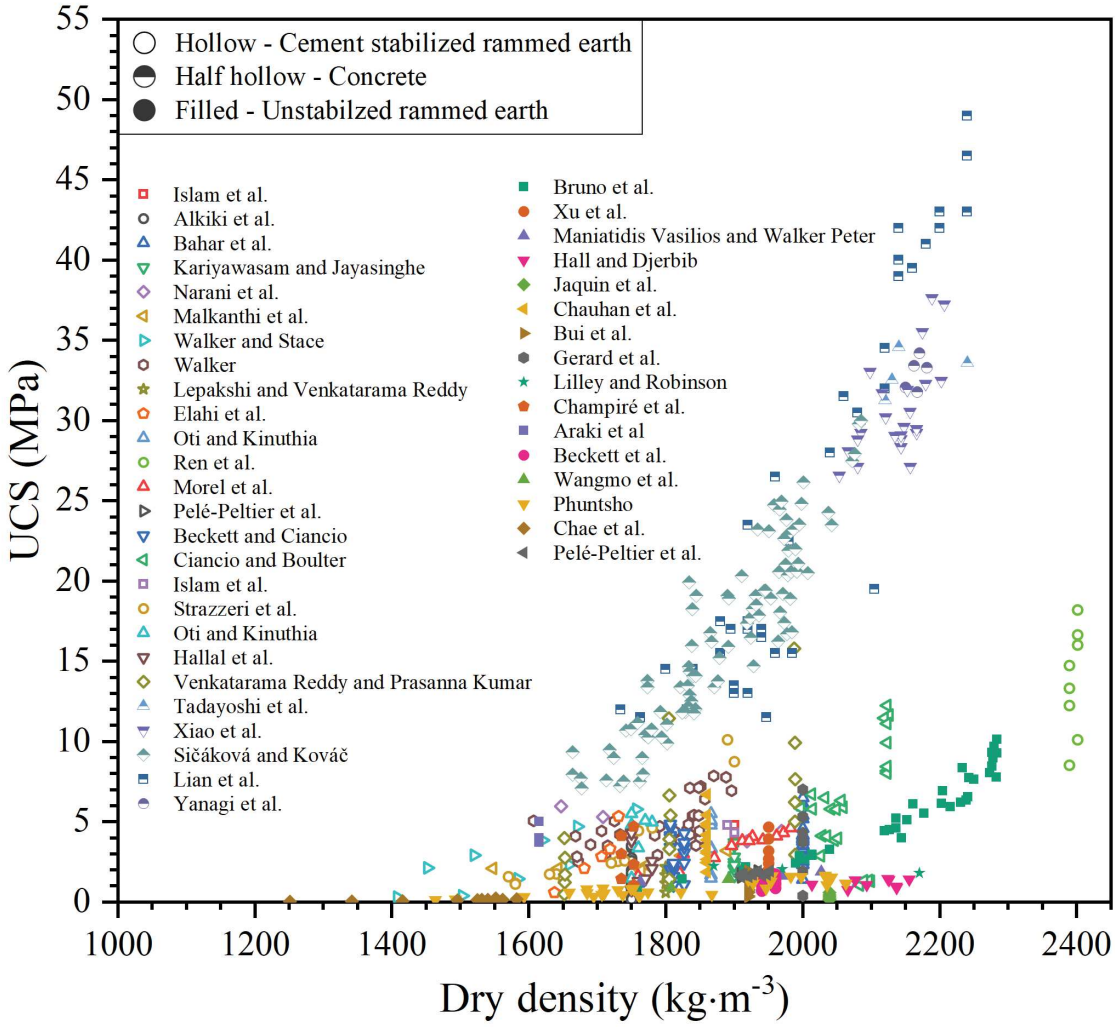

Figure 1.12. UCS of URE [27,31,60–67,69,83,89,93], CSRE [15,18,20,25,28,44,46,49,50,52–54,57,80,102,103] and concrete [104–108] according to dry density

As shown in Figure 1.12, the strength of concrete is generally higher than that of CSRE and URE. The CSRE processes the strength between URE and concrete due a moderate cement addition when the compaction dry density (ρ_d) remains the same. In addition, the UCS of these three materials trends to continuously increases with dry density (ρ_d) slowly when the dry density (ρ_d) remains in a lower range and increases rapidly when the dry density (ρ_d) become higher.

It is obvious that the cement hydration benefits the mechanical resistance of CSRE. However, more amount of hydration products may not always lead to a higher strength of CSRE. The experimental results from Beckett and Ciancio [80] show that even more hydration water is consumed (more hydration products are produced), the CSRE specimen with higher initial water still possesses a lower after-cured compressive strength. It means that the strength

enhancement caused by hydration is impeded by a wetter condition of the CSRE sample [98]. Therefore, the initial water content and initial cement content both influence the after-cured strength of CSRE [109]. The ratio of the initial water and initial cement content is called the water-cement ratio (by mass), which is popularly used to describe the after-cured (usually sealed for 7 or 28 days) strength of concrete [110]. This parameter is introduced by Beckett et al. [111] to CSRE in their work, and a comparable mechanical response is found as with concrete. The after-cured strength of CSRE increases with the decrease of the water-cement ratio [110]. During the curing process, the rate of gained strength is higher at the beginning and reduces with age later, while the precise prediction about the age required for stabilization is not established in worldwide standards [98]. The after-cured strength of CSRE has been predicted with the empirical equations proposed by some authors by considering the effect of water-cement ratio [112], 28-day strength (time) [97] and the combined effect of water-cement ratio and time [113], or water-cement ratio, time and dry density (ρ_d) [114] at laboratory curing conditions.

Specifically, a higher initial water to cement mass ratio leads to a lower strength of the cement-based materials [115,116]. The effects of water-cement ratio on the strength of CSRE [15,28,46,49,57] are investigated in this work and the results are presented in Figure 1.13. It can be observed from Figure 1.13 that the strength of CSRE decreased when the water-cement ratio increases. And the strength reduction magnitude is more significant for the material cured after 28 days than cured after 7 days when the water-cement ratio increment keeps the same.

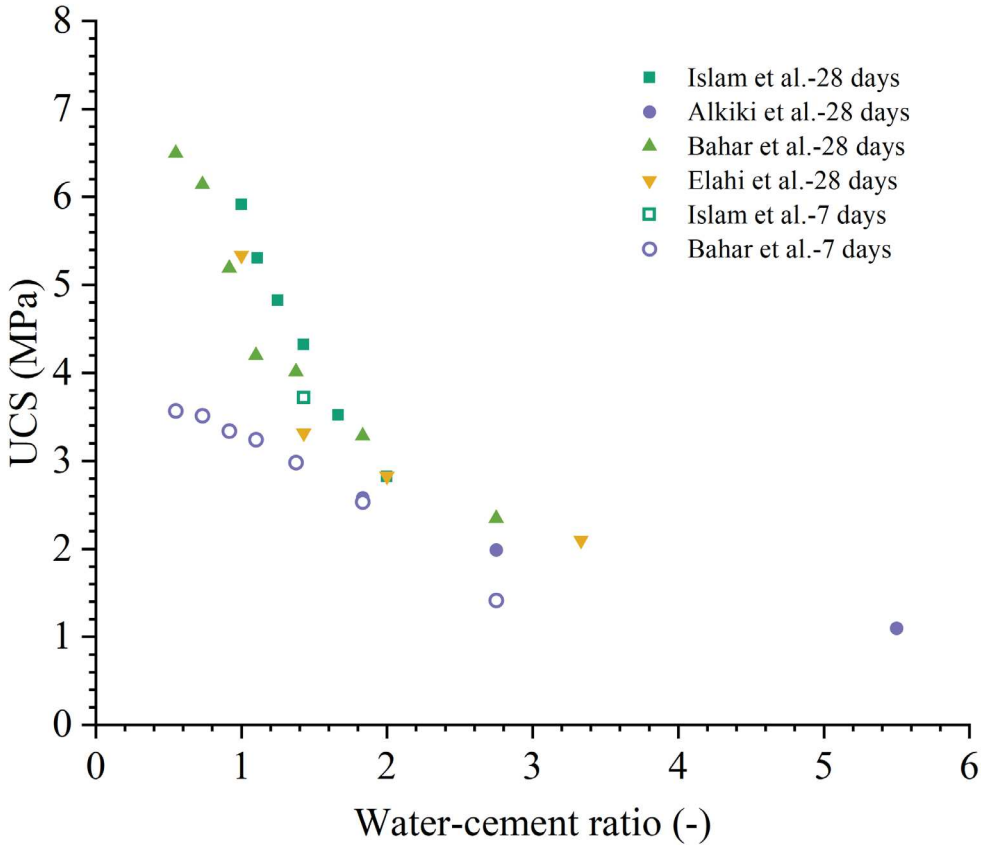

Figure 1.13. UCS of CSRE and according to water-cement ratio

In addition, the curing method also influences the after-cured strength [117]. When the hydration process proceeds in moist conditions, for example, in moisture air or sealed condition, the compressive strength increases contentiously and then trend to be stabilized with time [118]. When cement-based materials are exposed to normal dry air conditions, the strength increments contributed by cement hydration are weakened due to the evaporation process, while the strength increments caused by the decrease of water content (w) [102] are enhanced. The cement hydration process may be interrupted due to a hot and dry curing condition [119]. Moreover, the increases in the ambient curing temperature (T) [120] (under 60 ºC [121,122]) increase the degree of hydration (δ) of cement [123], which leads to a higher material strength [124]. On the contrary, if the temperature (T) is below the freezing point of water, the cement hydration process will not be contributed by water anymore [125]. For cement-based earth materials, a higher curing ambient relative humidity will lead to a higher mechanical resistance when the curing temperature (T) is constant [126]. In other words, the strength of CSRE is affected by the combined effects of cement content, temperature (T) and material humidity [127–129].

1.2.1.2 Tensile strength

The tensile strength of URE is usually estimated by using two different methods: direct tension test and splitting (Brazilian) test [49,57,67,69,85,87,88,92,130–134]. Araki et al. [67] found that tensile strength obtained by the direct tension test is 15%-20% lower than that obtained by the splitting test. In this work, the investigated tensile strength obtained through splitting (Brazilian) test is transferred to the direct tensile strength (T_f) with the ratio of 0.825. The direct tensile strengths (T_f) of URE and CSRE are introduced in section 1.2.1.2.1 and 1.2.1.2.2, respectively.

1.2.1.2.1 Tensile strength of URE

Gerard et al. [88] carried out the tensile strength tests under different suctions by using the Brazilian method and observed an increase of the tensile strength with suction (s), which means the tensile strength decreases when water content (w) increases. We investigated the effects of water on tensile strength of URE from different experimental results [67,88,92], and the results are illustrated Figure 1.14 in gravimetric water content (w) – tensile strength (T_f) scale.

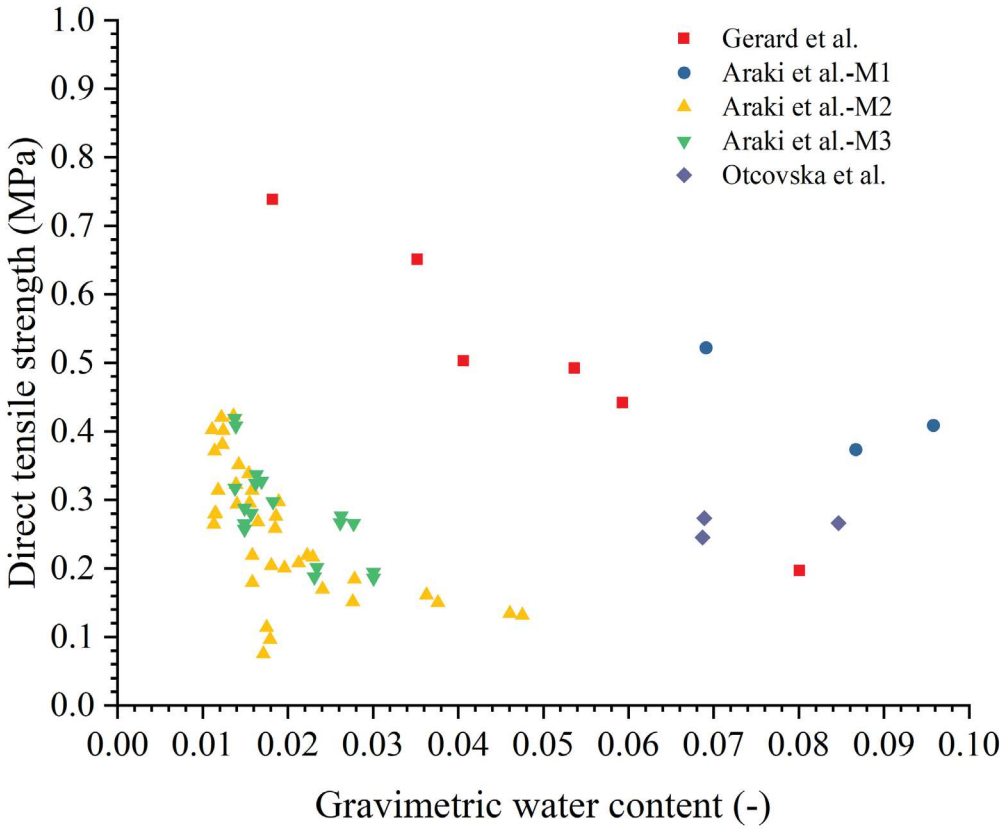

Figure 1.14. Direct tensile strength of URE according to gravimetric water content [67,88,92]

It can be observed from Figure 1.14 that the tensile strength of URE has the trend to be decreased due to the increase of water content (w). However, for the results from different authors or the results from the same author but different material types, the same water content (w) does not lead to the same tensile strength. It means that, similar to UCS, tensile strength of URE is also influenced by the GSD, dry density (ρ_d) and water. Instead of forecasting tensile strength based on the aforementioned parameters, researchers are more inclined to develop a relationship between tensile strength and UCS, because UCS is extensively and regularly used as a measure of the mechanical resistance of various URE materials. Bui et al. [130] found that tensile strength of URE may be estimated equal to 0.11 times of UCS value. Perić [81] recommended the ratio between tensile strength and UCS of URE equals to 0.1 when UCS over 1 MPa, and the ratio equals to 0.2 for URE with UCS lower than 1 MPa. To have a global view about the relation of direct tensile strength (T_f) and UCS of URE materials, the experimental results from different authors [67,87,88,92,130,135] are investigated in this work, and the results are presented in Figure 1.15.

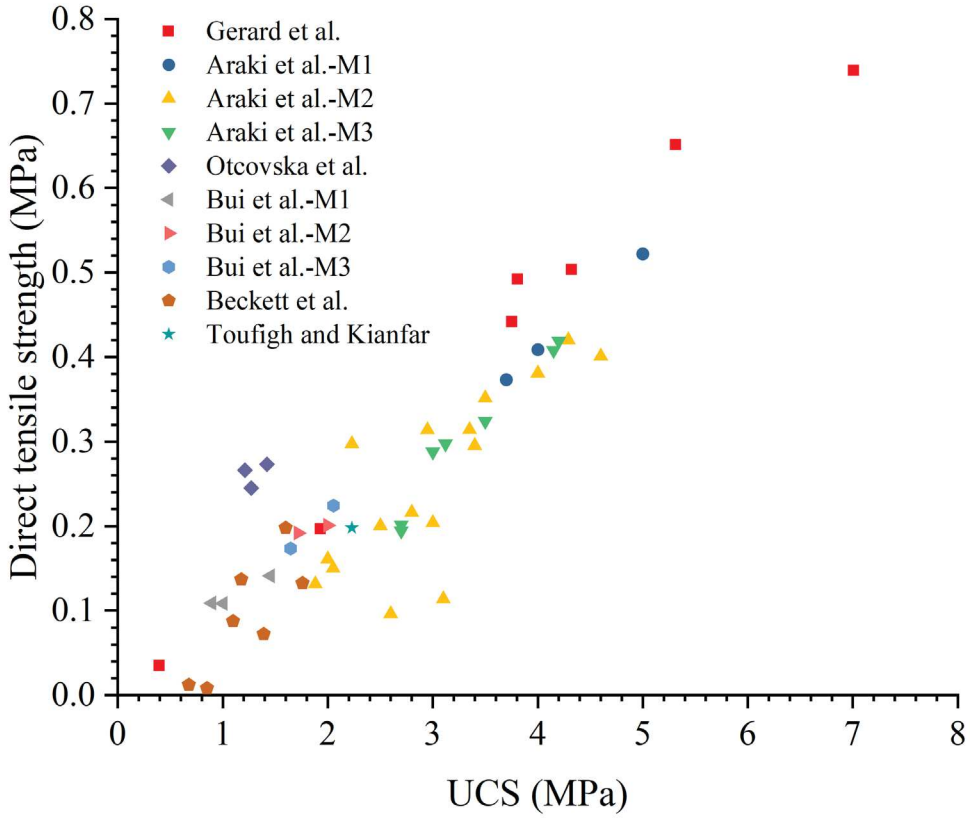

Figure 1.15. Direct tensile strength of URE according to UCS [67,87,88,92,130,135]

The results show that the tensile strength is more correlated to UCS than water content (w) for various UREs. Thus, it may be suitable to predict the tensile strength through UCS of URE materials in a global view.

1.2.1.2.2 Tensile strength of CSRE

Several experimental tests [46,49,57,67,85,87,88,92,100,130–137] are investigated with the purpose of having a global view about the relation between the direct tensile strength (T_f) and UCS of CSRE. These investigations are compared with the results for URE as described in Figure 1.15, and the relation and the comparation are then presented in Figure 1.16.

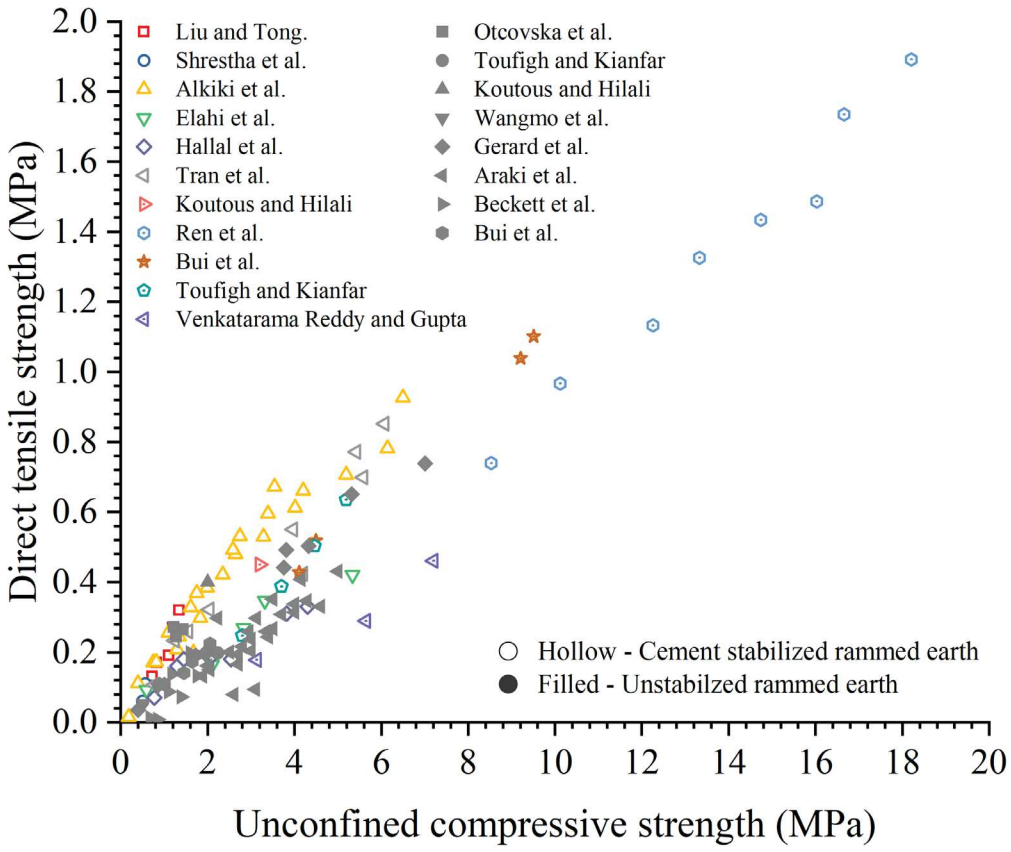

Figure 1.16. Direct tensile strength of URE and CSRE according to UCS [46,49,57,67,85,87,88,92,100,130–137]

An approximately linear relationship seems exits for the correlation of tensile strength and UCS for CSRE and URE. Bui et al. [130] examined the correlation between the tensile strength and UCS of CSRE with and without cement, and they proposed a constant ratio of 0.11 for their correlation. A similar ratio of 0.1 is recommended by Meek et al. [138] for CSRE materials.

1.2.1.3 Elastic modulus at failure

For a linear isotropic elastic material, its elastic behavior can be fully characterized by the knowledge of two elastic constants. Typical elastic constants used to characterize an isotropic solid are elastic modulus, Poisson's ratio (ν), the bulk modulus, the shear modulus, Lamé constants, and the components of the stiffness tensor. In this study, the CSRE and URE are considered as elastic perfectly plastic material, and two of the aforementioned parameters, namely, the elastic modulus at failure and Poisson's ratio (ν) are used to describe their elastic behaviors of URE and CSRE. This section introduces the elastic modulus of URE and CSRE. In actuality, the CSRE and URE are not the linear elastic material to a complete degree. Various studies have used different elastic modulus values (Figure 1.17) to appropriately represent the elasticity of a material.

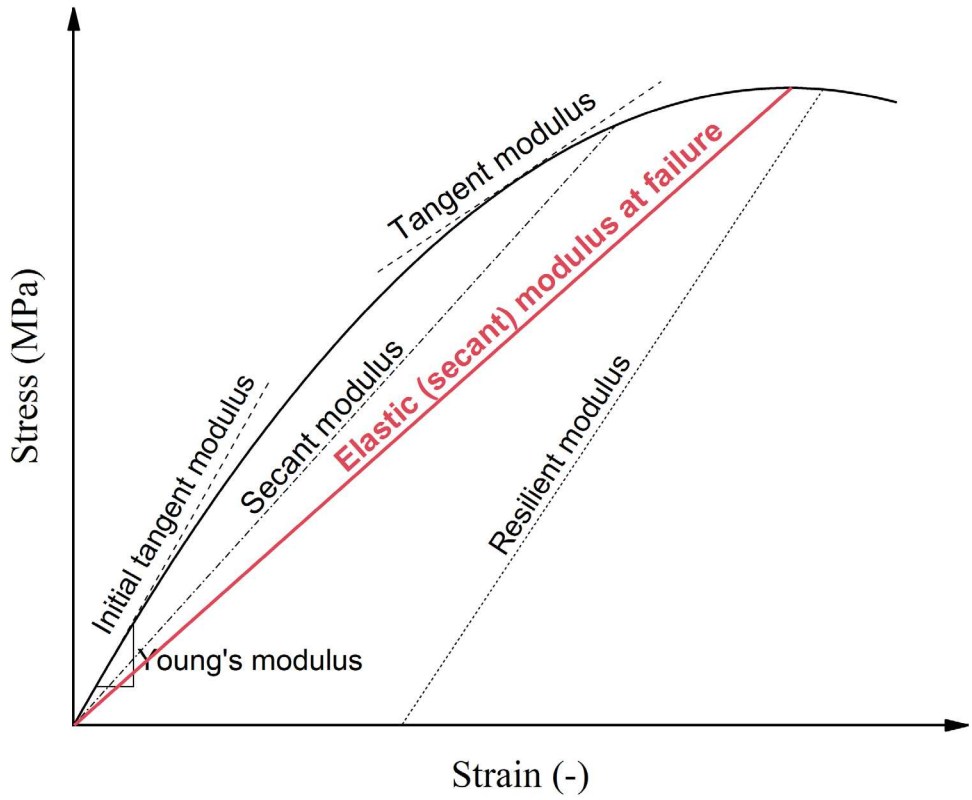

Figure 1.17. Schematic of various elastic modulus used to describe the elastic behaviors of CSRE and URE

1.2.1.3.1 Elastic modulus at failure of URE

Bui & Morel [139] studies the anisotropy of URE, and their experimental results show that the resilient modulus of URE first increases with loadings and then remains the same at a high stress level. They considered that the phenomenon may be generated by microcrack closures in

the perpendicular (compacting) direction and not in the parallel direction. The elastic modulus at failure in the two directions of the test are varying in almost the same range between 67 and 81 MPa perpendicular to layers and between 68 and 76 MPa parallel to layers. They observed that the low levels of preloading the failure moduli in the direction parallel to the layers are superior to those perpendicular to the layers (by about 25%). Parul Chauhan et al. [31] studies the variation of initial tangent modulus with different imposed suctions during UCS tests for the stress path of q/p=3. The initial tangent modulus decreases almost 3 times as the suction (s) reduces from 331.3 MPa to 3.8 MPa while it remains constant at high suction (s) values. In addition, their results show that the resilient modulus decreases as the loads of loading-unloading path increases. The decreasing of the resilient modulus during loading-unloading condition is also observed by Bui et al. [87]. Bertrand François et al. [86] studies the variation of Young's modulus of URE according to suction (s) by performing UCS test where the stress path is q/p=3. The Young's modulus was obtained as the steepest slope of the axial stress – axial strain curve in a strain interval of 0.2%. Bui et al. [87] obtained the Young's modulus for stresses below 15% of maximum stress value of 0.12MPa in their studies. Moreover, the elastic modulus at failure decreases on the wetting path and it increases on the drying path due to the variation of water content (w). Since the UCS is popularly used to estimate the elastic behavior of earth soil [140,141] and concrete [142–144], then the relation between UCS and elastic modulus at failure of URE is investigated by consulting the experimental results [31,64,83,88–90,135]. The related results are presented in Figure 1.18.

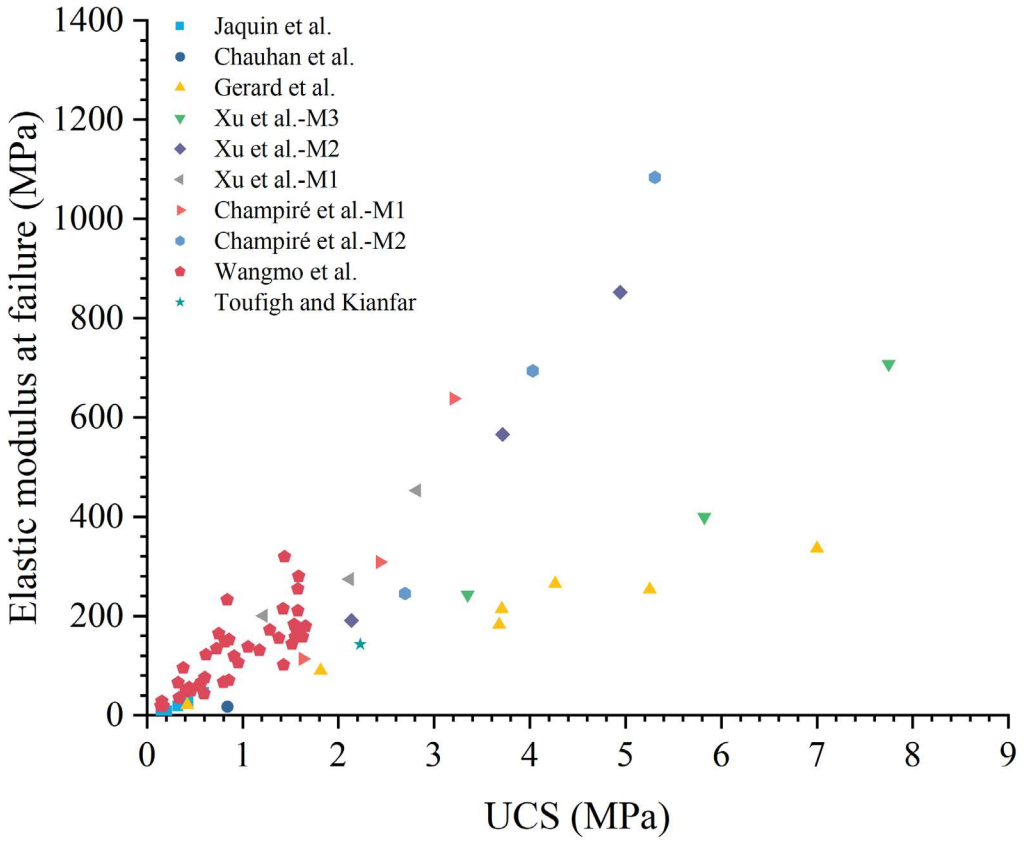

Figure 1.18. Elastic modulus at failure of URE according to UCS [31,64,83,88–90,135]

It can be observed from Figure 1.18 that the stiffness of URE is increased as the strength increases. In addition, an approximate linear relation is observed between the modulus at failure and UCS for URE material. However, the elastic behavior of URE still varies for the results from different authors when the UCS keeps the same. It means there are other potential factors, such as GSD, water, dry density, may influence the elastic characteristics of URE at the same time.

1.2.1.3.2 Elastic modulus at failure of CSRE

Some experimental results [28,31,38,46,54,57,64,83,88–90,135,135,145] are investigated with the purpose of having a global view about the relation between the elastic modulus at failure and UCS of CSRE. These investigations are compared with the results for URE as described in Figure 1.18, and the relation and the comparation are then presented in Figure 1.19.

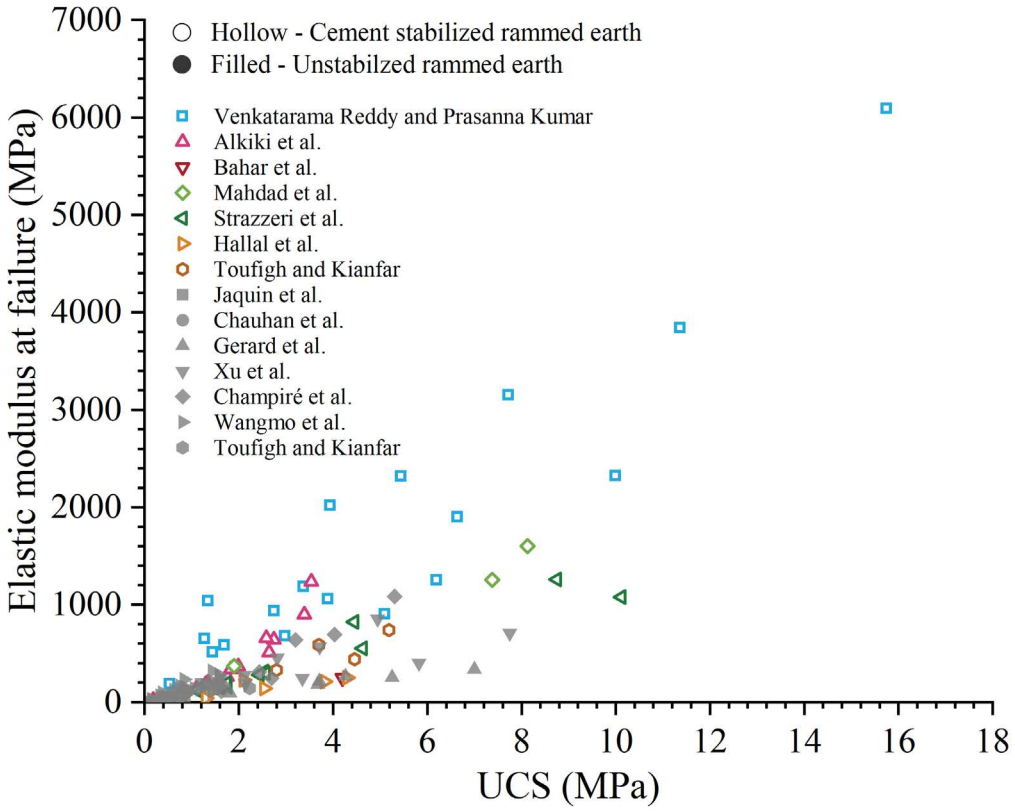

Figure 1.19. Elastic modulus at failure of CSRE and URE according to UCS [28,31,38,46,54,57,64,83,88–90,135,135,145]

The comparations described in Figure 1.19 shows that the stiffness of CSRE is also increases with UCS for all types of CSREs. Owing to the addition of cement, CSRE has a higher elastic modulus at failure than URE in a global view when UCS remains the same. Similar to URE, apparent discrepancies can be observed due to the variation in material types.

1.2.1.4 Poisson's ratio of URE and CSRE

It has been found in rock mechanics that the Poisson's ratio (ν) of rock [146] varies in the range of 0.05 to 0.4, and increases when elastic modulus [147] and suction (s) decreases [148]. And similar phenomena are showed by Xu et al. [90] and Champiré et al. [89]. By knowing the volumetric strain and vertical strain, the experimental results from Xu et al. and Champiré et al. show that the Poisson's ratio (ν) decreases when with suction (s) and loading pressure increases. In this work, since URE and CSRE are considered as isotropic elastic perfectly plastic material, the effects of loading pressure on Poisson's ratio (ν) are not considered. And the Poisson's ratio (ν) is correlated only to water content (w) for simplicity.

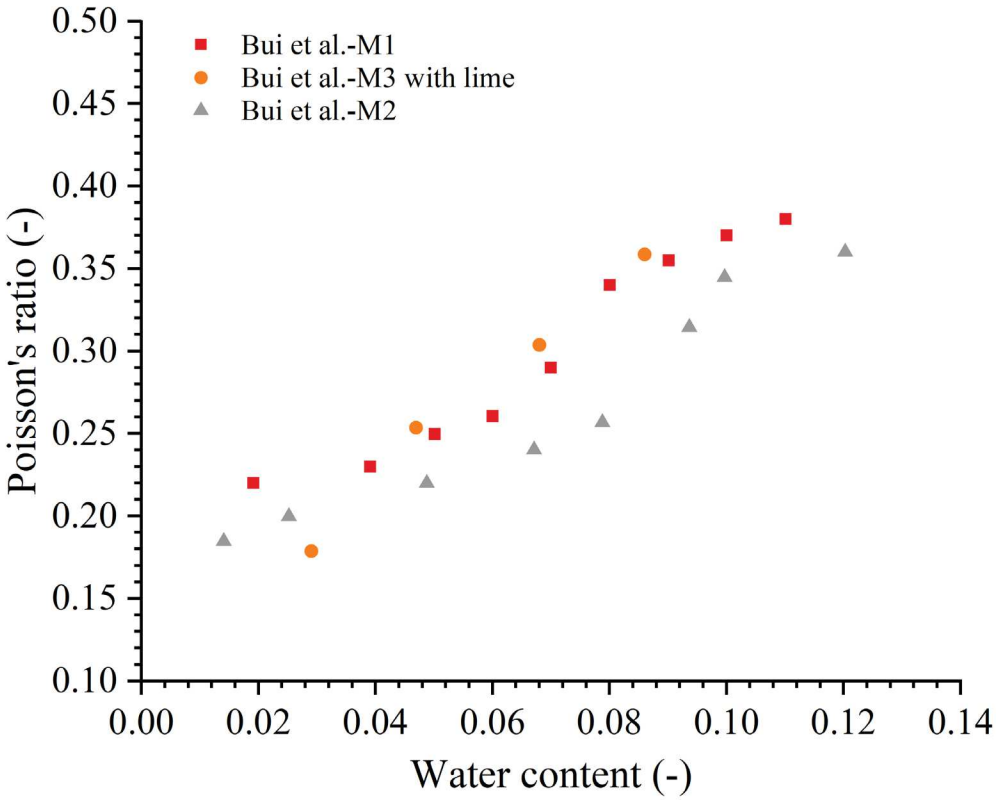

Figure 1.20. Poisson's ratio (ν) of URE and lime stabilized rammed earth according to water content (w) [87]

Anglade et al. [37] found that Poisson's ratio (ν) of URE changes in the range of 0.25 to 0.45. Bui et al. [87] observed that Poisson's ratio (ν) of URE is decreased from around 0.37 for a wet condition to about 0.2 when the material is dried (water content (w) <4%). François et al. [86] took the value of 0.25 to simulate the structural behaviour of URE building under hygroscopic conditions. Meek et al. [138] tests the Poisson's ratio (ν) of CSRE, and they considered the value of 0.2 may be a reasonable value for CSRE at dry conditions. The relation between Poisson's ratio (ν) and water content (w) for URE and lime stabilized rammed earth [87] are illustrated in Figure 1.20.

1.2.2 Thermal behaviors

When building materials are subjected to an inside thermal input, two main material thermal capacities are usually considered. One is the capacity of heat insulation, and another is the capacity of heat storage. And when the two capacities are considered at the same time, the thermal diffusivity is often used to indicate the capacity of the material to conduct thermal energy with reference to store thermal energy [149]. Materials with low thermal diffusivity require a larger time to return to an thermal equilibrium state than materials with high thermal

diffusivity [150]. In this section, the properties of heat insulation and storage of URE and CSRE are introduced with the notion of thermal conductivity and specific heat capacity, respectively.

1.2.2.1 Thermal conductivity

The RSI ($m^2 \cdot K \cdot W^{-1}$) value is defined as the thickness divided by thermal conductivity [151], which is a measure of resistance to heat flow through a given thickness of a building material. And the higher the RSI, the more thermal resistance the material has and therefore the better its insulating properties. According to the definition of RSI, the thermal resistance can be improved by increasing the wall thickness or decreasing the thermal conductivity of the building material. In this part, we focus on the thermal conductivity of the material itself, since the wall thickness can be changed easily in practice.

1.2.2.1.1 Dry density effect on thermal conductivity of URE

Various methods have been attempted to decrease the thermal conductivity of URE. Correia da Silva et al. [152] observed that the inclusion of 10% expanded granulated cork in URE improves the thermal insulation by 12% but reduces strength by 28% at the same time. Stone et al. [153] found that the 20% additions of expanded perlite in URE improves the thermal insulation by 2% but reduces strength by 50%. Karrech et al. [154] observed that the 25% additions of Polystyrene in CSRE increases the thermal insulation by 250% but decreases the strength by 91%. Moreover, the inclusion of Spinifex fibers increase the thermal resistance [155], and the additions of crumb rubber reduces the strength and the rate of temperature (T) variations [156,157]. The causes of these changes are still unclear and are under investigation.

Generally, URE materials have the thermal conductivities ranges from 0.6 to 1.6 $W \cdot m^{-1} \cdot K^{-1}$ [158], and it increases with the increase of density [82,135,159–161]. The thermal conductivity varies in the range of 0.6 to 1.5 $W \cdot m^{-1} \cdot K^{-1}$ which is considered as low thermal resistance [155]. To better understand the thermal conductivity of URE materials, we investigated the effects of dry density (ρ_d) [37,162–170] on the thermal conductivity of various URE materials and the related results are presented in Figure 1.21.

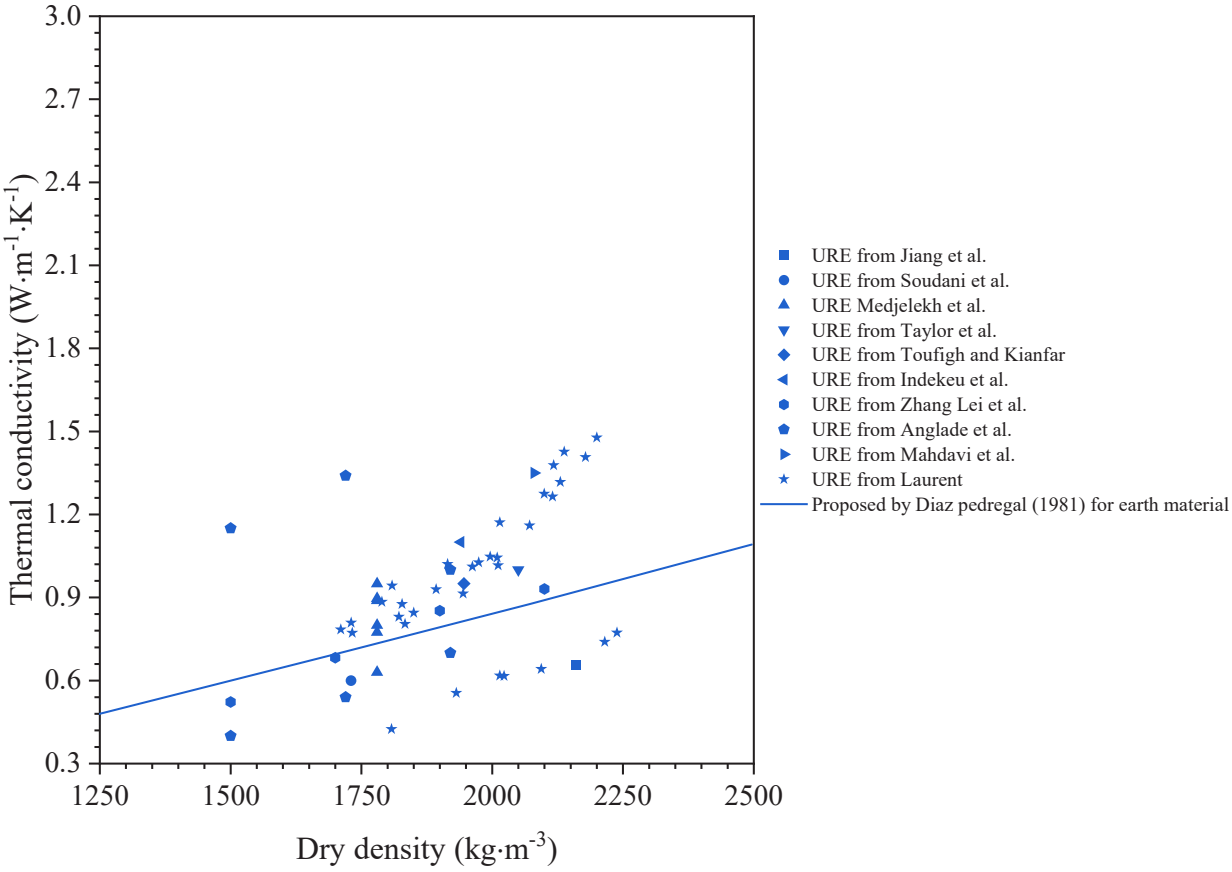

Figure 1.21. Effect of dry density on the thermal conductivity of URE materials [37,162–170]

1.2.2.1.2 Dry density effect on thermal conductivity of CSRE

When cement is added to URE material, URE will be transferred to CSRE material. The effect of additional cement on the thermal behaviors of CSRE are introduced in the following texts (effects on mechanical strength of CSRE have been illustrated in section 1.2.1).

Saidi et al. [171] found that the thermal conductivity of after-cured dry CSRE increases with initial cement content. However, Laurent [163] observed the thermal conductivity of after-cured dry CSRE slightly decreases with initial cement content. Some authors [172,173] found that the addition of cement and the hydration process has a negligible effect on the thermal conductivity of wet CSRE after curing. The experimental results from Laurent [163] indicates that the variations of temperature (T) in the range of 0 to 60 ºC does not have apparent effects on thermal conductivity of CSRE without cement (URE). Zhang et al. [173] have investigated the thermal conductivity of CSRE and concluded that the thermal conductivity of CSRE is mainly influenced by the dry density (ρ_d) and water content (w). Furthermore, when the dry density (ρ_d) keeps the same, the thermal conductivity of CSRE is mainly affected by water content (w) and less influenced by cement content [174]. To have a global understanding about rammed earth materials, by neglecting the effects of temperature (T) [175], we investigated the effects of dry

density (ρ_d) [37,135,154,162–170,176–188] on the thermal conductivity of various rammed earth materials from URE to CSRE, concrete, cement mortar and other stabilized rammed earth. And the investigation results are presented in Figure 1.22.

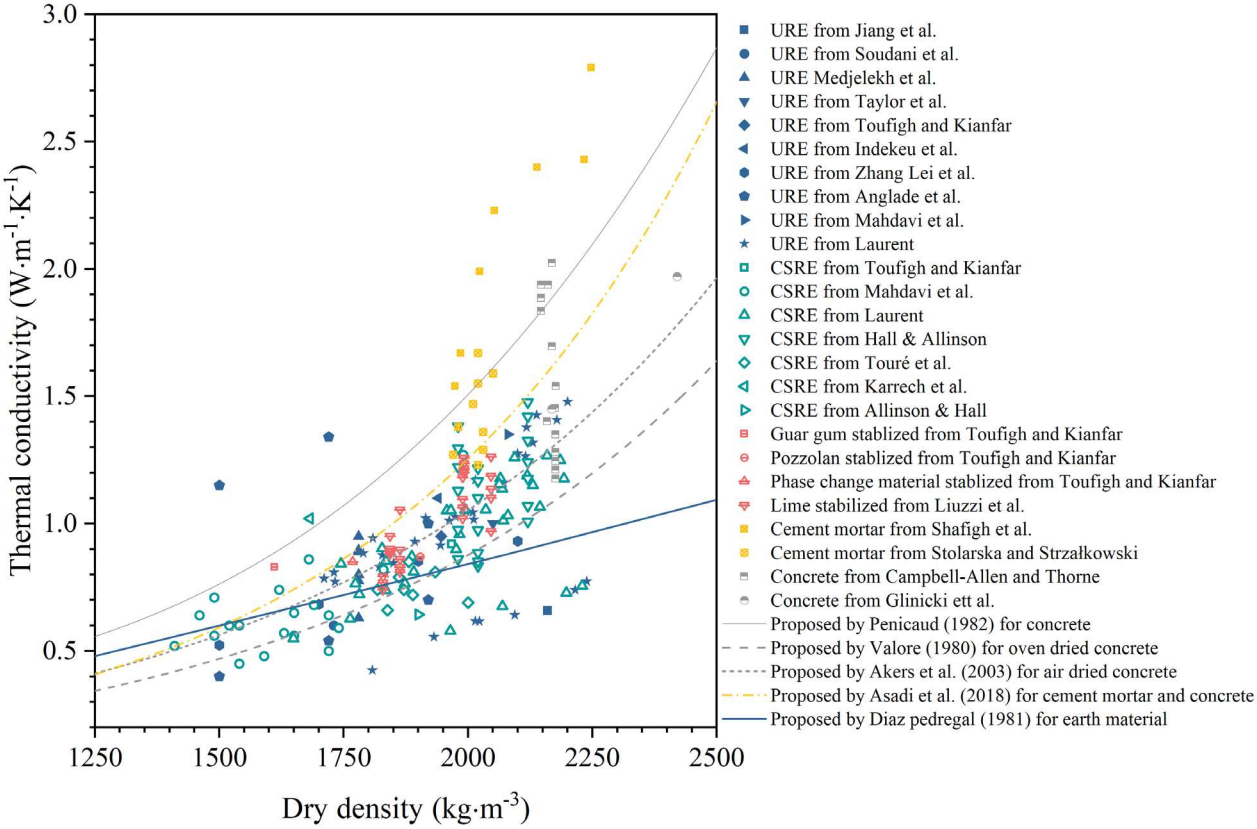

Figure 1.22. Effect of dry density on the thermal conductivity of URE, CSRE and other stabilized rammed earth materials [37,135,154,162–169,176–187]

It can be observed from Figure 1.22 that the thermal conductivity of the studied building materials changes in the range of 0.3 to 2.9 $W \cdot m^{-1} \cdot K^{-1}$. The thermal conductivities of all the studied materials are increased with the dry density (ρ_d). The cement mortar has the highest thermal conductivity than other materials due to a higher mass of water included in the material. And the cement mortar and concrete have relatively higher thermal conductivity (or lower thermal insulation) than all types of studied rammed earth materials. In addition, the thermal conductivity of rammed earth varies in the range of 0.3 to 1.6 $W \cdot m^{-1} \cdot K^{-1}$, and no apparent differences have been observed for URE, CSRE and other stabilized rammed earth materials. The results from Laurent and Toufigh & Kianfar indicate that the thermal conductivity of URE and CSRE is more influenced by dry density (ρ_d) than the cement additions. And the results from Anglade et al. show that, even with a low dry density (ρ_d) (<1800 $kg \cdot m^{-3}$), the saturated URE still process high thermal conductivity over 1.1 $W \cdot m^{-1} \cdot K^{-1}$. It means the effects of water

plays an important role in the thermal resistance of URE material. Valore [187] proposed an empirical equation to estimate oven dry concrete thermal conductivity based on dry density (ρ_d). Base on Valore's equation Akers et al. (ACI committee) [185] proposed to describe the air dried thermal conductivity of concrete, and these predictions show that oven dried concrete has lower thermal conductivity than air dried concrete due to the existence of water. However, the method proposed by Penicaud [188] shows a higher thermal conductivity of the concrete. These discrepancies indicate that the thermal conductivity of concrete cannot be accurately predicted solely by dry density (ρ_d), and the effects of water need to be at least considered. Similarly, predicting the thermal conductivity of earth materials solely based its dry density (ρ_d) [170,189] or water content [189] may not be convincing. If it is necessary, the other potential influential factors are needed to be confined. In fact, various models considering both the effects of dry density (or porosity) and water [190–198] have been proposed to estimate the thermal conductivity of unsaturated soils and their predictions are compared with the experimental data as presented in Fig 1.22.

1.2.2.1.3 Saturation effect on thermal conductivity of URE

As introduced in section 1.2.2.1.2, since URE are produced with the unsaturated soils and CSRE is in the middle of raw soil and ordinary concrete, therefore, the effects of water [37,154,162,164,165,176,177,179,180] on the thermal conductivity of rammed earth materials are also needed to be considered for better predicting their thermal behaviors. Most studies focus on one of these factors without controlling other parameters thoroughly and strictly. Therefore, the thermal properties of URE and CSRE are not well understood for the lack of considering the effects of water, density, soil mineral components etc. at the same time. To better understand the thermal behavior of CSRE and URE, the experimental results considering both the effects of material density and water (introduced in section 1.2.2.1.3 and 1.2.2.2.4) are investigated in this work.

At first, the effects of water saturation (S_r) on the thermal conductivity of various URE [37,162,164,165,180] are investigated, and the related results are presented in Figure 1.23.

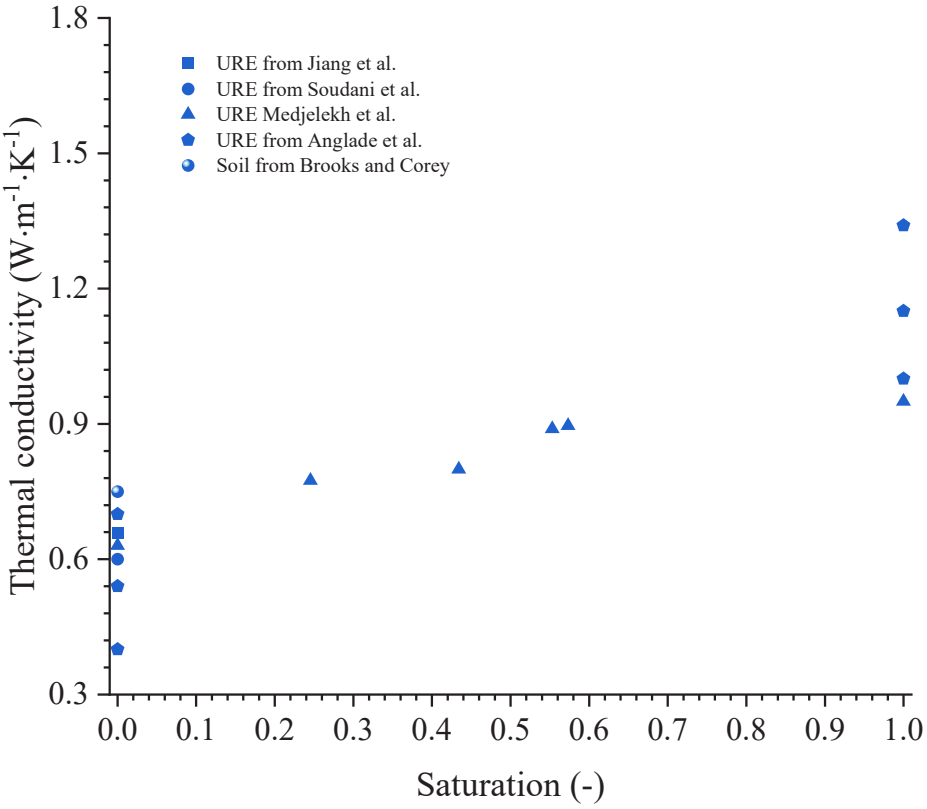

Figure 1.23. Effect of water saturation on the thermal conductivity of URE materials [37,162,164,165,180]

1.2.2.1.4 Saturation effect on thermal conductivity of CSRE

After that, the effects of water saturation (S_r) on thermal conductivity of CSRE as well as lime stabilized rammed earth are investigated, and the related results are combined and presented together in Figure 1.24.

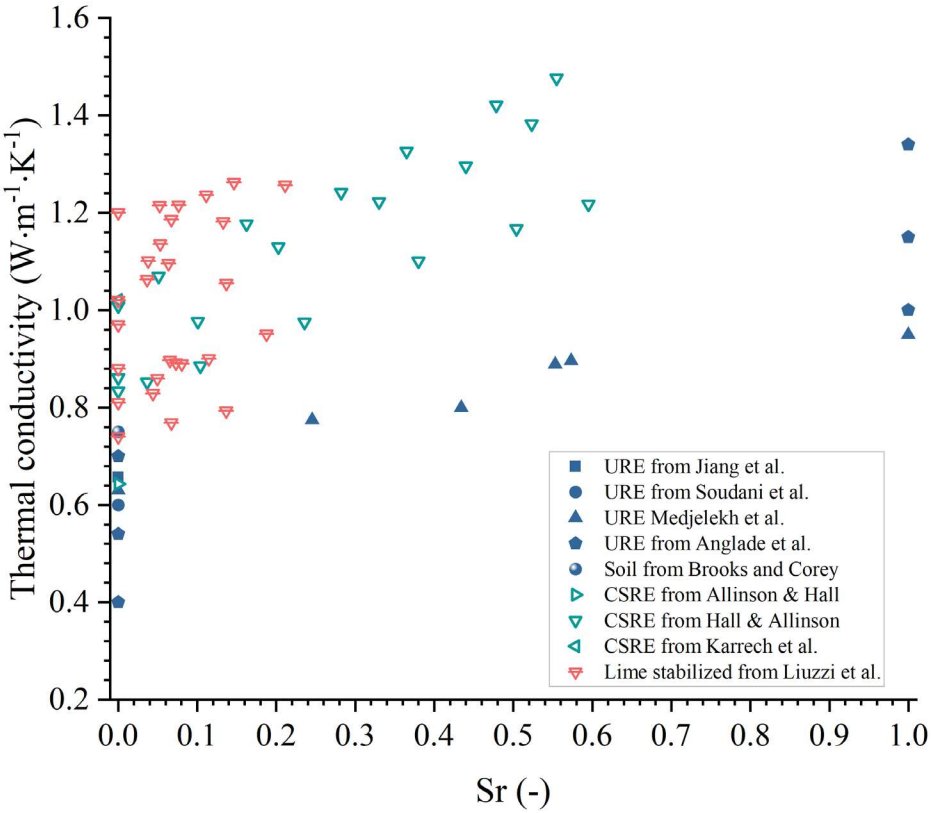

Figure 1.24. Effect of water saturation on the thermal conductivity of soil, URE, CSRE and lime stabilized rammed earth materials [37,154,162,164,165,176,177,179,180]

It can be observed from Figure 1.24 that the thermal conductivity of all types of rammed earth materials are increased with the water saturation (S_r). Confusingly, it seems that the addition of cement and lime increase the thermal conductivity of URE when the saturation (S_r) keeps the same. However, this phenomenon is caused due to the variations of material dry density (ρ_d). Because the investigated URE materials in Figure 1.24 have the dry density (ρ_d) varying in a lower range of 1500 to 1800 kg·m^{-3} than the range of 1800 to 2100 kg·m^{-3} for CSRE and lime stabilized rammed earth. Moreover, when both the dry density (ρ_d) and saturation (S_r) of CSRE and lime stabilized rammed earth remain the same, their thermal conductivity values are close.

1.2.2.2 Heat capacity of URE and CSRE

Minimizing the thermal conductivity or maximizing the RSI value [154] in the rammed earth components in order to minimize the heat transfer is perceived sufficient as a criterion of thermal performance. However, it neglects the significance of heat capacity which indicates the thermal energy storage capacity of the material [149]. Generally, two types of heat capacities are widely used in engineering field. One is the volumetric heat capacity reflecting the heat storage capacity in unit volume, and another is the specific heat capacity showing the heat

storage capacity in unit weight. The specific heat capacity is calculated by dividing the volumetric heat capacity with bulk density. In this work, the specific heat capacity is used for investigations.

The specific heat capacity of rammed earth material consists of three parts, namely, the specific heat capacity of solid, water and gas. The heat capacity of gas in rammed earth is usually not considered for its neglectable weight. Therefore, the combination of the other two main factors, namely, water and solid gives the specific heat capacity of rammed earth. It has been proved that the specific heat capacity of URE increases with water content (w) due to a high specific heat capacity of water [163,199]. Since the thermal properties of water is well measured and understood in history [200–202], the solid part in URE and CSRE material is mainly focused in this work. Since URE is produced solely by soil, then the specific heat capacity of dry soil is also investigated. To eliminate the effects of water, only the specified heat capacities of raw soil [180,203], URE [37,162,164,165,179], CSRE [154,176] and concrete [181] under dry conditions are investigated. And the results are presented in Figure 1.25.

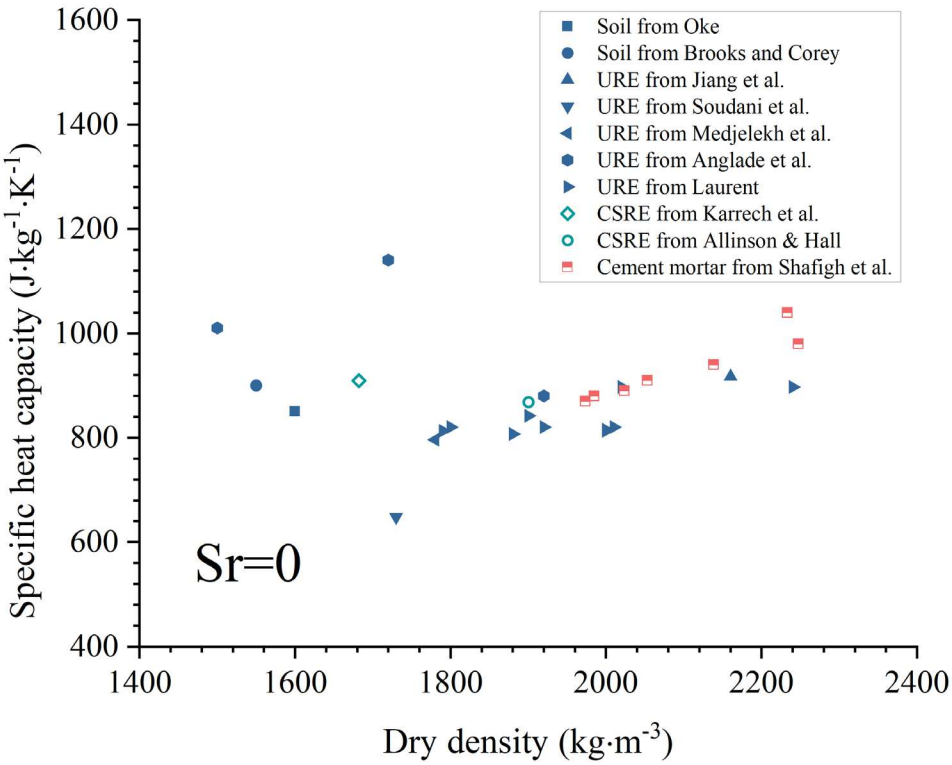

Figure 1.25. Specific heat capacity of dry soil, URE and CSRE according to material dry density [37,154,162,164,165,176,179,180,203]

It can be observed form Figure 1.25 that the dry density (ρ_d) is not the main factor influencing the specific heat capacities of the studied materials. In addition, the specific heat capacity of

dry CSRE and URE vary in the range of 600 to 1200 $J \cdot kg^{-1} \cdot K^{-1}$, and no apparent differences have been observed for the specific heat capacity of dry soil, URE and CSRE.

1.2.3 Hydraulic behaviors

As introduced in section 1.2.1 and 1.2.2, the water is one of the most essential factors influencing the mechanical and thermal behaviors of both URE and CSRE. The mass of water may change continuously with time after compaction, which makes the materials under saturated and unsaturated conditions. The water flow in unsaturated soil is dominated by the two main hydraulic properties [72,204,205], namely, the soil water retention curve (SWRC) and water permeability (or hydraulic conductivity). These two properties are introduced in the section 1.2.3.1 and 1.2.3.2 respectively.

1.2.3.1 Soil water retention curve (SWRC)

For earth materials, the water content (w) and suction (s) are related to each other, and the relations between them form a fundamental material property known as the soil water retention curve (SWRC). The water content (w) can be related to the gravimetric water content (w), volumetric water content (θ) or sometimes the degree of water saturation (S_r). Moreover, the degree of water saturation (S_r) is related to the volumetric water content through: $S_r = \theta / n$.

1.2.3.1.1 Soil water retention curve (SWRC) of URE

It has been observed that the [206] SWRC can be changed by saturation and desaturation cycle of the soil, and this effect is called the hysteresis of SWRC. We investigated the saturation-desaturation cycle on SWRC of URE with the results form Chauhan et al. [31], and the results show that hysteresis of SWRC for URE is not obvious. Furthermore, the effects of temperature on compacted soil with constant dry density is also studied by consulting the results from Villar and Lloret [207]. The effects of saturation-desaturation cycle and temperature on SWRC are presented in Figure 1.26.

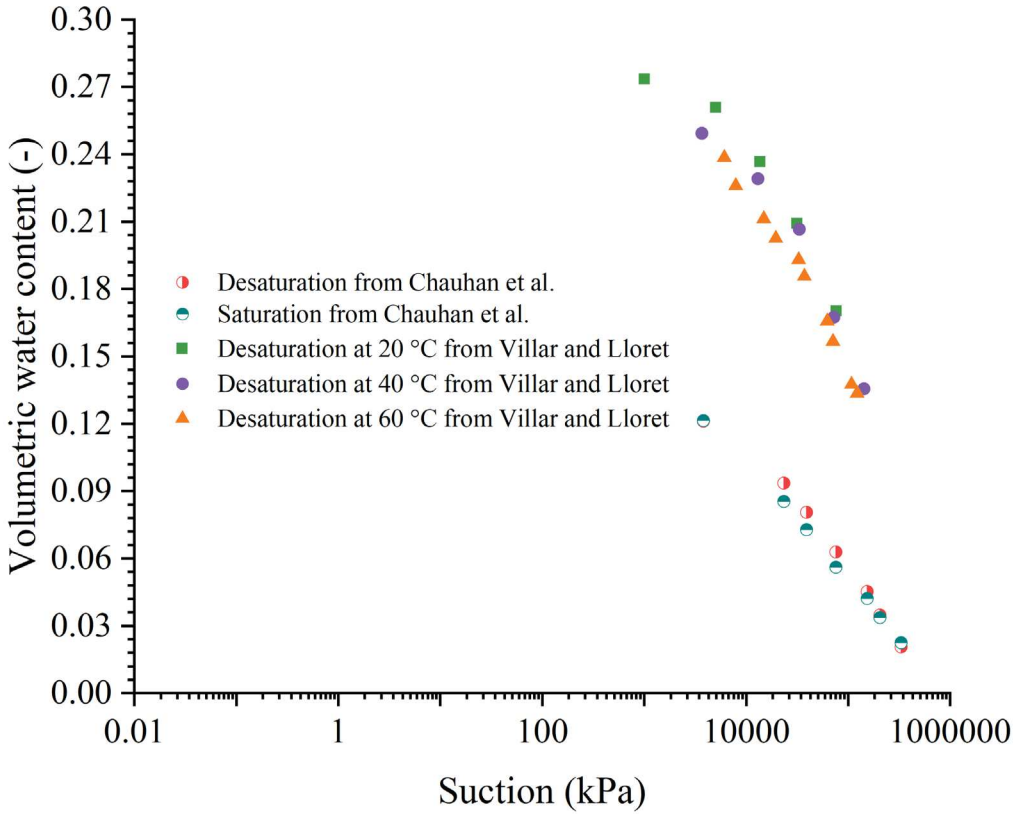

Figure 1.26. Effects of saturation-desaturation and temperature on SWRC of URE [31,207]

For the same material, it can be observed with the results from Chauhan et al. that the water retention capacity is decreased under the saturation process due to the decrease of suction. It has been found that the hysteresis effects seem diminish when the soil density (>1700kg·m^3) increases [208], and URE is compacted with raw soils and it is usually compacted at the highest dry density (MDD), thus, the hysteresis effects on URE is not apparent. Furthermore, the higher the temperature, the lower the water retention capacity for the same material [207]. However, the effects of temperature on SWRC are not significant. The non-obvious of temperature on SWRC is also concluded by Ye et al. for compacted soil [209]. Therefore, the effects of saturation-desaturation and temperature on SWRC of URE are not considered in this work.

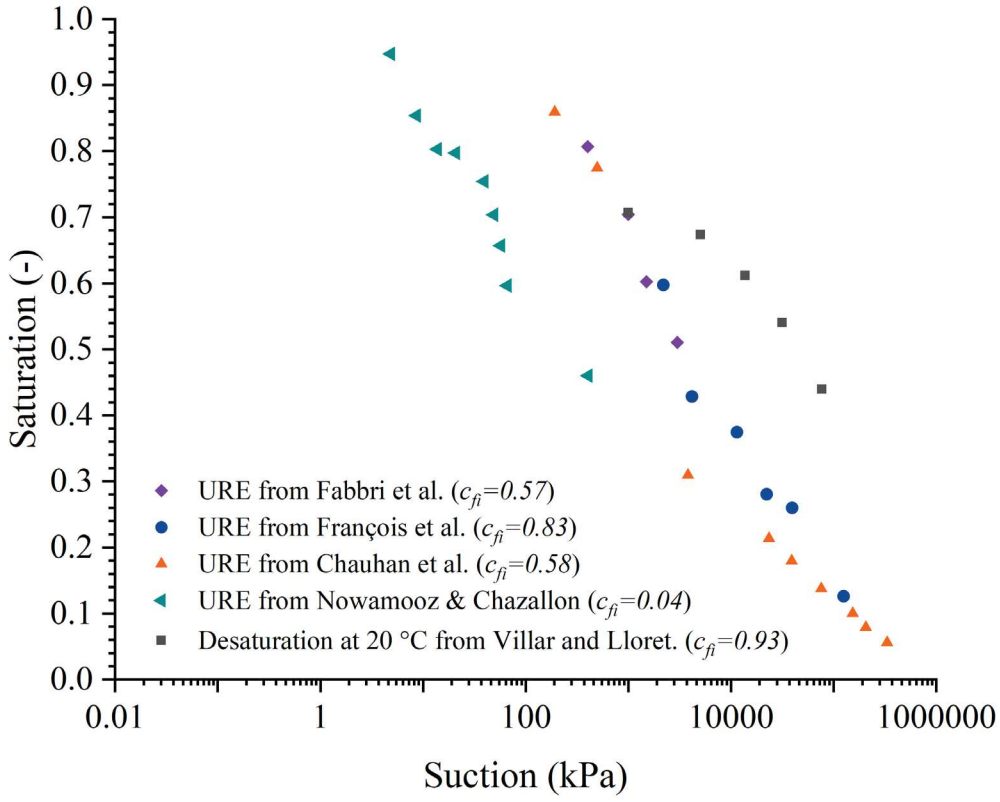

Figure 1.27. Effects of GSD on SWRC of URE [13,70,86,207,210,211]

It has widely been found that GSD has great influences on SWRC. In this work, the mineral effect of the soil is neglected, and the fine content is used to reflect the effects of GSD for simplicity. Some URE materials [13,70,86,207,210,211] with different fine contents are investigated, and the results are presented in Figure 1.27. The results show that SWRC is apparently influenced by the changings of fine content, and the retention capacity is increased when fine content increases.

1.2.3.1.2 Soil water retention curve (SWRC) of CSRE

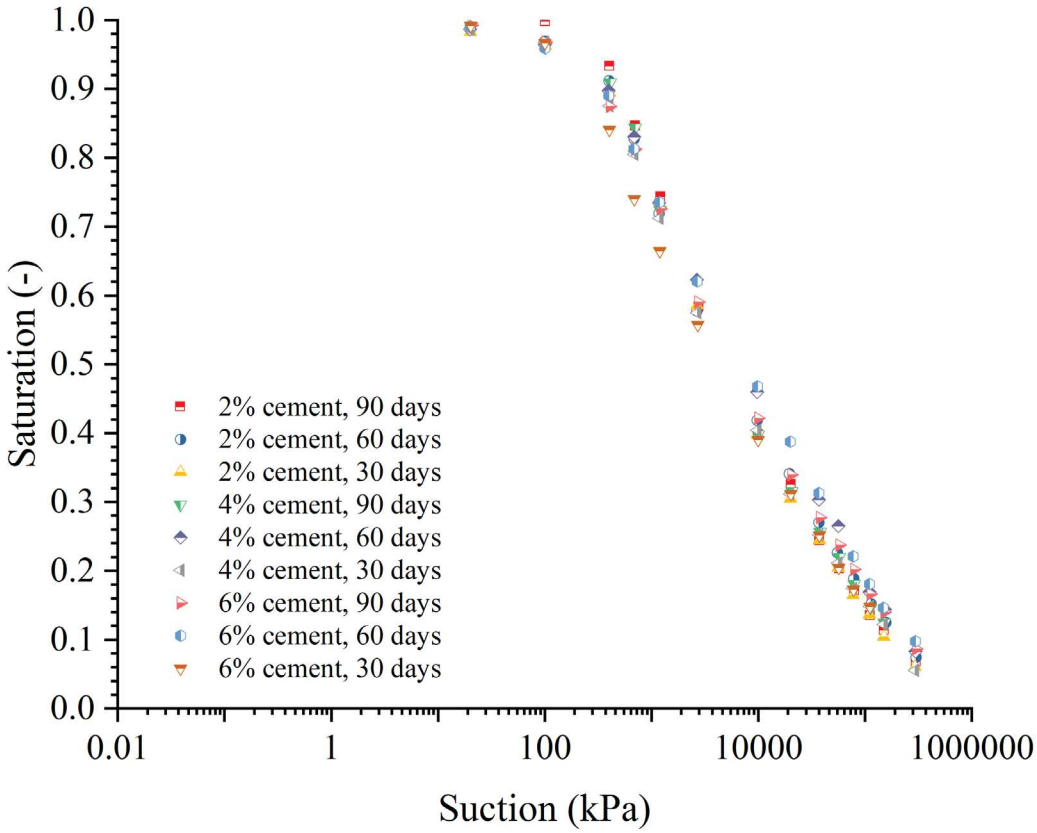

Figure 1.28. Effects of cement content and curing time on SWRC of CSRE [46]

After URE, the SWRC of CSRE is also studied. In Figure 1.28, the experimental results from Alkiki et al. [46] show that the CSRE follows similar SWRC. The SWRC of CSRE is not significantly affected by cement content and curing time. And this slight influences of cement hydration on the SWRC is also found by Vitale et al. [212] for cemented soil. Therefore, the effects of cement hydration on SWRC are not considered in this work.

1.2.3.2 Permeability of URE and CSRE

Generally, two parameters are frequently used in engineering field as the indicators to show the mobility of water within a porous media. One is the intrinsic permeability, and another is the hydraulic conductivity. The hydraulic conductivity can be calculated through intrinsic permeability by knowing the water density, water viscosity and gravity. It means that, when the hydraulic conductivity is used, the water mobility is also affected by water density, water viscosity and gravity. For example, the dynamic viscosity of liquid water is decreased when temperature increases [213], then the hydraulic conductivity of URE and CSRE can be also influenced by the temperature related properties of water. Therefore, to eliminate the effect of

having multiple variables at the same time, the intrinsic permeability is used in this work. It has been found that the intrinsic water permeability (hydraulic conductivity) of engineering materials, such as soil [214], rock [215] and concrete [216] is decreased when the material dry density increases. In addition, the intrinsic permeability of gas decreases [217] and intrinsic permeability of water increases [218,219] when water content increases. And the intrinsic permeability of gas and water can be decreased or increased over 10000 times [220–224] with the increment of water content. Theoretically, intrinsic permeability is solely depended on the pore geometry of the material, and it is independent of the properties of the fluid. Therefore, the intrinsic permeability measured by using the gas as the pore fluid at dry condition should be the same as that measured by using the water at saturated condition. However, Klinkenberg [225] observed that the saturated intrinsic permeability of gas is higher than that of water, because that the saturated water intrinsic permeability is obtained by suing Darcy's law which neglects the collisions between gas molecules and the solid particles. Tanikawa and Shimamoto [226] found that the intrinsic gas permeability is less than two times of the water permeability, when the intrinsic water permeability is higher than 10E-16 m^{-2}. Li et al. observed that the intrinsic gas permeability of dry cement paste almost equals to that of intrinsic saturated water permeability [227]. For the reason that CSRE (URE) experiences wide range of water content variations during its lifetime, and water has much more significant on the permeability (may be decreased or increased over 10000 times). Therefore, the Klinkenberg effect is not considered in this work, and the intrinsic saturated water permeability is considered equals to the intrinsic gas permeability under dry condition.

After that, the intrinsic gas permeabilities of a typical URE material under dry and wet conditions are investigated, and the experimental results are presented in Figure 1.29. The results [228] show that the investigated URE material has the intrinsic gas permeability around 1.2E-14 m^{-2} under dry condition. In addition, the gas permeability decreases with the water saturation. However, the intrinsic gas permeability decreases only about 30%, which is significantly lower than the soils [220–224] that are transferred from dry to totally saturated condition. This is caused by a narrow range of saturation variations from 0 to 0.16. Moreover, it can be observed that the drying and wetting cycle also influences the material permeability, namely, the saturation path increases the gas permeability. However, this hysteresis effect is not obvious compared to that of saturation.

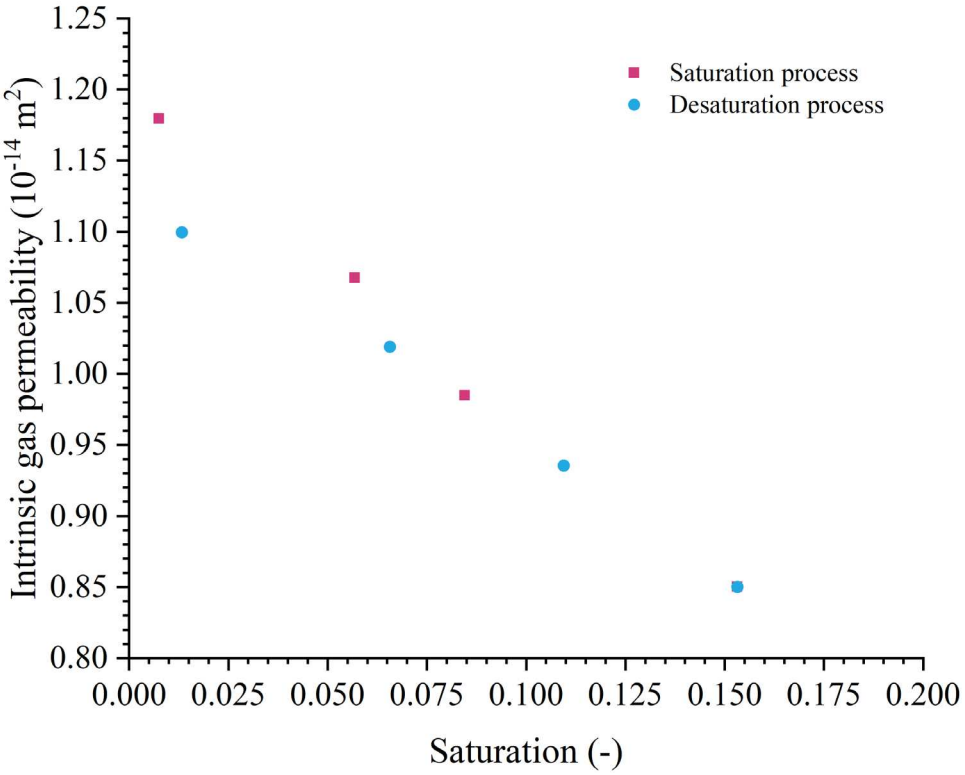

Figure. 1.29 illustrates the influence of curing time on the evolution of the gas permeability [228].

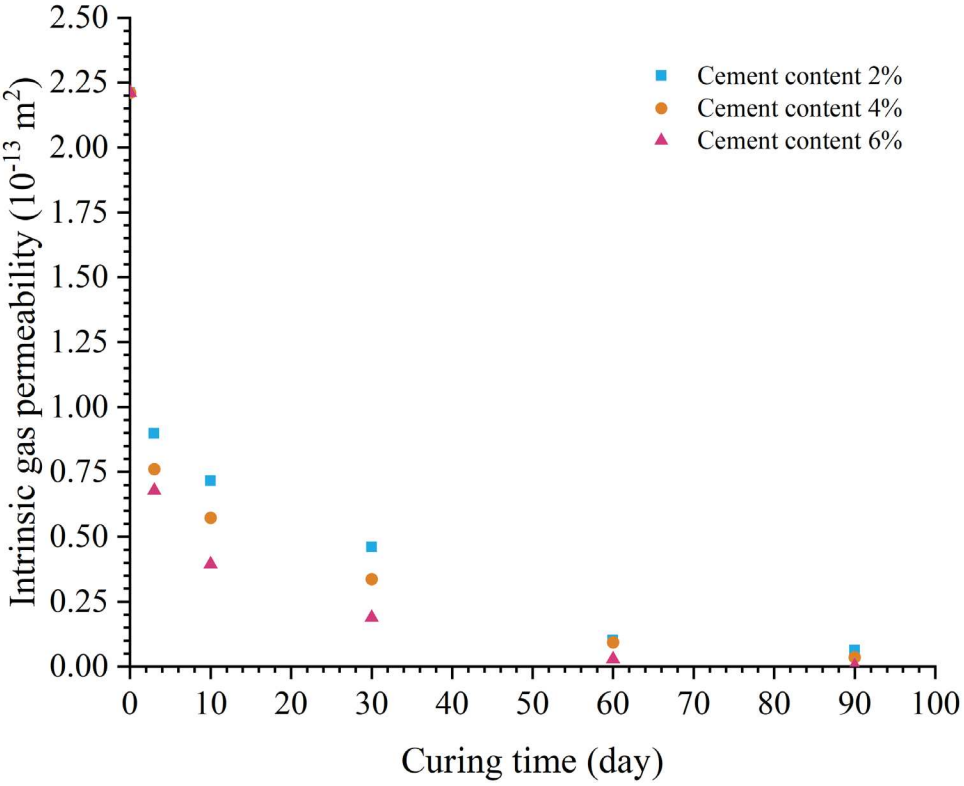

Figure. 1.30 illustrates the influence of curing time on the evolution of the gas permeability [46].

The permeability of various cementitious materials, for example, cement [229], cement paste [230], cement mortar [231] and concrete [232] decreases with the increases of cement content, and increases with the decrease of water cement ratio. We investigated the effects of water, cement and curing time on the permeability of CSRE [46], and the results are presented in Figure 1.30. It shows that, similar to the aforementioned cementitious materials, the permeability of CSRE also decreases with the increases of cement content, and increases with the decrease of water cement ratio. The behavior is caused by the reason that higher cement content leading more cement to be reacted with water, which produces more binders refining the pore structure and reducing the porosity of the material. In addition, the permeability increases with the decrease of water cement ratio, since lower water cement ratio decreases the pacing between cement particles [233]. Furthermore, as the curing time increases, the permeability decreases. This is caused by the increasing amount of cement hydration products during the hydration process with time. The hydration products lead to a progressive refinement of the pore structure and reduction of the porosity of the CSRE materials by means of filling the pores in the cemented matrix and blocking the interconnected pores by the aforementioned hydration products.

1.3 Conclusion

This chapter provides an overview of the rammed earth (RE) construction technique and its uses for the fabrication of unstabilized rammed earth (URE) and cement stabilized rammed earth (CSRE) materials. To understand their fundamental engineering properties and the factors influencing the properties of the two materials, as well as the interconnection and distinction between the researched materials, a literature review regarding the thermo-hydro-mechanical behaviors of URE is conducted. Since CSRE is produced based on URE, the chemo-thermo-hydro-mechanical behaviors of CSRE is investigated after URE. The literature research reveals that the properties of URE and CSRE vary greatly for different experimental results in the literatures, and the absence of a global perspective on all types of URE and CSRE materials impedes the development of a globally recognized standard for URE and CSRE materials. In addition, it has been discovered that the material type, the production method, and the later continuous interaction between the materials and the environment have a substantial impact on

the long-term chemo-thermo-hydro-mechanical (CTHM) properties of URE and CSRE . A model that can describe and forecast the time-dependent CTHM of all types of URE and CSRE materials from a global perspective is of essential importance for the application of these materials and the development of industry standards. In the subsequent chapter, a finite element model is proposed to estimate the long-term CTHM characteristics of various URE and CSRE materials.

Chapter 2. Numerical method

With the aim of understanding the structural behavior of both URE and CSRE construction by using a unique model, the chemo-thermo-hydro-mechanical equations used for the numerical simulations of CSRE (URE) including the cement hydration, moisture transfer, heat transfer, failure criterion as well as the interactions between CSRE (URE) constructions and the surrounding environments are introduced. In addition, the finite element method is used for simulation and the corresponding partial differential equations are solved with the software COMSOL Multiphysics.

2.1 Cement hydration process in CSRE (URE)

The chemical reaction between cement and water consumes the cement and water that are initially added in the raw soil, which leads to the decreases of water content and increases of degree of cement hydration. Moreover, the heat released during the hydration process accelerates the chemical reaction, which in turn increases the water and cement consumption. In this section, the water and temperature dependent cement hydration, the water consumption and the heat release during the hydration process are introduced.

2.1.1 Degree of cement hydration

Since there is no cement in the natural soil, the effects of cement hydration on the characteristics of URE and underground soil are disregarded. The hydration process in CSRE material is depicted by the notion of the degree of cement hydration, whose value is defined by dividing the chemically consumed mass of cement to the mass of cement that is initially added in CSRE. In addition, the degree of cement hydration is calculated according to Hansen & Pedersen [234]:

$$\delta = \delta_{\max} \cdot \delta_r = \delta_{\max} \cdot \exp\left[-\left(\frac{\alpha_h}{t_e}\right)^{\beta_h}\right] \quad (1)$$

where δ (-) is the degree of hydration, δ_r (-) is the relative degree of hydration, δ_{max} (-) is the maximum degree of hydration, α_h (h) and β_h (-) are constant time and shape parameters for hydration process, t_e (s) is the equivalent age.

The maximum degree of hydration depends on the amount of cement and water that are added to the soil mixture [235], whose value can be obtained through [236]:

$$\delta_{\max} = \frac{1.031 \cdot w_{ini}/c_{ini}}{0.194 + w_{ini}/c_{ini}} \quad (2)$$

where w_{ini} (-) is the initial water content in the material, c_{ini} (-) is the initial cement content.

Since the heat released by cement hydration [237] and the curing humidity also affect the hydration process, then the equivalent age of hydration are related to the current temperature [238] and the relative humidity of the material, whose value is obtained through [239] :

$$t_e = \int_0^t \left(\frac{RH-0.55}{0.45}\right)^4 \cdot \exp\left[\frac{E_a}{R}\left(\frac{1}{T_{hr}}-\frac{1}{T}\right)\right] dt \tag{3}$$

where RH (-) is the material relative humidity, E_a ($J \cdot mol^{-1}$) is the activation energy of cement hydration, R ($J \cdot mol^{-1} \cdot K^{-1}$) is the gas constant, T_{hr} (K) is the reference temperature (293.15K), T (K) is the material temperature, t (s) is the time.

The value of activation energy is adopted with the following equations [234]:

$$E_a = \begin{cases} 33500 + 1470(293.15-T), T < 293.15K \\ 33500, T \geqslant 293.15K \end{cases} \tag{4}$$

2.1.2 Water consumed by cement hydration

Throughout the hydration process, the proportion of water used by direct chemical reactions to the mass of hydrated cement remains constant [240]. In addition, the cement hydration products absorb almost the same quantity [240–242] of free water as is consumed by the chemical process, and the absorbed water exists as chemisorbed (physically adsorbed) water [243]. Therefore, the cement hydration water source is acquired using [244,245]:

$$w_{wh} = w_{wch} + w_{ab} = \alpha_{wch} \cdot w_{ch} + w_{ab} = 2\alpha_{wch} \cdot \rho_{dini} \cdot c_{ini} \cdot \delta \tag{5}$$

$$\alpha_{whc} = 0.187\gamma_{C_3S} + 0.158\gamma_{C_2S} + 0.665\gamma_{C_3A} + 0.213\gamma_{C_4AF} \tag{6}$$

where w_{wh} ($kg \cdot m^{-3}$) is the total water mass consumed in unit volume due to cement hydration, w_{wch} ($kg \cdot m^{-3}$) is the mass of chemically consumed water per unit volume during the hydration process, w_{ab} ($kg \cdot m^{-3}$) is the physically absorbed water by hydration products during the hydration process in unit volume, w_{ch} ($kg \cdot m^{-3}$) is the mass of cement chemically reacted with water in unit volume, α_{whc} (-) is the mass ratio of chemically reacted water to reacted cement, ρ_{dini} ($kg \cdot m^{-3}$) is the initial dry density, γ_i (-) means the mass content of the related component (C_3S, C_2S, C_3A, C_4AF, SO_3, FreeCaO, MgO) in the cement.

2.1.3 Heat released by cement hydration

The reaction between cement and water in CSRE generates additional heat. The source of heat created by the hydration process is characterized as:

$$Q_{hy} = \frac{\partial(\delta \cdot c_{ini} \cdot \rho_{dini} \cdot H_{cem})}{\partial t} \tag{7}$$

$$H_{cem} = 500\gamma_{C_3S} + 260\gamma_{C_2S} + 866\gamma_{C_3A} + 420\gamma_{C_4AF} + 624\gamma_{SO_3} + 1186\gamma_{FreeCaO} + 850\gamma_{MgO} \tag{8}$$

where Q_{hy} (W·m^{-3}) is the heat source due to the cement hydration, H_{cem} (J·m^{-3}) is the hydration heat when the cement is 100% hydrated.

2.2 Water flow in CSRE (URE)

Water is considered an incompressible liquid, and its density is considered to be influenced solely by the temperature [246,247]. CSRE is treated as an unsaturated porous material [13,70]. According to the classic theory used for unsaturated soil materials [78,248,249], the inside water flow by considering the volume changes can be described as:

$$\nabla \cdot (nS_r D_w)\nabla\rho_w + S_r\rho_w \frac{\partial n}{\partial t} - \frac{nC_m}{g}\frac{\partial s}{\partial t} + nS_r \frac{\partial \rho_w}{\partial t} + \nabla \cdot (\rho_w \boldsymbol{v_w}) + (nS_r\rho_w)\frac{\partial \varepsilon_v}{\partial t} - m_{wh} = 0 \tag{9}$$

where n (-) is the porosity, S_r (-) is the saturation, D_w (m^2·s^{-1}) is the diffusivity of water [250], ρ_w (kg·m^{-3}) is the density of liquid water [246], C_m (m^{-1}) is the specific liquid water capacity, g (m·s^{-2}) is the gravity acceleration, s (Pa) is the total suction, v_w (m·s^{-1}) is the liquid water velocity, ε_v (-) is the volumetric strain, m_{wh} (kg·m^{-3}·s^{-1}) is the total water source due to cement hydration.

The porosity of the material changes due to the mechanical deformation and accumulation of the hydration process, and its variation can be derived from the mass balance equation:

$$(1-n)\frac{\partial \rho_{so}}{\partial t} - \rho_{so}\frac{\partial n}{\partial t} + \rho_{so}(1-n)\frac{\partial \varepsilon_v}{\partial t} = m_{wch} = \frac{\partial w_{wch}}{\partial t} \tag{10}$$

where w_{wch} (kg·m^{-3}) is the mass of chemically consumed water during the hydration process in unit volume, and ρ_{so} (kg·m^{-3}) is the density of solid particles.

The initial porosity n_{ini} (-) of the material is calculated through:

$$n_{ini} = \frac{\rho_{dini}}{1+c_{ini}}\left(\frac{c_{ini}}{\rho_{cini}} + \frac{1}{\rho_{sini}}\right) \tag{11}$$

where ρ_{dini} (kg·m^{-3}), ρ_c (kg·m^{-3}) and ρ_s (kg·m^{-3}) are the initial dry density of CSRE, the cement particle density and the soil particle density.

The dry density of the CSRE (URE) material is considered to be obtained by knowing the mass of dry solid particles after the specimen has been crushed. Thus, the increased dry density of the material is calculated according to the mass of hydrated water that is consumed during the hydration process through:

$$\rho_d = (1-n)\cdot\rho_{so} = (1-n)\cdot\left(\rho_{soini}+\frac{w_{wh}}{1-n}\right) = (1-n)\cdot\left[\frac{(1+c_{ini})\rho_c\rho_s}{c_{ini}\rho_s+\rho_c}+\frac{w_{wh}}{1-n}\right] \quad (12)$$

where ρ_{so} (kg·m^{-3}) is the density of the solid particles, ρ_{soini} (kg·m^{-3}) is the initial density of the solid particles.

Since rammed earth materials are usually compacted at their MDD (OWC) conditions and then used for construction, thus, the initial water content (initial dry density) can be considered equal to OWC (MDD). Since the stabilizer has a negligible effect on the OWC [251] and MDD of CSRE (URE), the following equation [252] proposed for compacted raw soil (Figure 1.5) is used to describe the initial water content and initial dry density of CSRE (URE) in a global view:

$$\rho_{opt} = \frac{1000}{0.41935+w_{opt}} \quad (13)$$

where w_{opt} (-) is the optimum water content, ρ_{opt} (kg·m^{-3}) is the maximum dry density.

The total suction is calculated through Kelvin equation [253] by relative humidity and temperature variation:

$$s = -\frac{\rho_w RT}{M_w}\ln RH \quad (14)$$

where M_w (kg·mol^{-1}) is the molar mass of water molecule.

The liquid water velocity is calculated through Darcy's law [254]:

$$\boldsymbol{v_w} = -\frac{\kappa\kappa_{rw}}{\mu_w}\nabla(s+\rho_w gD) \quad (15)$$

where κ (m^2) is the saturated water liquid water permeability, κ_{rw} (-) is the relative liquid water permeability, μ_w (Pa·s) is the dynamic viscosity of liquid water, g (m·s^{-2}) is the gravity acceleration and D (m) is the water head.

The dynamic viscosity of liquid water is obtained through [255]:

$$\mu_w = 5.0\times10^{-6}(T-273.15)^2 - 3.0\times10^{-5}(T-273.15) + 0.0018 \quad (16)$$

The saturated liquid water permeability is obtained through Kozeny-Carman equation [256,257]:

$$\kappa = C_{KC}\cdot\frac{e_s^3}{1+e_s} \quad (17)$$

where C_{KC} (m^2) is a material constant parameter equal to 3.81*10^{-13} [228,258] and e_s (-) is the void ratio (obtained from the prosity of the material).

According to the Mualem equation [224], the relative permeability of water is obtained through:

$$\kappa_{rw} = \begin{cases} S_r^{l_{VG}} \left(1-\left(1-S_r^{\frac{n_{VG}}{n_{VG}-1}}\right)^{m_{VG}}\right)^2 & , s > 0 \\ 1 & , s < 0 \end{cases} \quad (18)$$

where l_{VG} (-) is a constant value equals 0.5 [259], m_{VG} (-) and n_{VG} (-) are material dependent constant, their values are corelated with the equation [72]:

$$m_{VG} = 1 - \frac{1}{n_{VG}} \quad (19)$$

The van Genuchten (VG) [72] model by considering the effect of fine content [158,260] for URE (zero cement content) is adopted to illustrate the SWRC (in suction-saturation scale) of CSRE whose average dry density is 2000 kg·m^{-3} through:

$$S_r = \frac{1}{\left(1-\left(\alpha_{VGp}\cdot\frac{s}{\rho_w}\right)^{n_{VG}}\right)^{m_{VG}}} \quad (20)$$

where α_{VGp} (kPa^{-1}) is a material-dependent constant value.

To obtain these SWRC parameters, several reported SWRCs of UREs in literature [13,31,64,86,87] are presented in the volumetric water content-suction plane in Figure 2.1. We fit these curves by using van Genuchten (VG) equations and the fitted parameters are presented in Table 2.1.

SWRC of various URE materials								
Reference	Dry density (kg·m^{-3})	Fine content (-)	α_{VGp} (kPa^{-1})	n_{VG} (-)	m_{VG} (-)	θ_r (-)	θ_s (-)	R^2
Nowamooz & Chazallon [13]	2000	0.04	0.02542	1.4	0.29	0.0068	0.230	0.97
François et al. [86]	2000	0.83	0.00085	1.4	0.29	0.0030	0.230	0.97
Bui et al. [87]- M1	1920	0.35	0.00119	1.4	0.29	0.0234	0.261	0.88
Bui et al. [87]- M2	1920	0.55	0.00342	1.4	0.29	0.0103	0.261	0.94
Bui et al. [87]- M3	1920	0.47	0.00129	1.4	0.29	0.0032	0.261	0.95
Chauhan et al. [31]- desaturation path	1860	0.61	0.00167	1.4	0.29	0.0115	0.285	0.96
Chauhan et al. [31]- saturation path	1860	0.61	0.00176	1.4	0.29	0.0091	0.285	0.97
Jaquin et al. [64]	2039	0.30	0.00610	1.4	0.29	0	0.216	0.98

Table 2.1. VG parameters for different reported SWRCs of URE materials [13,31,64,86,87]

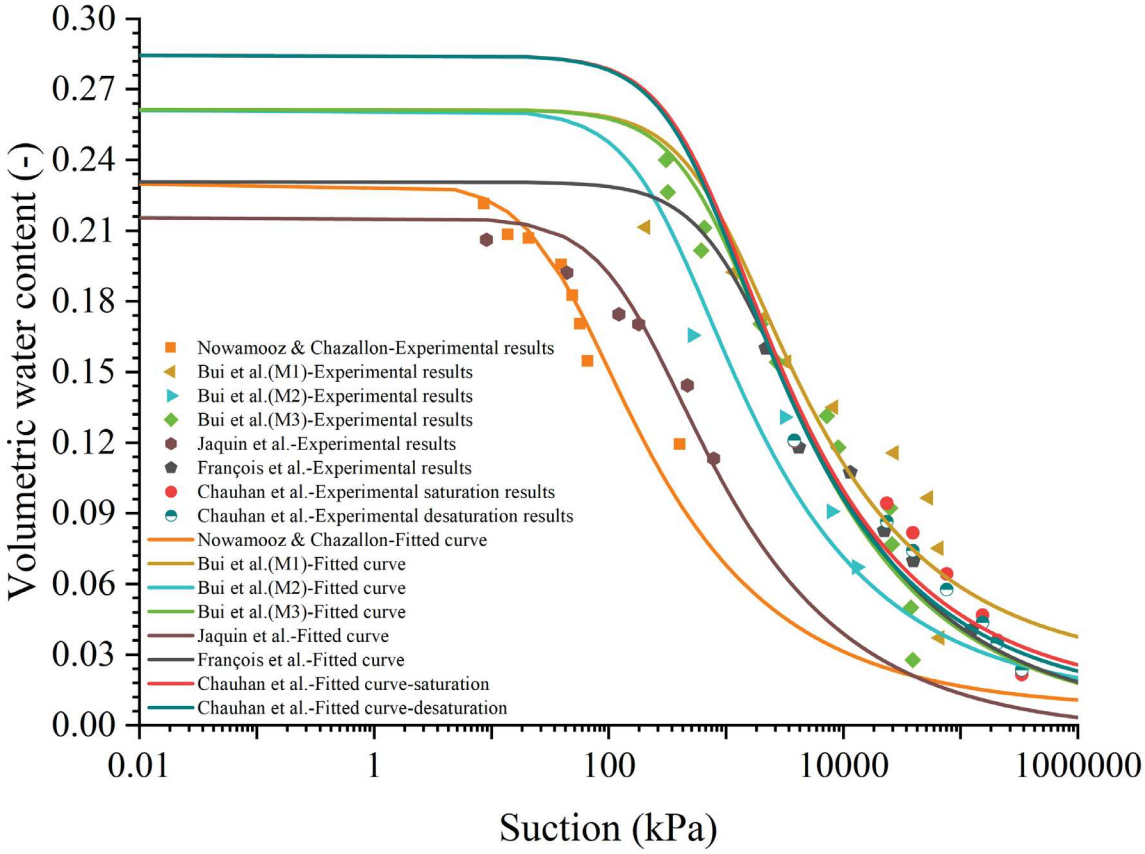

Figure 2.1. Fitted SWRC compared to experiment results reported by different authors[13,31,64,86,87] in volumetric water content -suction plane

The parameter n_{VG} (-) is assumed not affected [261,262] by dry density for a high range of suction of a typical CSRE construction drying in the environment. Therefore, the parameters m_{VG} (-) and n_{VG} (-) are respectively taken equal to 1.4 and 0.29 in this study. The residual volumetric water content θ_r (-) is considered constant equal to 0.0045. Since α_{VG} is inversely related to the air entry value [72]. As, a higher fine content leads to a higher air entry value, α_{VGp} is correlated to fine content through (Figure 2.2):

$$\alpha_{VGp} = 1000\frac{\alpha_{VG}}{\rho_w g} = 0.001 \cdot {c_{fi}}^{-1} \tag{21}$$

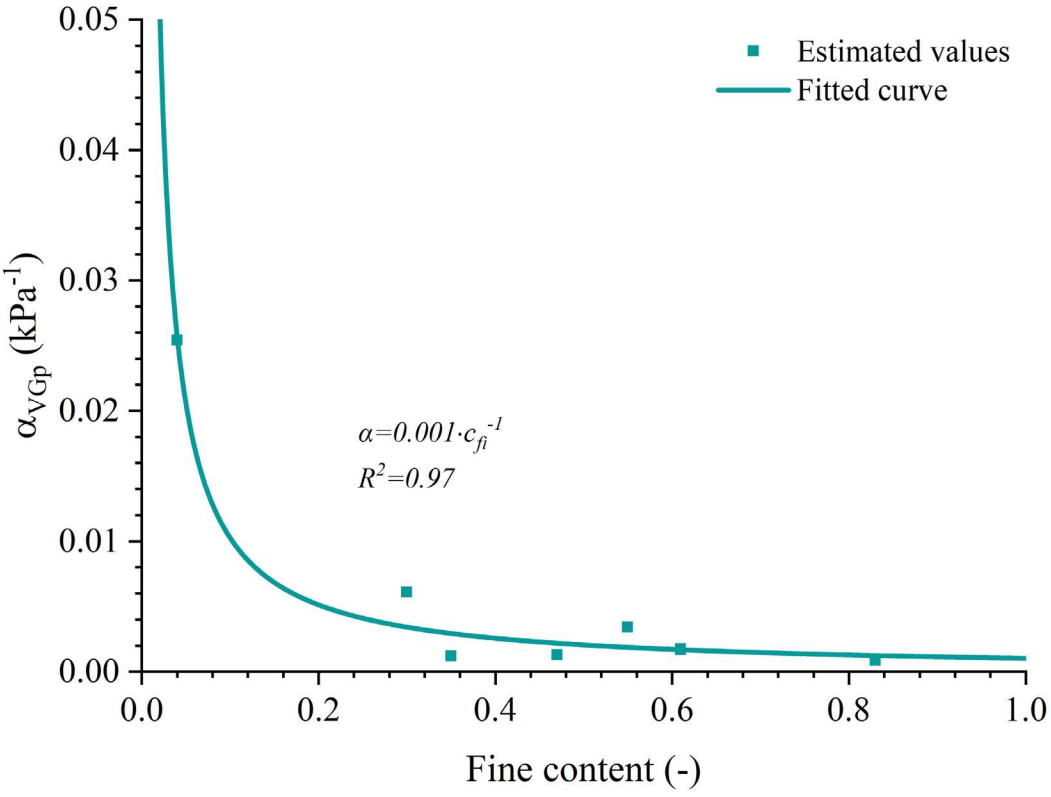

Figure 2.2. Variations of αVGp according to fine content

According to the van Genuchten model [72], the specific liquid water capacity is dominated by the variation of the degree of saturation due to the suction change, expressed by:

$$C_m = \begin{cases} \frac{\alpha_{VG} m_{VG}}{1-m_{VG}} (\theta_s - \theta_r) S_r^{\frac{1}{m_{VG}}} \left(1 - S_r^{\frac{1}{m_{VG}}}\right)^{m_{VG}} & , s > 0 \\ 0 & , s < 0 \end{cases} \quad (22)$$

Where θ_s (-) is the saturated volumetric water content.

The volumetric water content is calculated through the saturation and the residual volumetric water content:

$$\theta = \theta_r + S_r \cdot (\theta_s - \theta_r) \quad (23)$$

where θ (-) is the volumetric water content.

2.3 Heat transfer in CSRE (URE)

The variation of temperature influences the cement hydration, water flow and mechanical behaviors of the material, which leads to different material's chemo-hydro-mechanical characteristics. Therefore, it is necessary to consider the effect of temperature on the CTHM

properties of the material. The heat transfer process in the material is illustrated based on Fourier's law:

$$\rho_{eff}C_{eff}\frac{\partial T}{\partial t} = \rho_v C_v v_v \cdot \nabla T + \rho_w C_w v_w \cdot \nabla T + \rho_a C_a v_a \cdot \nabla T - \nabla \cdot \left(\lambda_{eff}\nabla T\right) \quad (24)$$

where C_{eff} ($J \cdot kg^{-1} \cdot K^{-1}$) is the effective specific heat capacity, ρ_{eff} ($kg \cdot m^{-3}$) is the effective density, C_v ($J \cdot kg^{-1} \cdot K^{-1}$) and C_a ($J \cdot kg^{-1} \cdot K^{-1}$) are water vapor specific heat capacity and dry air specific heat capacity [263], ρ_a ($kg \cdot m^{-3}$) dry air density, C_w ($J \cdot kg^{-1} \cdot K^{-1}$) is the liquid water specific heat capacity [200], λ_{eff} ($W \cdot m^{-1} \cdot K^{-1}$) is the effective thermal conductivity, v_v ($m \cdot s^{-1}$) and v_a ($m \cdot s^{-1}$) is water vapor velocity of dry air velocity which is considered equal to the liquid water velocity.

The density of water vapor is influenced by the temperature, relative humidity and saturated water vapor pressure:

$$\rho_v = \frac{M_w p_{sat} RH}{RT} \quad (25)$$

The dry air density ρ_a ($kg \cdot m^{-3}$) is obtained through:

$$\rho_a = M_a \cdot \left(\frac{p_{at} - p_{sat} RH}{RT}\right) \quad (26)$$

Where p_{at} (Pa) is the total atmospheric pressure and M_a ($kg \cdot mol^{-1}$) is the dry air molar mass.

The effective density ρ_{eff} ($kg \cdot m^{-3}$) of CSRE and underground soil are obtained through [199]:

$$\rho_{eff} = \rho_d + n[(1-S_r)\cdot(\rho_v+\rho_a)+S_r\rho_w] \quad (27)$$

For CSRE material, the effective specific heat capacity C_{eff} ($J \cdot kg^{-1} \cdot K^{-1}$) is calculated with the equation [199]:

$$C_{eff} = \left(\rho_d C_s + n\cdot\left((1-S_r)\cdot(\rho_v C_v+\rho_a C_a)+S_r\rho_w C_w\right)\right)/\rho_{eff} \quad (28)$$

where C_s ($J \cdot kg^{-1} \cdot K^{-1}$) is the current specific heat capacity of solid particles, which mainly varies on the range of 600 to 1200 $J \cdot kg^{-1} \cdot K^{-1}$ (Figure 1.25).

The specific heat capacity of water vapor C_v is calculated through [263]:

$$C_v = 1869.1 - 2.58 \times 10^{-1}(T-273.15) + 1.94 \times 10^{-2}(T-273.15)^2 \quad (29)$$

The specific heat capacity of dry air C_a is calculated through [263]:

$$C_a = 1034 - 0.3(T-273.15) + \frac{T^2}{8\times10^4} - \frac{(T-273.15)^3}{5\times10^7} + \frac{(T-273.15)^4}{1\times10^{10}} \quad (30)$$

The specific heat capacity of water C_w is given by [200]:

$$C_w = 8958.9 - 40.535T + 0.11243T^2 - 1.014 \times 10^{-4}T^3 \quad (31)$$

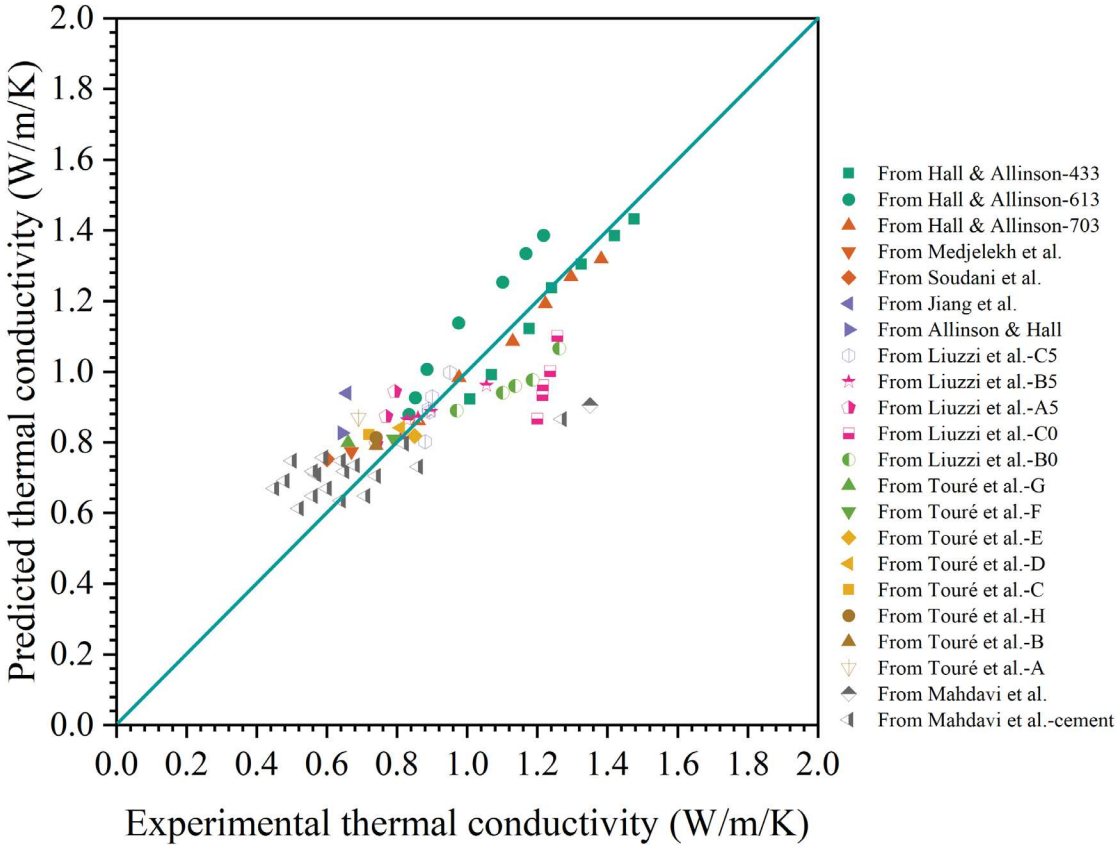

Figure 2.3. Comparison between the experimental results and analytical approach thermal conductivity [162,164–169,171,176,178,179,264,265]

The thermal conductivity of cement paste decreases with curing time [266], while the influence of cement on the thermal conductivity of cement-based soil can be neglected [172,173,267,268]. In addition, the thermal conductivities of CSRE are mainly dominated by the variation of dry density and saturation [173]. Based on the experimental results [162,164–169,171,176,178,179,264,265], their values are then calculated with the equation 32 according to the method from [260]. And the predicted thermal conductivities are compared with their experimental values in Figure 2.3.

$$\lambda_{eff} = 0.031\gamma_d \cdot \frac{2S_r}{1+S_r} + 0.044\gamma_d \tag{32}$$

where γ_d (kN·m^{-3}) is material dry unit weight.

2.4 Mechanical behavior during the hydration process

According to Newton's second law, the mechanical equations are described as:

$$\rho_{eff}\frac{\partial^2 \boldsymbol{u}}{\partial t^2} = \nabla\sigma + \rho_{eff}\boldsymbol{g} \tag{33}$$

where **u** is the displacement vector, σ is the Cauchy stress.

The stress increment of the material is described by using Hooke's law:

$$d\sigma_{ij} = D^{el}_{ijkl} d\varepsilon^{el}_{kl} \tag{34}$$

where D^{el}_{ijkl} is the elastic modulus tensor obtained according to Poisson's coefficient ν (-) and the elastic modulus E (Pa). $d\varepsilon^{el}_{kl}$ is the elastic strain increment.

The material strains are calculated through:

$$\varepsilon_{ij} = \varepsilon^{el}_{ij} + \varepsilon^{pl}_{ij} = \frac{1}{2}\left(\frac{\partial u_i}{\partial x_j} + \frac{\partial u_j}{\partial x_i}\right) \tag{35}$$

where ε_{ij} (-) is the engineering strain tensor, ε^{el}_{ij} (-) is the elastic strain tensor, ε^{pl}_{ij} (-) is the plastic strain tensor, u (m) is the displacement of a particle and x (m) is the position of the same particle in the deformed configuration.

The plastic strains are obtained according to the plastic consistency condition and the associate flow rule:

$$d\boldsymbol{\varepsilon}^{\boldsymbol{pl}} = d\lambda \frac{\partial Q_p}{\partial \boldsymbol{\sigma}} = d\lambda \frac{\partial F_{yield}}{\partial \boldsymbol{\sigma}} \tag{36}$$

$$\left(\frac{\partial F_{yield}}{\partial \boldsymbol{\sigma}}\right)^T d\boldsymbol{\sigma} + \left(\frac{\partial F_{yield}}{\partial \boldsymbol{\varepsilon}^{\boldsymbol{pl}}}\right)^T d\boldsymbol{\varepsilon}^{\boldsymbol{pl}} = 0 \tag{37}$$

where Q_p is the plastic potential, F_{yield} is a yield surface and dλ is harding parameter.

The yield surface of Hoek & Brown [269] (HB) dependent on the compressive strength (UCS) and tensile strength (T_f) is used in this study. The Hoek–Brown (HB) yield surface has the form:

$$F_{yield} = 2\sqrt{J_2}\sin\left(\theta_L + \frac{\pi}{3}\right) - UCS\sqrt{1 - m_{HB}\frac{\sigma_1}{UCS}} \tag{38}$$

$$\cos 3\theta_L = \frac{3\sqrt{3}}{2} \cdot \frac{J_3}{J_2^{3/2}} \tag{39}$$

where θ_L ($0 \le \theta_L \le \pi/3$) is the Lode angle, σ_1 (MPa) is the first principal stress, σ_3 (MPa) is the third principal stress, m_{HB} (-) is a constant whose value is related to the initial cement content, and UCS (MPa) is the unconfined compressive strength of CSRE (URE), J_2 and J_3 are respectively the second and third deviatoric stress invariants.

By consulting the experimental results in the literature, the fine content [158,260] is used to show the effect of suction on the UCS of different UREs that are compacted with the average dry density of 2000 kg·m^{-3}. It gives a global regression coefficient (R^2) of 0.93 in Figure 2.4 with the form:

$$UCS_0 = f_0(s, c_{fi}) = [u_0 + u_1 \cdot \ln(s+1)] \cdot (e^{c_{fi}} - 1) \tag{40}$$

where UCS_0 (MPa) is the unconfined compressive of unstabilized rammed earth (URE), u_0 (MPa) and u_1 (-) are constant parameters, and the suction s has the unit of MPa.

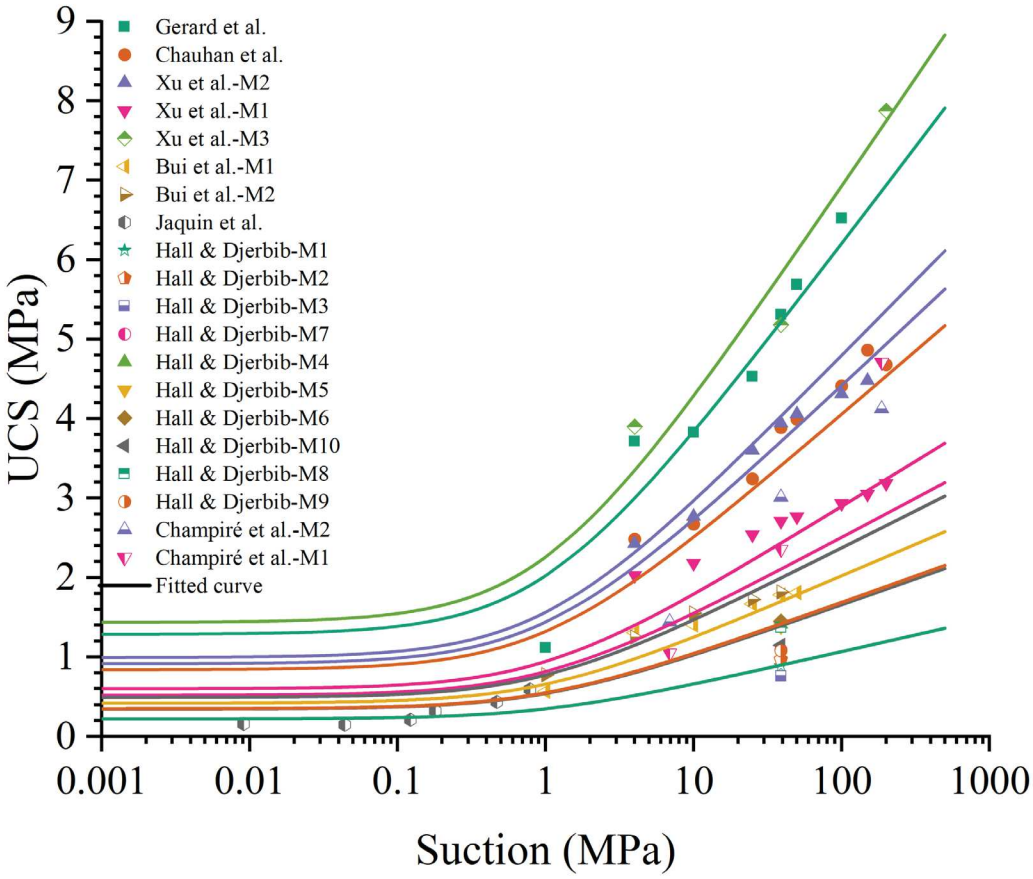

Figure 2.4. Calibration results of UCS values with suction and fine content compared to the experimental results[14,31,64,87–90]

The increment of mechanical resistance during the early curing periods is influenced strongly by the development of suction and the skeletal structure formed due to the cement hydration [270]. Once the additional cement is mixed in URE and compacted with the average dry density of 2000 kg·m^{-3}, the strength of the material will start being affected by the hydration products. The hydration process is affected by the mass of water and cement that is added initially to the soil, as well as the degree of cement hydration influenced by the curing temperature and ambient relative humidity. Since the strength of cemented material is influenced by the degree of hydration, and the strength is considered linearly [271–273] related to the degree of hydration with time. Thus the unconfined compressive strength (UCS) of cement stabilized rammed earth (CSRE) is predicted by multiplying the effect of the initial water-cement ratio [116,274] by the degree of hydration [275,276] with the power of 1 through:

$$UCS_1 = f_0(s,c_{fi}) + f_1(c_{ini},w_{ini},\delta) = UCS_0 + u_2 \cdot \left(\frac{c_{ini}}{w_{ini}}\right)^{u_3} \cdot \delta \quad (41)$$

where UCS_1 (MPa) is the unconfined compressive strength of cement stabilized rammed earth (CSRE) with the average dry density of 2000 kg·m^{-3}.

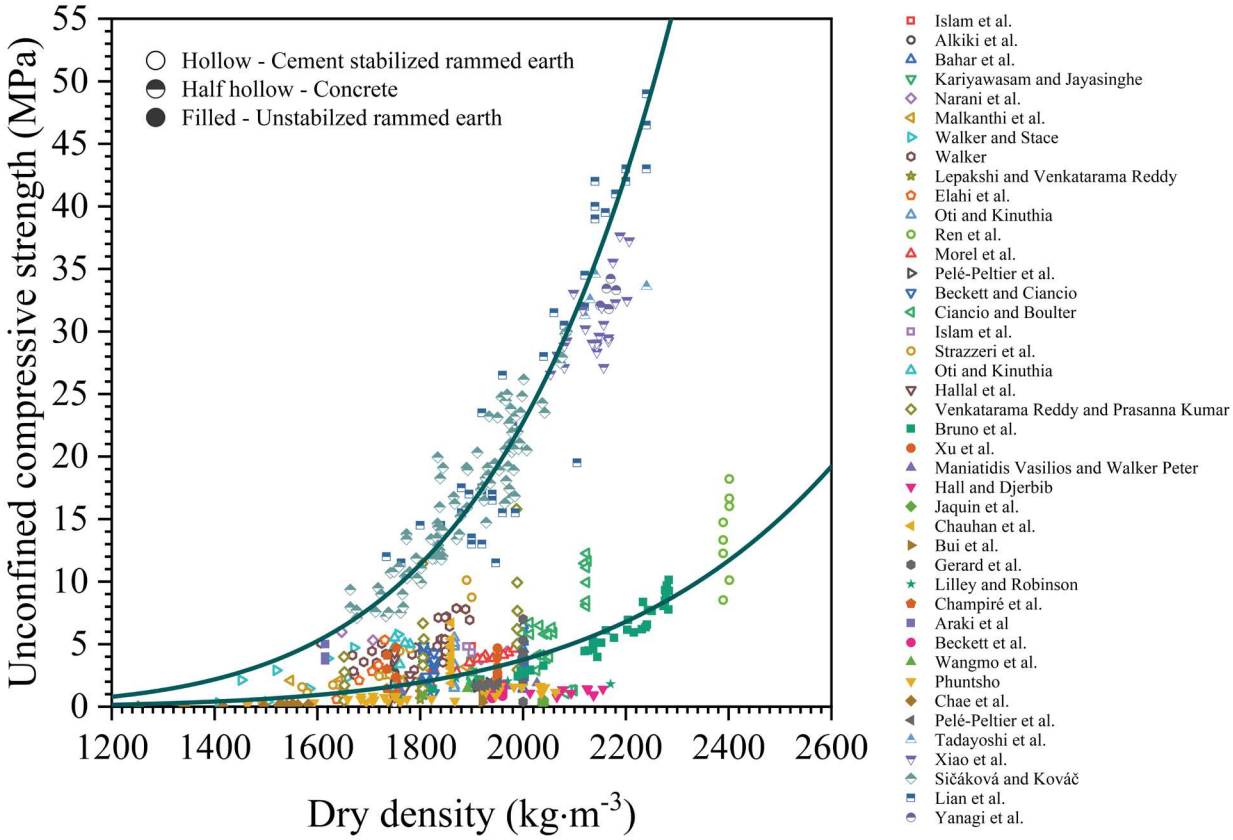

Figure 2.5. Unconfined compressive strength of CSRE with cement [15,18,20,25,28,44,46,49,50,52–54,57,80,102,103], concrete [104–108] and CSRE without cement [27,31,60–67,69,83,89,93] according to the dry density in normal scale

For the CSRE which is not compacted at the average dry density 2000 $kg \cdot m^{-3}$, the final strength may be different since the increase of initial dry density increases the strength of rammed earth. In the beginning, we focus on the strength of CSRE without cement (URE). The strength increments of URE, solely due to the density increases, consist of two parts. Firstly, a higher dry density increases the suction in porous material due to a decreased pore size, and the increased suction leads to higher effective stress accordingly. Secondly, the variations of dry density change the contact conditions of soil particles in the material leading to a higher mechanical resistance regardless of the saturation condition (strength increases even in saturated conditions [277,278]). For the first part, the influence of suction is reflected due to the variations of the soil water retention curve. For the second part, since a linear strength relation [279,280] exists between the strength under saturated and dry conditions, then the dry density is considered to have the same effect on URE strength in saturated and unsaturated conditions. The above two assumptions lead to $f_2(\rho_{ini})$ in the first part of equation 42.

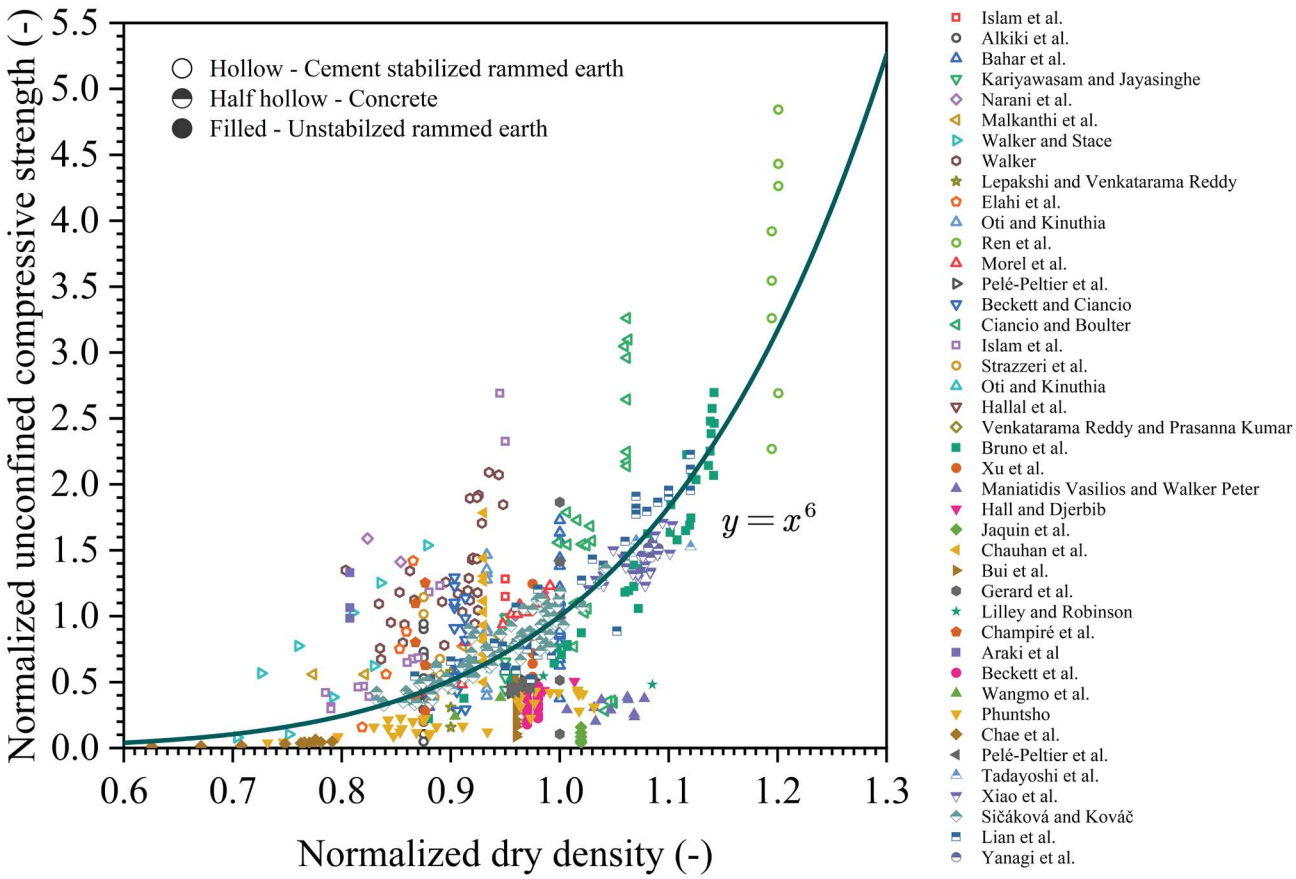

Figure 2.6. Unconfined compressive strength of CSRE with cement [15,18,20,25,28,44,46,49,50,52–54,57,80,102,103], concrete [104–108] and CSRE without cement [27,31,60–67,69,83,89,93] according to the dry density in normalized scale

Then, we focus on the strength of the soil with the added cement. The additional cement modifies URE with no cement to the CSRE with intermediate cement content and then to the concrete with the highest cement content. The effect of initial dry density on the strength of CSRE is described with f_3 (ρ_{ini}) in the second part of equation 42. The authors have investigated the effect of dry density on the compressive strength of these three types of materials, and the results are presented in Figure 2.5. For CSRE (with and without cement), the results in Figure 2.5 are normalized with the reference compressive strength of 3.76 MPa at the dry density of 2000 kg·m^{-3}. For the concrete with the maximum cement content [104–108], it is normalized by the compressive strength of 22 MPa corresponding to the dry density of 2000 kg·m^{-3}. The normalized results are presented in Figure 2.6. In the normalized scale, the value of u_4 is almost the same for both CSRE (6.2) and concrete (5.8). It reveals that the dry density has a similar effect (in percentage) on the strength increments of cement-based materials in this normalized scale. Therefore, the effects of dry density on the strength of URE, CSRE and concrete are considered to be the same. Eventually, the UCS of CSRE, by considering the effect of grain

size distribution, suction, initial water content, initial cement content, initial dry density and degree of cement hydration, is described in the form:

$$UCS = f_0(s,c_{fi}) \cdot f_2(\rho_{ini}) + f_1(c_{ini},w_{ini},\delta) \cdot f_3(\rho_{ini}) = \left[UCS_0 + u_2 \cdot \left(\frac{c_{ini}}{w_{ini}}\right)^{u_3} \cdot \delta\right] \cdot \left(\frac{\rho_{dini}}{2000}\right)^{u_4} \quad (42)$$

where the effects of initial dry density on the strength of URE is f_2 (ρ_{ini}) and on the increment strength of CSRE is f_3 (ρ_{ini}), UCS (MPa) is the unconfined compressive strength of cement stabilized rammed earth (CSRE), u_2 (MPa), u_3 (-) and u_4 (-) are constant fitting parameter.

It should be pointed out that the fitting parameters u_0 (MPa), u_1 (-), u_2 (MPa), u_3 (-) and u_4 (-) are not constant for different rammed earth materials. For a typical unstabilized rammed earth material, u_0 and u_1 are taken as 1 and 0.829 [158]. Globally, for a typical cement stabilized rammed earth material, u_4 is taken as 6 which value is obtained from the results presented in Figure 2.6 in the normalized scale. The value of u_2 varies in the range of 0.1 to 72, and u_3 varies between 0.5 and 3 for cemented soil [115,274,281–284]. In particular, when u_3 and δ are equal to 1, then the equation degrades to the Bolomey expression [285,286], which is often used to predict the strength of concrete materials. When the effect of dry density, grain size distribution (fine content) and suction is not considered, the proposed equation degrades to the generalized Abrams' law [281], which is used to predict the strength of cement mortars.

The shear strength or confined compressive strength of CSRE (CSRE) is obtained through the variation of m_{HB} according to the initial cement content. By fitting the experimental results from Lepakshi & Venkatarama Reddy [52] (Figure 2.7), it has the form:

$$m_{HB} = 9.9 + 53.4c_{ini} \quad (43)$$

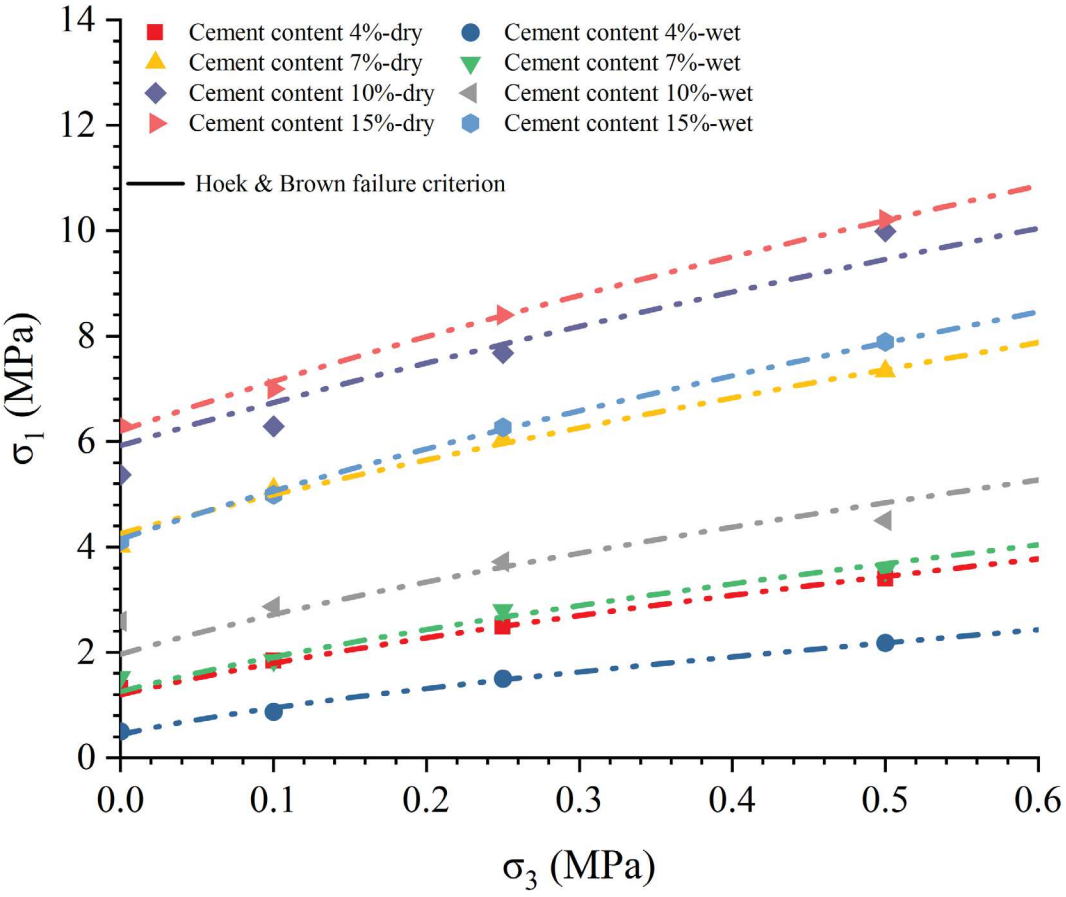

Figure 2.7. Comparisons of the experimental and predicted values for the shear strengths of CSRE under dry and wet conditions [52]

The power function is usually used for concrete [142] and soil [141] to estimate the elastic modulus based on the material UCS. Since the CSRE is a mixture of cement and soil, then the following power function is applied to describe the elastic modulus:

$$E = e_1 \cdot UCS^{e_2} \tag{44}$$

where e_1 (-) and e_2 (-) are fitting parameters for the elastic modulus (elastic modulus at failure point) and these values are respectively taken as 94.85 and 1.44 according to the experimental results [28,31,38,46,54,57,64,83,88–90,145,265] that are presented in Figure 2.8.

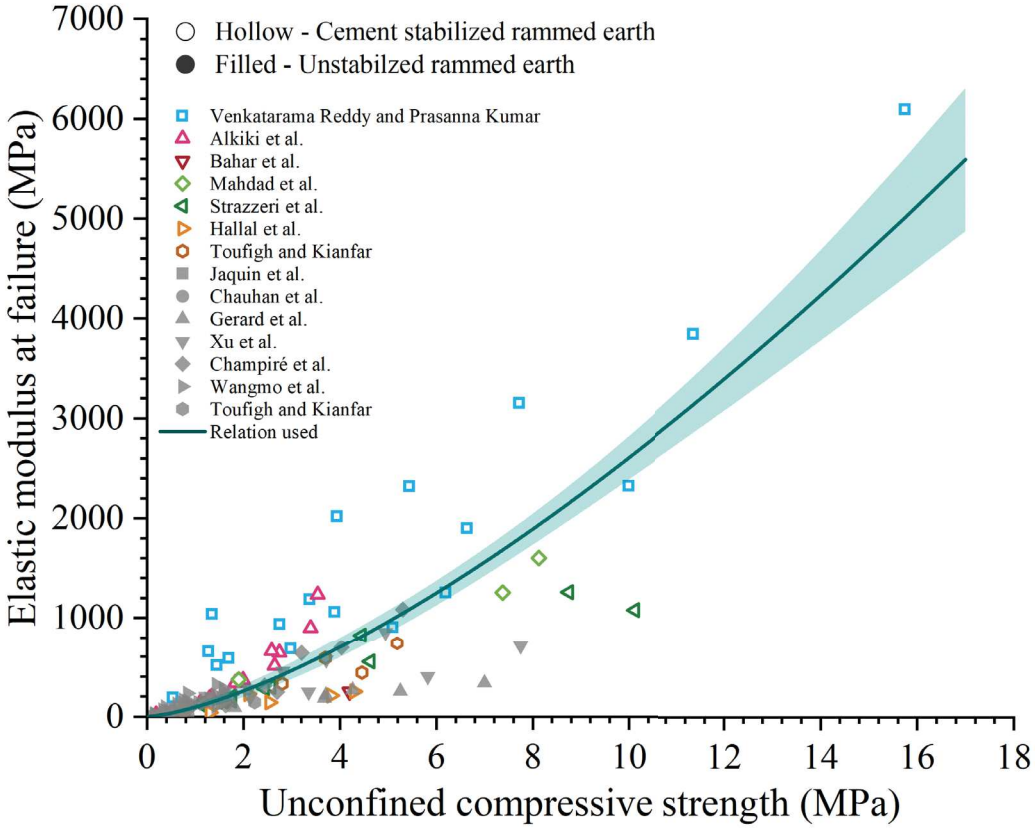

Figure 2.8. Elastic modulus according to the unconfined compressive strength of CSRE with cement [28,38,46,54,57,145,265] and without cement [31,64,83,88–90,265]

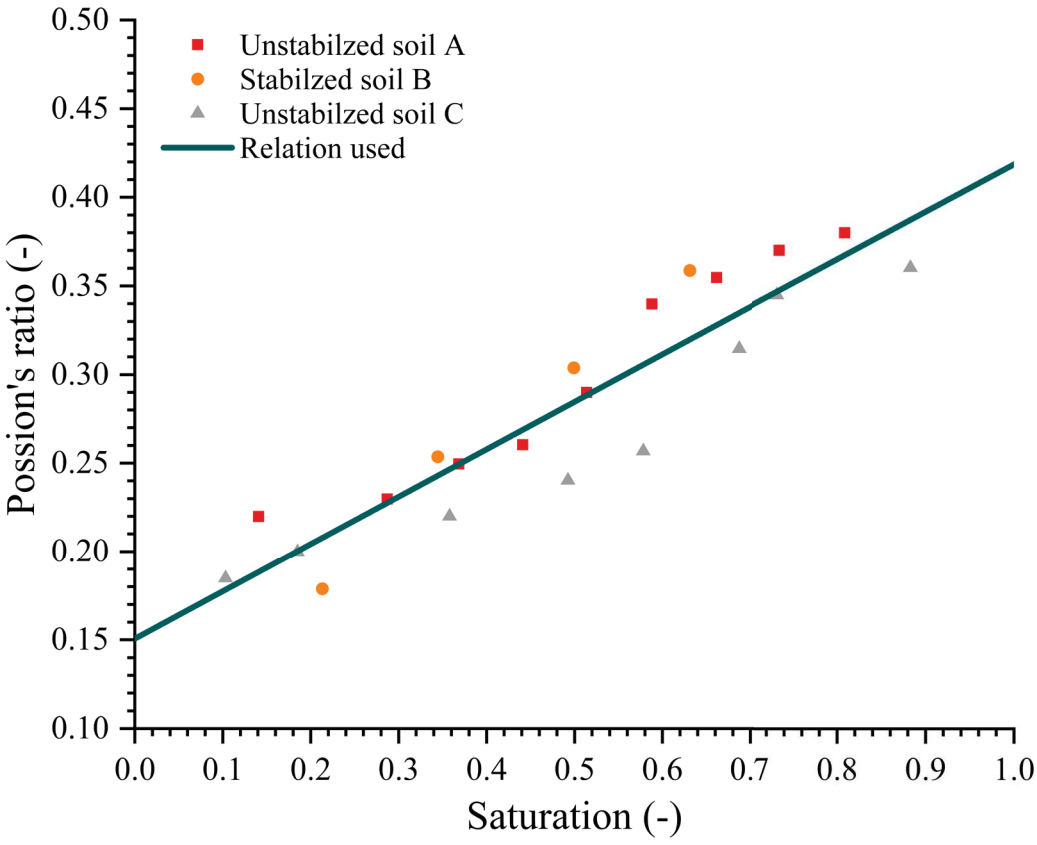

Figure 2.9. Poisson's ratio according to saturation [65]

The characteristic curve of Poisson's ratio [287] is related to the saturation according to the three types of rammed earth from the literature [65], and the results are presented in Figure 2.9 with a linear equation for simplicity:

$$\nu = 0.15 + 0.27 \cdot S_r \tag{45}$$

2.5 Boundary consitions

Once CSRE (URE) sample is produced in laboratory condition, the water and heat stored in the material will continually exchange with the environment through the air-exposed surfaces of the materials, which consequently leads to the change of their mechanical behaviors. Moreover, when CSRE (URE) is manufactured under in-situ condition, apart from the interactions with the environment air, the heat and water exchanges also exist between CSRE (URE) structure and underground soil. These interactions are reproduced in the numerical model by applying different boundary conditions. In this section, the boundary conditions triggered by the geological and environmental interactions with CSRE (URE) structure (or sample) are introduced. For the sample that are produced under laboratory conditions, the effects of radiation heat, wind effect and underground soil effect are not considered, unless the experiment is designed to address these influences, in which case their effects will be specifically described in the following parts.

2.5.1 Water exchange between CSRE (URE) and environment

The water is transferred via evaporation and condensation on the surface of the CSRE (URE) material:

$$m_{tot} = m_{ec} = \frac{h_m M_w}{RT}(RH_e p_{sat} - RH_i p_{sat}) \tag{46}$$

Where m_{tot} ($kg \cdot m^{-3} \cdot s^{-1}$) is the total water source on the boundary, m_{ec} ($kg \cdot m^{-3} \cdot s^{-1}$) is the evaporation water source and condensation water source, h_m ($m \cdot s^{-1}$) is the moisture transfer coefficient, RH_e and RH_i are the external and internal relative humidity on the surface, respectively.

Since the surrounding wind velocity significantly affects the strength of cementitious materials [288], the wind's impact is also addressed. The moisture transfer coefficient is influenced by

the wind speed v_{wind} ($m \cdot s^{-1}$). When wind speed is zero (general in laboratory conditions), its value is obtained based on the results from Tong et al. [289]. When the wind speed exists, a higher moisture transfer coefficient is used, and its value is calculated according to the pure water in porous materials without considering the effect of cracks in the evaporation process [290]:

$$h_m = \begin{cases} \frac{R\sqrt{T \cdot C_{wi0}}}{M_w}, v_{wind} = 0 \\ \frac{nD_v Sh}{L}, v_{wind} > 0 \end{cases} \quad (47)$$

where C_{wi0} ($s^2 \cdot m^{-2} \cdot K^{-1}$) is a constant dependent on the material, the diffusivity of water vapor is D_v ($m^2 \cdot s^{-1}$) , Sh (-) is the Sherwood number, L (m) is constant equals to 0.3m [291].

In addition, the wind affects principally the hydro-thermal properties of the CSRE (URE) structures through evaporation, and consequently its mechanical behavior. The wind speed changes with different height levels and the wind speed on the external surface of the wall and it can be calculated through Hellmann exponential law[292–295]:

$$v_{wind} = v_{wind0} \cdot \left(\frac{H}{H_0}\right)^{\alpha_H} \quad (48)$$

v_{wind0} ($m \cdot s^{-1}$) is the speed to the height H_0 (m), which is frequently referred to as a 10m, H (m) is the height of wall, and α_H (-) is the Hellman exponent taken as 0.4 for the buildings in city residential areas. v_{wind0} is obtained from the average value of the wind speed at 10m height.

The diffusivity of water vapor is obtained through [296]:

$$\mu_v = \left(80.58+0.4(T-273.15)\right) \cdot 10^{-6} \quad (49)$$

The Sherwood number used for evaporation is obtained according to [297]:

$$Sh = 0.145Re^{0.69}Sc^{0.87} = 0.145\left(\frac{v_{wind}\rho_v L}{\mu_v}\right)^{0.69}\left(\frac{\mu_v}{D_v\rho_v}\right)^{0.87} \quad (50)$$

where Re (-) is the Reynolds number depending on the surrounding air, Sc (-) is the Sherwood number, μ_v (Pa·s) represents the water vapor dynamic viscosity.

Under laboratory condition, the surrounding relative humidity of the sample is obtained through the relative humidity in the indoor condition. For the in-situ case, the long-term outdoor environment relative humidity (RH_{ext}) is calibrated with the sinusoidal functions [298,299]. Due to the human activities, the indoor environment relative humidity values usually range between 0.2-0.8 [166,300]. The indoor relative humidity of the wall (RH_{int}) is correlated to the outdoor relative humidity of the wall (RH_{ext}) [301]:

$$RH_{ext} = RH_{av} + RH_{am}\sin\left(\pi\frac{t+t_{RH}}{t_{ref}}\right) \quad (51)$$

$$RH_{int} = 0.45RH_{ext} + 0.17 \quad (52)$$

where RH_{av} (-) is the average relative humidity, RH_{am} (-) and t_{RH} (day) are respectively the amplitude and phase of relative humidity depending on local metrological conditions, t_{ref} (day) is the reference period time, RH_{int} (-) is the indoor environment relative humidity.

2.5.2 Water exchange between underground soil and environment

The water exchange between underground soil and the environment is dominated through, for example, raining precipitations, vegetations, rivers and lakes, water evaporations and condensations, etc. In lieu of numerically evaluating all these complex aspects simultaneously, the suction on the underground soil is obtained directly according to the in-situ hydrogeological conditions, and its value is given by applying Dirichlet boundary conditions to the ground surface.

2.5.3 Heat exchange between CSRE (URE) wall and environment

For the CSRE (URE) materials that are exposed under indoor environment, the convective heat Q_{cv} ($W \cdot m^{-2}$) and evaporation (condensation) heat Q_{ec} ($W \cdot m^{-2}$) are considered. For the CSRE (URE) structures that are exposed under outdoor condition, the convective heat Q_{cv} ($W \cdot m^{-2}$), evaporation (condensation) heat Q_{ec} ($W \cdot m^{-2}$) and radiant heat Q_r ($W \cdot m^{-2}$) together comprise the heat transported through the outdoor surface of the wall:

$$Q_{tot} = Q_{cv} + Q_{ec} + Q_r = h_{eff}(T_e - T_i) - L_v m_{ec} + Q_r \quad (53)$$

where Q_{tot} ($W \cdot m^{-2}$) is the total heat source on the boundary.

The latent heat of evaporation is calculated by [162]:

$$L_v = \left(2500 - 2.4(T - 273.15)\right) \times 10^3 \quad (54)$$

The radiation heat on the material surface is the sum of solar shortwave, solar longwave, and ground longwave radiation:

$$Q_r = (1 - a_{lb})R_s + \left(R_{Lg} + R_{La} - \varepsilon_e \sigma_B {T_e}^4\right) \quad (55)$$

where Q_{cv} ($W \cdot m^{-2}$) is the convective heat caused by the temperature gradient on the surface, Q_{ec} ($W \cdot m^{-2}$) is the heat source of water evaporation and condensation, Q_r ($W \cdot m^{-2}$) is the heat source of radiation, h_{eff} ($W \cdot m^{-2} \cdot K^{-1}$) is the effective heat transfer coefficient, L_v ($J \cdot kg^{-1}$) is the evaporation latent heat [162], T_e (K) and T_i (K) are respectively the temperatures on the external and internal part of a surface, R_s ($W \cdot m^{-2}$) is the global shortwave radiation in the local condition,

a_{lb} (-) is albedo, R_{Lg} (W·m^{-2}) is the incoming ground longwave radiation, R_{La} (W·m^{-2}) is the incoming environmental longwave radiation, ε_e (-) is the emissivity, σ_B (W·m^{-2}·K^{-4}) is the Stefan-Boltzmann constant. The solar-caused radiation parameters R_s (W·m^{-2}), R_{La} (W·m^{-2}) and R_{Lg} (W·m^{-2}) can be determined based on the local weather conditions.

The sinusoidal equation is used to describe the periodic variation of global shortwave radiation caused by the Earth Rotation. In addition, since CSRE (URE) structures are usually erected in vertical direction, thus, the average outdoor local shortwave radiation is obtained by fixing the azimuth angles equal to 180 degrees (South facing) and tilt angle 90 degrees (vertical wall) through the following equation:

$$R_s = 116 + 28\sin\left(\frac{\pi(t-106)}{t_{ref}}\right) \tag{56}$$

The environmental longwave radiation is obtained through [302–304]:

$$R_{La} = (5.61^{-13}(T_{ext}+273.15)^6 \cdot (1-C_c) + (5.61^{-13}(T_{ext}+273.15)^6+69.3C_c) \cdot C_c) \cdot K_1 + K_3 \cdot \left(0.09(1-(0.9203+0.0043T_{ext})\cdot C_c)\right) \cdot \sigma_B \cdot (T_{ext}+273.15)^4 \tag{57}$$

in which C_c (-) is the cloud cover factor taken as 0.41, K_1 (-) and K_3 (-) are the parameters dependent on the inclination angle of the wall taken respectively as 0.5 and 0.3457 for a vertical wall.

The ground longwave radiation R_{Lg} incident upon the building surface is calculated through [302]:

$$R_{Lg} = (159.5+2.77T_{ext})\sin^2(\beta_{inc}/2) \tag{58}$$

where β_{inc} is the wall inclination angle equals to $\pi/2$.

Shortwave radiation is affected by the albedo value of the wall, which is a function of its Meter Munsell color value [305]:

$$a_{lb} = 0.069c_{cv} - 0.114 \tag{59}$$

where c_{cv} (-) is the Meter Munsell color value of the material.

The effective heat transfer coefficient is influenced by the speed of the wind and whose value is obtained through [306]:

$$h_{eff} = -0.0203v_{wind}^2 + 1.766v_{wind} + 12.263 \tag{60}$$

The long-term outdoor environment temperature (T_{ext}) is calibrated with the sinusoidal functions [298,299]:

$$T_{ext} = T_{av} + T_{am}\sin\left(\pi\frac{t-t_T}{t_{ref}}\right) \tag{61}$$

where T_{av} (K) is the average temperature, T_{am} (K) and t_T (day) are respectively the amplitude and phase of temperature depending on local metrological conditions.

Due to the human activities, the indoor environment temperature values usually range respectively between 18-30 ℃ [166,300]. The internal temperature (T_{int}) is correlated with the external temperature (T_{ext}) through[301]:

$$T_{int} = \begin{cases} 18.9 + 0.04(T_{ext} - 273.155), T_{ext} < 285.85K \\ 14.201 + 0.41(T_{ext} - 273.155), T_{ext} > 285.85K \end{cases} \quad (62)$$

where T_{int} (K) is the indoor environment temperature.

2.5.4 Heat exchange between underground soil and environment

Applying Dirichlet boundary conditions to the underground soil surface yields the near-ground temperature, and the temperature imposed as boundary conditions is collected directly from in-situ observations.

2.6 Conclusion

Based on a systematic review of the literature, it has been discovered that the characteristics of CSRE (URE) materials vary significantly across experimental studies, making their application under in-situ conditions more challenging. The lack of a worldwide perspective on all types of CSRE (URE) materials hinders the creation of a globally accepted standard for CSRE (URE) materials. Consequently, to globally estimate the long-term CTHM behavior of different CSRE (URE) materials, the characteristics of CSRE (URE) needed to be predicted from the designing stage.

Therefore, in this chapter, a novel finite element framework applicable to both URE and CSRE materials by considering the combined effects of initial water content, initial dry density, initial grain size distribution, initial cement content, curing conditions, and curing duration is proposed to explain the linked CTHM behaviors of these materials from long-term point of view. The numerical method mainly consists of four parts, namely, the cement hydration, unsaturated water flow, heat transfer and mechanical responses. By applying appropriate boundary conditions, the proposed method should be able to estimate the time-dependent CTHM properties of CSRE (URE) under the laboratory and in-situ conditions. After that, the proposed method is used to predicted some characteristics of CSRE (URE) reported in the literatures, and the predictions are compared with the experimental results in the following chapter.

Chapter 3. Validations of the numerical method

Since it is complicated to have the experimental results to cover all the coupled CTHM properties of CSRE (URE) simultaneously, several CTHM configurations are investigated to evaluate the capacity of the proposed theoretical framework.

3.1 Validations for URE materials

To evaluate the numerical approach, the water flow reported by [31,88] are simulated. The specimen properties are summarized in Table 3.1. The specimens used for simulation are all saturated at the beginning, and then different suction and temperature values according to experimental conditions are applied on the surfaces of the specimens as the boundary condition. The initial time point of the simulation starts once the saturation/water content decreases to the initial value of the experimental conditions. Figure 3.1a and 3.1b present the variation of gravimetric water content and degree of saturation in URE specimens by time compared to the experimental results.

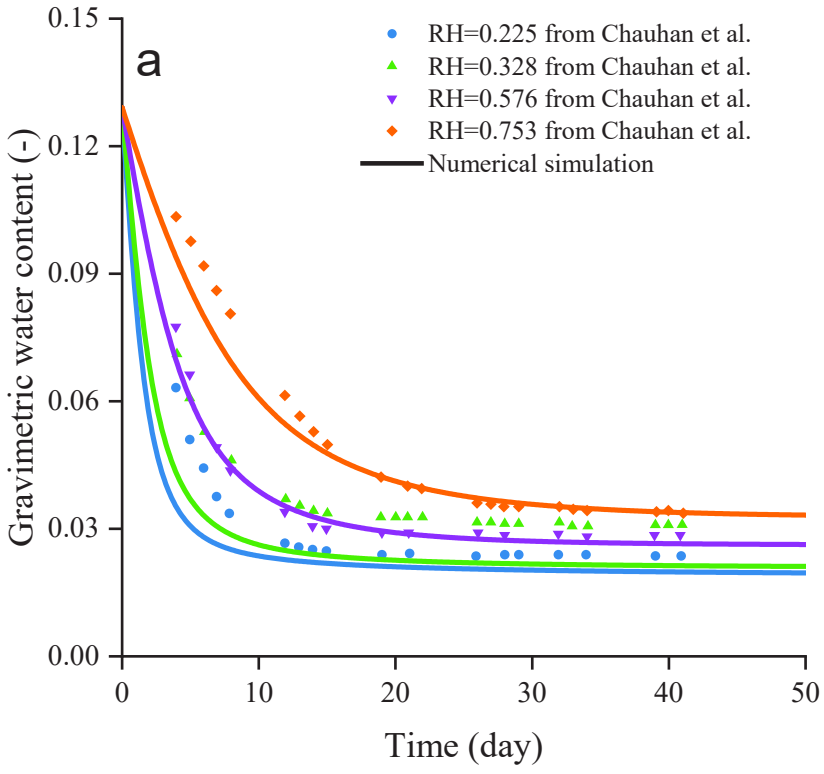

(a)

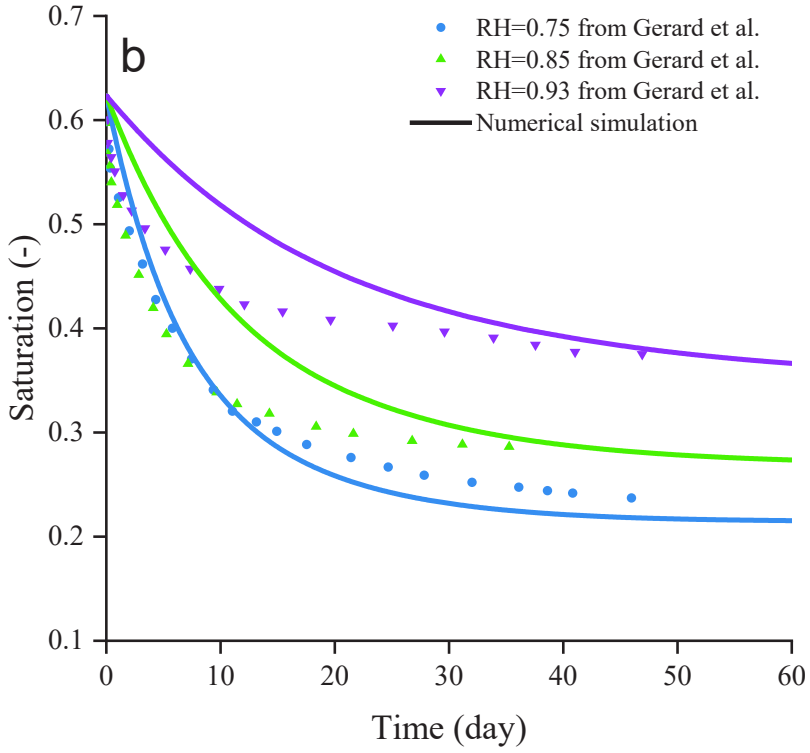

(b)

Figure 3.1. Comparison between the experimental results [31,88] and the numerical simulations for (a) gravimetric water content [31] and (b) saturation [88].

Compression tests							
Author	sample size(mm)		s(MPa)	c_{fi}(-)	confining pressure(MPa)	T(°C)	ρ_d(kg·m^{-3})
	diameter	height					
Chauhan et al. (2019) [31]	50	100	3.8, 23.4, 39, 75.9, 153.4, 205.3, 331.3	0.61	0	20	1860
Gerard et al. (2015) [88]	36	72	2.4, 4.12, 11.23, 22.01, 38.95, 124.07	0.826	0	20	2000
Xu et al. (2018) [90]-M3	35	70	4, 39, 201	0.42, 0.65, 0.89	0.1	20	1950

Table 3.1. Initial parameters of the experimental results reported by [23,58,60]

To give more credit to our prediction for the hydro-thermal properties, the experimental results from Jiang et al. [162] are also simulated. The specimen was built with the height, length and width of 0.24m, 0.12m and 0.18m. Then, the temperature/relative humidity with the respective values of 29°C/0.87 on the external surface and 18°C/0.70 on the internal surface were applied to the cube URE specimen. The initial inside temperature and relative humidity were respectively 25°C and 0.7. All the parameters obtained directly from the experimental results

and then used for the verification are summarized in Table 3.2. The comparisons between the simulations and the experimental results are presented in Figure 3.2.

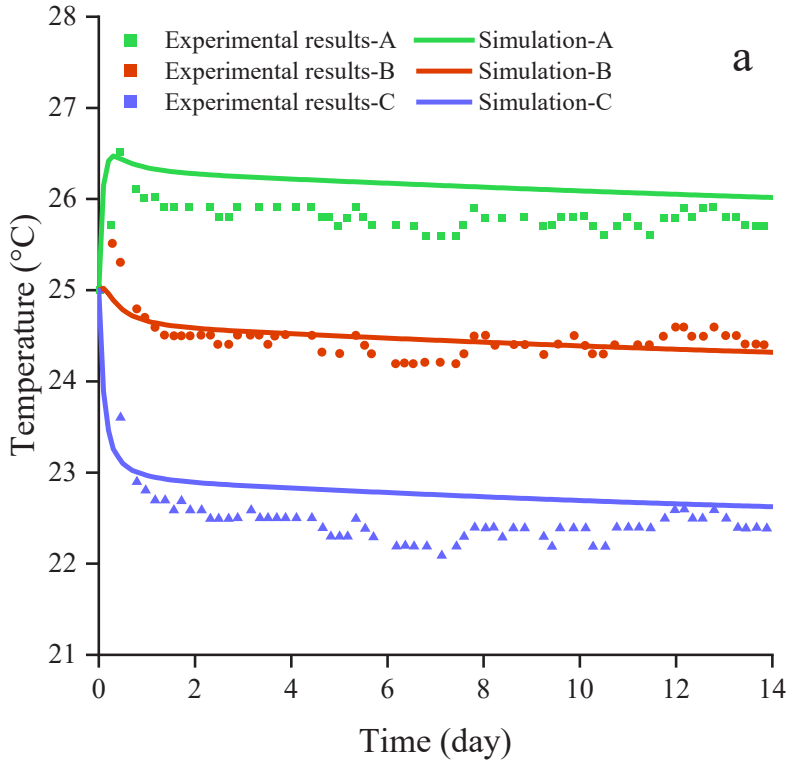

(a)

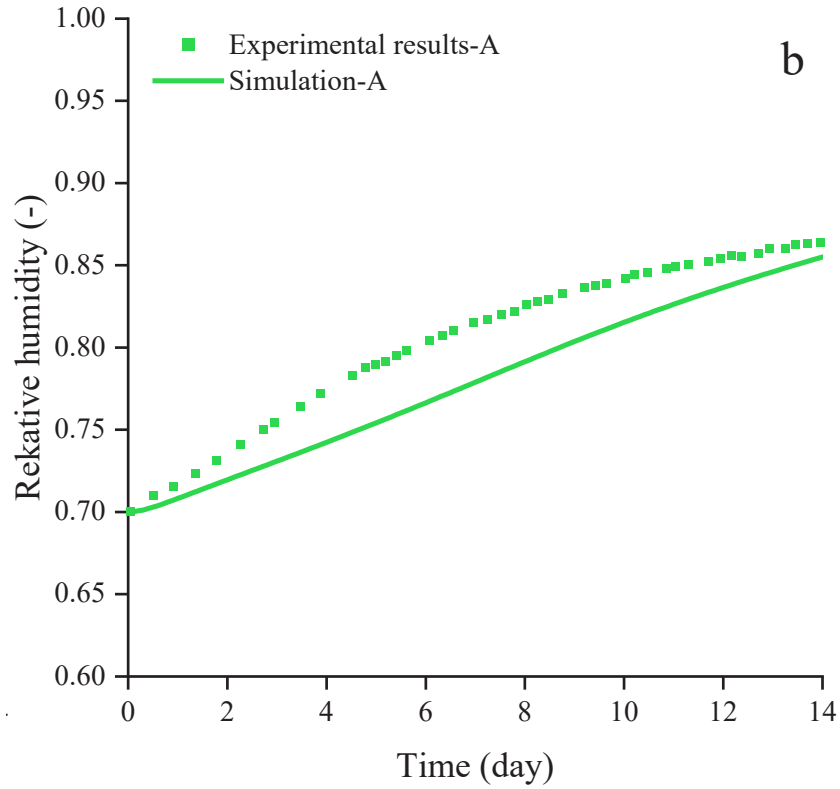

(b)

Figure 3.2. Comparison between the experimental results [162] and the numerical simulations for (a) temperature and (b) relative humidity.

External T(C)	External RH(-)	Internal T(C)	Internal RH(-)	Initial inside T(C)	Initial inside RH(-)	External h_{eff} ($W \cdot m^{-2} \cdot K^{-1}$)
29	0.87	18	0.7	25	0.7	23.26
$\alpha_{VG}(m^{-1})$	m(-)	n(-)	θ_s(-)	θ_r(-)	$\rho_d(kg \cdot m^{-3})$	Internal h_{eff} ($W \cdot m^{-2} \cdot K^{-1}$)
0.0125	0.29	1.4	0.16923	0.0045	2160	8.72

Table 3.2. Parameters used for the the experimental results from Jiang et al. [162]

The compression or tensile tests reported by Chauhan et al. [31], Xu et al. [90], Bui et al. [87] and Gerard et al.[88] are also simulated in this part. The initial parameters used in the numerical simulation are presented in Table 3.3. The compression tests are respectively performed with no confining pressure for the UCS tests and with different confining pressures for the unconsolidated undrained (UU) tests. To respect the experimental conditions, a constant vertical displacement of 0.01 mm is applied per step. The gravity effect is neglected since it has little effect in our simulations. The movement of the bottom surface is vertically fixed. The side surface of URE samples moves freely without boundary restrictions for UCS tests. The confining pressure is applied horizontally along the perimeter of the cylinder for UU tests. Figure 3.3a and 3.3b compare the simulation results of the compression and tensile strengths with the experimental results for different URE materials. Figure 3.4 shows the simulation results of axial stress with axial strain at different suctions based on Hoek-Brown criterion for two materials respectively studied by Gerard et al. [88] and by Xu et al. [90]. Globally, the simulation results show that Hoek-Brown criteria can be used to estimate the strengths of URE materials.

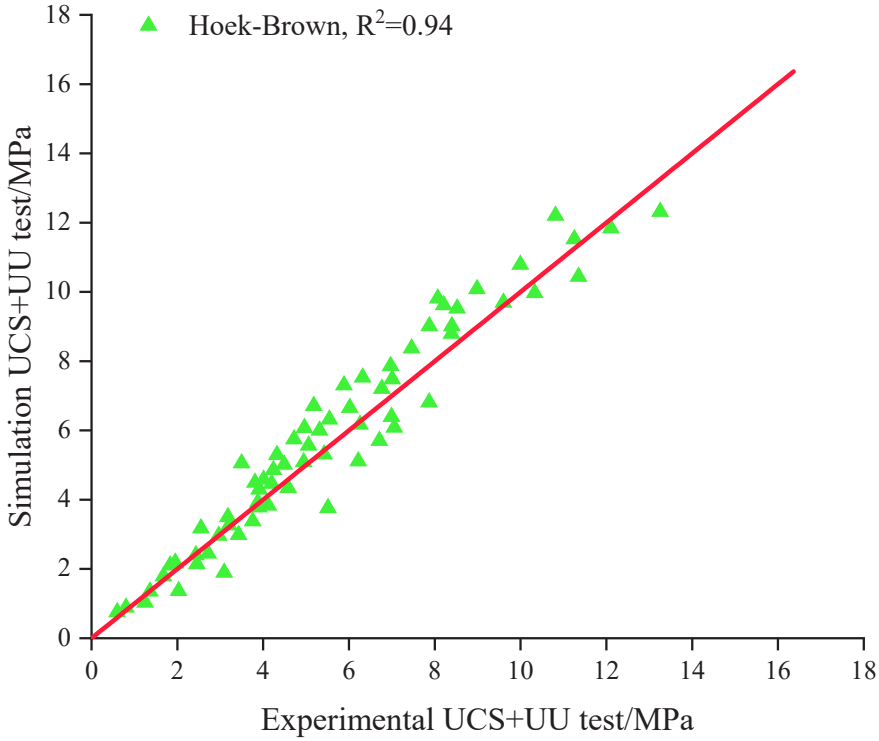

(a)

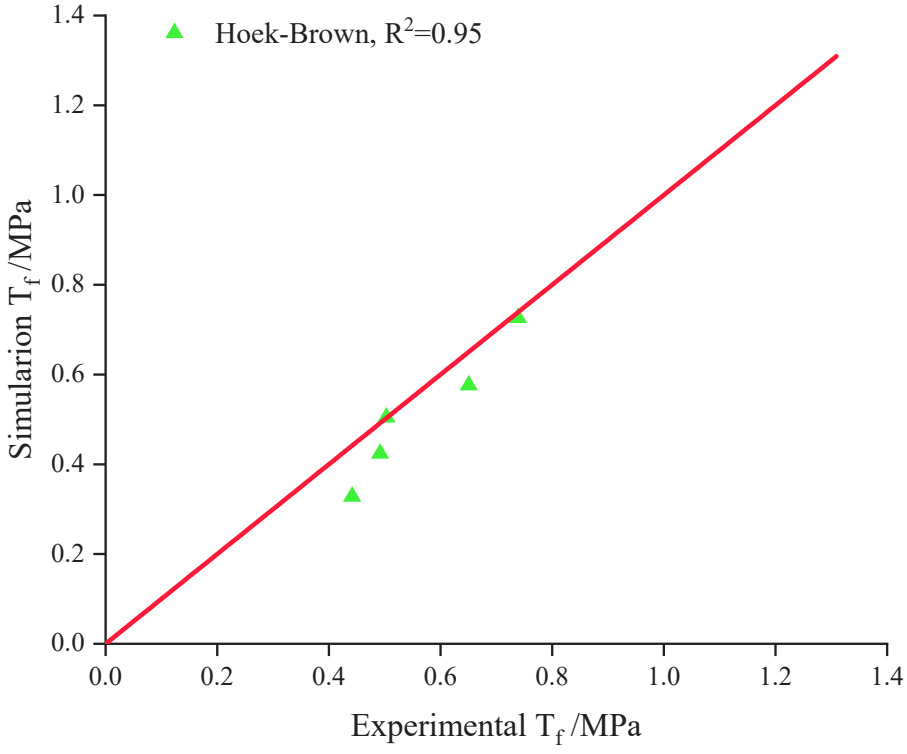

(b)

Figure 3.3. Simulation results of (a) UCS values and (b) Tf values compared to their respective experimental results

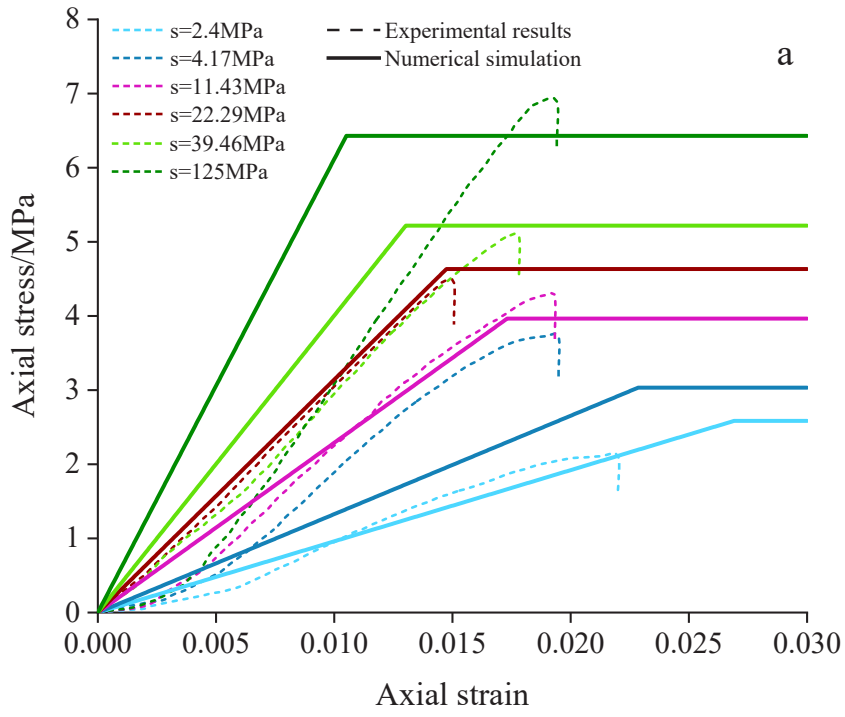

(a)

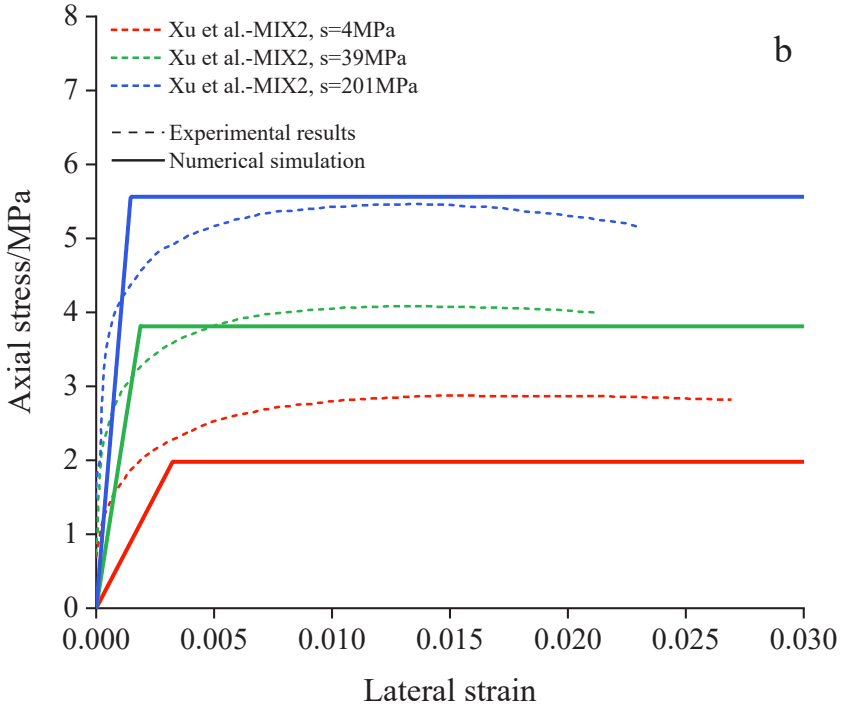

(b)

Figure 3.4. Compression simulation results by applying HB compared to the experimental results reported by (a) Gerard et al. [88] and (b) Xu et al. [90]

	Compression tests				
Author	sample size(mm)	s(MPa)	c_{fi}(-)	T(°C)	ρ_d(kg·m^{-3})

	diameter	height			confining pressure(MPa)		
Xu et al. (2018) [90]-M3	35	70	4, 39, 201	0.42, 0.65, 0.89	0, 0.1, 0.6	20	1950
Chauhan et al. (2019) [31]	50	100	3.8, 23.4, 39, 75.9, 153.4, 205.3, 331.3	0.61	0, 0.2, 1, 1.5	20	1860
Bui et al.(2014) [87]	160	300	1.22, 2.05, 3.29, 8.23, 25.56, 55.04, 62.56, 65.61	0.35	0	20	1920
Gerard et al. (2015) [88]	36	72	2.4, 4.12, 11.23, 22.01, 38.95, 124.07	0.826	0	20	2000
Tensile tests							
Gerard et al. (2015) [88]	36	72	2.4, 4.12, 11.23, 22.01, 38.95, 124.07	0.826	0	20	2000

Table 3.3. Initial parameters used for numerical simulation of different reported tensile or compression tests.

3.2 Validations for CSRE materials

To assess the capacity of the proposed numerical framework to simulate the cement hydration, the experimental cement hydration results from Schindler & Folliard [238] [307] have been investigated for the validation of the cement hydration process. In this phase, we focus only on the hydrothermal coupling and the mechanical part in the numerical framework is not considered. The sample is cured under a hydro-thermal insulated condition, then the heat and moisture transfer on the surface is neglected. The relative humidity is considered to be over 95% [308]. The initial material temperature is 294.25 K, the initial water content, cement content and dry density are respectively 0.07, 0.18 and 2400 $kg \cdot m^{-3}$. Since the initial temperature is higher than 293.15 K, then the activation energy is 33500 $J \cdot mol^{-1}$, the constant time and shape parameters for the hydration process are 29 h and 0.69, respectively. The constant parameters used for simulation are summarized and presented in Table 3.4. And the simulation results are compared with the experimental tests, and the comparations are shown in Figure 3.5.

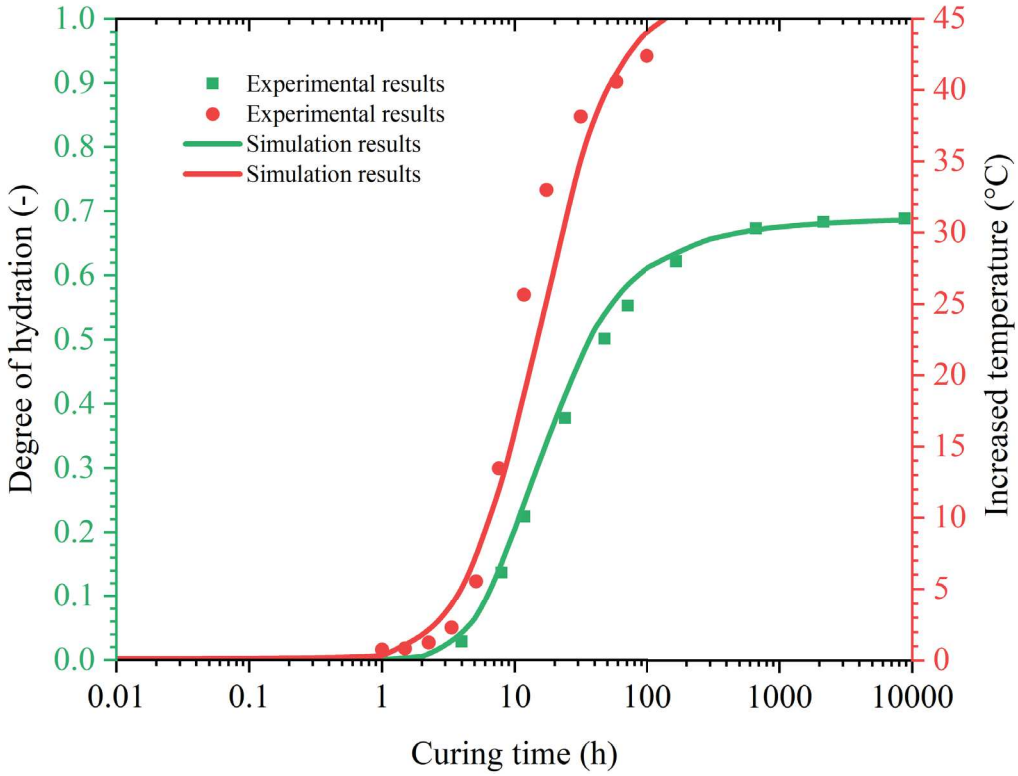

Figure 3.5. Comparison of the experimental results reported by Schindler & Folliard [238] and our numerical predictions for the cement hydration

$T_{i,e}$ (K)	w_{ini} (-)	c_{ini} (-)	ρ_{dini} (kg·m^{-3})	E_a (J·mol^{-1})	α_h (h)	β_h (-)	H_{cem} (J·g^{-1})
294.25	0.07	0.18	2400	33500	23	0.69	477

Table 3.4. Constant parameters used for the simulation of the cement hydration reported by Schindler & Folliard [238].

The rising temperature accelerates the hydration process of CSRE. Consequently, a higher curing temperature leads to a higher strength [124]. Therefore, the effects of temperature on the cement hydration process are simulated based on the experimental results from Poole et al. [309]. The components of the cement used for hydration are summarized and presented in Table 3.5. The specimens are prepared with five different initial temperatures (K): 278.15, 288.15, 296.15, 311.15, and 333.15. After that, the specimens are cured in the same temperature condition as preparation for around 85 h. The constant parameters used for numerical simulation are summarized in Table 6, and the comparisons of the experiments and simulations are illustrated in Figure 3.6.

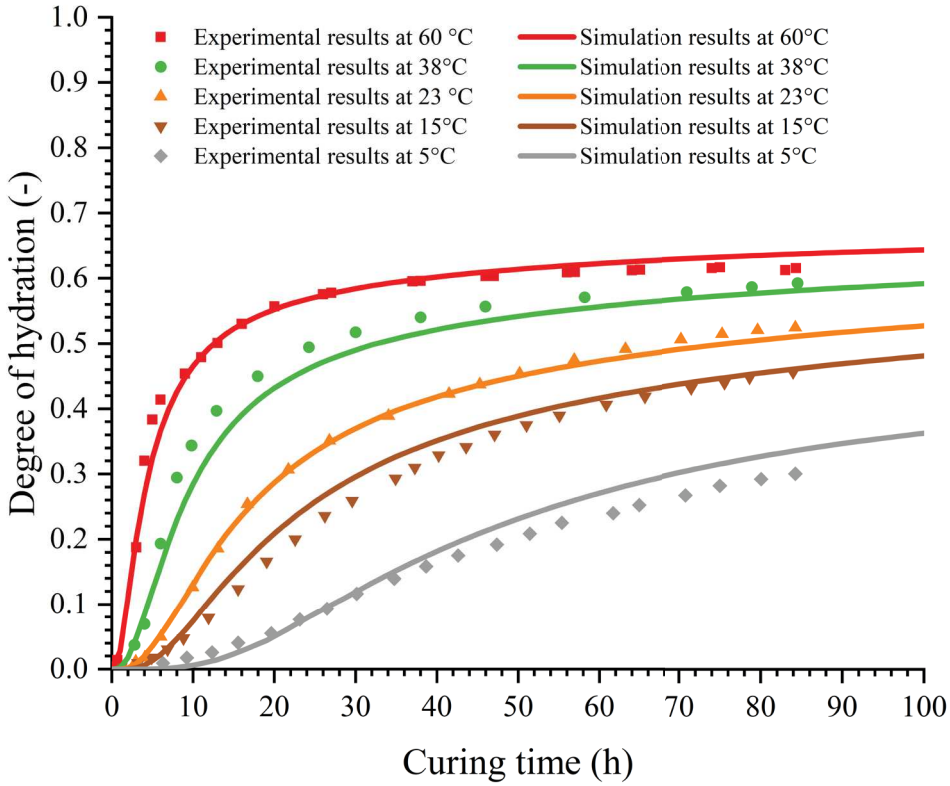

Figure 3.6. Comparison of the experimental results by Poole et al. [309] and our numerical predictions for the effect of temperature on cement hydration

C_3S (-)	C_2S (-)	C_3A (-)	C_4AF (-)	SO_3 (-)	MgO (-)	FreeCaO (-)	h_{eff} ($W \cdot m^{-2} \cdot K^{-1}$)
0.6315	0.1096	0.0734	0.07	0.032	0.0109	0	3
$T_{i,e}$ (K)		w_{ini} (-)	δ_{max} (-)	c_{ini} (-)	ρ_{dini} ($kg \cdot m^{-3}$)	α_h (h)	β_h (-)
278.15, 288.15, 296.15, 311.15, 333.15		0.066	0.716	0.15	2400	23	0.69

Table 3.5. Constant parameters used for the simulation of the temperature effect on cement hydration for the results reported by Poole et al. [309].

In the process of the cement hydration in CSRE, the free water will be transformed into evaporable water (oven-dried at 105 °C) in the form of chemically reacted water and chemisorbed (physically adsorbed) water [243]. The decrements of free water increase the suction and the mechanical resistance ability. In addition, the generated hydration products increase the current dry density and the cohesion (binder effects) of the material, which further increases the material strength. During the construction of CSRE structures, the material may not be compacted at the optimum conditions. Thus, the initial dry density and initial water

content will be above, below, and at the optimum state for a given CSRE material. Beckett & Ciancio [80] investigated the water consumption and strength increment mechanism of CSRE which are not all compacted with the optimum water content, by using the freeze-drying technique. All the CSRE specimens are prepared with the same initial cement content of 5%. These specimens access different initial dry densities 1807, 1827, 1811 kg·m^{-3} and different initial water contents of 10.4%, 12.4%, and 14.4%. After compaction, the specimens were wrapped and cured under the conditions with a temperature of 294.15 K for around 29 days. The average composition content of the ordinary Portland cement [310–312] is used for numerical simulations. All the constant parameters used for simulation are presented in Table 3.6, and the related comparisons are illustrated in Figure 3.7.

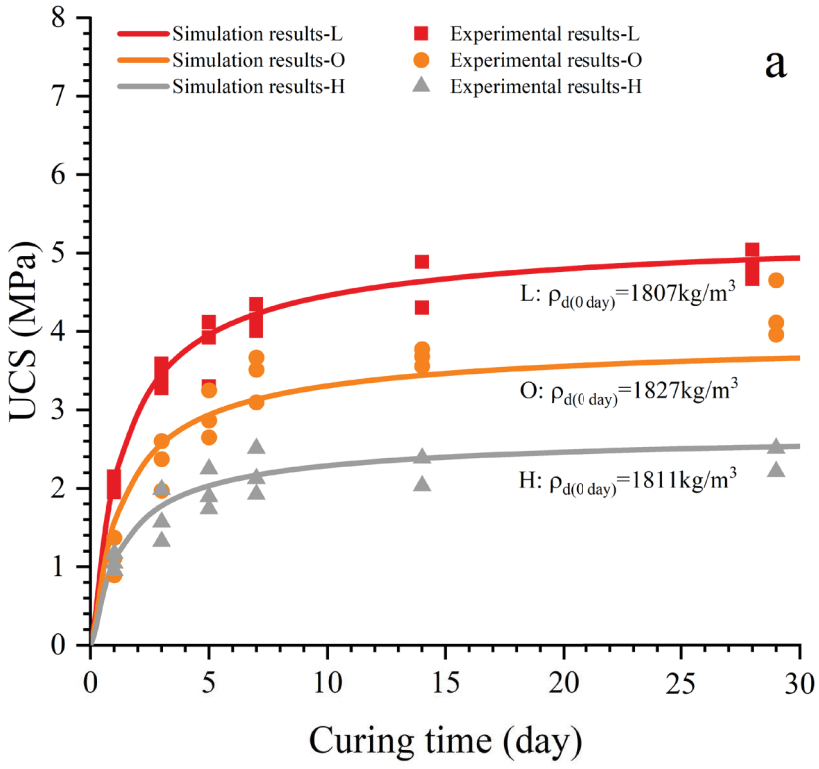

(a)

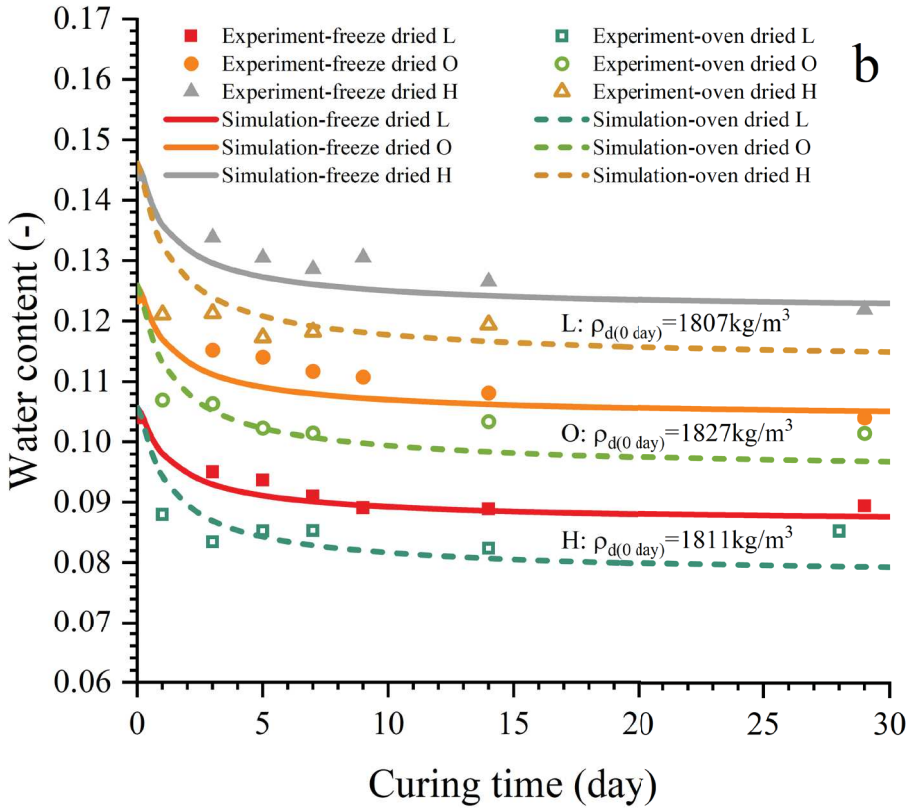

(b)

Figure 3.7. The numerical predictions of the (a) compressive strength and (b) water content of CSRE for the results reported by Beckett & Ciancio [80]

C_3S (-)	C_2S (-)	C_3A (-)	C_4AF (-)	SO_3 (-)	MgO (-)	FreeCaO (-)	v_{wind} ($m \cdot s^{-1}$)	u_2 (MPa)	c_{fi} (-)
0.56232	0.15717	0.095283	0.085917	0.03	0.013	0.003	0	52.6	0.013

$T_{i,e}$ (K)	c_{ini} (-)	w_{ini} (-)	ρ_{dini} ($kg \cdot m^{-3}$)	ρ_c ($kg \cdot m^{-3}$)	C_s ($J \cdot kg^{-1} \cdot K^{-1}$)	α_h (h)	β_h (-)	u_3 (-)
294.15	0.05	0.104, 0.124, 0.144	1807, 1827, 1811	3150	1081	23	0.69	2.17

Table 3.6. Constant values that are used for the simulation of the CTHM behavior for the results reported by Beckett & Ciancio [80]

As described in the introduction, both the initial water content and initial cement content influence the strength of CSRE material. The specimens [111] compacted with the initial cement content of 5%, 10%, 15%, initial water content 8.7%, 7.9%, 8.1%, and average initial

dry density ($kg \cdot m^{-3}$) 2040, 2034, 2036 are used for simulations. After compaction, the specimens were cured under conditions with a relative humidity of 94% humidity and temperature of 294.15 K for 28 days to ensure suction equilibration. The comparisons between the experimental and simulation results for the UCS at 28 days are presented in Figure 3.8, and the constant parameters used for simulation are summarized in Table 3.7.

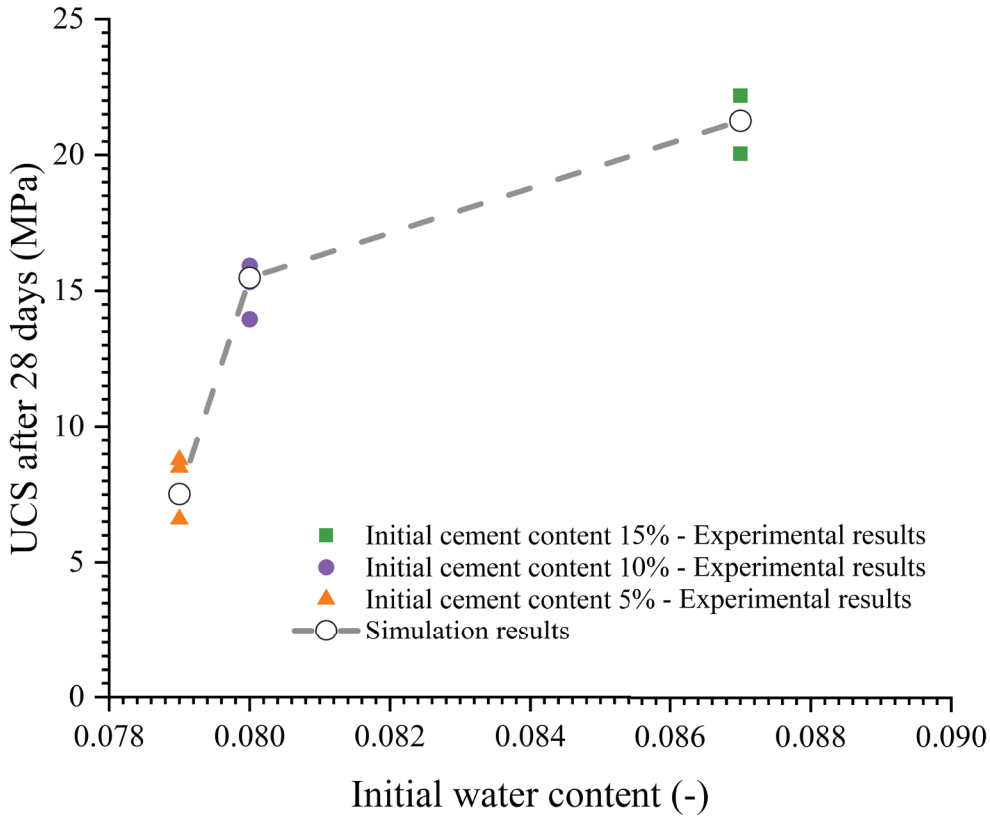

Figure 3.8. Comparison of the experimental results reported by Beckett et al. [111] and our numerical predictions for compressive strength at the different initial water content

C_3S (-)	C_2S (-)	C_3A (-)	C_4AF (-)	SO_3 (-)	MgO (-)	FreeCaO (-)	v_{wind} ($m \cdot s^{-1}$)	u_2 (MPa)	u_3 (-)
0.56232	0.15717	0.095283	0.085917	0.03	0.013	0.003	0	13	1.25
$T_{i,e}$ (K)	c_{ini} (-)	w_{ini} (-)	ρ_{dini} (kg·m-3)	ρ_c ($kg \cdot m^{-3}$)	C_s ($J \cdot kg^{-1} \cdot K^{-1}$)	α_h (h)	β_h (-)	RH (-)	c_{fi} (-)
294.15	0.15, 0.05, 0.1	0.087, 0.079, 0.081	2040, 2034, 2036	3150	1081	23	0.69	0.94	0.21

Table 3.7. Constant parameters used for the simulation of the 28 days UCS for the results reported by Beckett et al. [111]

3.3 Conclusion

The purpose of this chapter is to evaluate a number of previously published experimental data for URE and CSRE materials to validate the theoretical framework that was established in the previous chapter. The investigated experimental results including the drying process, heat and relative humidity transfer, compressive strength, tensile strength, stress-strain relation, cement hydration process, effects of water-cement ratio, etc. are compared with the numerical predictions. The comparations show a good capacity of the proposed model to explain the time-dependent CTHM properties of CSRE (URE) materials in the laboratory conditions. After that, the suggested numerical framework is utilized and expanded to estimate the characteristics of typical CSRE (URE) walls under in-situ conditions, and the associate numerical simulations are introduced in the following chapter.

Chapter 4. Applications and case studies

4.1 Case study for URE structures

Once constructed on the ground, URE structures interact continually with the environment and the ground. Since URE structures are often constructed by directly embedding the material surface in the environment, environmental effects are constantly present. However, the impacts of the ground on URE might vary from site to site due to the fact that the bottom of a URE structure can be built with or without a basement. Section 4.1.1 depicts the impacts of various local environments on the THM behavior of URE walls, excluding the effects of underground soil due to the reason of basement. Section 4.1.2 illustrates the environmental and underground soil impacts on the THM properties of URE walls constructed without a basement.

4.1.1 Thermo-hydro-mechanical (THM) behavior of unstabilized rammed earth (URE) wall submitted to environmental and mechanical loadings

The behavior of URE materials is greatly influenced by the variation of suction, relative humidity, temperature and stress state. The hydro-thermal properties and soil types have a considerable impact on the stability of earth structures [313]. Climate changes significantly affect the properties of earth structures [314–317]. Generally, URE materials are prepared at their OWCs, but the water contents in the material may change with time in its structural life due to environmental loadings. In this section, the effects of environment air and raw soil type (for URE construction) on themo-hydro-mechanical behaviors of typical two stories residential buildings constructed with the basements are investigated through numerical simulation. The effects of the underground soil on the walls are not considered in this case study. And the URE walls built with a height of 3 m, a thickness of 0.3 m and a width of 4 m at the first stoery of the buildings are investigated in the numerical simulations of this section (Figure 4.1).

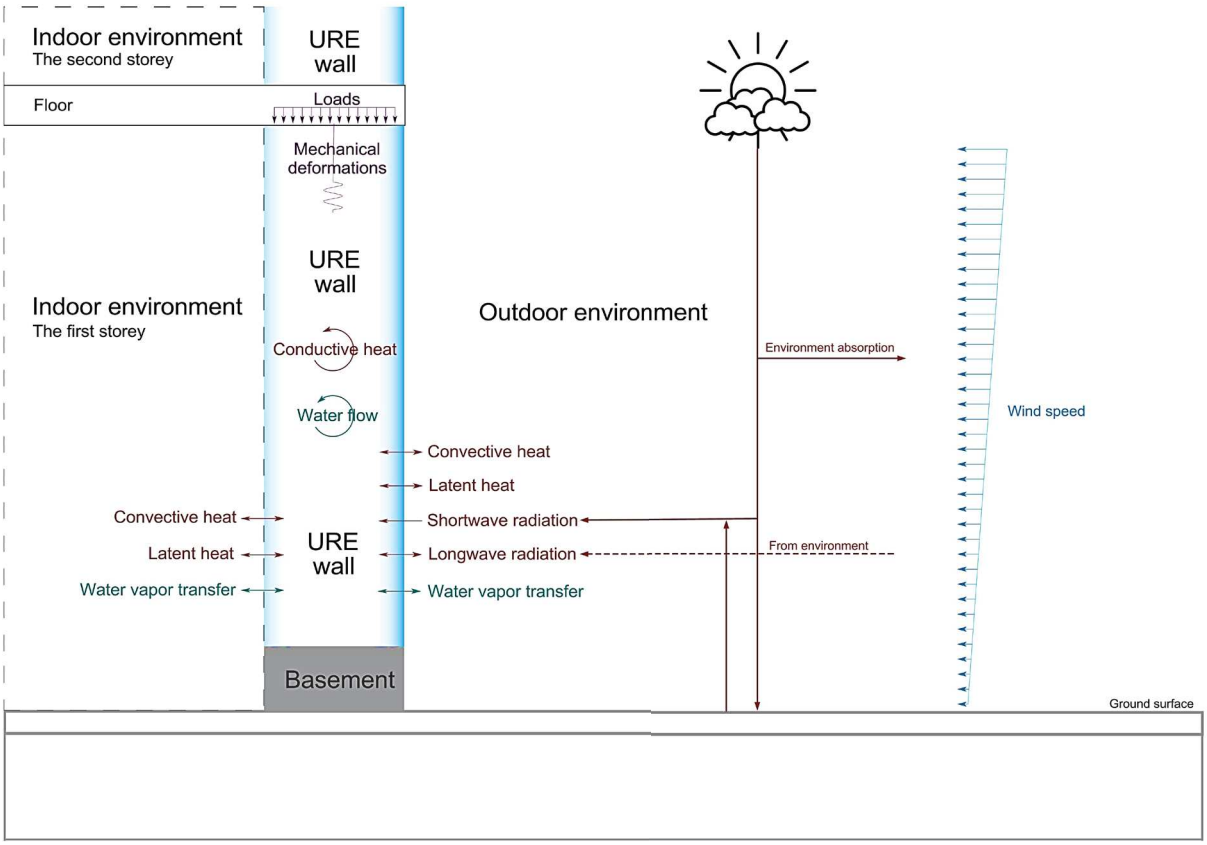

Figure 4.1. Schematic diagram of a fresh URE wall in interaction with indoor/outdoor environment

4.1.1.1 The studied walls and the geoclimatic conditions

The Free Tetrahedral is used for the mesh and the generated meshes are denser on the wall surfaces where the material properties are more sensitive to the climate conditions. A boundary layer mesh with four layers was deployed due to the steep temperature and suction gradients. In total, 22003 elements with the number of degrees of freedom 172090 were generated for this numerical simulation model. The geometry and its mesh are shown in Figure 4.2.

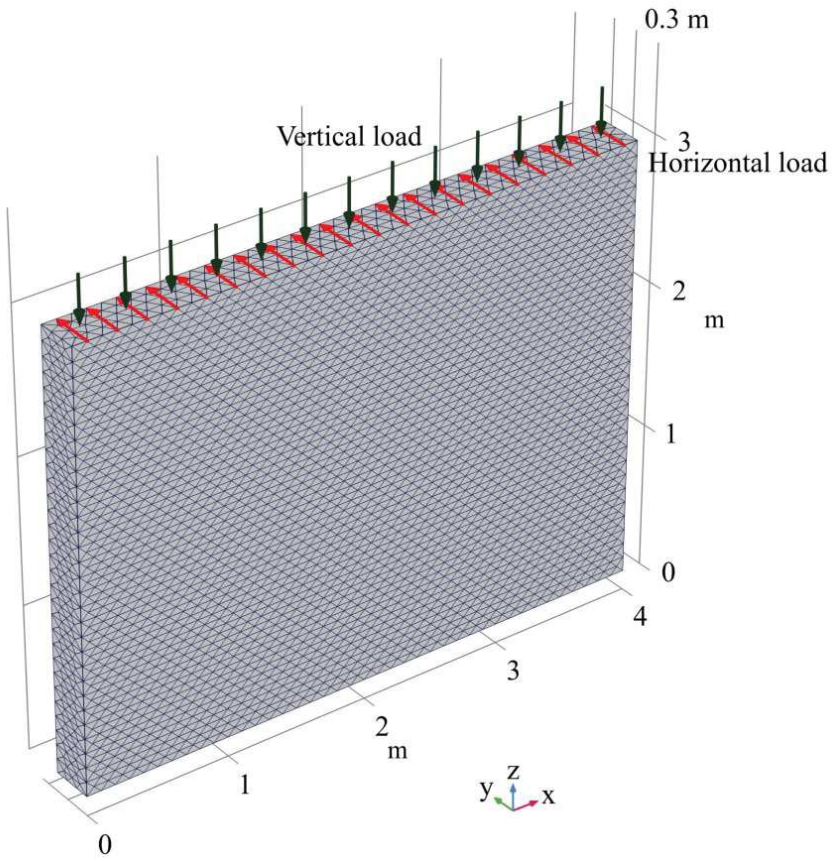

Figure 4.2. Meshed geometry of the studied URE wall and its mechanical loadings

The URE walls are supposed to be built in France where the meteorological conditions can be divided into six climate regions (Figure 4.3) [318]. The central region in France is mainly dominated by a modified oceanic climate. The east and the west of France are respectively characterized by oceanic and semi-continental climate types. The southwest is dominated by the Aquitaine oceanic climate. However, the weather of the central south and southwest of France is characterized by a mountainous climate. Finally, the south coast of France is generally dominated by a Mediterranean climate. Variations of relative humidity and temperature in 40 years (1979-2019) are investigated in the above six regions. Finally, two more representative climate regions (Regions 2 and 3) are selected to recreate the natural climate conditions for the reason that the climate variations in the other four regions are more moderate.

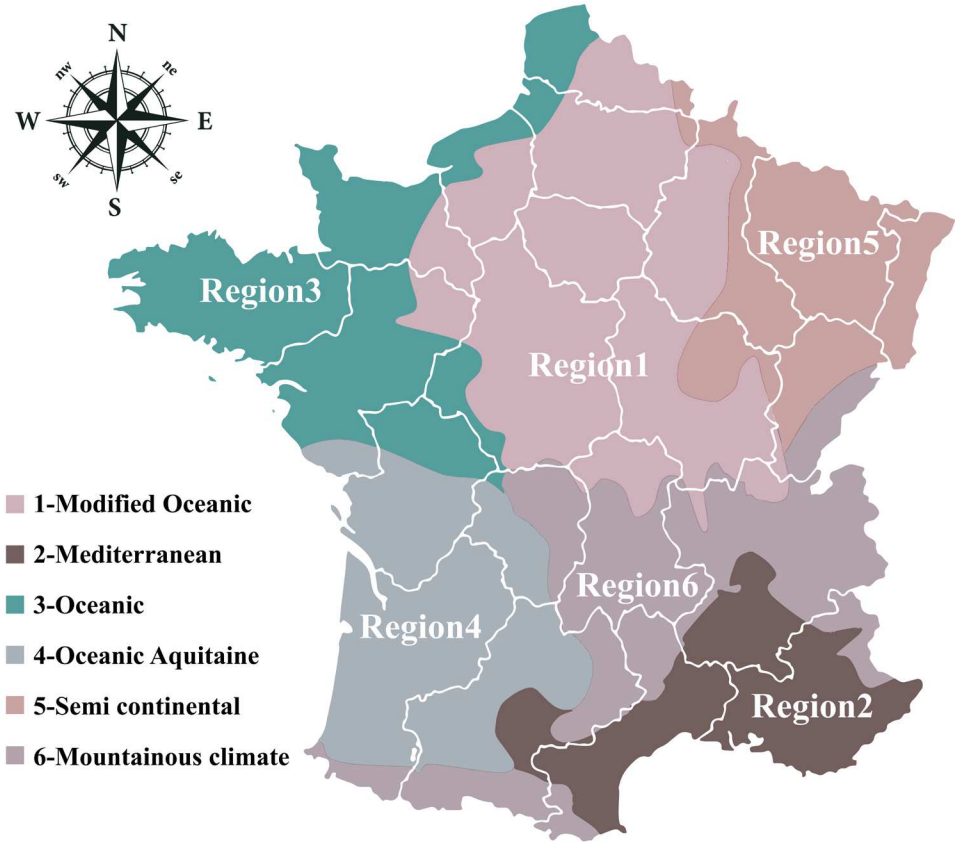

Figure 4.3. Climate types of the studied regions (Region 2, 3)

Moreover, the walls are assumed to be compacted with the same dry density 2000 kg·m^{-3}. Since the soil particles can be different due to the variations of the geological and geotechnical layer as well as the depth of excavation, therefore, two fine contents of 0.3 and 0.7 are used to illustrate these changes.

The indoor relative humidity (RH_{int}) and temperature (T_{int}) are respectively fixed 0.5 and 20°C [301]. The initial relative humidity (RH_{ini}) inside URE wall is also assumed constant, equal to 0.99. The initial inside temperature (T_{ini}) is equal to the average external temperature.

The studied walls correspond to a typical residential building with one ground floor and one floor. Thus, constant vertical stress of 61.7 kPa is applied to the wall corresponding to live and dead loads of the residential building. The movement at the bottom of the wall in all directions is fixed while the other displacements are free. In addition, the elastic modulus and the thermal conductivity of the wall are obtained through [158].

The related boundary conditions for this case study are summarized in Table 4.1 and constant values used for the numerical simulations are summarized and presented in Table 4.2.

Local conditions	Values

Outdoor relative humidity	Equation 51
Outdoor temperature	Equation 61
Indoor relative humidity	0.5
Indoor temperature	20°C
Outdoor wind speed	Equation 48
Local Shortwave radiation	Equation 56
Local environmental longwave radiation	Equation 57
Ground longwave radiation	Equation 58
Ground surface temperature	Thermal insulation
Ground surface suction	Water insulation
Vertical load on the top of the wall	61.7 kPa

Table 4.1. Boundary conditions for the numerical simulations

Constant parameters used for numerical simulations

Constant for different regions			Common constant for region 2 and region 3					
parameter	Region 2	Region 3	parameter	value	parameter	value	parameter	value
	value	value						
			C_3S (-)	0	T_{am} (K)	7.01	v_{wind0} ($m \cdot s^{-1}$)	4.27
			C_2S (-)	0	T_{hr} (K)	293.15	α_H (-)	0.4
RH_{av}(-)	0.69448	0.80475	C_3A (-)	0	u_0 (MPa)	1	β_{inc} (-)	$\pi/2$
RH_{am}(-)	0.12878	0.09246	C_4AF (-)	0	u_1 (-)	0.829	ε_e (-)	0.97
t_{RH}(day)	57.4	68.23	SO_3 (-)	0	u_2 (MPa)	13	w_{ini} (-)	0.081
T_{av}(°C)	14.29	11.3	MgO (-)	0	u_3 (-)	1.25	ρ_{dini} ($kg \cdot m^{-3}$)	2000
T_{am}(°C)	8.92	7.01	FreeCaO (-)	0	u_4 (-)	6	θ_r (-)	0.0045
t_T(day)	120.76	120.58	a_{lb} (-)	0.25	t_{ref} (day)	182.5	n_{ini} (-)	0.23077
t_{ref}(day)	182.5		C_{KC} (m^2)	3.81E-13	α_h (h)	23	σ_B (-)	5.67E-08
RH_{int}(-)	0.5		C_s ($J \cdot kg^{-1} \cdot K^{-1}$)	1105	β_h (-)	0.69	c_{ini} (-)	0
T_{int}(°C)	20		C_{wi0} ($s^2 \cdot m^{-2} \cdot K^{-1}$)	6.88E-15	L (m)	0.3	ρ_c ($kg \cdot m^{-3}$)	3150
w_{ini} (-)	0.081		e_1 (-)	85.92	l_{VG} (-)	0.5	c_{fi} (-)	0.4

T_{ini}(°C)	14.29	11.3	e_2 (-)	1.766	M_a (kg·mol^{-1})	29	p_{at} (Pa)	101325
v_{wind0}(m·s^{-1})	3.91	4.27	g (m·s^{-2})	9.8	M_w (kg·mol^{-1})	18	ρ_s (kg·m^{-3})	2600
ρ_d(kg·m^{-3})	2000		H_0 (m)	10	n_{VG} (-)	1.4	RH_{am} (-)	0.09246
c_{fi}(-)	0.3, 0.7		K_1 (-)	0.5	T_{av} (K)	284.45	RH_{av} (-)	0.80475
			C_c (-)	0.41	K_3 (-)	0.3457	t_{RH} (day)	65.73
			t_T (day)	120.58	ν (-)	0.25	h_{eff} (W·m^{-2}·K^{-1})	10

Table 4.2. Constant values used for the numerical simulations

4.1.1.2 Simulation results

The simulations are performed for a period of 5 years after the construction of the wall in both climate regions to obtain the variation of volumetric water content, suction and temperature inside the wall.

Figure 4.3 shows the evaluation of average volumetric water content and suction inside URE wall built in regions 2 and 3 in France. It can be observed that both fine content and climate condition influence the drying process of the wall. All URE walls have almost the same initial suctions because of the same initial relative humidity (RH_{ini}) in the walls. Consequently, the initial volumetric water contents are different because of the different SWRCs of the studied URE materials. For the walls with lower fine content, a less amount of water is required to have the same suction values compared to a wall with a higher fine content. The results confirm that the material type plays an important role in the hydraulic properties of the URE wall. Moreover, the drying process mainly takes place in the first year after construction as the water content/suction decreases/increases to 70%/43% during the first year. After that, the suction and water content gradually reach an equilibrium stage after 5 years. In addition, with the same climate condition, the wall with a higher fine content has a higher suction. This is because that the wall with a higher fine content is made up of more small pores, which leads to a smaller effective radius between pores and consequently a higher suction based on Young–Laplace equation. On the other hand, the wall with a lower fine content has a lower suction value. This is caused by larger pore spaces between pores. For the same fine content, the wall in region 2 has higher suction values than that in region 3 due to a dryer climate condition.

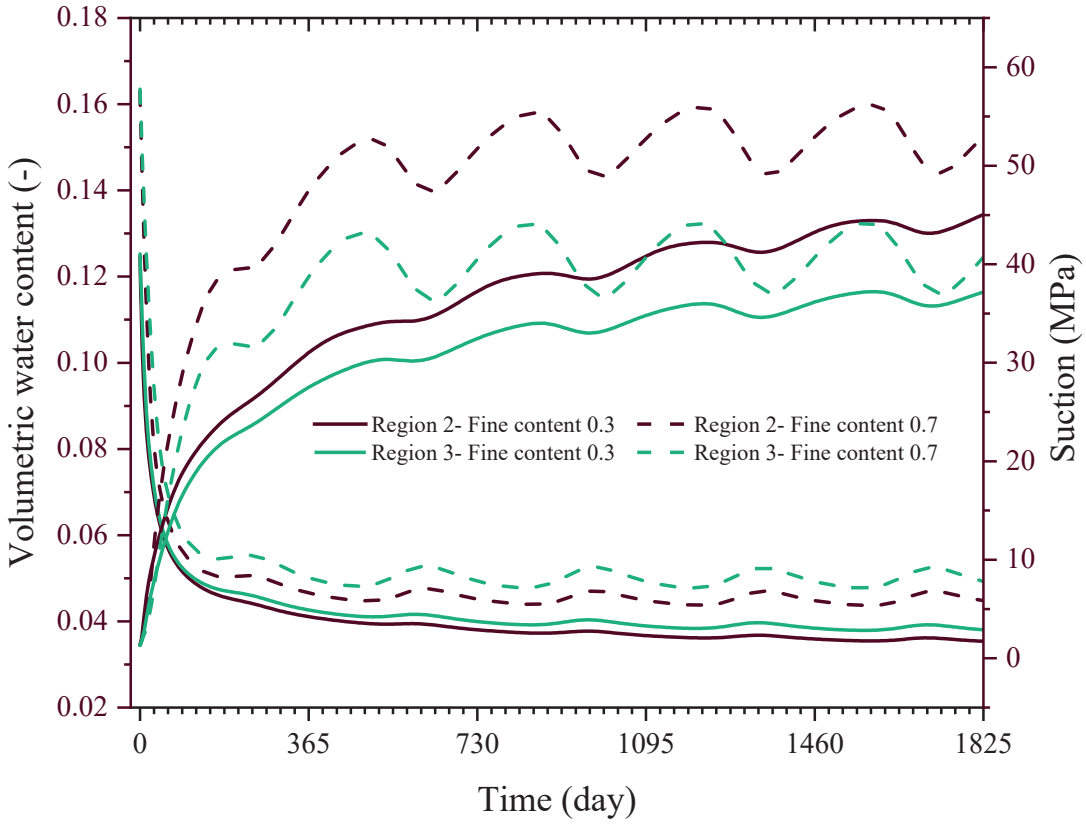

Figure 4.4. Variation of average volumetric water content and suction in URE walls in regions 2 and 3 in France in 5 years

Figure 4.5 presents the variations of the average temperature in the URE wall built in the two regions 2 and 3. From the long-term point of view, it can be observed that the average temperature inside the wall is not influenced obviously by the humidity and the fine content of the wall but varies seasonally due to the seasonal temperature changes on the external side of the wall in different climate regions.

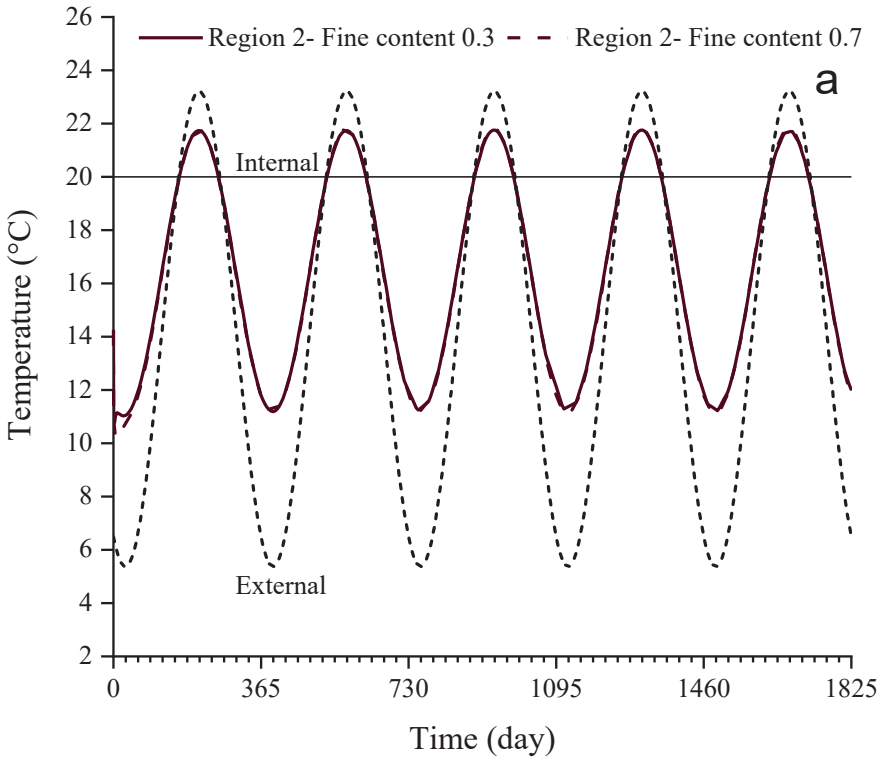

(a)

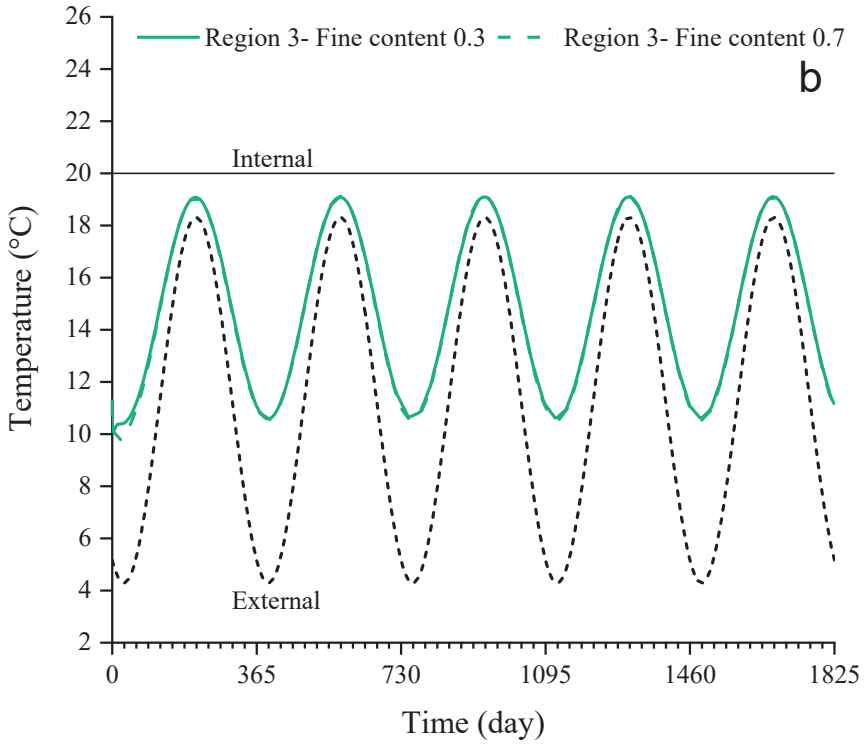

(b)

Figure 4.5. Variation of average temperature in URE walls corresponding to internal and external wall temperature in regions 2 and 3 in France in 5 years

At the end of different times after construction, the horizontal loads are applied in the direction presented with red arrows in Figure 4.2 to obtain the ultimate strength of URE walls. The horizontal wind loads are neglected due to the low average wind speed on the wall (around $0.3 m \cdot s^{-1}$). The horizontal loads increase gradually with an incremental surface load until the failure occurred. Therefore, an increasing rate of $10 kN \cdot s^{-1}$ is applied on the top surface of the wall.

The wall in region 2 with the fine content 0.7 is selected to show the typical failure mode of the wall after five years of equilibrium. Figure 4.6a shows the stress distribution in two front and back sides of the wall. The stress is higher near the bottom side of the wall due to the imposed horizontal movements on the top of the wall. In addition, the highest compressive and tensile stresses occur respectively on the front and back side of the wall. Since the compressive strength of URE materials is largely higher than their tensile strength (usually ten times), the tensile damage occurs on the bottom back side of the wall (and not on the front side under compression). Figure 4.6b shows also the evolution of plastic strain in front and back sides of the wall. The damage mode can be observed in back side plane of Figure 4.6b as the plastic strains occurred in the areas where the tensile stresses are concentrated.

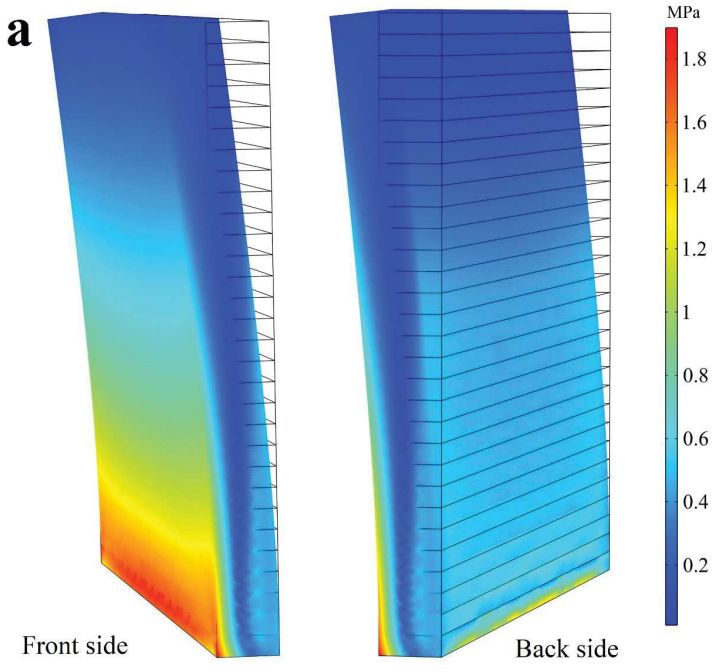

(a)

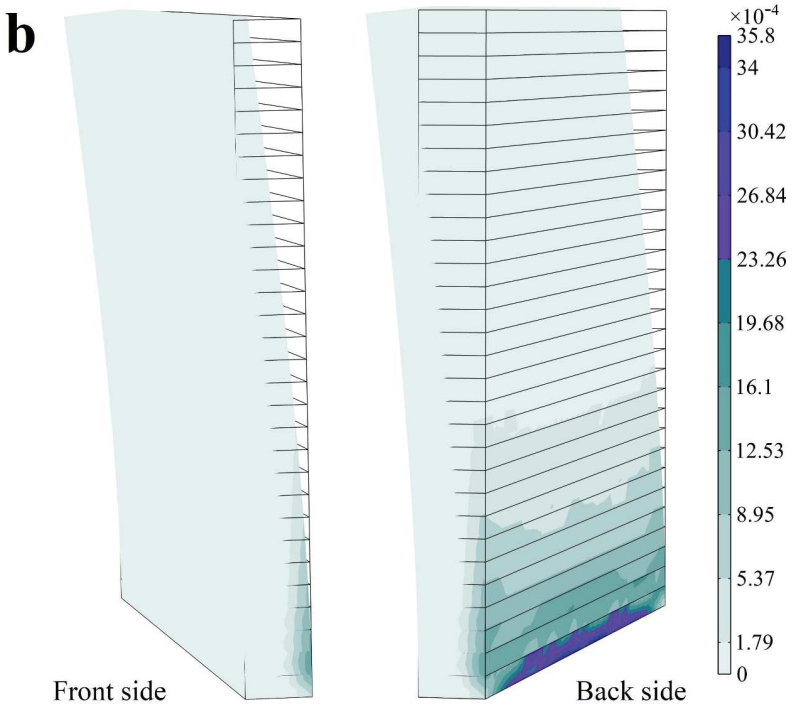

(b)

Figure 4.6. The typical failure mode of the wall a) stresses and b) plastic strains in front and back sides of the wall

When the failure occurred, the corresponding loads applied on the top surface of the wall are recorded as the horizontal strength of the wall. The simulation results in Figure 4.7 shows that the horizontal strength of URE wall increases ~43% for the wall with the fine content of 0.3 and ~75% for the wall with the fine content of 0.7 in both regions. After five years, the horizontal strength stabilizes with time. The final stabilized values after five years increase around two times in both regions when the fine content of the local soil increases from 0.3 to 0.7 (from ~11 to ~23 kN). The figure shows also that the wall with the higher fine content shows more sensitivity to climate variations. This is because of a more variation of the effective radius in the small pore spaces leading to a higher variation of suction and consequently horizontal strength. Moreover, the walls have relatively higher strength in summer (for example after 550 days) than in winter (for example after 730 days). When the fine content is the same, the wall in region 2 has a slightly higher horizontal strength than that built in region 3 due to its dryer climate condition. However, this increase is less significant compared to the effect of time and fine content.

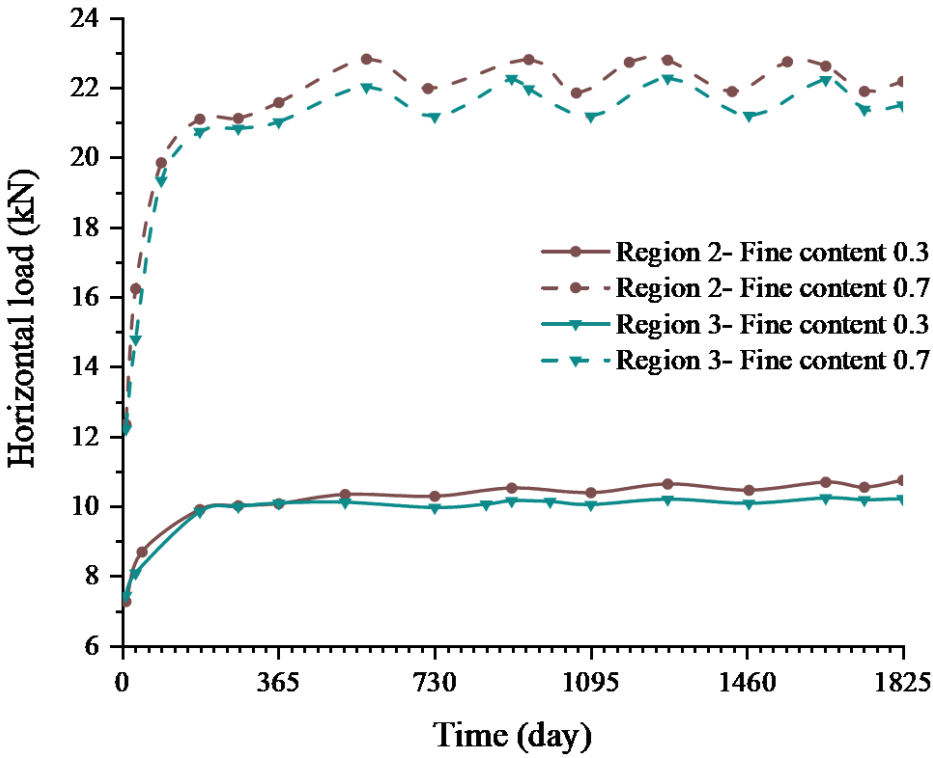

Figure 4.7. Ultimate shear strengths of URE walls with the horizontal load in regions 2 and 3

Globally, the results show that the strength of URE wall in the above two regions in France is highly dependent on the geological conditions and less sensitive to climate changes. The wall strength can be improved by maintaining its dry state and making the source soils contain more smaller particles.

4.1.2 Effect of rising damp in URE walls

Once URE structures are constructed, especially without the protection of the basement, rising damp and water evaporation will significantly influences their properties [319]. The rising water occurs because of bad indoor conditions, poor thermal insulation, and materials deterioration [320]. This reduces highly the mechanical properties of URE walls. In contrast, the water loss caused by water evaporation prevents this reduction and improves masonry structure properties [321]. The rising damp occurs when groundwater flows into the base of construction driven by the capillary force. The water rises from the ground then transports into earth materials, and the water on the surface is then subjected to evaporation in the form of water vapor. The process of water flow and evaporation coexist until an equilibrium stage is reached. The equilibrium condition can be disturbed at any time due to a time-dependent

atmosphere variation. Eventually, the water kept inside causes a wet condition of the materials. Since URE is produced with earth where its characteristics are sensitive to water [322], the rising damp and climate variations have important implications on URE materials.

In summary, the rising damp and time-dependent climate changes have significant influences on the thermal-hydro-mechanical characteristics of URE materials, and these properties are of vital importance for the practical utilization of this material. This section aims to study the effect of the rising damp in an in-situ environmental condition on the long-term THM assessment of a typical newly constructed URE wall after a long period at its equilibrium stage, and the proposed numerical approach is used to simulate the rising damp with time in a URE wall built in Brittany region (situated in west of France) by considering rising damp, indoor/outdoor temperature, indoor/outdoor relative humidity, wind speed, shortwave and longwave radiation and mechanical solicitations (Figure 4.8).

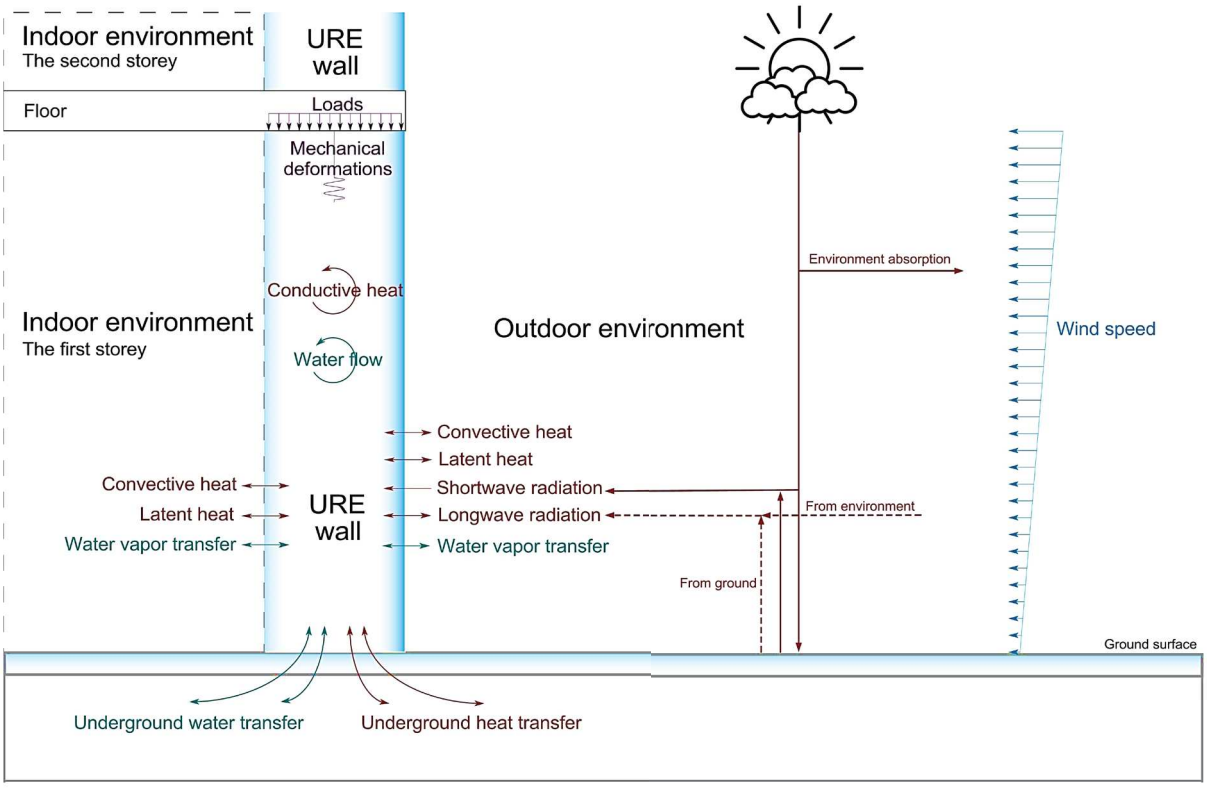

Figure 4.8. Schematic diagram of a fresh URE wall in interaction with indoor/outdoor environment and ground

4.1.2.1 The studied walls and the geoclimatic conditions

The same building as introduced in section 4.1.1 but without basement is used for numerical simulation. The URE wall at the first stoery with a height of 3 m, a thickness of 0.3 m and a

width of 4 m is studied. The wall is supposed to be constructed vertically in layers of 10 cm. The wall faces to the South orientation and the annual energy availability is taken into consideration [323]. The fine content of the URE material is taken 0.4 corresponding to the dominant geology of the Brittany region in France. The dry density attributed to this soil is 2000 $kg \cdot m^{-3}$ in each layer. The free triangular method is used for the mesh and 58353 elements are generated for this numerical simulation model. The geometry and its mesh are shown in Figure 4.9.

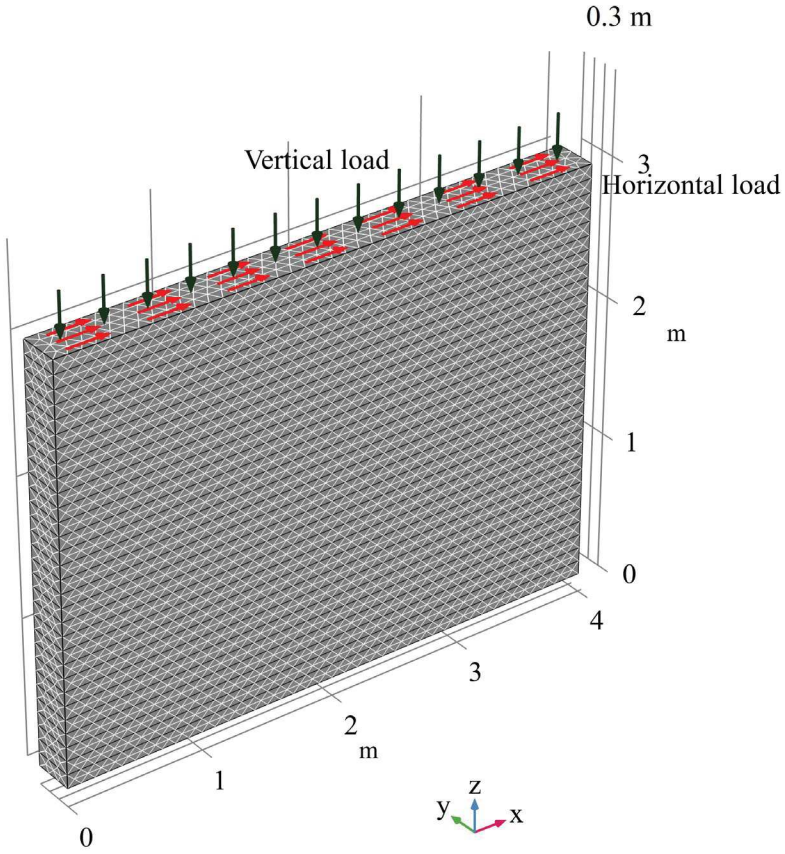

Figure 4.9. Geometry and mechanical boundary conditions of the studied URE wall

The studied walls correspond to a typical residential building with one ground floor and one floor. Thus, constant vertical stress of 61.7 kPa is applied to the wall corresponding to live and dead loads of the residential building. The movement at the bottom of the wall in all directions is fixed while the other displacements are free. The rising damp in masonry walls has been usually studied in the laboratory with the bottom surface of the wall soaked under saturated conditions [324,325], while in reality, the water on the ground may penetrate downside into soil leading to an unsaturated condition. Therefore, the total suction on the bottom of the wall is given by an average near-ground suction value of 1 MPa [259,298] for the case with the rising damp. For the condition without rising damp, the bottom surface is assumed to be insulated

with no water flow. Moreover, the temperature on the bottom is assumed to be equal to the soil surface temperature which is the outdoor temperature. The initial relative humidity (RH_{ini}) inside the wall is considered constant, equal to 0.99 (around the optimum water content). The initial inside temperature (T_{ini}) is equal to the average external temperature. The boundary conditions are summarized in Table 4.3 and the constant parameters used for numerical simulations are summarized and presented in Table 4.4.

Local conditions	**Values**	
Outdoor relative humidity	Equation 51	
Outdoor temperature	Equation 61	
Indoor relative humidity	Equation 52	
Indoor temperature	Equation 62	
Outdoor wind speed	Equation 48	
Local Shortwave radiation	Equation 56	
Local environmental longwave radiation	Equation 57	
Ground longwave radiation	Equation 58	
Ground surface temperature	Equation 61	
Ground surface suction	Without damp: water insulation	With damp: 1 MPa
Vertical load on the top of the wall	61.7 kPa	

Table 4.3. Boundary conditions for the numerical simulations

Constant parameters used for numerical simulations							
C_3S (-)	C_2S (-)	C_3A (-)	C_4AF (-)	SO_3 (-)	MgO (-)	FreeCaO	a_{lb} (-)
0	0	0	0	0	0	0	0.25
C_{KC} (m^2)	C_s ($J \cdot kg^-$	C_{wi0} ($s^2 \cdot m^-$	e_1 (-)	e_2 (-)	g ($m \cdot s^{-2}$)	H_0 (m)	K_1 (-)
3.81E-13	1081	6.88E-15	85.92	1.766	9.8	10	0.5
T_{am} (K)	T_{hr} (K)	u_0 (MPa)	u_1 (-)	u_2 (MPa)	u_3 (-)	u_4 (-)	t_{ref} (day)
7.01	293.15	1	0.829	13	1.25	6	182.5
α_h (h)	β_h (-)	L (m)	l_{VG} (-)	M_a	M_w	n_{VG} (-)	T_{av} (K)
23	0.69	0.3	0.5	29	18	1.4	284.45
v_{wind0} ($m \cdot s^{-1}$)	α_H (-)	β_{inc} (-)	ε_e (-)	w_{ini} (-)	ρ_{dini} ($kg \cdot m^-$	θ_r (-)	n_{ini} (-)
4.27	0.4	$\pi/2$	0.97	0.081	2000	0.0045	0.23077
σ_B (-)	c_{ini} (-)	ρ_c ($kg \cdot m^{-3}$)	c_{fi} (-)	p_{at} (Pa)	ρ_s ($kg \cdot m^{-3}$)	RH_{am} (-)	RH_{av} (-)
5.67E-08	0	3150	0.4	101325	2600	0.09246	0.80475
C_c (-)	K_3 (-)	t_{RH} (day)	t_T (day)	ν (-)			
0.41	0.3457	68.23	120.58	0.25			

Table 4.4. Constant values used for the numerical simulations

4.1.2.2 Simulation results

In this section, we simulate the main THM characteristics of URE wall at different time steps and areas of the wall with and without the effect of damp rising. The simulations are performed for a period of 5 years after the construction of the walls to obtain the variations of suction, volumetric water content, temperature, thermal conductivity, elastic modulus and unconfined compressive stress with and without rising damp effects.

The vertical line in the middle of the wall, the horizontal line at height 0.5m and the intersection point in the wall are selected as the probes to show respectively the effect of wall height, wall thickness and time on the THM properties of the wall (Figure 4.10).

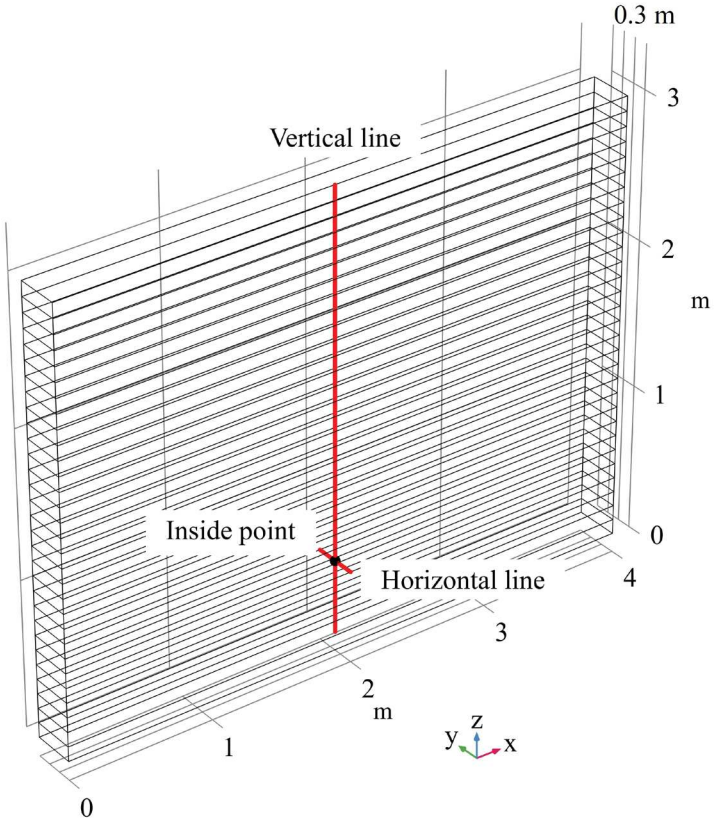

Figure 4.10. Selected point and lines for the presentation of the results

Figure 4.11 shows the variations of suction and volumetric water content in the walls. It can be observed for the wall not affected by rising damp (Figure 4.11a) that the volumetric water content decreases 68.8% after five years of construction. However, this value is only 19.9% when the rising damp exists. It indicates that the rising damp prevents significantly the drying process of URE wall. For the wall not affected by rising damp, the hydraulic condition changes mainly in the first year before reaching a stabilized equilibrium stage which varies periodically in the latter four years. While the rising damp accelerates this process and reaches the equilibrium stage within 100 days (less than one year). This is caused by more water movements

at the bottom side of the wall with the rising damp. Figure 4.11b presents the hydraulic variations in the vertical direction after 5 years of construction. The results show that the volumetric water content/suction decreases/increases with height due to the rising damp, evaporation and gravity. It shows that the volumetric water content remains almost constant without rising damp while the volumetric water content varies 3.5 times (and suction over 20 times) with height with the rising damp. The results also show that the height of 1.5 m is a distinctive height non affected by the rising damp. At this height, the wall passes abruptly from dry state to wet state. Figure 4.11c shows that the hydraulic condition varies also with the wall thickness after 5 years of construction. The results show that the wall is dryer on its surface and wetter inside. However, the suction value remains almost the same at the height of 0.5 m with rising damp while it changes around 2 times more without rising damp.

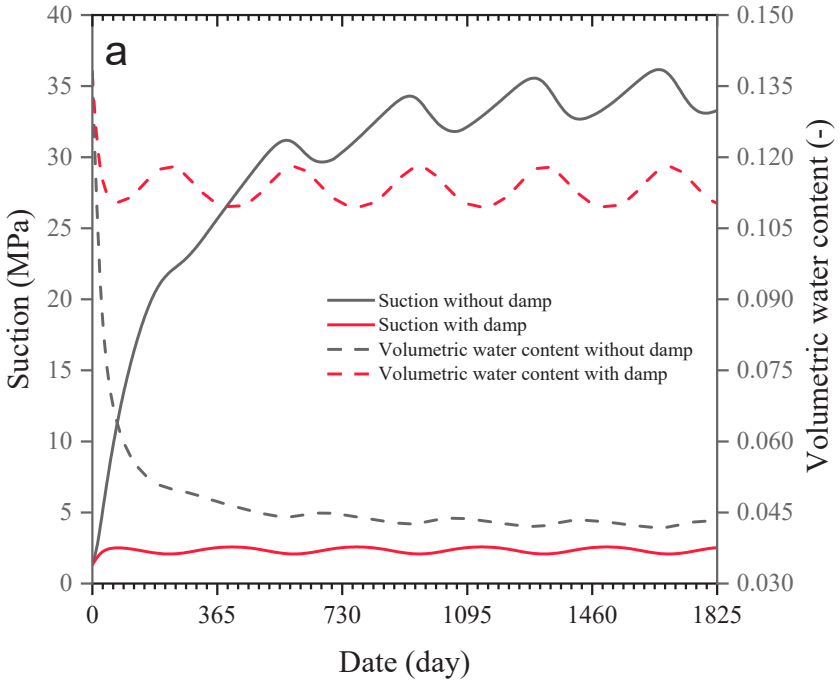

(a)

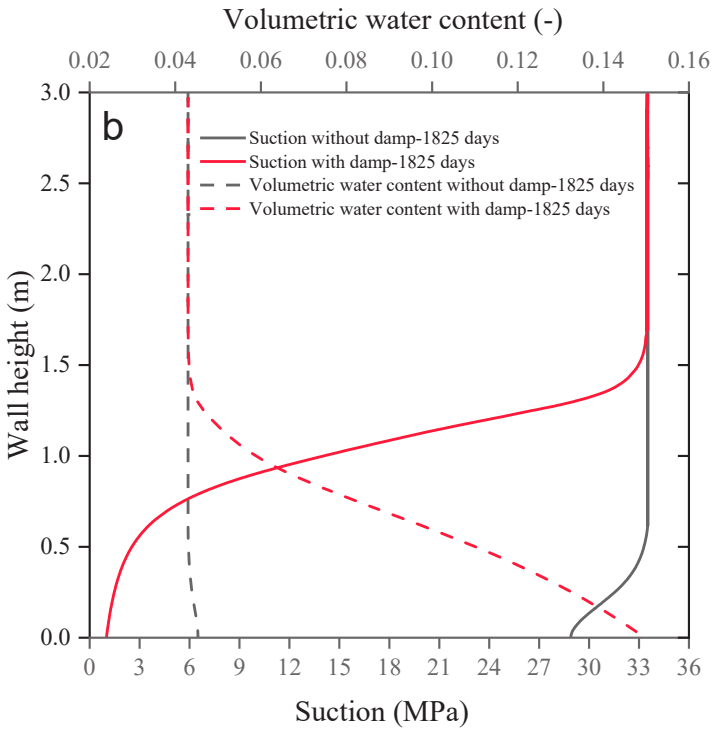

(b)

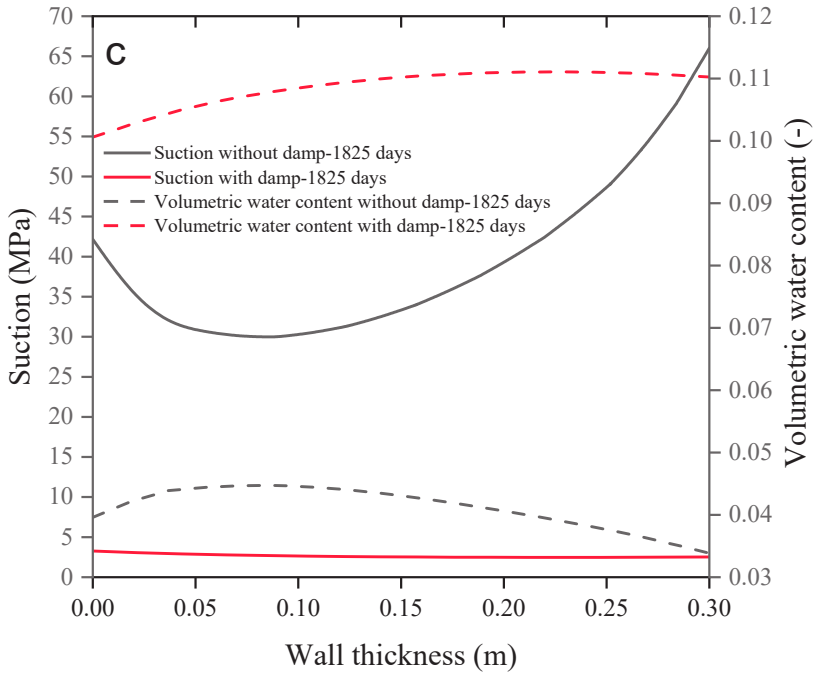

(c)

Figure 4.11. Suction and volumetric water content value of the selected probes according to (a) time (b) wall height (c) wall thickness for the condition with and without rising damp.

Figure 4.12 shows the variations of temperature and thermal conductivity in the walls. It can be observed in Figure 4.12a that the temperature reaches an equilibrium stage and changes

seasonally with the ambient temperature in the first days. Since the thermal conductivity is influenced by the hydraulic condition of the wall, the variation of thermal conductivity according to time has a similar variation of water content as presented in Figure 4.11a. This means also that the temperature has less influence on the thermal conductivity. It can be observed in Figure 4.12b that the thermal conductivity remains almost the same in the vertical direction without rising damp and increases 28% with height with the rising damp after 5 years of construction. It illustrates that the temperature in the vertical direction is dominated by the ground temperature of earth. The temperature is lower in the vertical direction with the rising damp indicating that the rising damp has a cooling effect on the wall. Figure 4.12c illustrates the variation of temperature and thermal conductivity with thickness at the height of 0.5 m after 5 years of construction. It shows that the wall has a higher thermal conductivity inside the wall than on its surface. The temperature changes linearly with the wall thickness and it is mainly controlled by the temperature on the wall surface.

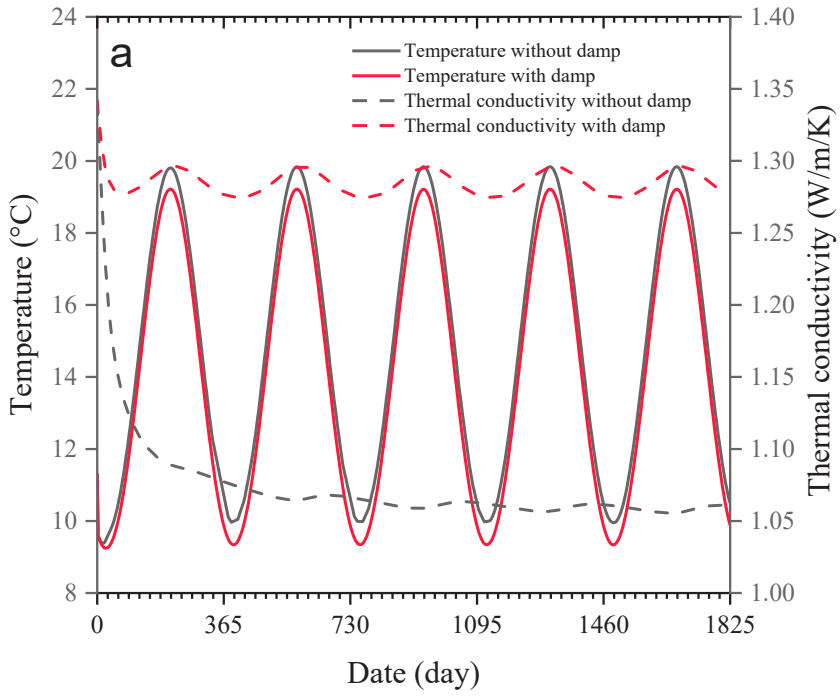

(a)

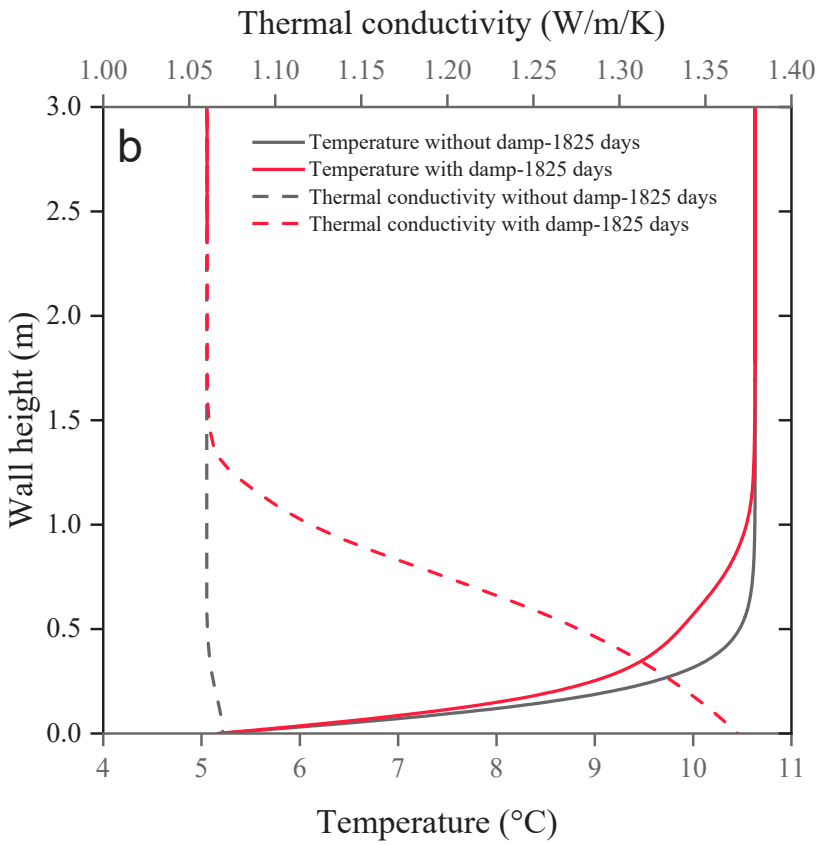

(b)

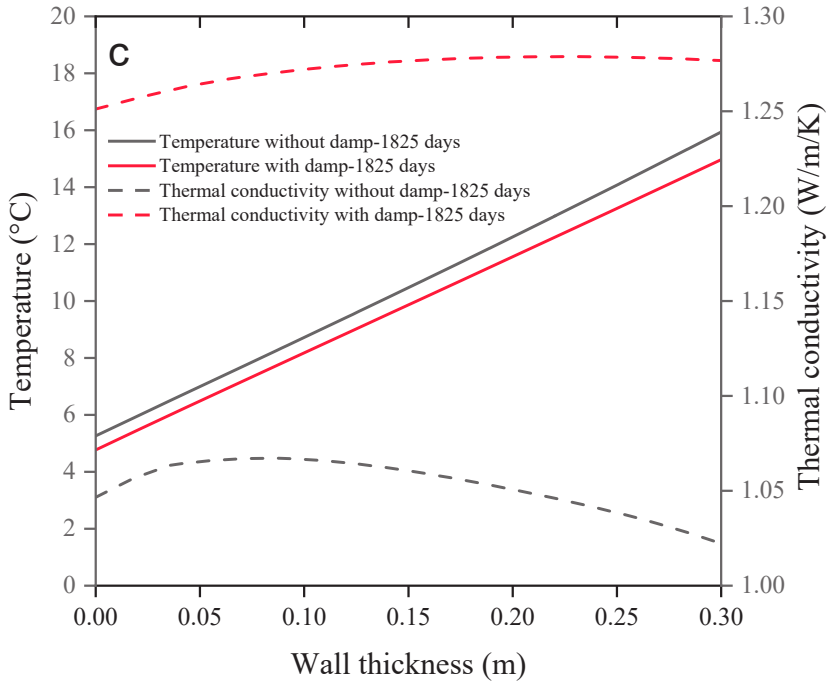

(c)

Figure 4.12. Temperature and thermal conductivity of the selected probes according to (a) time (b) wall height (c) wall thickness for the condition with and without rising damp.

Figure 4.13 shows the variations of elastic modulus and unconfined compressive strength (UCS) in the wall. Figure 4.13a shows that the elastic modulus and UCS vary seasonally with time. Moreover, the elastic modulus increases around 5 times in the first year without rising damp and then stabilizes around 270 MPa for the latter four years. With the rising damp, the elastic modulus stabilizes around 80 MPa within 100 days. The UCS values in the wall are stabilized around 1 MPa and 1.9 MPa respectively with and without rising damp. After 5 years of construction, the elastic modulus and UCS increase with height (Figure 4.13b). Figure 4.13c shows that the wall at the height of 0.5m has lower values of elastic modulus and UCS inside the wall than on its surface after 5 years of construction. It means that the evaporation process increases the mechanical characteristics of URE wall, while the rising damp and gravity has an opposite effect.

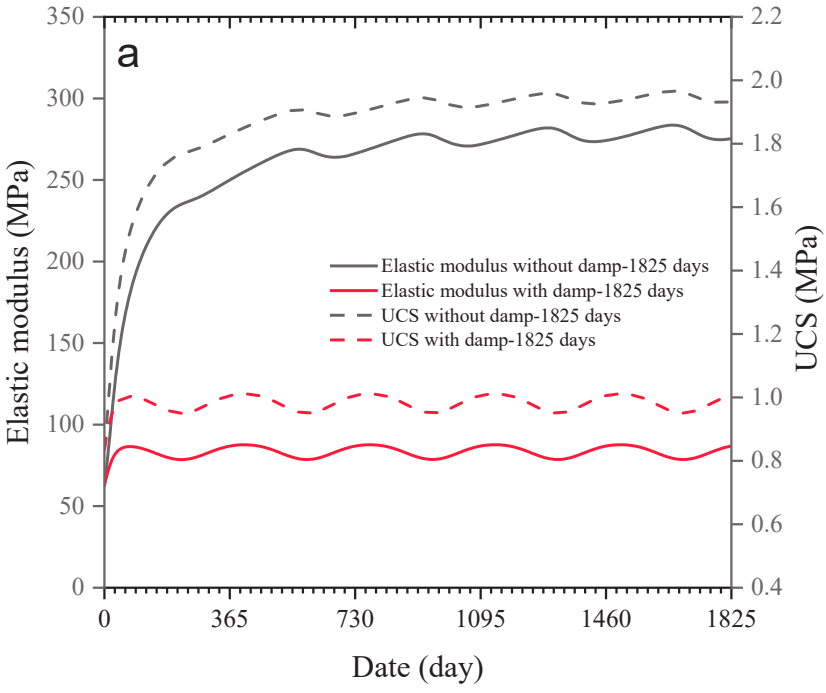

(a)

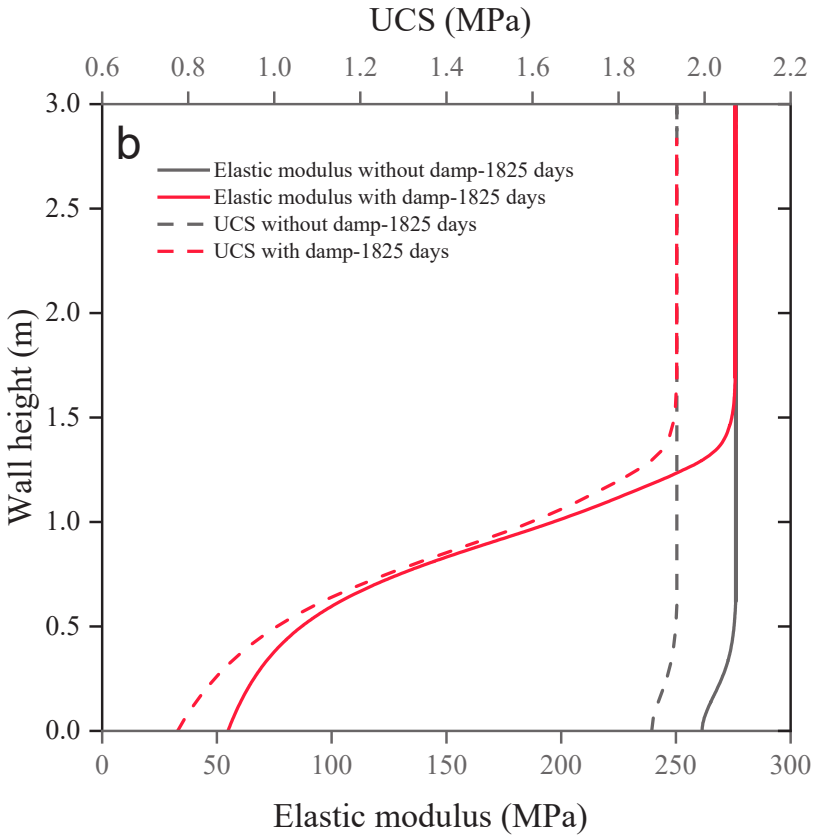
UCS (MPa)
0.6
0.8
1.0
1.2
1.4
1.6
1.8
2.0
2.2
b
Elastic modulus without damp-1825 days
Elastic modulus with damp-1825 days
UCS without damp-1825 days
UCS with damp-1825 days
Wall height (m)
3.0
2.5
2.0
1.5
1.0
0.5
0.0
0
50
100
150
200
250
300
Elastic modulus (MPa)

(b)

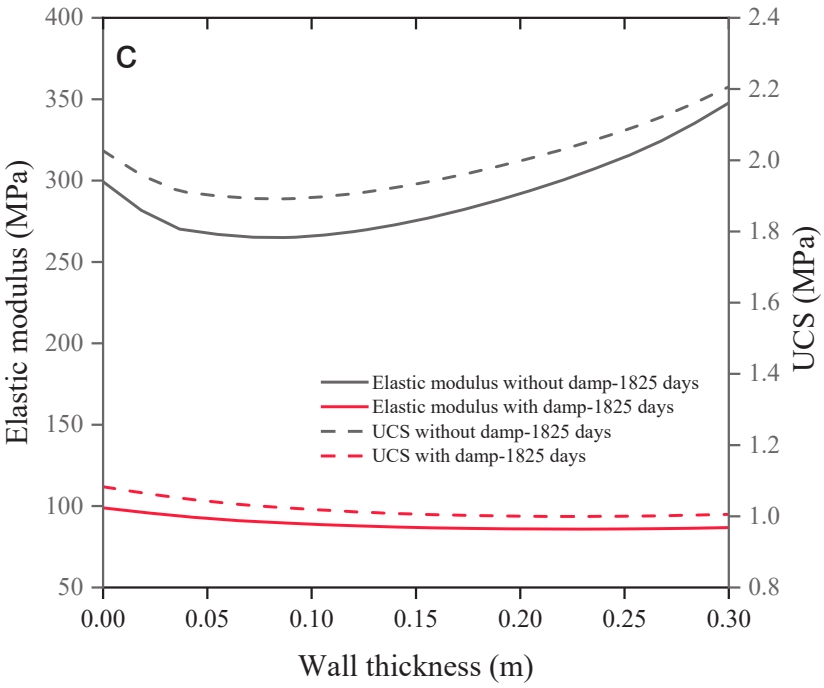
c
Elastic modulus without damp-1825 days
Elastic modulus with damp-1825 days
UCS without damp-1825 days
UCS with damp-1825 days
Elastic modulus (MPa)
400
350
300
250
200
150
100
50
UCS (MPa)
2.4
2.2
2.0
1.8
1.6
1.4
1.2
1.0
0.8
0.00
0.05
0.10
0.15
0.20
0.25
0.30
Wall thickness (m)

(c)

Figure 4.13. Elastic modulus and unconfined compressive strength (UCS) of the selected probes according to (a) time (b) wall height (c) wall thickness for the condition with and without rising damp.

The variation of the ultimate horizontal capacity applied on the top surface of the wall with the horizontal deformation is presented in Figure 4.14. It can be observed that time has a positive effect on the mechanical capacity of the wall where the horizontal deformation/the horizontal bearing capacity decreases/increases with time. In addition, the wall (after 7 days of construction) has a similar ultimate mechanical behavior with and without rising damp because of the same humid condition of the wall. However, the wall with rising damp has slightly lower values of ultimate bearing capacity and elastic modulus compared to those without rising damp. Moreover, the water flows out through the lateral surface of the wall with time, which leads to an increase of the mechanical capacity of the wall in the long term. It can be observed that the horizontal bearing capacity increases 47% from 76.8 to 112.6 kN without rising damp (Table 4.5). However, the presence of rising damp prevents this strength improvement. It can be observed that after long-term equilibrium, the wall affected by rising damp remains almost at the same strength level of 75 kN with only 10% of improvement (Table 4.5). This is caused by the similar effect of rising damp in the wall with the creation of a soft region at its bottom (Figure 4.11 b).

It should be pointed out that the results in Figure 4.14 are based on the numerical model in this paper, while in reality, once the wall reaches its ultimate strength point, the load would rapidly drop upon horizontal failure [326,327].

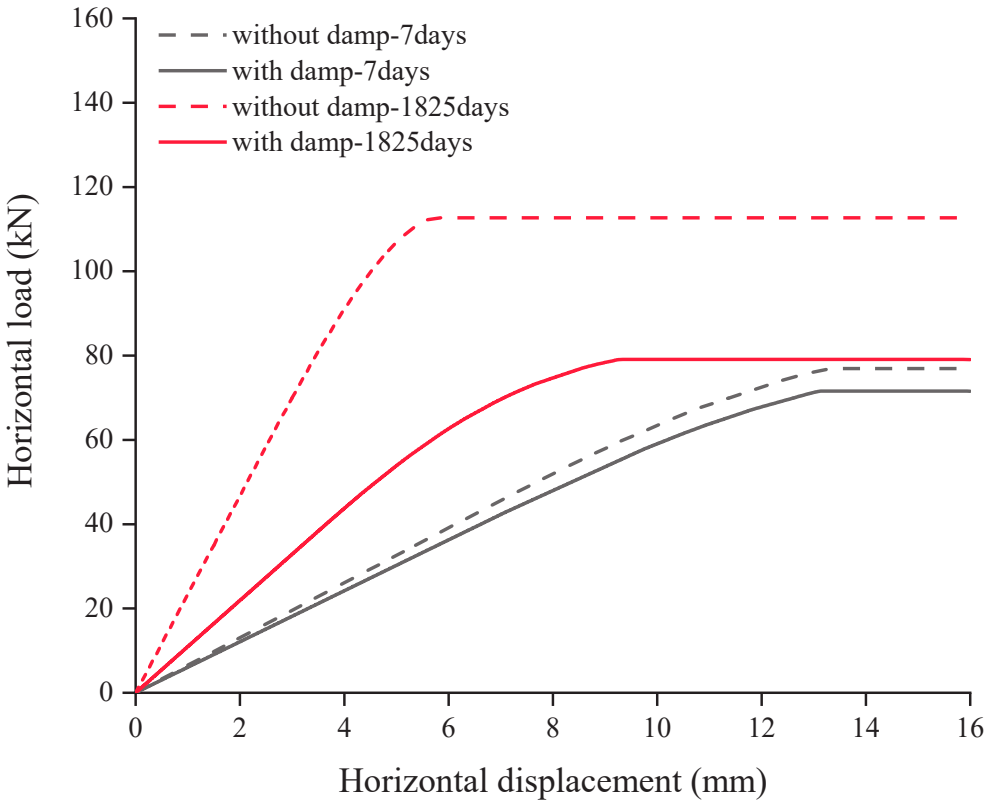

Figure 4.14. Force-displacement diagrams for URE walls

To cover the evolution of all THM properties, Table 4.5 summarizes also the variation of the average thermal insulation resistance (RSI) and the average hydraulic conductivity of the wall with and without rising damp. It shows that the RSI value increases 17% and 22% respectively with and without rising damp after five years. The material becomes almost impermeable after 5 years without damp (~100% of decrease). This decrease of hydraulic permeability is limited to 67% with rising damp.

	With damp (7 days)	Without damp (7 days)	With damp (1825 days)	Without damp (1825 days)
Thermal insulation resistance ($K \cdot m^2 \cdot W^{-1}$)	0.23	0.232	0.269	0.285
Hydraulic conductivity ($m \cdot s^{-1}$)	4.26E-11	2.87E-11	1.41E-11	6.79E-15
Pushover strength (kN)	71.5	76.9	79.1	112.6

Table 4.5. Average THM properties of a typical URE wall

Although two factors of time and evaporation play a positive role on THM properties of URE walls because of the reduction of humidity, the rising damp reduces significantly these improvements. An appropriate drying period and a reducing rising damp technique are highly demanded for the construction of URE materials.

4.2 Case study for CSRE structures

A typical CSRE wall freshly constructed under in-situ conditions is analyzed numerically to evaluate its CTHM qualities under environmental and underground soil solicitations. The behavior of the underground soil is analyzed and compared with in-situ data. Then, the CSRE wall is constructed on the aforementioned underground soil to demonstrate its long-term CTHM behaviors.

4.2.1 CTHM behavior of CSRE wall in interaction with environment and underground soil

A schematic diagram showing the interactions of a fresh CSRE wall, indoor/outdoor environment and underground soil is presented in Figure 4.15 to show the CSRE structure built under in-situ condition.

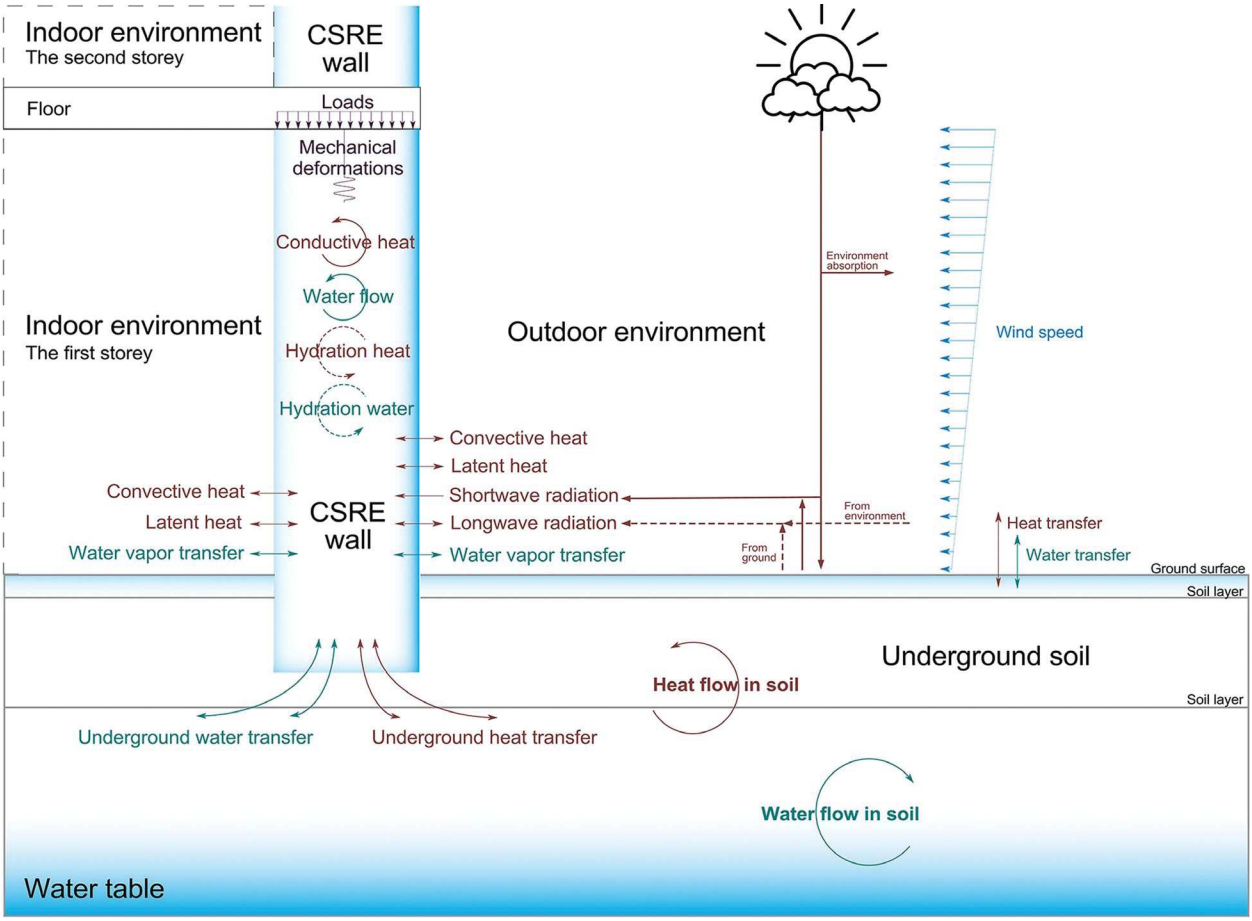

Figure 4.15. Schematic diagram of a fresh CSRE wall (sample) in interaction with indoor/outdoor environment and underground soil

4.2.1.1 The studied wall and the geoclimatic conditions

A two-storey CSRE building is assumed to be built on the underground soil as presented in Figure 4.16. For the reason that the CSRE is built on the underground soil and the CTHM properties of the wall are influenced by the interactions between the wall and soil, therefore, to understand the wall's behaviors, the behaviors of the underground soil needed to be predicted correctly at first.

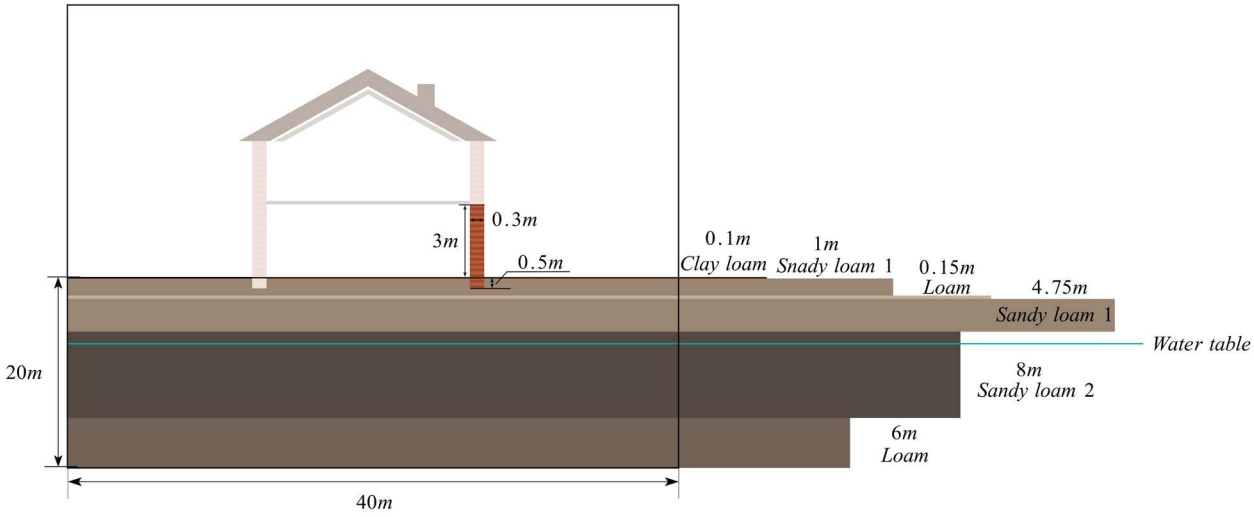

Figure 4.16. The geometry of the studied field and the investigated CSRE wall

To evaluate the capacity of the proposed numerical framework for predicting the hydro-thermal properties of the underground soil, the temperature and humidity of the underground soil located in the Alsace region (France) are measured for one year from September 18th, and the in-situ data are compared with the numerical simulation results [298]. During field measurements, the temperature and humidity probes are placed at a depth of 1.1 m and 1.11 m, respectively, in order to measure the variations in soil temperature and humidity over the course of one year. Two additional sets of temperature probes are planted at depths of 0.6 m and 1.25 m to demonstrate the influence of depth on the temperature of underground soil. The earth with a depth of 20 m and a width of 40 m is employed for numerical simulations. In addition, the underground soil used for calculation consists of six layers, and the thicknesses contained in each layer from top to bottom are respectively 0.1 m, 1 m, 0.15 m, 4.75 m, 8 m, and 6 m, and the soil compositions are clay loam, sandy loam 1, loam, sandy loam 1, sandy loam 2, loam, respectively. The properties of the related underground soil components are summarized in Table 4.6.

	ρ_s (kg·m^{-3})	ρ_d (kg·m^{-3})	x_s (-)	θ_s (-)	θ_r (-)	α_{VG} (m^{-1})	n_{VG} (-)	l_{VG} (-)	C_{KC} (m^2)
Clay loam	2700	1350	0.35	0.50	0.03	1.99	1.22	0.5	1.56E-13
Sandy loam 1	2620	1600	0.80	0.39	0.02	2.6	1.52	0.5	1.82E-12
Loam	2680	1420	0.50	0.47	0.02	2.35	1.38	0.5	2.24E-13
Sandy loam 2	2670	1600	0.60	0.40	0.02	2.48	1.5	0.5	1.48E-12

Table 4.6. Underground soil properties

The local temperature (K) and approximated suction (MPa) on the land surface is directly measured through in-situ tests, and the results are then applied as Dirichlet boundary conditions on the top surface of the first soil layer (Table 4.7). The underground soil has a water table with a depth of 7.63 m in this region. No water transportation exists on the base and side boundaries. Meanwhile, there is no heat transfer along the side borders, and the temperature beneath the earth rises with a gradient of 0.1 K·m^{-1} as soil depth increases to 20 m with a measured temperature of 287.15 K. After the aforementioned hydro-thermal circumstances achieve an equilibrium state, the simulated temperature and volumetric water content are compared to the observed values. The comparisons between the simulation outputs and the on-situ observations are provided in Figure 4.17.

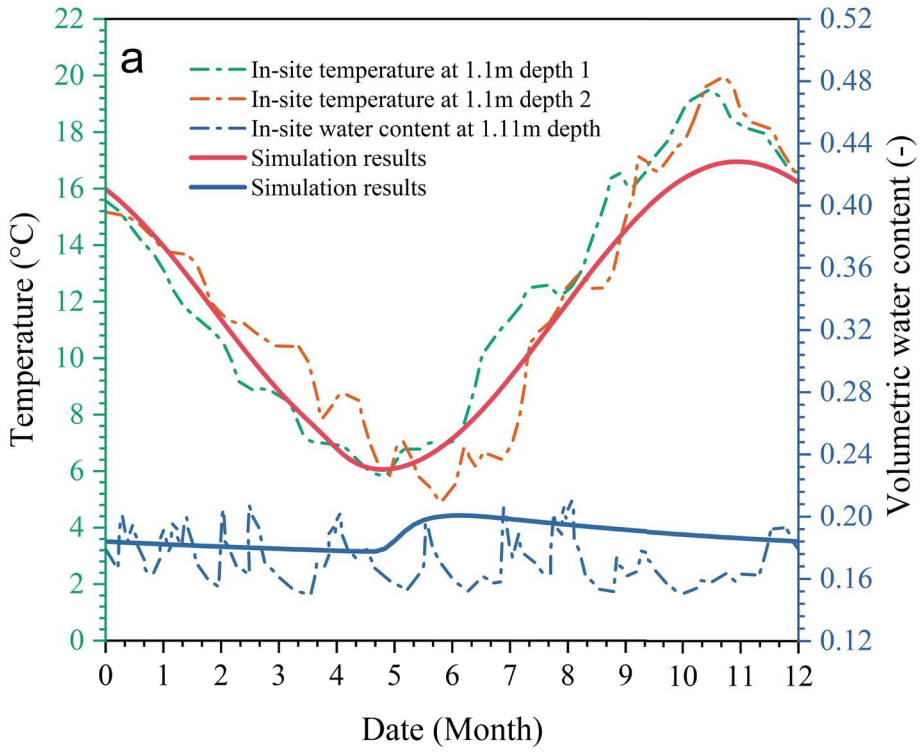

(a)

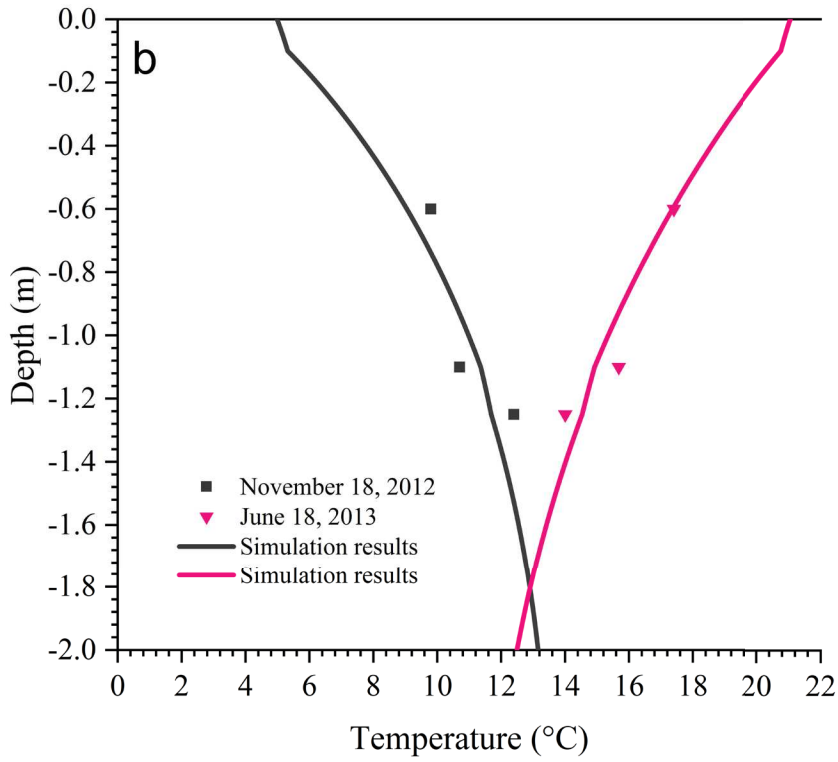

(b)

Figure 4.17. (a) Variations in temperature and moisture content of underground soil throughout one year (b) depth and time impacts on the temperature of underground soil

After that, the CSRE structure is then constructed on the same underground soil as described previously. The CSRE structure is scheduled to be completed on January 1st, utilizing local raw soil with a fine content of 25% in the Alsace area (France). The raw soil is subsequently stabilized by adding Portland cement with a mass percentage of 6%. The mixes are then compacted with the optimal water content of 8 percent and the maximum dry density of 2000 $kg \cdot m^{-3}$ to provide the highest mechanical performance. It is considered that no chemical reaction occurs during the construction process. A CSRE wall erected in the first storey of the building with a size of 4*0.3*3.5 m^3 (length*thickness*height) is selected for numerical simulations. Other portions of the CSRE wall are visible to the air, while its base of 0.5 m is hidden in the earth. The underground soil is deemed incompressible, and the part of the wall in contact with the underground soil is fixed in all directions. The initial temperature of the wall is considered to be the same as the surface temperature of the underground soil. The top surface of the CSRE wall is subjected to vertical stress of 61.7 kPa due to the combined dead and live loads of the second storey.

After compaction, the CSRE walls are placed and cured in the local environment for five years. The local outdoor relative humidity (RH_{ext}) and temperature (T_{ext}) over the last forty years (1979-2022) are investigated and described with the sinusoidal functions due to the earth's revolution. The indoor temperature and relative humidity are correlated with outdoor temperature and relative humidity [301]. The local shortwave radiation is obtained according to [260], and its value is influenced by the soil color [305] through the albedo value of the wall. The environmental longwave affected by the cloud and ground longwave radiation incident upon the wall is obtained according to [302–304].

The initial temperature and humidity (suction) of the CSRE wall and the underground soil are presented in Figure 4.18.

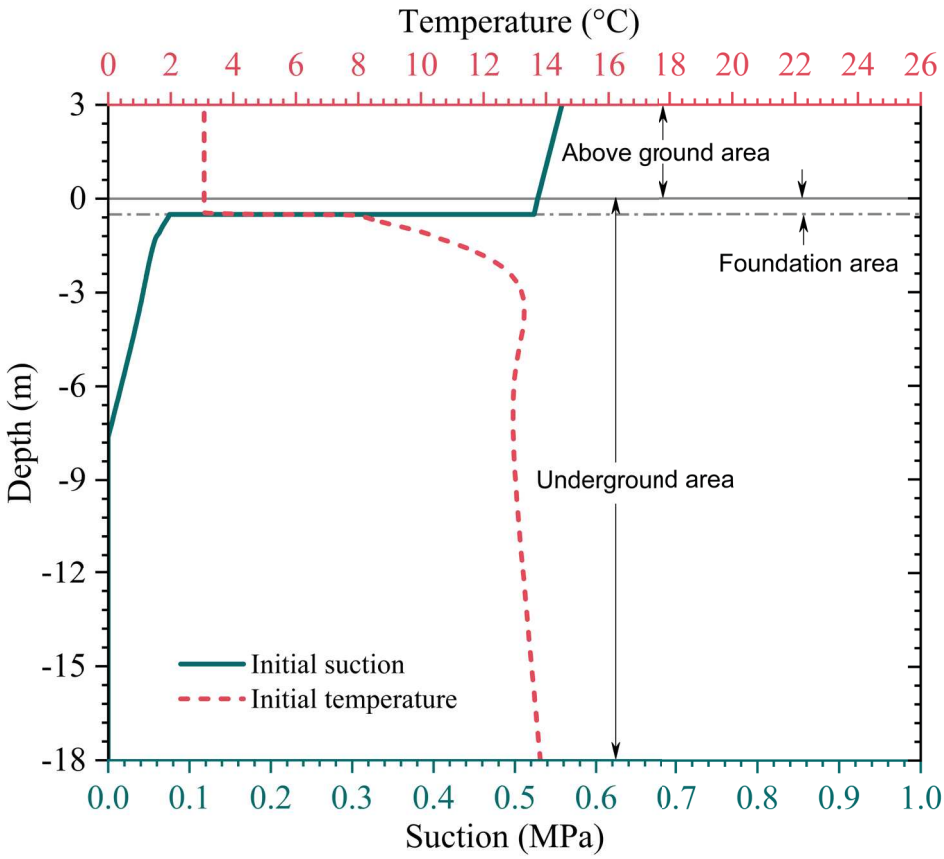

Figure 4.18. Initial hydro-thermal condition of the underground soil and CSRE wall

Table 4.7 provides a summary of the equations that are utilized to simulate the local environmental conditions. Moreover, the constant parameters used for numerical simulations are also summarized and presented in Table 4.8.

Local conditions	**Values**
Outdoor relative humidity	Equation 51

Outdoor temperature	Equation 61
Indoor relative humidity	Equation 52
Indoor temperature	Equation 62
Outdoor wind speed	Equation 48
Local Shortwave radiation	Equation 56
Local environmental longwave radiation	Equation 57
Ground longwave radiation	Equation 58
Ground surface temperature	$T = 284.65 + 10\sin(\pi(t+58.25)/182.5)$
Ground surface suction	$s = 1.005 - 0.995\sin(\pi(t+58.25)/182.5)$
Vertical load on the top of the wall	61.7 kPa

Table 4.7. Boundary conditions for the numerical simulations

Constant parameters used for numerical simulations							
C_3S (-)	C_2S (-)	C_3A (-)	C_4AF (-)	SO_3 (-)	MgO (-)	FreeCaO	a_{lb} (-)
0.56232	0.15717	0.095283	0.085917	0.03	0.013	0.003	0.25
C_{KC} (m^2)	C_s ($J \cdot kg^-$	C_{wi0} ($s^2 \cdot m^-$	e_1 (-)	e_2 (-)	g ($m \cdot s^{-2}$)	H_0 (m)	K_1 (-)
3.81E-13	1081	6.88E-15	94.85	1.44	9.8	10	0.5
T_{am} (K)	T_{hr} (K)	u_0 (MPa)	u_1 (-)	u_2 (MPa)	u_3 (-)	u_4 (-)	t_{ref}
9.45	293.15	1	0.829	13	1.25	6	182.5
α_h (h)	β_h (-)	L (m)	l_{VG} (-)	M_a	M_w	n_{VG} (-)	T_{av} (K)
23	0.69	0.3	0.5	29	18	1.4	282.6
v_{wind0} ($m \cdot s^{-1}$)	α_H (-)	β_{inc} (-)	ε_e (-)	w_{ini} (-)	ρ_{dini}	θ_r (-)	n_{ini} (-)
3.71	0.4	$\pi/2$	0.97	0.081	2000	0.0045	0.23077
σ_B (-)	c_{ini} (-)	c_{cv} (-)	c_{fi} (-)	p_{at} (Pa)	ρ_s ($kg \cdot m^{-3}$)	RH_{am} (-)	RH_{av} (-)
5.67E-08	0.06	3.5	0.25	101325	2600	0.12	0.80
C_c (-)	K_3 (-)	t_{RH} (day)	t_T (day)	ρ_c ($kg \cdot m^-$			
0.41	0.3457	60.12	115.54	3150			

Table 4.8. Constant values used for the numerical simulations

4.2.1.2 Simulation results

4.2.1.2.1 Average behavior of the wall

The variation in the average degree of hydration, temperature, relative humidity, dry density, thermal conductivity, and compressive strength of the CSRE wall (above the earth) caused by the effect of the surrounding Geo-climatic conditions is simulated to gain a global perspective on the properties of the wall over the five years after construction. The relevant results are displayed on a logarithmic scale in Figure 4.19a to better illustrate the behaviors of the wall

throughout the course of the initial 30 days and the last four years. Figure 4.19b depicts, on a linear scale, the behavior of the wall throughout the first year.

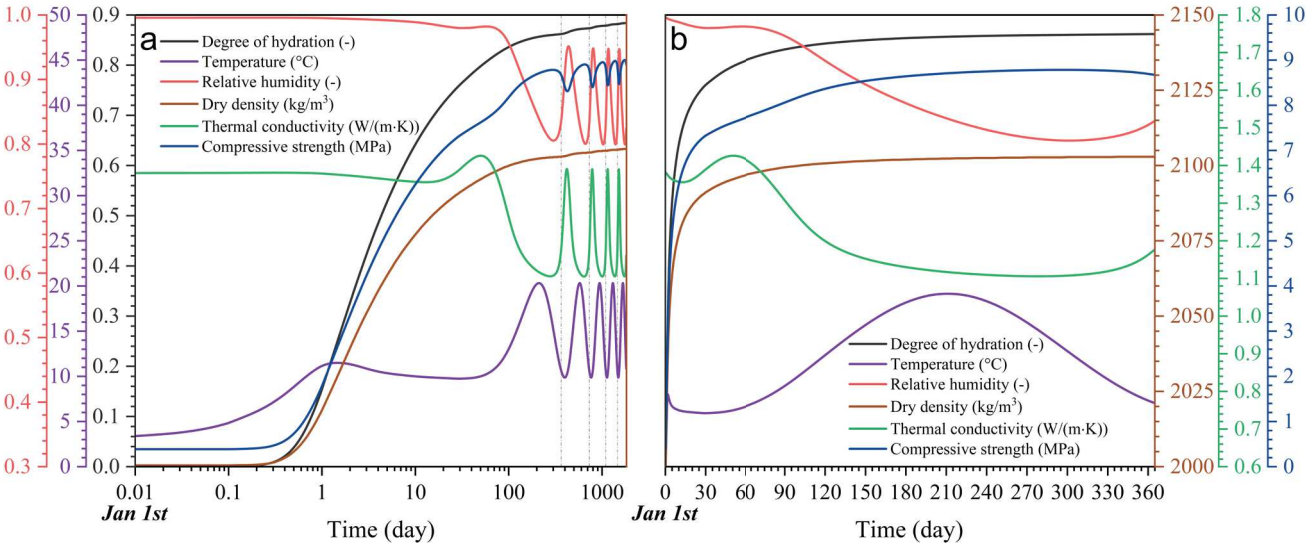

Figure 4.19. The average degree of hydration, temperature, relative humidity, dry density, thermal conductivity, and compressive strength of CSRE wall above the earth (a) in 1825 days and (b) 365 days after construction

After construction, the cement in the CSRE wall begins to react with water, and significant increases (from 0 to 0.8) in the degree of cement hydration are noticed within the first 30 days. After that, the degree of cement hydration rises annually, although the increment rate decreases. It can be observed that even after five years of curing, the cement is still not completely consumed by the chemical reaction. As a result of the heat released during the hydration process, the highest temperature of the first 30 days is attained around one day after construction. After that, the wall temperature reaches its highest value in the first year in summer and decreases to its lowest value in winter. For the reason that the rate of cement hydration decreases to a lower value than that of the beginning, the wall temperature after one day is not dominated by the hydration process anymore but instead declines to an equilibrium stage due to the sounding temperature, and then varies annually with time in the following days. After that, the humidity of the wall in the following five years after construction is also studied. During the manufacturing process, the CSRE structures are often compacted to their optimal conditions, which results in an initial state that is more humid than the surrounding air. Consequently, the mass of water in the wall has the trend to continuously decrease with age, not only due to cement hydration but also to water evaporation after the wall has been erected. Therefore, the humidity of the wall decreases in the first year and finally attains a dynamic

balance with the surrounding. The average relative humidity decreases in the first 30 days as a consequence of evaporation and hydration, and subsequently increases in 30 to 60 days as a result of water infiltration from the ground soils into the wall. The average thermal conductivity of the wall drops during the first 15 days due to water evaporation but subsequently rises as a result of growing dampness and the buildup of hydration products. After about 50 days of curing, the average dry density of the wall continues steady growth, and the humidity of the wall fluctuates yearly with time, causing the average thermal conductivity to be influenced mainly by the humidity of the wall and to thus vary seasonally. After the wall has been constructed and cured in its local environment, a portion of the water will transfer to the hydration products by reacting with the cement. Consequently, the average dry density and the degree of hydration of the wall undergo comparable variations throughout time. The average unconfined compressive strength of the wall tends to increase and then stabilize with curing time in the investigated five years. The average wall strength rises consistently with time due to drying-wetting cycles caused by the environment, which is also observed by [328]. However, a deceleration zone of increasing wall strength appears between 30 and 60 days as a result of a wetter state caused by rising damp water. In the following four years, the change in the degree of cement hydration is not significant compared to that in the first year, although changes in the mass of water (used for chemical reaction) due to growing damp persist. For the reason that strength increments of cementitious soil mainly come from the combined effects of cement hydration and increased suction, the average compressive strength of the wall is then fixed around a certain value but still fluctuates in a range in the later four years.

4.2.1.2.2 Structural behavior of the wall

In reality, the CSRE wall may have different engineering characteristics in different parts of the wall. To gain a better and more convenient understanding about the properties of the investigated wall, the contour surface plots are used to visualize the variation of the degree of cement hydration, volumetric water content, thermal conductivity, and compressive strength in the wall.

Degree of cement hydration of CSRE wall

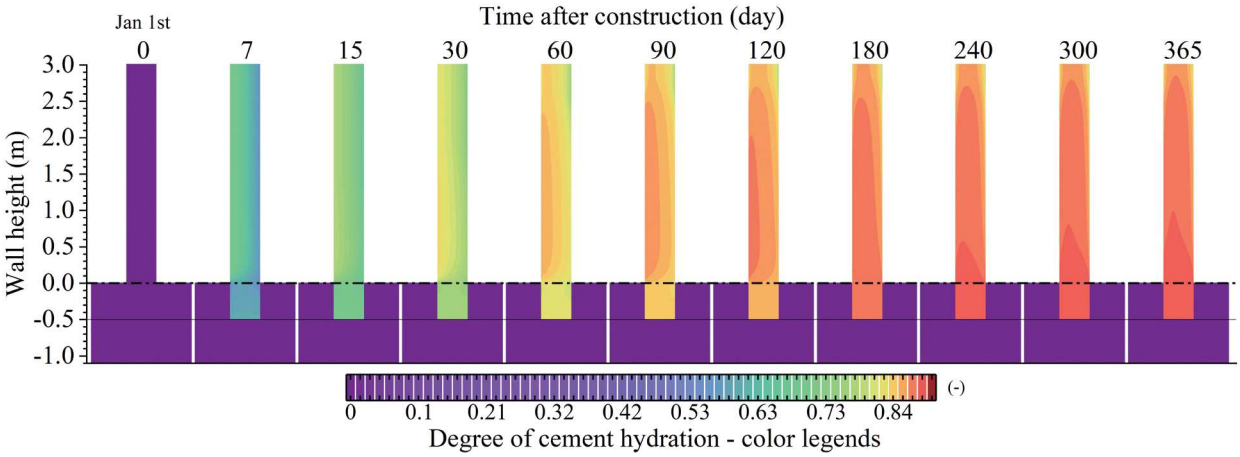

Figure 4.20. Variation of the degree of cement hydration in CSRE wall and nearby underground soil after 0, 7, 15, 30, 60, 90, 120, 180, 240, 300 and 365 days of construction

Figure 4.20 shows the distribution of the degree of cement hydration in the CSRE wall and in nearby underground soil after 0, 7, 15, 30, 60, 90, 120, 180, 240, 300 and 365 days of construction. It can be observed that no cement reacts with water at the beginning. In the first 15 days after construction, the cement hydration process is mainly controlled by the chemical reactions occurring uniformly within the wall, which leads to nearly uniform distributions of the degree of hydration. Furthermore, a higher degree of cement hydration is observed near the indoor side of the wall compared to the parts near the outside and underneath the ground because of higher indoor temperature. And this phenomenon continued until the degree of hydration in all parts of the wall reaches a high level, and then trends to stabilize with time in the following days. In particular, the water that flows into the CSRE wall from the bottom due to a wetter ground soil in winter replenishes the water required for hydration reaction, enhancing the degree of hydration near the bottom side at 300 and 365 days.

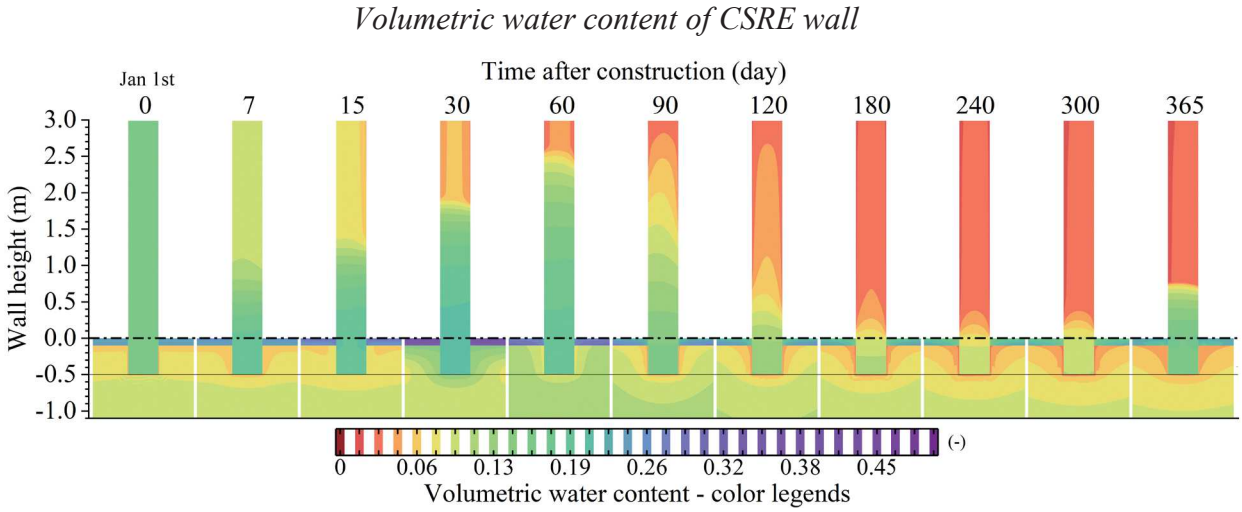

Figure 4.21. Variation of the volumetric water content in CSRE wall and nearby underground soil after 0, 7, 15, 30, 60, 90, 120, 180, 240, 300 and 365 days of construction

Figure. 4.21 depicts the distribution of the volumetric water content in the CSRE wall and adjacent underground soil at various times. Due to the combined effects of gravity and evaporation, the simulation results indicate that the upper side of the wall is drier than the lower side after 7 days of construction. Due to the increased rate of evaporation caused by the wind, the outdoor portions of the wall are drier than the wall near the indoor side after 15 days. Moreover, from 7 to 60 days, the wetter areas increase with time due to the rising damp water. Intriguingly, a greater proportion of the wall is wetter at 60 days than at 30 days, although underground soil achieves its wettest state at about 30 days. This delayed impact is caused by the fact that the water that flowed into the wall in the first 30 days did not evaporate in time but was stored as a water source in the wall, which makes the wet areas expand upward later. After 60 days following construction, the water in CSRE wall continuously flows out due to dryer ambient air and drier underground soil in summer. Furthermore, at 365 days, when the surrounding environment turns humid during the winter, the wall gets wet again.

Volumetric water content of CSRE wall

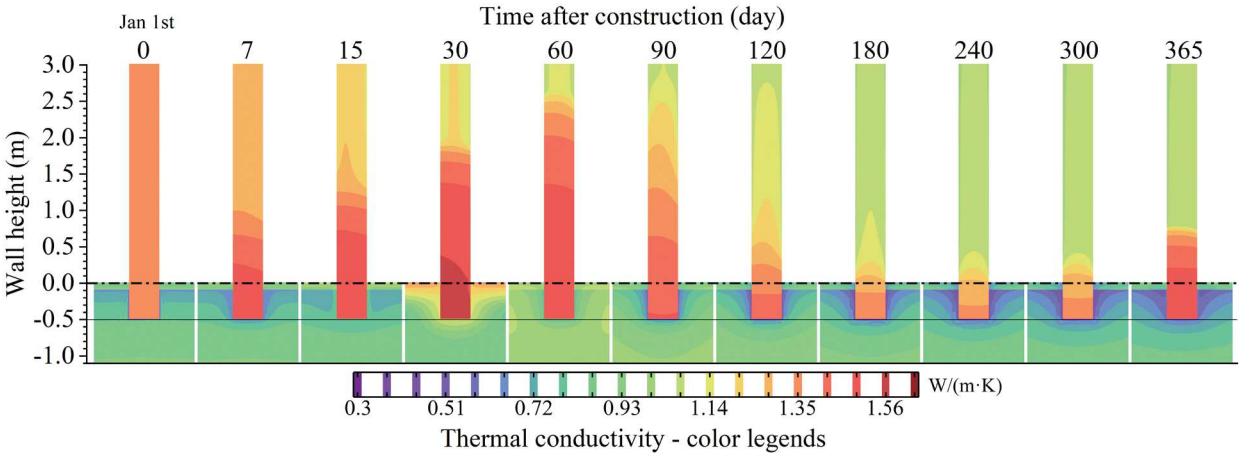

Figure 4.22. Variation of thermal conductivity in CSRE wall and nearby underground soil after 0, 7, 15, 30, 60, 90, 120, 180, 240, 300 and 365 days of construction

Afterwards, the distribution of thermal conductivity in the CSRE wall and nearby earth at various time nodes after construction is simulated, and the results are displayed in Figure 4.22. In general, a greater proportion of water in CSRE results in a low thermal resistance (higher thermal conductivity). Consequently, similar distributions of thermal conductivity and volumetric water content are observed in the wall. These results reveal that water has a significant impact on the thermal isolation qualities of the wall. Since a greater dry density reduces the distance between soil particles, enabling more solid particles to transfer heat in contact with each other, a higher dry density (degree of hydration) of the CSRE material results in a higher thermal conductivity of the material. It can be noted that the variations in thermal conductivity after 60 days closely parallel the changes in the volumetric water content of the wall. This is due to the fact that the average dry density of the wall reaches a relatively constant value after 60 days (Figure 4.19), and the changes in the thermal resistance of the material are driven mainly by fluctuations in water content. During the first 60 days, the thermal conductivity of the wall is unstable since both the water content and dry density of the wall are undergoing fast changes.

Compressive strength of CSRE wall

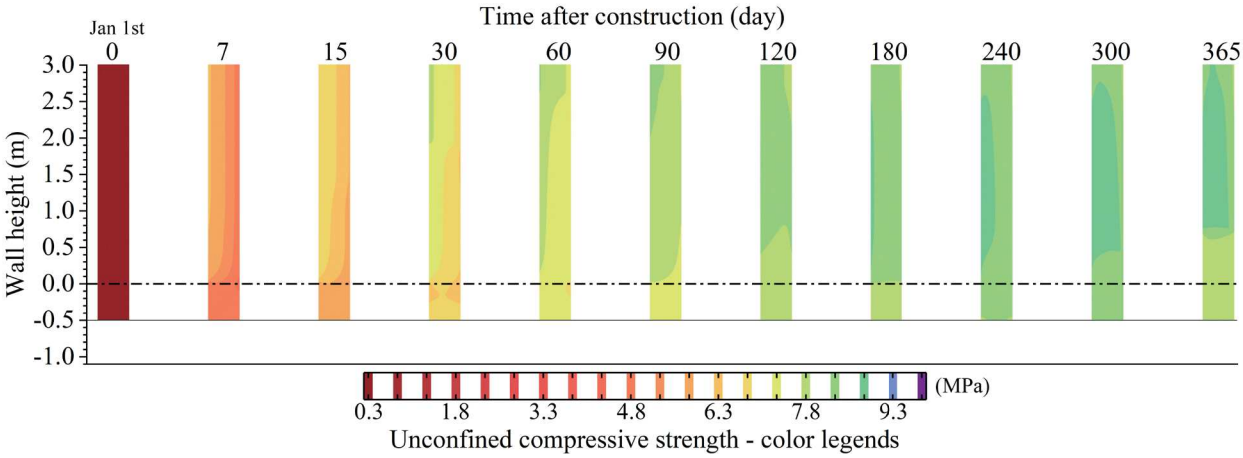

Figure 4.23. Variation of the compressive strength in CSRE wall after 0, 7, 15, 30, 60, 90, 120, 180, 240, 300 and 365 days of construction

After that, the distribution of the compressive strength in CSRE wall is also studied and the results are presented in Figure 4.23. For a certain type of CSRE, the material strength is affected by the mass of produced binders (hydration products), dry density and water content. From the results at 300 and 365 days, it can be observed that the compressive strength of the wall is clearly impacted by the moisture in the ground soil. Moreover, in the first 15 days following construction, the wall maintains a relatively moist state (Figure 4.19) without significant fluctuations in the relative humidity; therefore, the wall strength is mainly dominated by cement hydration. For the majority of the period following construction, the strength of the wall is affected visibly both by cement hydration and material humidity. Different from the distributions of thermal conductivity exhibiting a weak correlation with dry density when the dry density changes in a narrow range between 2000 to 2100 $kg \cdot m^{-3}$, but a strong relation with water. The compressive strength of CSRE walls is more susceptible to binder-induced dry density variations, which results in more irregular distributions of compressive strength in the wall.

Compressive strength variation at typical points on the wall

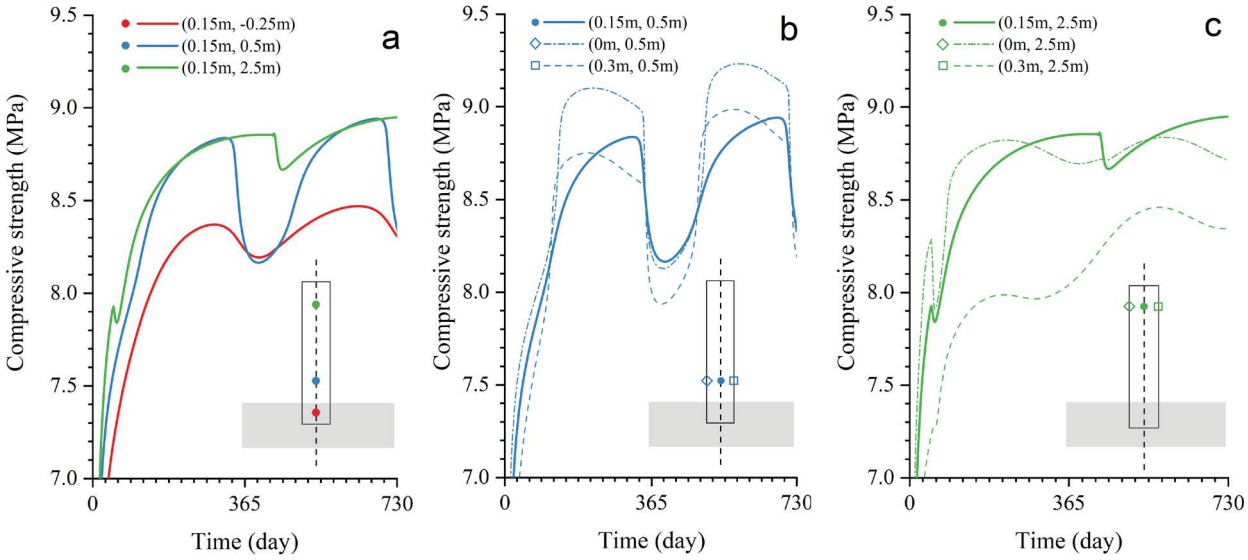

Figure 4.24. Time effect on the compression strength of different points in (a) the middle with different heights (b) different parts with the height of 0.5 m (c) different parts with the height of 2.5 m

A number of points in distinct wall areas are selected to show more precisely the effect of time on the compressive strength of the wall. Three separate points in the middle of the wall with the height of -0.25 m, 0.5 m, and 2.5 m are used to illustrate the effects of height on the long-term compressive strength, and the results are shown in Figure 4.24a. It is obvious that the direct contact of the wall with the ground soils makes the compressive strength of the wall decrease as its height decreases. As a result of rising damp, water is replenished from the bottom to the upper portion of the wall (Figure 4.21, 60 days); therefore, the point on the upward portion of the wall experiences a rapid decline in compressive strength at around 60 days in the first 180 days. For the points with a height of -0.25 m and 0.5 m, however, the compressive strength does not decrease without a sudden drop in the first 180 days owing to consistent and moderate moisture changes. In addition, the point in the higher portion loses its strength later than the points in the lower part of the wall since it takes longer for water to transport from the ground soil to the upper side of the wall. Six different points with the same height of 0.5 m/2.5 m but placed in the indoor, outdoor, and central parts of the wall are then selected to display the strength changes in the bottom/upper portion of the wall; the simulation results are shown in Figure 4.24b/Figure 4.24c. Due to sufficient contact between the wall surface and the air, moisture is transferred more efficiently, leading the points on the wall's surface to suffer a

decrease in strength before the point in the wall's middle throughout the year. Moreover, since the water supply is sufficient for the three points at the height of 0.5 m, the point on the indoor surface of the wall has the highest compressive strength due to a greater degree of hydration and lower water content as a consequence of a warmer and drier indoor environment. On the one hand, due to evaporation and gravitational impacts, the mass of water that may react with cement is limited for the points located on the wall surface with a height of 2.5 m. On the other hand, the shortage of water causes the hydration process to be governed chiefly by temperature. Therefore, the point on the outdoor surface has a lower degree of hydration than on the indoor surface, resulting in a lower compressive strength.

4.3 Conclusion

The proposed numerical model is utilized to investigate the structural behaviors of CSRE (URE) constructions in situ. Initially, the long-term structural behaviors of URE walls are investigated by comparing the effects of different kinds of environments on the walls. The simulation results reveal that the distribution of soil grain size has a larger effect on the THM characteristics of the wall than the local environment. Moreover, the majority of the drying process takes place in the first year after construction. Later, apart from the effects of the environment, the effects of rising damp from the ground are also included to better understand the long-term characteristics of the URE walls without the protection of the basement. The simulation results demonstrate that time has a positive effect on the THM characteristics of a URE wall, since the evaporation process reduces the wall's humidity and increases its thermal insulation and mechanical strength. On the contrary, the rising damp reduces the heat resistance of the walls and increases their vapor resistance, making the URE structure less inhabitable. Eventually, the long-term CTHM characteristics of the CSRE wall under the interactions of the environment and underground soil are studied. It has been observed that the cement is not completely hydrated even after five years of curing. In the first year after construction, the degree of cement hydration is higher near the indoor side of the wall compared to the parts near the outside and underneath the ground because of the higher indoor temperature. The compressive strength of the wall is mainly controlled by cement hydration at an early age but also impacted by the humidity of the environment and the underground soil. The higher portion of the wall loses its strength later than the lower part since it takes longer for water to get from the ground soil to the upper side. This delay effect is dissipated on the wall surface as a result

of sufficient air contact. The lack of water on the upper side of the wall causes the hydration process in this region to be governed primarily by temperature.

General conclusions

To globally describe and forecast the general chemo-thermo-hydro-mechanical (CTHM) behaviors of a typical CSRE (URE) wall under in-situ conditions, the authors conduct literature reviews in order to acquire a comprehensive understanding of the fundamental engineering characteristics of CSRE (URE) and the factors influencing the properties of the researched materials. According to the literature review, the production process, material interactions, and continual environmental changes have a significant effect on the long-term chemo-thermo-hydro-mechanical characteristics CSRE (URE).

It has been found that, for different (CSRE) URE materials, the thermal conductivity increases with the increasing of dry density and water content; the specific heat capacity of dry CSRE (URE) is not apparently influenced by the material dry density; the intrinsic water permeability decreases with dry density and increases with water content; the retention ability increases when the fine content increases; the unconfined compressive strength first slowly and then rapidly increases with material dry density; the elastic modulus at failure reduces on the wetting path and increases on the drying path; the decrease in water content and the increase of fine content enhance the unconfined compressive strength and tensile strength; the tensile strength is frequently estimated through the unconfined compressive strength by researchers; the Poisson's ratio increases with water content. For CSRE materials, in comparison to the effect of other parameters, such as grain size distribution, dry density, water content, etc., the effect of cement hydration on the fluctuations of soil water retention curve (saturation-suction scale) and thermal conductivity is insignificant. The hydration process consumes free water in the form of chemically reacted water and chemisorbed water. In addition, cement hydration increases the mechanical resistance of CSRE over time, and this resistance is affected by the curing conditions. The growth in strength is facilitated by a rise in conditioning temperature and humidity and impeded by a fall in conditioning temperature and humidity.

On the basis of the literature review, it has been found that the characteristics of CSRE (URE) materials vary significantly across experimental studies, making their application under in-situ condition more challenging. The absence of a global perspective on all sorts of CSRE (URE) materials impedes the development of an internationally recognized standard for CSRE (URE) materials. Consequently, to estimate the long-term CTHM behavior of CSRE (URE) materials, the combined effects of initial water content, initial dry density, initial grain size distribution, initial cement content, curing conditions, and curing duration should be assessed simultaneously throughout the design phase.

Therefore, in this study, a novel finite element framework applicable to both URE and CSRE materials is proposed to explain the linked CTHM behaviors of these materials. To validate the proposed theoretical framework, several experimental results for URE and CSRE materials from the existing literature are recreated. The suggested numerical framework is then utilized to estimate the features of typical CSRE (URE) walls.

The proposed numerical model is then extended to study the structural behaviors of CSRE (URE) constructions under in-situ conditions. First, the long-term structural behaviors of URE walls are studied by considering the effects of different environment types on the walls. The simulation findings indicate that the distribution of soil grain size has a significant effect on the THM properties of wall. Moreover, the majority of the drying process occurs in the first year following construction. The average temperature inside the wall is not noticeably impacted by the wall's relative humidity and fine content, but rather by the temperature changes in the surrounding environment. The horizontal pushover strength rises sharply in the first year, and then tends to stabilize over time. For the same fine content, walls in a drier climate have a greater strength than those in a moister climate.

Later, apart from the effects of the environment, the effects of rising damp from the ground are also studied for the long-term characteristics of the URE walls. The simulation results indicate that time has a favorable effect on the THM attributes of a URE wall because the evaporation process decreases the wall's humidity, increases thermal insulation and mechanical strength. For the wall that is not covered by a waterproof basement, water travels from the bottom to the interior, and water evaporates through the surfaces of the wall, achieving equilibrium and leaving the wall wet on the bottom and dry on the top. In addition, the growing damp diminishes the heat resistance of the walls and raises their vapor resistance, making the URE building less livable. In the absence of rising damp, the horizontal bearing capacity increases by 47 percent between 7 days and 1825 days following construction, whereas this increase is only 10 percent when rising damp is present. After five years, the wall's thermal insulation resistance decreases and its vapor resistance increases less due to growing humidity.

Eventually, the long-term CTHM characteristics of the CSRE wall under the interactions of the environment and underground soil are studied. It has been observed that the average degree of cement hydration of the wall increases annually, while the rate of the increment decreases with time. The cement is not completely hydrated even after five years of curing. In the first year after construction, the degree of cement hydration is higher near the indoor side of the wall compared to the parts near the outside and underneath the ground because of the higher indoor

temperature. The upper and indoor sides of the wall are generally drier than the lower and outdoor sides. The rising damp water that does not evaporate in time stores as a water source in the wall, making the wet areas expand in the following days. The average wall temperature first increases due to the hydration heat and later varies seasonally with the environment. The thermal insulation of the wall decreases due to rising damp but increases owing to water evaporation. The compressive strength of the wall is mainly controlled by cement hydration at an early age but also impacted in the later four years by the humidity of the environment and the underground soil. The higher portion of the wall loses its strength later than the lower part since it takes longer for water to get from the ground soil to the upper side. This delay is dissipated on the wall surface owing to sufficient contact with the air. The shortage of water on the upper side of the wall leads the hydration process in this area to be governed chiefly by temperature.

References

[1] Q. Angulo-Ibáñez, Á. Mas-Tomás, V. Galvañ-LLopis, J.L. Sántolaria-Montesinos, Traditional braces of earth constructions, Constr. Build. Mater. 30 (2012) 389–399. https://doi.org/10.1016/j.conbuildmat.2011.11.024.

[2] S. Burroughs, Recommendations for the Selection, Stabilization, and Compaction of Soil for Rammed Earth Wall Construction, J. Green Build. 5 (2010) 101–114. https://doi.org/10.3992/jgb.5.1.101.

[3] H. Houben, H. Guillaud, CRAterre, Intermediate Technology Publications, Earth construction: a comprehensive guide, Intermediate Technology Publications, London, 1994.

[4] F. Pacheco-Torgal, S. Jalali, Earth construction: Lessons from the past for future eco-efficient construction, Constr. Build. Mater. 29 (2012) 512–519. https://doi.org/10.1016/j.conbuildmat.2011.10.054.

[5] M.C.J. Delgado, I.C. Guerrero, Earth building in Spain, Constr. Build. Mater. 20 (2006) 679–690. https://doi.org/10.1016/j.conbuildmat.2005.02.006.

[6] N. Cristelo, S. Glendinning, T. Miranda, D. Oliveira, R. Silva, Soil stabilisation using alkaline activation of fly ash for self compacting rammed earth construction, Constr. Build. Mater. 36 (2012) 727–735. https://doi.org/10.1016/j.conbuildmat.2012.06.037.

[7] D. Ciancio, C. Augarde, Capacity of unreinforced rammed earth walls subject to lateral wind force: elastic analysis versus ultimate strength analysis, Mater. Struct. 46 (2013) 1569–1585. https://doi.org/10.1617/s11527-012-9998-8.

[8] J.C. Morel, A. Mesbah, M. Oggero, P. Walker, Building houses with local materials: means to drastically reduce the environmental impact of construction, Build. Environ. 36 (2001) 1119–1126. https://doi.org/10.1016/S0360-1323(00)00054-8.

[9] P.-A. Chabriac, A. Fabbri, J.-C. Morel, J.-P. Laurent, J. Blanc-Gonnet, A Procedure to Measure the in-Situ Hygrothermal Behavior of Earth Walls, Materials. 7 (2014) 3002–3020. https://doi.org/10.3390/ma7043002.

[10] Q.B. Bui, J.C. Morel, B.V. Venkatarama Reddy, W. Ghayad, Durability of rammed earth walls exposed for 20 years to natural weathering, Build. Environ. 44 (2009) 912–919. https://doi.org/10.1016/j.buildenv.2008.07.001.

[11] T. Padfield, The Technical University of Denmark, The role of absorbent building materials in moderating changes of relative humidity, s.n., S.l., 1998.

[12] Rammed Earth Construction, Fine Homebuilding. (2019). https://www.finehomebuilding.com/2019/03/13/rammed-earth-construction (accessed July 15, 2022).

[13] H. Nowamooz, C. Chazallon, Finite element modelling of a rammed earth wall, Constr. Build. Mater. 25 (2011) 2112–2121. https://doi.org/10.1016/j.conbuildmat.2010.11.021.

[14] M. Hall, Y. Djerbib, Rammed earth sample production: context, recommendations and consistency, Constr. Build. Mater. 18 (2004) 281–286. https://doi.org/10.1016/j.conbuildmat.2003.11.001.

[15] M.S. Islam, T.E. Elahi, A.R. Shahriar, N. Mumtaz, Effectiveness of fly ash and cement for compressed stabilized earth block construction, Constr. Build. Mater. 255 (2020) 119392. https://doi.org/10.1016/j.conbuildmat.2020.119392.

[16] C. Jayasinghe, N. Kamaladasa, Compressive strength characteristics of cement stabilized rammed earth walls, Constr. Build. Mater. 21 (2007) 1971–1976. https://doi.org/10.1016/j.conbuildmat.2006.05.049.

[17] D. Ciancio, C.T.S. Beckett, J.A.H. Carraro, Optimum lime content identification for lime-stabilised rammed earth, Constr. Build. Mater. 53 (2014) 59–65. https://doi.org/10.1016/j.conbuildmat.2013.11.077.
[18] S.S. Narani, P. Zare, M. Abbaspour, A. Fahimifar, S. Siddiqua, S.M. Mir Mohammad Hosseini, Evaluation of fiber-reinforced and cement-stabilized rammed-earth composite under cyclic loading, Constr. Build. Mater. 296 (2021) 123746. https://doi.org/10.1016/j.conbuildmat.2021.123746.
[19] S. Raj S., A.K. Sharma, K.B. Anand, Performance appraisal of coal ash stabilized rammed earth, J. Build. Eng. 18 (2018) 51–57. https://doi.org/10.1016/j.jobe.2018.03.001.
[20] K.K.G.K.D. Kariyawasam, C. Jayasinghe, Cement stabilized rammed earth as a sustainable construction material, Constr. Build. Mater. 105 (2016) 519–527. https://doi.org/10.1016/j.conbuildmat.2015.12.189.
[21] Y. Amini, A. Hamidi, Triaxial shear behavior of a cement-treated sand–gravel mixture, J. Rock Mech. Geotech. Eng. 6 (2014) 455–465. https://doi.org/10.1016/j.jrmge.2014.07.006.
[22] F. Ávila, E. Puertas, R. Gallego, Characterization of the mechanical and physical properties of stabilized rammed earth: A review, Constr. Build. Mater. 325 (2022) 126693. https://doi.org/10.1016/j.conbuildmat.2022.126693.
[23] G. Giada, R. Caponetto, F. Nocera, Hygrothermal Properties of Raw Earth Materials: A Literature Review, Sustainability. 11 (2019) 5342. https://doi.org/10.3390/su11195342.
[24] A. Cuccurullo, D. Gallipoli, A.W. Bruno, C. Augarde, P. Hughes, C. La Borderie, Influence of particle grading on the hygromechanical properties of hypercompacted earth, J. Build. Pathol. Rehabil. 5 (2019) 2. https://doi.org/10.1007/s41024-019-0066-4.
[25] J.-C. Morel, A. Pkla, P. Walker, Compressive strength testing of compressed earth blocks, Constr. Build. Mater. 21 (2007) 303–309.
[26] A.J. Bryan, Criteria for the suitability of soil for cement stabilization, Build. Environ. 23 (1988) 309–319. https://doi.org/10.1016/0360-1323(88)90037-6.
[27] A.W. Bruno, D. Gallipoli, C. Perlot, J. Mendes, Effect of very high compaction pressures on the physical and mechanical properties of earthen materials, E3S Web Conf. 9 (2016) 14004. https://doi.org/10.1051/e3sconf/20160914004.
[28] R. Bahar, M. Benazzoug, S. Kenai, Performance of compacted cement-stabilised soil, Cem. Concr. Compos. 26 (2004) 811–820. https://doi.org/10.1016/j.cemconcomp.2004.01.003.
[29] S. NZS, 4298: 1998 materials and workmanship for earth buildings, Wellingt. Stand. N. Z. SNZ. (1998).
[30] S. Shimobe, E. Karakan, A. Sezer, Improved dataset for establishing novel relationships between compaction characteristics and physical properties of soils, Bull. Eng. Geol. Environ. 80 (2021) 8633–8663. https://doi.org/10.1007/s10064-021-02456-3.
[31] P. Chauhan, A. El Hajjar, N. Prime, O. Plé, Unsaturated behavior of rammed earth: Experimentation towards numerical modelling, Constr. Build. Mater. 227 (2019) 116646. https://doi.org/10.1016/j.conbuildmat.2019.08.027.
[32] H. Nowamooz, C. Chazallon, M.I. Arsenie, P. Hornych, F. Masrouri, Unsaturated resilient behavior of a natural compacted sand, Comput. Geotech. 38 (2011) 491–503. https://doi.org/10.1016/j.compgeo.2011.02.013.
[33] H. Nowamooz, F. Masrouri, Hydromechanical behaviour of an expansive bentonite/silt mixture in cyclic suction-controlled drying and wetting tests, Eng. Geol. 101 (2008) 154–164. https://doi.org/10.1016/j.enggeo.2008.04.011.

[34] S. Burroughs, Relationships between the density and strength of rammed earth, Proc. Inst. Civ. Eng. - Constr. Mater. 162 (2009) 113–120. https://doi.org/10.1680/coma.2009.162.3.113.
[35] V.O. Okonkwo, I.K. Omaliko, N.M. Ezema, Stabilization of Lateritic Soil with Portland Cement and Sand for Road Pavement, OALib. 09 (2022) 1–15. https://doi.org/10.4236/oalib.1108560.
[36] R.K. Sharma, Utilization of Fly Ash and Waste Ceramic in Improving Characteristics of Clayey Soil: A Laboratory Study, Geotech. Geol. Eng. 38 (2020) 5327–5340. https://doi.org/10.1007/s10706-020-01366-7.
[37] E. Anglade, J.-E. Aubert, A. Sellier, A. Papon, Physical and mechanical properties of clay–sand mixes to assess the performance of earth construction materials, J. Build. Eng. 51 (2022) 104229. https://doi.org/10.1016/j.jobe.2022.104229.
[38] B.V. Venkatarama Reddy, P. Prasanna Kumar, Cement stabilised rammed earth. Part A: compaction characteristics and physical properties of compacted cement stabilised soils, Mater. Struct. 44 (2011) 681–693. https://doi.org/10.1617/s11527-010-9658-9.
[39] M.A. Dafalla, The Compressibility and Swell of Mixtures for Sand-Clay Liners, Adv. Mater. Sci. Eng. 2017 (2017) e3181794. https://doi.org/10.1155/2017/3181794.
[40] S. Pongsivasathit, S. Horpibulsuk, S. Piyaphipat, Assessment of mechanical properties of cement stabilized soils, Case Stud. Constr. Mater. 11 (2019) e00301. https://doi.org/10.1016/j.cscm.2019.e00301.
[41] P. Narloch, P. Woyciechowski, Assessing Cement Stabilized Rammed Earth Durability in A Humid Continental Climate, Buildings. 10 (2020) 26. https://doi.org/10.3390/buildings10020026.
[42] I. Shooshpasha, R.A. Shirvani, Effect of cement stabilization on geotechnical properties of sandy soils, Geomech. Eng. 8 (2015) 17–31. https://doi.org/10.12989/gae.2015.8.1.017.
[43] O.Q. Jan, B.A. Mir, Strength Behaviour of Cement Stabilised Dredged Soil, Int. J. Geosynth. Ground Eng. 4 (2018) 16. https://doi.org/10.1007/s40891-018-0133-y.
[44] P.J. Walker, Strength, durability and shrinkage characteristics of cement stabilised soil blocks, Cem. Concr. Compos. 17 (1995) 301–310. https://doi.org/10.1016/0958-9465(95)00019-9.
[45] A.J. Bryan, Soil/cement as a walling material—I. Stress/strain properties, Build. Environ. 23 (1988) 321–330. https://doi.org/10.1016/0360-1323(88)90038-8.
[46] I.M. Alkiki, M.D. Abdulnafaa, A. Aldaood, Geotechnical and other characteristics of cement-treated low plasticity clay, Soils Rocks. 44 (2021). https://doi.org/10.28927/SR.2021.053120.
[47] P.L. Narloch, P. Woyciechowski, P. Jęda, The influence of loam type and cement content of the compressive strength of rammed earth, Arch. Civ. Eng. (2015) 73--88. https://doi.org/10.1515/ace-2015-0005.
[48] D. Ciancio, J. Gibbings, Experimental investigation on the compressive strength of cored and molded cement-stabilized rammed earth samples, Constr. Build. Mater. 28 (2012) 294–304. https://doi.org/10.1016/j.conbuildmat.2011.08.070.
[49] T.E. Elahi, A.R. Shahriar, M.S. Islam, Engineering characteristics of compressed earth blocks stabilized with cement and fly ash, Constr. Build. Mater. 277 (2021) 122367. https://doi.org/10.1016/j.conbuildmat.2021.122367.
[50] S.N. Malkanthi, N. Balthazaar, A.A.D.A.J. Perera, Lime stabilization for compressed stabilized earth blocks with reduced clay and silt, Case Stud. Constr. Mater. 12 (2020) e00326. https://doi.org/10.1016/j.cscm.2019.e00326.
[51] P. Walker, T. Stace, Properties of some cement stabilised compressed earth blocks and mortars, Mater. Struct. 30 (1997) 545–551. https://doi.org/10.1007/BF02486398.

[52] R. Lepakshi, B.V. Venkatarama Reddy, Shear strength parameters and Mohr-Coulomb failure envelopes for cement stabilised rammed earth, Constr. Build. Mater. 249 (2020) 118708. https://doi.org/10.1016/j.conbuildmat.2020.118708.
[53] J.E. Oti, J.M. Kinuthia, Stabilised unfired clay bricks for environmental and sustainable use, Appl. Clay Sci. 58 (2012) 52–59. https://doi.org/10.1016/j.clay.2012.01.011.
[54] V. Strazzeri, A. Karrech, M. Elchalakani, Micromechanics modelling of cement stabilised rammed earth, Mech. Mater. 148 (2020) 103540. https://doi.org/10.1016/j.mechmat.2020.103540.
[55] D.D. Tripura, K.D. Singh, Characteristic Properties of Cement-Stabilized Rammed Earth Blocks, J. Mater. Civ. Eng. 27 (2015) 04014214. https://doi.org/10.1061/(ASCE)MT.1943-5533.0001170.
[56] D. Ciancio, M. Boulter, Stabilised rammed earth: a case study in Western Australia, Proc. Inst. Civ. Eng. - Eng. Sustain. 165 (2012) 141–154. https://doi.org/10.1680/ensu.10.00003.
[57] M.M. Hallal, S. Sadek, S.S. Najjar, Evaluation of Engineering Characteristics of Stabilized Rammed-Earth Material Sourced from Natural Fines-Rich Soil, J. Mater. Civ. Eng. 30 (2018) 04018273. https://doi.org/10.1061/(ASCE)MT.1943-5533.0002481.
[58] L.R. Blotz, C.H. Benson, G.P. Boutwell, Estimating Optimum Water Content and Maximum Dry Unit Weight for Compacted Clays, J. Geotech. Geoenvironmental Eng. 124 (1998) 907–912. https://doi.org/10.1061/(ASCE)1090-0241(1998)124:9(907).
[59] M.S. Islam, N. Tausif-E-Elahi, A.R. Shahriar, K. Nahar, T.R. Hossain, Strength and Durability Characteristics of Cement-Sand Stabilized Earth Blocks, J. Mater. Civ. Eng. 32 (2020) 04020087. https://doi.org/10.1061/(ASCE)MT.1943-5533.0003176.
[60] M. Hall, Y. Djerbib, Rammed earth sample production: context, recommendations and consistency, Constr. Build. Mater. 18 (2004) 281–286. https://doi.org/10.1016/j.conbuildmat.2003.11.001.
[61] L. Xu, K.K. Wong, A. Fabbri, F. Champiré, D. Branque, Loading-unloading shear behavior of rammed earth upon varying clay content and relative humidity conditions, Soils Found. 58 (2018) 1001–1015. https://doi.org/10.1016/j.sandf.2018.05.005.
[62] D.M. LILLEY, J. ROBINSON, ULTIMATE STRENGTH OF RAMMED EARTH WALLS WITH OPENINGS., Proc. Inst. Civ. Eng. - Struct. Build. Proc. Inst. Civ. Eng. - Struct. Build. 110 (1995) 278–287.
[63] Maniatidis Vasilios, Walker Peter, Structural Capacity of Rammed Earth in Compression, J. Mater. Civ. Eng. 20 (2008) 230–238. https://doi.org/10.1061/(ASCE)0899-1561(2008)20:3(230).
[64] P.A. Jaquin, C.E. Augarde, D. Gallipoli, D.G. Toll, The strength of unstabilised rammed earth materials, Géotechnique. 59 (2009) 487.
[65] Q.-B. Bui, J.-C. Morel, S. Hans, P. Walker, Effect of moisture content on the mechanical characteristics of rammed earth, Constr. Build. Mater. 54 (2014) 163–169. https://doi.org/10.1016/j.conbuildmat.2013.12.067.
[66] P. Gerard, M. Mahdad, A. Robert McCormack, B. François, A unified failure criterion for unstabilized rammed earth materials upon varying relative humidity conditions, Constr. Build. Mater. 95 (2015) 437–447. https://doi.org/10.1016/j.conbuildmat.2015.07.100.
[67] H. Araki, J. Koseki, T. Sato, Tensile strength of compacted rammed earth materials, Soils Found. 56 (2016) 189–204. https://doi.org/10.1016/j.sandf.2016.02.003.
[68] J.C. Smith, C. Augarde, Optimum water content tests for earthen construction materials, Proc. Inst. Civ. Eng.-Constr. Mater. 167 (2014) 114–123.

[69] C.T.S. Beckett, C.E. Augarde, D. Easton, T. Easton, Strength characterisation of soil-based construction materials, Géotechnique. 68 (2017) 400–409. https://doi.org/10.1680/jgeot.16.P.288.
[70] P. Chauhan, N. Prime, O. Plé, Benefit of Unsaturated Soil Mechanics Approach on the Modeling of Early-Age Behavior of Rammed Earth Building, Materials. 15 (2022) 362. https://doi.org/10.3390/ma15010362.
[71] N. Lu, Is Matric Suction a Stress Variable?, J. Geotech. Geoenvironmental Eng. 134 (2008) 899–905. https://doi.org/10.1061/(ASCE)1090-0241(2008)134:7(899).
[72] M.T. van Genuchten, A Closed-form Equation for Predicting the Hydraulic Conductivity of Unsaturated Soils, Soil Sci. Soc. Am. J. 44 (1980) 892–898. https://doi.org/10.2136/sssaj1980.03615995004400050002x.
[73] M.D. Fredlund, G.W. Wilson, D.G. Fredlund, Use of the grain-size distribution for estimation of the soil-water characteristic curve, Can. Geotech. J. 39 (2002) 1103–1117. https://doi.org/10.1139/t02-049.
[74] M.D. Fredlund, D.G. Fredlund, G.W. Wilson, An equation to represent grain-size distribution, Can. Geotech. J. 37 (2000) 817–827. https://doi.org/10.1139/t00-015.
[75] N. Lu, W.J. Likos, Suction Stress Characteristic Curve for Unsaturated Soil, J. Geotech. Geoenvironmental Eng. 132 (2006) 131–142. https://doi.org/10.1061/(ASCE)1090-0241(2006)132:2(131).
[76] M. Uesugi, H. Kishida, Frictional Resistance at Yield between Dry Sand and Mild Steel, Soils Found. 26 (1986) 139–149. https://doi.org/10.3208/sandf1972.26.4_139.
[77] S.A. Harehdasht, M. Hussien, M. Karray, V. Roubtsova, M. Chekired, Influence of particle size and gradation on shear strength–dilation relation of granular materials, Can. Geotech. J. (2019). https://doi.org/10.1139/CGJ-2017-0468.
[78] A.W. Bishop, G.E. Blight, Some Aspects of Effective Stress in Saturated and Partly Saturated Soils, Géotechnique. 13 (1963) 177–197. https://doi.org/10.1680/geot.1963.13.3.177.
[79] A. Zaoui, Continuum Micromechanics: Survey, J. Eng. Mech. 128 (2002) 808–816. https://doi.org/10.1061/(ASCE)0733-9399(2002)128:8(808).
[80] C. Beckett, D. Ciancio, Effect of compaction water content on the strength of cement-stabilized rammed earth materials, Can. Geotech. J. 51 (2014) 583–590. https://doi.org/10.1139/cgj-2013-0339.
[81] A. Perić, I. Kraus, J. Kaluđer, L. Kraus, Experimental Campaigns on Mechanical Properties and Seismic Performance of Unstabilized Rammed Earth—A Literature Review, Buildings. 11 (2021) 367. https://doi.org/10.3390/buildings11080367.
[82] F. Ávila, E. Puertas, R. Gallego, Characterization of the mechanical and physical properties of unstabilized rammed earth: A review, Constr. Build. Mater. 270 (2021) 121435. https://doi.org/10.1016/j.conbuildmat.2020.121435.
[83] P. Wangmo, K.C. Shrestha, T. Aoki, Exploratory study of rammed earth walls under static element test, Constr. Build. Mater. 266 (2021) 121035. https://doi.org/10.1016/j.conbuildmat.2020.121035.
[84] N.M. Kouakou, O. Cuisinier, F. Masrouri, Estimation of the shear strength of coarse-grained soils with fine particles, Transp. Geotech. 25 (2020) 100407. https://doi.org/10.1016/j.trgeo.2020.100407.
[85] Q. Liu, L. Tong, Engineering properties of unstabilized rammed earth with different clay contents, J. Wuhan Univ. Technol.-Mater Sci Ed. 32 (2017) 914–920. https://doi.org/10.1007/s11595-017-1690-y.
[86] B. François, L. Palazon, P. Gerard, Structural behaviour of unstabilized rammed earth constructions submitted to hygroscopic conditions, Constr. Build. Mater. 155 (2017) 164–175. https://doi.org/10.1016/j.conbuildmat.2017.08.012.

[87] Q.-B. Bui, J.-C. Morel, S. Hans, P. Walker, Effect of moisture content on the mechanical characteristics of rammed earth, Constr. Build. Mater. 54 (2014) 163–169. https://doi.org/10.1016/j.conbuildmat.2013.12.067.
[88] P. Gerard, M. Mahdad, A. Robert McCormack, B. François, A unified failure criterion for unstabilized rammed earth materials upon varying relative humidity conditions, Constr. Build. Mater. 95 (2015) 437–447. https://doi.org/10.1016/j.conbuildmat.2015.07.100.
[89] F. Champiré, A. Fabbri, J.-C. Morel, H. Wong, F. McGregor, Impact of relative humidity on the mechanical behavior of compacted earth as a building material, Constr. Build. Mater. 110 (2016) 70–78. https://doi.org/10.1016/j.conbuildmat.2016.01.027.
[90] L. Xu, K.K. Wong, A. Fabbri, F. Champiré, D. Branque, Loading-unloading shear behavior of rammed earth upon varying clay content and relative humidity conditions, Soils Found. 58 (2018) 1001–1015. https://doi.org/10.1016/j.sandf.2018.05.005.
[91] K.C. Shrestha, T. Aoki, M. Miyamoto, P. Wangmo, Pema, J. Zhang, N. Takahashi, Strengthening of rammed earth structures with simple interventions, J. Build. Eng. 29 (2020) 101179. https://doi.org/10.1016/j.jobe.2020.101179.
[92] T.P. Otcovska, B. Muzikova, P. Padevet, Mechanical Properties of Rammed Earth with Respect to Clay Mixture Composition, Acta Polytech. 59 (2019) 372–383. https://doi.org/10.14311/AP.2019.59.0372.
[93] W. Phuntsho, Seismic Vulnerability Assessment and Possible Strengthening, (2021).
[94] A. Herzog, J.K. Mitchell, REACTIONS ACCOMPANYING STABILIZATION OF CLAY WITH CEMENT, Highw. Res. Rec. (1963). https://trid.trb.org/view/121675 (accessed February 23, 2022).
[95] Patrice Doat, Alain Hays, Hugo Houben, Sylvie Matuk, François Vitoux, Construire En Terre, Ed. Alternative et Parallèles, 1979. http://archive.org/details/ConstruireEnTerre (accessed February 23, 2022).
[96] S.-W. Moon, G. Vinoth, S. Subramanian, J. Kim, T. Ku, Effect of fine particles on strength and stiffness of cement treated sand, Granul. Matter. 22 (2019) 9. https://doi.org/10.1007/s10035-019-0975-6.
[97] M. abd allah Abd elaty, Compressive strength prediction of Portland cement concrete with age using a new model, HBRC J. 10 (2014) 145–155. https://doi.org/10.1016/j.hbrcj.2013.09.005.
[98] Ł. Rosicki, P. Narloch, Studies on the Ageing of Cement Stabilized Rammed Earth Material in Different Exposure Conditions, Materials. 15 (2022) 1090. https://doi.org/10.3390/ma15031090.
[99] M.A.H. Sarker, I. Mahmud, Compressed Stabilized Earth Block as a Sustainable Building Material, Civ. Environ. Res. 10 (2018) 49. https://www.iiste.org/Journals/index.php/CER/article/view/44968 (accessed October 3, 2021).
[100] J. Ren, S. Wang, G. Zang, Effects of recycled aggregate composition on the mechanical characteristics and material design of cement stabilized cold recycling mixtures using road milling materials, Constr. Build. Mater. 244 (2020) 118329. https://doi.org/10.1016/j.conbuildmat.2020.118329.
[101] K. Himouri, A. Hamouine, L. Guettatfi, Effects of portland cement and quicklime on physical and mechanical characteristics of earth concrete, Jordan J Civ Eng. 15 (2021) 597–610.
[102] A. Pelé-Peltier, A. Fabbri, J.-C. Morel, E. Hamard, M. Lhenry, A similitude relation to assessing the compressive strength of rammed earth from scale-down samples, Case Stud. Constr. Mater. 16 (2022) e00921. https://doi.org/10.1016/j.cscm.2022.e00921.

[103] B.V. Venkatarama Reddy, P. Prasanna Kumar, Cement stabilised rammed earth. Part B: compressive strength and stress–strain characteristics, Mater. Struct. 44 (2011) 695–707. https://doi.org/10.1617/s11527-010-9659-8.
[104] C. Lian, Y. Zhuge, S. Beecham, The relationship between porosity and strength for porous concrete, Constr. Build. Mater. 25 (2011) 4294–4298. https://doi.org/10.1016/j.conbuildmat.2011.05.005.
[105] A. Sičáková, M. Kováč, Relationships between Functional Properties of Pervious Concrete, Sustainability. 12 (2020) 6318. https://doi.org/10.3390/su12166318.
[106] K. Yanagi, Y. Kasai, S. Kaga, M. Abe, Experimental study on the applicability of recycled aggregate concrete to cast-in-place concrete pile, in: Sustain. Constr. Use Recycl. Concr. Aggreg., Thomas Telford Publishing, 1998: pp. 359–370. https://doi.org/10.1680/scuorca.27268.0031.
[107] F. Tadayoshi, Strength and drying shrinkage of concrete using concrete crushed aggregate, in: Proc. 2nd Int. RILEM Symp. Demolition Reuse Concr. Mason. Tokyo Jpn., 1988: pp. 7–11.
[108] J. Xiao, J. Li, Ch. Zhang, Mechanical properties of recycled aggregate concrete under uniaxial loading, Cem. Concr. Res. 35 (2005) 1187–1194. https://doi.org/10.1016/j.cemconres.2004.09.020.
[109] T.A. Pham, H. Kyokawa, J. Koseki, D. Dias, A new index for the strength analysis and prediction of cement-mixed soils, Eur. J. Environ. Civ. Eng. 0 (2022) 1–23. https://doi.org/10.1080/19648189.2022.2086929.
[110] B. Felekoğlu, S. Türkel, B. Baradan, Effect of water/cement ratio on the fresh and hardened properties of self-compacting concrete, Build. Environ. 42 (2007) 1795–1802. https://doi.org/10.1016/j.buildenv.2006.01.012.
[111] C. Beckett, D. Ciancio, S. Manzi, M.-C. Bignozzi, Strengthening mechanisms in cement-stabilised rammed earth, Rammed Earth Constr. Cut.-Edge Res. Tradit. Mod. Rammed Earth. (2015) 41–46. https://doi.org/10.1201/b18046.
[112] F.A. Oluokun, Fly ash concrete mix design and the water-cement ratio law, Mater. J. 91 (1994) 362–371.
[113] I.-C. Yeh, Generalization of strength versus water–cementitious ratio relationship to age, Cem. Concr. Res. 36 (2006) 1865–1873. https://doi.org/10.1016/j.cemconres.2006.05.013.
[114] S. Li, J. Yang, P. Zhang, Water-Cement-Density Ratio Law for the 28-Day Compressive Strength Prediction of Cement-Based Materials, Adv. Mater. Sci. Eng. 2020 (2020) e7302173. https://doi.org/10.1155/2020/7302173.
[115] M. Meera, S. Gupta, Development of a strength model for foam concrete based on water – cement ratio, Mater. Today Proc. 32 (2020) 923–927. https://doi.org/10.1016/j.matpr.2020.04.888.
[116] S.B. Singh, P. Munjal, N. Thammishetti, Role of water/cement ratio on strength development of cement mortar, J. Build. Eng. 4 (2015) 94–100. https://doi.org/10.1016/j.jobe.2015.09.003.
[117] L.S. Ho, K. Nakarai, M. Duc, A.L. Kouby, A. Maachi, T. Sasaki, Analysis of strength development in cement-treated soils under different curing conditions through microstructural and chemical investigations, Constr. Build. Mater. 166 (2018) 634–646. https://doi.org/10.1016/j.conbuildmat.2018.01.112.
[118] H.B. Nagaraj, M.V. Sravan, T.G. Arun, K.S. Jagadish, Role of lime with cement in long-term strength of Compressed Stabilized Earth Blocks, Int. J. Sustain. Built Environ. 3 (2014) 54–61. https://doi.org/10.1016/j.ijsbe.2014.03.001.

[119] G.J. Singh, V. Kumar, B.N. Singh, R. Kumar, Impact of Drying the Concrete before Its Complete Curing: Plain and Fly Ash–Based Cement Concrete, J. Mater. Civ. Eng. 34 (2022) 04021442. https://doi.org/10.1061/(ASCE)MT.1943-5533.0004290.
[120] J. Wang, A.C. Fayish, B. Hoffheins, M.L. McCahan, The evaluation of chemical admixtures on the performance of cement stabilized materials in cold weather, Transp. Geotech. 30 (2021) 100618. https://doi.org/10.1016/j.trgeo.2021.100618.
[121] D. Niu, S. Zhang, Y. Wang, M. Hong, Z. Li, Effect of temperature on the strength, hydration products and microstructure of shotcrete blended with supplementary cementitious materials, Constr. Build. Mater. 264 (2020) 120234. https://doi.org/10.1016/j.conbuildmat.2020.120234.
[122] Y. Yu, L. Yu, L. Fan, L. Sun, Z. Zhang, Effect of Mineral Admixtures on the Performance of Ceramsite Shotcrete for High Geothermal Underground Engineering, ACS Omega. 7 (2022) 5774–5781. https://doi.org/10.1021/acsomega.1c05720.
[123] S. Rahimi-Aghdam, Z.P. Bažant, M.J. Abdolhosseini Qomi, Cement hydration from hours to centuries controlled by diffusion through barrier shells of C-S-H, J. Mech. Phys. Solids. 99 (2017) 211–224. https://doi.org/10.1016/j.jmps.2016.10.010.
[124] R.J. Zhang, Y.T. Lu, T.S. Tan, K.K. Phoon, A.M. Santoso, Long-Term Effect of Curing Temperature on the Strength Behavior of Cement-Stabilized Clay, J. Geotech. Geoenvironmental Eng. 140 (2014) 04014045. https://doi.org/10.1061/(ASCE)GT.1943-5606.0001144.
[125] J. Zhang, G.W. Scherer, Comparison of methods for arresting hydration of cement, Cem. Concr. Res. 41 (2011) 1024–1036. https://doi.org/10.1016/j.cemconres.2011.06.003.
[126] U.N. Hayri, B. Baradan, The effect of curing temperature and relative humidity on the strength development of Portland cement mortar, Sci. Res. Essays. 6 (2011) 2504–2511.
[127] F. López Gayarre, C. López-Colina Pérez, M.A. Serrano López, A. Domingo Cabo, The effect of curing conditions on the compressive strength of recycled aggregate concrete, Constr. Build. Mater. 53 (2014) 260–266. https://doi.org/10.1016/j.conbuildmat.2013.11.112.
[128] I.I. Akinwumi, Z.O. Gbadamosi, Effects of curing condition and curing period on the compressive strength development of plain concrete, Int. J. Civ. Environ. Res. 1 (2014) 83–99.
[129] A. Boyd, J. Skalny, Environmental Deterioration Of Concrete, (2007). https://doi.org/10.2495/978-1-84564-032-3/05.
[130] T.-T. Bui, Q.-B. Bui, A. Limam, S. Maximilien, Failure of rammed earth walls: From observations to quantifications, Constr. Build. Mater. 51 (2014) 295–302. https://doi.org/10.1016/j.conbuildmat.2013.10.053.
[131] P. Wangmo, K.C. Shrestha, M. Miyamoto, T. Aoki, Assessment of out-of-plane behavior of rammed earth walls by pull-down tests, Int. J. Archit. Herit. 13 (2019) 273–287. https://doi.org/10.1080/15583058.2018.1433903.
[132] C. Beckett, J.C. Smith, D. Ciancio, C. Augarde, Tensile strengths of flocculated compacted unsaturated soils, Géotechnique Lett. 5 (2015) 254–260. https://doi.org/10.1680/jgele.15.00087.
[133] K.C. Shrestha, T. Aoki, M. Miyamoto, P. Wangmo, Pema, In-Plane Shear Resistance between the Rammed Earth Blocks with Simple Interventions: Experimentation and Finite Element Study, Buildings. 10 (2020) 57. https://doi.org/10.3390/buildings10030057.
[134] A. Koutous, E. Hilali, Reinforcing rammed earth with plant fibers: A case study, Case Stud. Constr. Mater. 14 (2021) e00514. https://doi.org/10.1016/j.cscm.2021.e00514.

[135] V. Toufigh, E. Kianfar, The effects of stabilizers on the thermal and the mechanical properties of rammed earth at various humidities and their environmental impacts, Constr. Build. Mater. 200 (2019) 616–629. https://doi.org/10.1016/j.conbuildmat.2018.12.050.
[136] K.Q. Tran, T. Satomi, H. Takahashi, Improvement of mechanical behavior of cemented soil reinforced with waste cornsilk fibers, Constr. Build. Mater. 178 (2018) 204–210. https://doi.org/10.1016/j.conbuildmat.2018.05.104.
[137] B.V. Venkatarama Reddy, A. Gupta, Characteristics of soil-cement blocks using highly sandy soils, Mater. Struct. 38 (2005) 651. https://doi.org/10.1007/BF02481596.
[138] A.H. Meek, M. Elchalakani, C.T.S. Beckett, M. Dong, Alternative stabilised rammed earth materials incorporating recycled waste and industrial by-products: A study of mechanical properties, flexure and bond strength, Constr. Build. Mater. 277 (2021) 122303. https://doi.org/10.1016/j.conbuildmat.2021.122303.
[139] Q.-B. Bui, J.-C. Morel, Assessing the anisotropy of rammed earth, Constr. Build. Mater. 23 (2009) 3005–3011. https://doi.org/10.1016/j.conbuildmat.2009.04.011.
[140] N.Z. Standard, Engineering design of earth buildings, Stand. Zealand Wellingt. N. Z. 1988 (1998).
[141] S. Shibuya, H. Tanaka, Estimate of Elastic Shear Modulus In Holocene Soil Deposits, Soils Found. 36 (1996) 45–55. https://doi.org/10.3208/sandf.36.4_45.
[142] R.V. Silva, J. de Brito, R.K. Dhir, Establishing a relationship between modulus of elasticity and compressive strength of recycled aggregate concrete, J. Clean. Prod. 112 (2016) 2171–2186. https://doi.org/10.1016/j.jclepro.2015.10.064.
[143] T. Noguchi, K.M. Nemati, Relationship between compressive strength and modulus of elasticity of high-strength concrete, J Struct Constr Eng. 60 (1995) 1–10.
[144] F. Tomosawa, T. Noguchi, Relationship between compressive strength and modulus of elasticity of high-strength concrete, in: Proc. Third Int. Symp. Util. High-Strength Concr., Norwegian Concrete Assn Lillehammer, Norway, 1993: pp. 1247–1254.
[145] M. Mahdad, A. Benidir, A. Brara, Experimental assessment of mechanical behavior of a compressed stabilized earth blocks (CSEB) and walls, J. Mater. Eng. Struct. « JMES ». 8 (2021) 95–110. http://revue.ummto.dz/index.php/JMES/article/view/2460 (accessed October 1, 2021).
[146] H. Gercek, Poisson's ratio values for rocks, Int. J. Rock Mech. Min. Sci. 44 (2007) 1–13. https://doi.org/10.1016/j.ijrmms.2006.04.011.
[147] T.K. Koca, M.Y. Koca, Classification of weathered andesitic rock materials from the İzmir Subway line on the basis of strength and deformation, Bull. Eng. Geol. Environ. 78 (2019) 3575–3592. https://doi.org/10.1007/s10064-018-1346-y.
[148] M.R. Vergara, T. Triantafyllidis, Influence of Water Content on the Mechanical Properties of an Argillaceous Swelling Rock, Rock Mech. Rock Eng. 49 (2016) 2555–2568. https://doi.org/10.1007/s00603-016-0938-8.
[149] F.P. Incropera, D.P. DeWitt, T.L. Bergman, A.S. Lavine, Fundamentals of heat and mass transfer, Wiley New York, 1996.
[150] S. Verbeke, A. Audenaert, Thermal inertia in buildings: A review of impacts across climate and building use, Renew. Sustain. Energy Rev. 82 (2018) 2300–2318.
[151] G. Minke, Building with earth: design and technology of a sustainable architecture, Walter de Gruyter, 2012.
[152] J.J. Correia da Silva, J.P.B. Pereira, J. Sirgado, Improving rammed earth wall thermal performance with added expanded granulated cork, Archit. Sci. Rev. 58 (2015) 314–323. https://doi.org/10.1080/00038628.2014.997183.

[153] C. Stone, M. Balintova, M. Holub, Feasibility of Integrated Insulation in Rammed Earth, IOP Conf. Ser. Mater. Sci. Eng. 96 (2015) 012030. https://doi.org/10.1088/1757-899X/96/1/012030.
[154] A. Karrech, V. Strazzeri, M. Elchalakani, Improved thermal insulance of cement stabilised rammed earth embedding lightweight aggregates, Constr. Build. Mater. 268 (2021) 121075. https://doi.org/10.1016/j.conbuildmat.2020.121075.
[155] V. Strazzeri, A. Karrech, Energy and thermal performance of a typical rammed earth residential building in Western Australia, Energy Build. 260 (2022) 111901.
[156] H. Porter, J. Blake, N.K. Dhami, A. Mukherjee, Rammed earth blocks with improved multifunctional performance, Cem. Concr. Compos. 92 (2018) 36–46. https://doi.org/10.1016/j.cemconcomp.2018.04.013.
[157] D. Jain, A. Mukherjee, H. Porter, J. Blake, Enhanced thermal resistance of rammed earth blocks with recycled industry by-products, Int. J. Therm. Sci. 138 (2019) 447–458. https://doi.org/10.1016/j.ijthermalsci.2019.01.017.
[158] X. Zhang, H. Nowamooz, Thermo-hydro-mechanical (THM) behavior of Unstabilized Rammed Earth (URE) wall submitted to environmental and mechanical loadings, Mater. Struct. 54 (2021) 198. https://doi.org/10.1617/s11527-021-01798-4.
[159] P. Walker, R. Keable, J. Martin, V. Maniatidis, Rammed earth: design and construction guidelines, (2005).
[160] V. Soebarto, Analysis of indoor performance of houses using rammed earth walls, in: Elev. Int. IBPSA Conf., 2009: pp. 27–30.
[161] P. Taylor, M.B. Luther, Evaluating rammed earth walls: a case study, Sol. Energy. 76 (2004) 79–84.
[162] B. Jiang, T. Wu, W. Xia, J. Liang, Hygrothermal performance of rammed earth wall in Tibetan Autonomous Prefecture in Sichuan Province of China, Build. Environ. 181 (2020) 107128. https://doi.org/10.1016/j.buildenv.2020.107128.
[163] J.-P. Laurent, Contribution à la caractérisation thermique des milieux poreux granulaires: optimisation d'outils de mesure" in-situ" des paramètres thermiques, application à l'étude des propriétés thermiques du matériau terre, Grenoble INPG, 1986.
[164] L. Soudani, A. Fabbri, J.-C. Morel, M. Woloszyn, P.-A. Chabriac, H. Wong, A.-C. Grillet, Assessment of the validity of some common assumptions in hygrothermal modeling of earth based materials, Energy Build. 116 (2016) 498–511. https://doi.org/10.1016/j.enbuild.2016.01.025.
[165] D. Medjelekh, L. Ulmet, F. Gouny, F. Fouchal, B. Nait-Ali, P. Maillard, F. Dubois, Characterization of the coupled hygrothermal behavior of unfired clay masonries: Numerical and experimental aspects, Build. Environ. 110 (2016) 89–103. https://doi.org/10.1016/j.buildenv.2016.09.037.
[166] P. Taylor, R.J. Fuller, M.B. Luther, Energy use and thermal comfort in a rammed earth office building, Energy Build. 40 (2008) 793–800. https://doi.org/10.1016/j.enbuild.2007.05.013.
[167] M. Indekeu, M. Woloszyn, A.-C. Grillet, L. Soudani, A. Fabbri, Towards hygrothermal characterization of rammed earth with small-scale dynamic methods, Energy Procedia. 132 (2017) 297–302. https://doi.org/10.1016/j.egypro.2017.09.731.
[168] L. Zhang, L. Yang, B.P. Jelle, Y. Wang, A. Gustavsen, Hygrothermal properties of compressed earthen bricks, Constr. Build. Mater. 162 (2018) 576–583. https://doi.org/10.1016/j.conbuildmat.2017.11.163.
[169] A. Mahdavi, B. Martens, R. Scherer, eWork and eBusiness in Architecture, Engineering and Construction: ECPPM 2014, CRC Press, 2014.

[170] p Diaz pedregal, Les caractéristiques thermophysiques de la terre, Sol. 1 Megazine. 11 (1981) 20–25.
[171] M. Saidi, A.S. Cherif, B. Zeghmati, E. Sediki, Stabilization effects on the thermal conductivity and sorption behavior of earth bricks, Constr. Build. Mater. 167 (2018) 566–577. https://doi.org/10.1016/j.conbuildmat.2018.02.063.
[172] P. Narloch, W. Piątkiewicz, B. Pietruszka, The Effect of Cement Addition on Water Vapour Resistance Factor of Rammed Earth, Materials. 14 (2021) 2249. https://doi.org/10.3390/ma14092249.
[173] L. Zhang, A. Gustavsen, B.P. Jelle, L. Yang, T. Gao, Y. Wang, Thermal conductivity of cement stabilized earth blocks, Constr. Build. Mater. 151 (2017) 504–511. https://doi.org/10.1016/j.conbuildmat.2017.06.047.
[174] A.B. Costantini Romero, F.M. Francisca, I. Giomi, Hygrothermal properties of soil–cement construction materials, Constr. Build. Mater. 313 (2021) 125518. https://doi.org/10.1016/j.conbuildmat.2021.125518.
[175] L.L. Sparks, Thermal conductivity of a concrete mortar from 95 K to 320 K, 0 ed., National Bureau of Standards, Gaithersburg, MD, 1981. https://doi.org/10.6028/NBS.IR.81-1651.
[176] D. Allinson, M. Hall, Hygrothermal analysis of a stabilised rammed earth test building in the UK, Energy Build. 42 (2010) 845–852. https://doi.org/10.1016/j.enbuild.2009.12.005.
[177] M. Hall, D. Allinson, Analysis of the hygrothermal functional properties of stabilised rammed earth materials, Build. Environ. 44 (2009) 1935–1942. https://doi.org/10.1016/j.buildenv.2009.01.007.
[178] P.M. Touré, V. Sambou, M. Faye, A. Thiam, M. Adj, D. Azilinon, Mechanical and hygrothermal properties of compressed stabilized earth bricks (CSEB), J. Build. Eng. 13 (2017) 266–271. https://doi.org/10.1016/j.jobe.2017.08.012.
[179] S. Liuzzi, M.R. Hall, P. Stefanizzi, S.P. Casey, Hygrothermal behaviour and relative humidity buffering of unfired and hydrated lime-stabilised clay composites in a Mediterranean climate, Build. Environ. 61 (2013) 82–92. https://doi.org/10.1016/j.buildenv.2012.12.006.
[180] R.H. Brooks, A.T. Corey, HYDRAULIC PROPERTIES OF POROUS MEDIA, (n.d.) 37.
[181] P. Shafigh, I. Asadi, A.R. Akhiani, N.B. Mahyuddin, M. Hashemi, Thermal properties of cement mortar with different mix proportions, Mater. Constr. 70 (2020) e224–e224. https://doi.org/10.3989/mc.2020.09219.
[182] A. Stolarska, J. Strzałkowski, The Thermal Parameters of Mortars Based on Different Cement Type and W/C Ratios, Materials. 13 (2020) 4258. https://doi.org/10.3390/ma13194258.
[183] D. Campbell-Allen, C.P. Thorne, The thermal conductivity of concrete, Mag. Concr. Res. 15 (1963) 39–48. https://doi.org/10.1680/macr.1963.15.43.39.
[184] M.A. Glinicki, R. Jaskulski, W. Pichór, M. Dąbrowski, M. Sobczak, Investigation of thermal properties of shielding concrete, in: Proc Int Symp Brittle Matrix Compos., 2015: pp. 371–380.
[185] D.J. Akers, R.D. Gruber, B.W. Ramme, M.J. Boyle, J.G. Grygar, S.K. Rowe, T.W. Bremner, E.S. Kluckowski, S.R. Sheetz, R.G. Burg, Guide for structural lightweight-aggregate concrete, ACI 213R-03 Am. Concr. Inst. ACI Mich. (2003).
[186] I. Asadi, P. Shafigh, Z.F.B. Abu Hassan, N.B. Mahyuddin, Thermal conductivity of concrete – A review, J. Build. Eng. 20 (2018) 81–93. https://doi.org/10.1016/j.jobe.2018.07.002.

[187] R.C. Valore, Calculations of U-values of hollow concrete masonry, Concr. Int. 2 (1980) 40–63.
[188] H. Penicaud, Caractéristiques thermophysiques du matériau terre, Actual. Constr. En Terre En Fr. (1982).
[189] C. Lyu, Q. Sun, W. Zhang, J. Geng, A predictive model for the thermal conductivity of silty clay soil based on soil porosity and saturation, Arab. J. Geosci. 13 (2020) 312. https://doi.org/10.1007/s12517-020-05284-z.
[190] M.S. Kersten, Thermal Properties of Soils, (1949). http://conservancy.umn.edu/handle/11299/124271 (accessed July 29, 2022).
[191] O. Johansen, Thermal conductivity of soils, Cold Regions Research and Engineering Lab Hanover NH, 1977.
[192] H. Sakashita, T. Kumada, Heat transfer model for predicting thermal conductivity of highly compacted bentonite, Nippon Genshiryoku Gakkai-Shi. 40 (1998) 235–240.
[193] J. Côté, J.-M. Konrad, A generalized thermal conductivity model for soils and construction materials, Can. Geotech. J. 42 (2005) 443–458.
[194] V. Balland, P.A. Arp, Modeling soil thermal conductivities over a wide range of conditions, J. Environ. Eng. Sci. 4 (2005) 549–558.
[195] S. Lu, T. Ren, Y. Gong, R. Horton, An improved model for predicting soil thermal conductivity from water content at room temperature, Soil Sci. Soc. Am. J. 71 (2007) 8–14.
[196] S.X. Chen, Thermal conductivity of sands, Heat Mass Transf. 44 (2008) 1241–1246.
[197] H. Nowamooz, S. Nikoosokhan, J. Lin, C. Chazallon, Finite difference modeling of heat distribution in multilayer soils with time-spatial hydrothermal properties, Renew. Energy. 76 (2015) 7–15. https://doi.org/10.1016/j.renene.2014.11.008.
[198] D. a. D. Vries, Thermal Conductivity of Soil, Nature. 178 (1956) 1074–1074. https://doi.org/10.1038/1781074a0.
[199] K.A. Alnefaie, N.H. Abu-Hamdeh, Specific heat and volumetric heat capacity of some saudian soils as affected by moisture and density, in: Int. Conf. Mech. Fluids Heat Elast. Electromagn. Fields, 2013: pp. 139–143.
[200] M.M.U. Rehman, T.A. Cheema, F. Ahmad, M. Khan, A. Abbas, Thermodynamic Assessment of Microchannel Heat Sinks with Novel Sidewall Ribs, J. Thermophys. Heat Transf. 34 (2019) 243–254. https://doi.org/10.2514/1.T5770.
[201] C.A. Angell, W.J. Sichina, M. Oguni, Heat capacity of water at extremes of supercooling and superheating, J. Phys. Chem. 86 (1982) 998–1002.
[202] D.C. Ginnings, G.T. Furukawa, Heat Capacity Standards for the Range 14 to 1200° K., J. Am. Chem. Soc. 75 (1953) 522–527.
[203] T.R. Oke, Boundary layer climates, Routledge, 2002.
[204] M. Aubertin, M. Mbonimpa, B. Bussière, R.P. Chapuis, A model to predict the water retention curve from basic geotechnical properties, Can. Geotech. J. 40 (2003) 1104–1122. https://doi.org/10.1139/t03-054.
[205] R.H. Brooks, A.T. Corey, Properties of Porous Media Affecting Fluid Flow, J. Irrig. Drain. Div. 92 (1966) 61–88. https://doi.org/10.1061/JRCEA4.0000425.
[206] Y. Mualem, Hydraulic Conductivity of Unsaturated Soils: Prediction and Formulas, in: Methods Soil Anal., John Wiley & Sons, Ltd, 1986: pp. 799–823. https://doi.org/10.2136/sssabookser5.1.2ed.c31.
[207] M.V. Villar, A. Lloret, Influence of temperature on the hydro-mechanical behaviour of a compacted bentonite, Appl. Clay Sci. 26 (2004) 337–350. https://doi.org/10.1016/j.clay.2003.12.026.
[208] E. Eyo, S. Abbey, J. Oti, S. Ng'ambi, E. Ganjian, E. Coakley, Microstructure and Physical-Mechanical Characteristics of Treated Kaolin-Bentonite Mixture for

Application in Compacted Liner Systems, Sustainability. 13 (2021) 1617. https://doi.org/10.3390/su13041617.
[209] W. Ye, M. Wan, B. Chen, Y. Chen, Y. Cui, J. Wang, Effect of temperature on soil-water characteristics and hysteresis of compacted Gaomiaozi bentonite, J. Cent. South Univ. Technol. 16 (2009) 821–826. https://doi.org/10.1007/s11771-009-0136-x.
[210] A. Fabbri, L. Soudani, F. McGregor, J.-C. Morel, Analysis of the water absorption test to assess the intrinsic permeability of earthen materials, Constr. Build. Mater. 199 (2019) 154–162. https://doi.org/10.1016/j.conbuildmat.2018.12.014.
[211] M. Villar, Caracterización termo-hidro-mecánica de una bentonita de Cabo de Gata, 2001.
[212] E. Vitale, O. Cuisinier, G. Russo, D. Deneele, D.D. Sarno, M.V. Nicotera, R. Papa, G. Urciuoli, Water retention curves of lightweight cemented soils, E3S Web Conf. 195 (2020) 06004. https://doi.org/10.1051/e3sconf/202019506004.
[213] J. Kestin, M. Sokolov, W.A. Wakeham, Viscosity of liquid water in the range− 8 C to 150 C, J. Phys. Chem. Ref. Data. 7 (1978) 941–948.
[214] R.P. Chapuis, Predicting the saturated hydraulic conductivity of soils: a review, Bull. Eng. Geol. Environ. 71 (2012) 401–434. https://doi.org/10.1007/s10064-012-0418-7.
[215] T.B. Boving, P. Grathwohl, Tracer diffusion coefficients in sedimentary rocks: correlation to porosity and hydraulic conductivity, J. Contam. Hydrol. 53 (2001) 85–100. https://doi.org/10.1016/S0169-7722(01)00138-3.
[216] F. Montes, L. Haselbach, Measuring Hydraulic Conductivity in Pervious Concrete, Environ. Eng. Sci. 23 (2006) 960–969. https://doi.org/10.1089/ees.2006.23.960.
[217] A. Abbas, M. Carcasses, J.-P. Ollivier, Gas permeability of concrete in relation to its degree of saturation, Mater. Struct. 32 (1999) 3–8. https://doi.org/10.1007/BF02480405.
[218] A. Timur, An investigation of permeability, porosity, and residual water saturation relationships, in: SPWLA 9th Annu. Logging Symp., OnePetro, 1968.
[219] R.J. Millington, J.P. Quirk, Permeability of Porous Media, Nature. 183 (1959) 387–388. https://doi.org/10.1038/183387a0.
[220] M.D. Jackson, P.H. Valvatne, M.J. Blunt, Prediction of Wettability Variation Within an Oil/Water Transition Zone and Its Impact on Production, SPE J. 10 (2005) 185–195. https://doi.org/10.2118/77543-PA.
[221] S. Berg, M. Rücker, H. Ott, A. Georgiadis, H. van der Linde, F. Enzmann, M. Kersten, R.T. Armstrong, S. de With, J. Becker, A. Wiegmann, Connected pathway relative permeability from pore-scale imaging of imbibition, Adv. Water Resour. 90 (2016) 24–35. https://doi.org/10.1016/j.advwatres.2016.01.010.
[222] M.P. Anderson, W.W. Woessner, CHAPTER 12 - ADVANCED TOPICS, in: M.P. Anderson, W.W. Woessner (Eds.), Appl. Groundw. Model., Academic Press, San Diego, 2002: pp. 316–341. https://doi.org/10.1016/B978-0-08-088694-7.50017-1.
[223] U. Fischer, M.A. Celia, Prediction of relative and absolute permeabilities for gas and water from soil water retention curves using a pore-scale network model, Water Resour. Res. 35 (1999) 1089–1100. https://doi.org/10.1029/1998WR900048.
[224] Y. Mualem, A new model for predicting the hydraulic conductivity of unsaturated porous media, Water Resour. Res. 12 (1976) 513–522. https://doi.org/10.1029/WR012i003p00513.
[225] L.J. Klinkenberg, The permeability of porous media to liquids and gases, Am Pet. Inst Drill. Prod. Pract. 2 (1941) 200–213.
[226] W. Tanikawa, T. Shimamoto, Comparison of Klinkenberg-corrected gas permeability and water permeability in sedimentary rocks, Int. J. Rock Mech. Min. Sci. 46 (2009) 229–238. https://doi.org/10.1016/j.ijrmms.2008.03.004.

[227] K. Li, M. Stroeven, P. Stroeven, L.J. Sluys, Investigation of liquid water and gas permeability of partially saturated cement paste by DEM approach, Cem. Concr. Res. 83 (2016) 104–113. https://doi.org/10.1016/j.cemconres.2016.02.002.
[228] A. Fabbri, N. Al Haffar, F. McGregor, Measurement of the relative air permeability of compacted earth in the hygroscopic regime of saturation, Comptes Rendus Mécanique. 347 (2019) 912–919. https://doi.org/10.1016/j.crme.2019.11.017.
[229] H.F. Taylor, Chemistry of cements, (1966).
[230] M. Fall, D. Adrien, J.C. Célestin, M. Pokharel, M. Touré, Saturated hydraulic conductivity of cemented paste backfill, Miner. Eng. 22 (2009) 1307–1317. https://doi.org/10.1016/j.mineng.2009.08.002.
[231] Z. Lafhaj, M. Goueygou, A. Djerbi, M. Kaczmarek, Correlation between porosity, permeability and ultrasonic parameters of mortar with variable water/cement ratio and water content, Cem. Concr. Res. 36 (2006) 625–633. https://doi.org/10.1016/j.cemconres.2005.11.009.
[232] J.W. Figg, Methods of measuring the air and water permeability of concrete, Mag. Concr. Res. 25 (1973) 213–219. https://doi.org/10.1680/macr.1973.25.85.213.
[233] D.P. Bentz, P.-C. Aitcin, The Hidden Meaning of Water-Cement Ratio, Concr. Int. 30 (2008) 51–54. https://www.concrete.org/publications/internationalconcreteabstractsportal/m/details/id/19782 (accessed August 4, 2022).
[234] P.F. Hansen, E.J. Pedersen, MATURITY COMPUTER FOR CONTROLLED CURING AND HARDENING OF CONCRETE, Nord. Betong. (1977). https://trid.trb.org/view/58993 (accessed April 2, 2022).
[235] K.O. Kjellsen, R.J. Detwiler, O.E. Gjørv, Development of microstructures in plain cement pastes hydrated at different temperatures, Cem. Concr. Res. 21 (1991) 179–189. https://doi.org/10.1016/0008-8846(91)90044-I.
[236] R.H. Mills, FACTORS INFLUENCING CESSATION OF HYDRATION IN WATER CURED CEMENT PASTES, Highw. Res. Board Spec. Rep. (1966). https://trid.trb.org/view/101449 (accessed April 2, 2022).
[237] G. De Schutter, Hydration and temperature development of concrete made with blast-furnace slag cement, Cem. Concr. Res. 29 (1999) 143–149. https://doi.org/10.1016/S0008-8846(98)00229-4.
[238] A.K. Schindler, K.J. Folliard, Influence of supplementary cementing materials on the heat of hydration of concrete, in: Adv. Cem. Concr. IX Conf. Copp. Mt. Conf. Resort Colo., 2003.
[239] B. Sun, T. Noguchi, G. Cai, W. Zhao, Effect of temperature and relative humidity on the development of the compressive strength of surface-layer cement mortar, Constr. Build. Mater. 281 (2021) 122626. https://doi.org/10.1016/j.conbuildmat.2021.122626.
[240] T.C. Powers, T.L. Brownyard, Studies of the Physical Properties of Hardened Portland Cement Paste, J. Proc. 43 (1946) 101–132. https://doi.org/10.14359/8745.
[241] T.C. Powers, Structure and Physical Properties of Hardened Portland Cement Paste, J. Am. Ceram. Soc. 41 (1958) 1–6. https://doi.org/10.1111/j.1151-2916.1958.tb13494.x.
[242] T.C. Hansen, Physical structure of hardened cement paste. A classical approach, Mater. Struct. 19 (1986) 423–436. https://doi.org/10.1007/BF02472146.
[243] F.M. Lea, THE CHEMISTRY OF CEMENT AND CONCRETE. THIRD EDITION, (1970). https://trid.trb.org/view.aspx?id=94833 (accessed April 24, 2022).
[244] H.J.H. Brouwers, The work of Powers and Brownyard revisited: Part 1, Cem. Concr. Res. 34 (2004) 1697–1716. https://doi.org/10.1016/j.cemconres.2004.05.031.
[245] H.J.H. Brouwers, The work of Powers and Brownyard revisited: Part 2, Cem. Concr. Res. 35 (2005) 1922–1936. https://doi.org/10.1016/j.cemconres.2005.04.009.

[246] W. Wagner, H.-J. Kretzschmar, eds., IAPWS Industrial Formulation 1997 for the Thermodynamic Properties of Water and Steam, in: Int. Steam Tables Prop. Water Steam Based Ind. Formul. IAPWS-IF97, Springer, Berlin, Heidelberg, 2008: pp. 7–150. https://doi.org/10.1007/978-3-540-74234-0_3.
[247] A. c. Jacinto, M. v. Villar, A. Ledesma, Influence of water density on the water-retention curve of expansive clays, Géotechnique. 62 (2012) 657–667. https://doi.org/10.1680/geot.7.00127.
[248] R.A. Freeze, Three-dimensional, transient, saturated-unsaturated flow in a groundwater basin, Water Resour. Res. 7 (1971) 347–366.
[249] J. Bear, Dynamics of fluids in porous media, Courier Corporation, 2013.
[250] P. Ben Ishai, E. Mamontov, J.D. Nickels, A.P. Sokolov, Influence of Ions on Water Diffusion—A Neutron Scattering Study, J. Phys. Chem. B. 117 (2013) 7724–7728. https://doi.org/10.1021/jp4030415.
[251] S. Horpibulsuk, Strength and Microstructure of Cement Stabilized Clay, IntechOpen, 2012. https://doi.org/10.5772/35225.
[252] G. Spagnoli, S. Shimobe, An overview on the compaction characteristics of soils by laboratory tests, Eng. Geol. 278 (2020) 105830. https://doi.org/10.1016/j.enggeo.2020.105830.
[253] A.W. Adamson, A.P. Gast, Physical chemistry of surfaces, Interscience publishers New York, 1967.
[254] H. Darcy, Recherches expérimentales relatives au mouvement de l'eau dans les tuyaux, Mallet - Bachelier, 1857. https://books.google.fr/books?id=BaQ_AAAAcAAJ.
[255] J.R. Cooper, R.B. Dooley, Release of the IAPWS formulation 2008 for the viscosity of ordinary water substance, Int. Assoc. Prop. Water Steam. (2008).
[256] D.W. Taylor, Fundamentals of Soil Mechanics, Soil Sci. 66 (1948) 161. https://journals.lww.com/soilsci/Citation/1948/08000/Fundamentals_of_Soil_Mechanics.8.aspx (accessed February 16, 2021).
[257] P.C. Carman, Fluid flow through granular beds, Chem. Eng. Res. Des. 75 (1997) S32–S48. https://doi.org/10.1016/S0263-8762(97)80003-2.
[258] R.A. dos Santos, E.R. Esquivel, Saturated anisotropic hydraulic conductivity of a compacted lateritic soil, J. Rock Mech. Geotech. Eng. 10 (2018) 986–991. https://doi.org/10.1016/j.jrmge.2018.04.005.
[259] F. Tang, H. Nowamooz, Outlet temperatures of a slinky-type Horizontal Ground Heat Exchanger with the atmosphere-soil interaction, Renew. Energy. 146 (2020) 705–718. https://doi.org/10.1016/j.renene.2019.07.029.
[260] X. Zhang, H. Nowamooz, Effect of rising damp in unstabilized rammed earth (URE) walls, Constr. Build. Mater. 307 (2021) 124989. https://doi.org/10.1016/j.conbuildmat.2021.124989.
[261] E. Romero, J. Vaunat, Retention curves of deformable clays, Exp. Evid. Theor. Approaches Unsaturated Soils. 91 (2000) 106.
[262] E.U. Eyo, S. Ng'ambi, S.J. Abbey, An overview of soil–water characteristic curves of stabilised soils and their influential factors, J. King Saud Univ. - Eng. Sci. 34 (2022) 31–45. https://doi.org/10.1016/j.jksues.2020.07.013.
[263] P.T. Tsilingiris, Thermophysical and transport properties of humid air at temperature range between 0 and 100°C, Energy Convers. Manag. 49 (2008) 1098–1110. https://doi.org/10.1016/j.enconman.2007.09.015.
[264] M. Hall, D. Allinson, Assessing the effects of soil grading on the moisture content-dependent thermal conductivity of stabilised rammed earth materials, Appl. Therm. Eng. 29 (2009) 740–747. https://doi.org/10.1016/j.applthermaleng.2008.03.051.

[265] V. Toufigh, E. Kianfar, The effects of stabilizers on the thermal and the mechanical properties of rammed earth at various humidities and their environmental impacts, Constr. Build. Mater. 200 (2019) 616–629. https://doi.org/10.1016/j.conbuildmat.2018.12.050.
[266] M.J. Abdolhosseini Qomi, F.-J. Ulm, R.J.-M. Pellenq, Physical Origins of Thermal Properties of Cement Paste, Phys. Rev. Appl. 3 (2015) 064010. https://doi.org/10.1103/PhysRevApplied.3.064010.
[267] D.P. Bentz, A review of early-age properties of cement-based materials, Cem. Concr. Res. 38 (2008) 196–204. https://doi.org/10.1016/j.cemconres.2007.09.005.
[268] P. Nshimiyimana, S. Omar Sore, C. Hema, O. Zoungrana, A. Messan, L. Courard, A discussion of "optimisation of compressed earth blocks (CEBs) using natural origin materials: A systematic literature review," Constr. Build. Mater. 325 (2022) 126887. https://doi.org/10.1016/j.conbuildmat.2022.126887.
[269] Underground excavations in rock: Hoek, E; Brown, E T London: Institution of Mining and Metallurgy, 1980, 527P, Int. J. Rock Mech. Min. Sci. Geomech. Abstr. 18 (1981) 27. https://doi.org/10.1016/0148-9062(81)90809-3.
[270] P. Jing, X. Song, J. Zhang, H. Nowamooz, A review of hydro-mechanical coupling behaviour of cement-treated materials, Constr. Build. Mater. 322 (2022) 126446. https://doi.org/10.1016/j.conbuildmat.2022.126446.
[271] H. Ahmadi Moghadam, A. Mirzaei, Z. Abedi Dehghi, The relation between porosity, hydration degree and compressive strength of Portland cement pastes in the presence of aluminum chloride additive, Constr. Build. Mater. 250 (2020) 118884. https://doi.org/10.1016/j.conbuildmat.2020.118884.
[272] A.M. Soliman, M.L. Nehdi, Self-Accelerated Reactive Powder Concrete Using Partially Hydrated Cementitious Materials, ACI Mater. J. 108 (2011). https://trid.trb.org/view/1126681 (accessed May 7, 2022).
[273] Y. Pan, A. Prado, R. Porras, O.M. Hafez, J.E. Bolander, Lattice Modeling of Early-Age Behavior of Structural Concrete, Materials. 10 (2017) 231. https://doi.org/10.3390/ma10030231.
[274] F.-H. Lee, Y. Lee, S.-H. Chew, K.-Y. Yong, Strength and Modulus of Marine Clay-Cement Mixes, J. Geotech. Geoenvironmental Eng. 131 (2005) 178–186. https://doi.org/10.1061/(ASCE)1090-0241(2005)131:2(178).
[275] G. De Schutter, L. Taerwe, Degree of hydration-based description of mechanical properties of early age concrete, Mater. Struct. 29 (1996) 335. https://doi.org/10.1007/BF02486341.
[276] D.P. Bentz, Three-dimensional computer simulation of Portland cement hydration and microstructure development, J Am Ceram Soc. 80 (1997) 3–21.
[277] A. Fahimifar, H. Soroush, A Moisture Index Classification System for Rocks (MiC System), Rock Mech. Rock Eng. 40 (2007) 63–79. https://doi.org/10.1007/s00603-005-0079-y.
[278] S.M. Davarpanah, M. Sharghi, A. Tarifard, Á. Török, B. Vásárhelyi, Studies on the Mechanical Properties of Dry, Saturated, and Frozen Marls Using Destructive and Non-destructive Laboratory Approaches, Iran. J. Sci. Technol. Trans. Civ. Eng. 46 (2022) 1311–1328. https://doi.org/10.1007/s40996-021-00690-z.
[279] Á. Török, B. Vásárhelyi, The influence of fabric and water content on selected rock mechanical parameters of travertine, examples from Hungary, Eng. Geol. 115 (2010) 237–245. https://doi.org/10.1016/j.enggeo.2010.01.005.
[280] M.I. Smorodinov, Determinations of correlation relationships between strength and some physical characteristics of rocks, in: Proc 1st Int Congr. ISRM Lisvbon, 1966.

[281] G.A. Rao, Generalization of Abrams' law for cement mortars, Cem. Concr. Res. 31 (2001) 495–502. https://doi.org/10.1016/S0008-8846(00)00473-7.
[282] A. Kargari, H. Eskandari-Naddaf, R. Kazemi, Effect of cement strength class on the generalization of Abrams' law, Struct. Concr. 20 (2019) 493–505. https://doi.org/10.1002/suco.201700275.
[283] G.H. Nalon, R.O.G. Martins, R. de C.S.S. Alvarenga, G.E.S. de Lima, L.G. Pedroti, W.J. dos Santos, Effect of Specimens' Shape and Size on the Determination of Compressive Strength and Deformability of Cement-lime Mortars, Mater. Res. 20 (2018) 819–825. https://doi.org/10.1590/1980-5373-MR-2016-1006.
[284] J. De Brito, R. Kurda, P. Raposeiro da Silva, Can We Truly Predict the Compressive Strength of Concrete without Knowing the Properties of Aggregates?, Appl. Sci. 8 (2018) 1095. https://doi.org/10.3390/app8071095.
[285] L.F. Nielsen, Strength development in hardened cement paste: examination of some empirical equations, Mater. Struct. 26 (1993) 255–260. https://doi.org/10.1007/BF02472946.
[286] J. Bolomey, Determination de la résistance à la compression des mortiers et bétons, F. Rouge & Company, 1925.
[287] S. Kumar Thota, T. Duc Cao, F. Vahedifard, Poisson's Ratio Characteristic Curve of Unsaturated Soils, J. Geotech. Geoenvironmental Eng. 147 (2021) 04020149. https://doi.org/10.1061/(ASCE)GT.1943-5606.0002424.
[288] T.-K. Kim, S.-J. Choi, J.-H.J. Kim, B.-Y. Kim, Performance Based Evaluation of Concrete Strength under Various Curing Conditions to Investigate Climate Change Effects, Sustainability. 7 (2015) 10052–10077. https://doi.org/10.3390/su70810052.
[289] F. Tong, L. Jing, R.W. Zimmerman, A fully coupled thermo-hydro-mechanical model for simulating multiphase flow, deformation and heat transfer in buffer material and rock masses, Int. J. Rock Mech. Min. Sci. 47 (2010) 205–217. https://doi.org/10.1016/j.ijrmms.2009.11.002.
[290] Y. Cui, Soil–atmosphere interaction in earth structures, J. Rock Mech. Geotech. Eng. 14 (2022) 35–49. https://doi.org/10.1016/j.jrmge.2021.11.004.
[291] T. Poós, E. Varju, Mass transfer coefficient for water evaporation by theoretical and empirical correlations, Int. J. Heat Mass Transf. 153 (2020) 119500. https://doi.org/10.1016/j.ijheatmasstransfer.2020.119500.
[292] Estado del arte y tendencias de la tecnología eoloeléctrica, UNAM, Programa Universitario de Energía, 1998.
[293] G.M. Masters, M.G. M, Renewable and Efficient Electric Power Systems, John Wiley & Sons, 2004.
[294] R.C. Bansal, T.S. Bhatti, D.P. Kothari, On some of the design aspects of wind energy conversion systems, Energy Convers. Manag. 43 (2002) 2175–2187.
[295] F. Bañuelos-Ruedas, C. Angeles-Camacho, S. Rios-Marcuello, Methodologies Used in the Extrapolation of Wind Speed Data at Different Heights and Its Impact in the Wind Energy Resource Assessment in a Region, Wind Farm - Tech. Regul. Potential Estim. Siting Assess. (2011). https://doi.org/10.5772/20669.
[296] H. Saito, J. Šimůnek, B.P. Mohanty, Numerical Analysis of Coupled Water, Vapor, and Heat Transport in the Vadose Zone, Vadose Zone J. 5 (2006) 784–800. https://doi.org/10.2136/vzj2006.0007.
[297] F. Heymes, L. Aprin, A. Bony, S. Forestier, S. Cirocchi, G. Dusserre, An experimental investigation of evaporation rates for different volatile organic compounds, Process Saf. Prog. 32 (2013) 193–198. https://doi.org/10.1002/prs.11566.

[298] F. Tang, H. Nowamooz, Long-term performance of a shallow borehole heat exchanger installed in a geothermal field of Alsace region, Renew. Energy. 128 (2018) 210–222. https://doi.org/10.1016/j.renene.2018.05.073.
[299] H. Assadollahi, H. Nowamooz, Long-term analysis of the shrinkage and swelling of clayey soils in a climate change context by numerical modelling and field monitoring, Comput. Geotech. 127 (2020) 103763. https://doi.org/10.1016/j.compgeo.2020.103763.
[300] S. Kumar, J. Mathur, S. Mathur, M.K. Singh, V. Loftness, An adaptive approach to define thermal comfort zones on psychrometric chart for naturally ventilated buildings in composite climate of India, Build. Environ. 109 (2016) 135–153. https://doi.org/10.1016/j.buildenv.2016.09.023.
[301] J.L. Nguyen, J. Schwartz, D.W. Dockery, The relationship between indoor and outdoor temperature, apparent temperature, relative humidity, and absolute humidity, Indoor Air. 24 (2014) 103–112. https://doi.org/10.1111/ina.12052.
[302] H. Nowak, Modelling of the longwave radiation incident upon a building, Arch. Civ. Eng. 47 (2001) 243–267.
[303] J. Monteith, M. Unsworth, Principles of Environmental Physics: Plants, Animals, and the Atmosphere, Academic Press, 2013.
[304] R.J. Cole, The longwave radiation incident upon inclined surfaces, Sol. Energy. 22 (1979) 459–462.
[305] D.F. Post, A. Fimbres, A.D. Matthias, E.E. Sano, L. Accioly, A.K. Batchily, L.G. Ferreira, Predicting Soil Albedo from Soil Color and Spectral Reflectance Data, Soil Sci. Soc. Am. J. 64 (2000) 1027–1034. https://doi.org/10.2136/sssaj2000.6431027x.
[306] L. Zhang, N. Zhang, F. Zhao, Y. Chen, A genetic-algorithm-based experimental technique for determining heat transfer coefficient of exterior wall surface, Appl. Therm. Eng. 24 (2004) 339–349. https://doi.org/10.1016/j.applthermaleng.2003.07.005.
[307] S.A. Wade, A.K. Schindler, R.W. Barnes, J.M. Nixon, Evaluation of the Maturity Method to Estimate Concrete Strength, (n.d.) 307.
[308] W. Saengsoy, Effect of curing conditions on hydration reaction and compressive strength development of Fly Ash-cement pastes, Div. Solid Waste Resour. Geoenvironmental Eng. Hokkaido Univ. Http13387. 123 (2008) e3.
[309] J.L. Poole, K.A. Riding, K.J. Folliard, M.C.G. Juenger, A.K. Schindler, Methods for Calculating Activation Energy for Portland Cement, Mater. J. 104 (2007) 303–311. https://doi.org/10.14359/18499.
[310] H. Awang, M.H. Ahmad, M.Z. Al-Mulali, Influence of kenaf and polypropylene fibres on mechanical and durability properties of fibre reinforced lightweight foamed concrete, J. Eng. Sci. Technol. 10 (2015) 496–508.
[311] S.-T. Lee, D.-W. Park, K.-Y. Ann, Mitigating effect of chloride ions on sulfate attack of cement mortars with or without silica fume, Can. J. Civ. Eng. 35 (2008) 1210–1220. https://doi.org/10.1139/L08-065.
[312] K. Sobolev, M. Moini, S. Muzenski, R. Pradoto, M. Kozhukhova, I. Flores-Vivian, S. Cramer, L. Pham, A. Faheem, Laboratory Study of Optimized Concrete Pavement Mixtures, Wisconsin Highway Research Program Madison, WI, USA, 2015.
[313] S. Yuan, J. Du, Effective stress-based upper bound limit analysis of unsaturated soils using the weak form quadrature element method, Comput. Geotech. 98 (2018) 172–180. https://doi.org/10.1016/j.compgeo.2018.02.008.
[314] N. An, S. Hemmati, Y. Cui, C. Maisonnave, I. Charles, C. Tang, Numerical analysis of hydro-thermal behaviour of Rouen embankment under climate effect, Comput. Geotech. 99 (2018) 137–148. https://doi.org/10.1016/j.compgeo.2018.03.008.

[315] C. Liang, M.B. Jaksa, B. Ostendorf, Y.L. Kuo, Influence of river level fluctuations and climate on riverbank stability, Comput. Geotech. 63 (2015) 83–98. https://doi.org/10.1016/j.compgeo.2014.08.012.
[316] J. Zhang, D.N. Little, N. Hariharan, Y.-R. Kim, Prediction of climate specific vertical movement of pavements with expansive soils based on long-term 2D numerical simulation of rainwater infiltration, Comput. Geotech. 115 (2019) 103172. https://doi.org/10.1016/j.compgeo.2019.103172.
[317] D. Wu, Y. Zhang, R. Zhao, T. Deng, Z. Zheng, A coupled thermal-hydraulic-mechanical application for subway tunnel, Comput. Geotech. 84 (2017) 174–182. https://doi.org/10.1016/j.compgeo.2016.12.006.
[318] H. Assadollahi Tejaragh, The impact of climatic events and drought on the shrinkage and swelling phenomenon of clayey soils interacting with constructions, Theses, Université de Strasbourg, 2019. https://tel.archives-ouvertes.fr/tel-02331567 (accessed September 20, 2020).
[319] E. Franzoni, State-of-the-art on methods for reducing rising damp in masonry, J. Cult. Herit. 31 (2018) S3–S9. https://doi.org/10.1016/j.culher.2018.04.001.
[320] E. Franzoni, Rising damp removal from historical masonries: A still open challenge, Constr. Build. Mater. 54 (2014) 123–136. https://doi.org/10.1016/j.conbuildmat.2013.12.054.
[321] I. Torres, New technique for treating rising damp in historical buildings: Wall base ventilation, J. Cult. Herit. 31 (2018) S60–S70. https://doi.org/10.1016/j.culher.2018.04.015.
[322] J.E. Aubert, A. Fabbri, J.C. Morel, P. Maillard, An earth block with a compressive strength higher than 45MPa!, Constr. Build. Mater. 47 (2013) 366–369. https://doi.org/10.1016/j.conbuildmat.2013.05.068.
[323] Z. Long, H. Li, X. Bu, W. Ma, L. Zhao, Solar radiation on vertical surfaces for building application in different climate zones across China, J. Renew. Sustain. Energy. 5 (2013) 021418. https://doi.org/10.1063/1.4798492.
[324] Y. Li, Z. Kong, H. Xie, Y. Ma, B. Mu, S. Hokoi, Construction type influences features of rising damp of blue-brick masonry walls, Constr. Build. Mater. 284 (2021) 122791. https://doi.org/10.1016/j.conbuildmat.2021.122791.
[325] E. Rirsch, Z. Zhang, Rising damp in masonry walls and the importance of mortar properties, Constr. Build. Mater. 24 (2010) 1815–1820. https://doi.org/10.1016/j.conbuildmat.2010.04.024.
[326] R. El Nabouch, Mechanical behavior of rammed earth walls under Pushover tests, Theses, Université Grenoble Alpes, 2017. https://tel.archives-ouvertes.fr/tel-01707009 (accessed September 20, 2020).
[327] D. Ciancio, C. Augarde, Capacity of unreinforced rammed earth walls subject to lateral wind force: elastic analysis versus ultimate strength analysis, Mater. Struct. 46 (2013) 1569–1585. https://doi.org/10.1617/s11527-012-9998-8.
[328] A. Arrigoni, R. Pelosato, G. Dotelli, C.T.S. Beckett, D. Ciancio, Weathering's beneficial effect on waste-stabilised rammed earth: a chemical and microstructural investigation, Constr. Build. Mater. 140 (2017) 157–166. https://doi.org/10.1016/j.conbuildmat.2017.02.009.

Résumé de la thèse intitulée : Modélisation de couplage chemo-thermo-hydro-mécanique (CTHM) dans les structures en pisé

Pour décrire et prévoir globalement le comportement chemo-thermo-hydro-mécanique (CTHM) d'un mur typique en pisé dans des conditions in-situ, les auteurs effectuent cette étude sur les caractéristiques fondamentales du pisé stabilisé au ciment (CSRE) et du pisé non stabilisé (URE).

Dans un premier temps, la technique de construction en pisé non stabilisé (URE), et en pisé stabilisé au ciment (CSRE) est présentée. Pour comprendre leurs propriétés fondamentales, ainsi que la distinction entre les matériaux étudiés, une revue de la littérature concernant le comportement thermo-hydro-mécaniques de l'URE est ensuite menée. Puisque les CSRE sont produits à partir des URE, les comportements chemo-thermo-hydro-mécaniques des CSRE sont étudiés par la suite.

Il a été constaté que, pour les différents matériaux (URE ou CSRE), la conductivité thermique augmente avec la densité sèche et la teneur en eau ; la capacité thermique spécifique du CSRE (URE) n'est pas influencée par la densité sèche du matériau ; la perméabilité à l'eau intrinsèque diminue avec la densité sèche et augmente avec la teneur en eau ; la capacité de rétention augmente lorsque la teneur en fines augmente ; la résistance à la compression non confinée augmente d'abord lentement puis rapidement avec la densité sèche du matériau ; le module d'élasticité à la rupture diminue sur le chemin de mouillage et augmente sur le chemin de séchage ; la diminution de la teneur en eau et l'augmentation de la teneur en fines améliorent la résistance à la compression et la résistance à la traction ; la résistance à la traction est fréquemment estimée par les chercheurs à partir de la résistance à la compression ; le coefficient de Poisson augmente avec la teneur en eau. Pour les matériaux CSRE, l'effet de l'hydratation du ciment sur les fluctuations de la courbe de rétention d'eau du sol (échelle de saturation-suction) et de la conductivité thermique est insignifiant. Le processus d'hydratation consomme de l'eau libre sous forme d'eau ayant réagi chimiquement et d'eau chimisorbée. En outre,

l'hydratation du ciment augmente la résistance mécanique du CSRE au fil du temps, et cette résistance est affectée par les conditions de durcissement. La croissance de la résistance est facilitée par une augmentation de la température et de l'humidité et limitée par une baisse de la température et de l'humidité.

La recherche documentaire révèle que les propriétés de l'URE et du CSRE varient grandement en fonction des résultats expérimentaux obtenus dans la littérature, et l'absence d'une perspective globale sur tous les types de matériaux URE et CSRE empêche le développement d'une norme mondialement reconnue pour les matériaux URE et CSRE. En plus, il a été découvert que le type de matériau, la méthode de production et l'interaction entre les matériaux et l'environnement ont un impact substantiel sur le comportement chemo-thermo-hydro-mécanique (CTHM) à long terme de l'URE et du CSRE. Un modèle capable de décrire et de prévoir ce comportement en fonction du temps de tous les types de matériaux URE et CSRE d'un point de vue global est d'une importance essentielle pour l'application de ces matériaux et le développement de normes industrielles.

Ensuite, un modèle par éléments finis est proposé pour estimer les caractéristiques CTHM à long terme de divers matériaux URE et CSRE. Une revue systématique de la littérature a permis de découvrir que les caractéristiques de ces matériaux (CSRE ou URE) varient considérablement d'une étude expérimentale à l'autre, ce qui rend leur application dans les conditions in situ plus difficile. L'absence d'une perspective mondiale sur tous les types de matériaux (CSRE ou URE) entrave la création d'une norme mondialement acceptée pour les matériaux (CSRE ou URE). Par conséquent, pour estimer globalement le comportement CTHM à long terme de différents matériaux (CSRE ou URE), leurs caractéristiques doivent être prédites dès la phase de conception.

Par conséquent, un nouveau cadre d'éléments finis applicable aux matériaux URE et CSRE en considérant les effets combinés de la teneur en eau initiale, de la densité sèche initiale, de la distribution granulométrique initiale, de la teneur en ciment initiale, des

conditions de cure et de la durée de la cure est proposé pour expliquer le comportement CTHM liés à ces matériaux. La méthode numérique se compose principalement de quatre parties, à savoir l'hydratation du ciment, le flux d'eau non saturée, le transfert de chaleur et les réponses mécaniques. En appliquant des conditions aux limites appropriées, la méthode proposée devrait être capable d'estimer les propriétés CTHM dépendantes du temps du CSRE (URE) dans les conditions de laboratoire et in-situ. Ensuite, la méthode proposée est utilisée pour prédire certaines caractéristiques du CSRE (URE) rapportées dans la littérature, et les prédictions sont comparées aux résultats expérimentaux.

Ensuite, un certain nombre de données expérimentales pour les matériaux URE et CSRE sont utilisées pour valider le cadre théorique, établi dans cette étude. Les résultats expérimentaux étudiés, notamment le processus de séchage, le transfert de chaleur et d'humidité relative, la résistance à la compression, la résistance à la traction, la relation contrainte-déformation, le processus d'hydratation du ciment, les effets du rapport eau-ciment, etc. sont comparés aux prédictions numériques. Les comparaisons montrent une bonne capacité du modèle proposé à expliquer les propriétés CTHM en fonction du temps des matériaux (CSRE ou URE) dans des conditions de laboratoire. Ensuite, le cadre numérique proposé est utilisé et étendu pour estimer les caractéristiques de murs typiques (en CSRE ou URE) dans des conditions in-situ, et les simulations numériques associées sont présentées dans le chapitre suivant.

Enfin, le modèle numérique proposé est utilisé pour étudier le comportement structurel des constructions (CSRE ou URE) à l’in situ. Dans un premier temps, le comportement structurel à long terme des murs URE sont étudiés en comparant les effets de différentes conditions environnementales sur les murs. Les résultats de la simulation révèlent que la distribution de la taille des grains du sol a un effet plus important sur les caractéristiques THM du mur que l'environnement local. De plus, la majorité du processus de séchage a lieu au cours de la première année après la construction. Par la suite, outre les effets de l'environnement, les effets de l'humidité ascendante provenant du sol sont également inclus pour mieux comprendre les caractéristiques à long terme des murs URE sans la

protection du sous-sol. Les résultats de la simulation montrent que le temps a un effet positif sur les caractéristiques THM d'un mur URE, puisque le processus d'évaporation réduit l'humidité du mur et augmente son isolation thermique et sa résistance mécanique. Au contraire, l'humidité ascendante réduit la résistance thermique des murs et augmente leur résistance à la vapeur, rendant la structure URE moins habitable. Enfin, les caractéristiques à long terme d'un mur en CSRE sous les interactions de l'environnement et du sol souterrain sont étudiées. Il a été observé que le ciment n'est pas complètement hydraté même après cinq ans de cure. Au cours de la première année après la construction, le degré d'hydratation du ciment est plus élevé au côté intérieur du mur par rapport aux parties de l'extérieur et sous le sol en raison de la température intérieure plus élevée. La résistance à la compression du mur est principalement contrôlée par l'hydratation du ciment à un âge précoce, mais elle est également influencée par l'humidité de l'environnement et du sol souterrain. La partie supérieure du mur perd sa résistance plus tard que la partie inférieure, car l'eau met plus de temps à passer dans cette partie supérieure. Cet effet de retard est dissipé à la surface du mur grâce à un contact suffisant avec l'air. En raison du manque d'eau sur la face supérieure du mur, le processus d'hydratation dans cette région est principalement régi par la température.

Les auteurs espèrent que cette étude numérique est complémentaire aux études expérimentales. Ils souhaitent aussi que cette étude sera utile pour le développement des normes de construction en CSRE ou URE.

Xiang ZHANG

Modélisation de couplage chemo-thermo-hydro-mécanique (CTHM) dans les structures en pisé

Résumé

Le pisé est une technique de construction ancienne que l'on retrouve sur de nombreux sites patrimoniaux à travers le monde. Ce matériau est compacté avec le sol à l'aide d'un système de compactage pneumatique ou manuel dans un coffrage. Ces dernières années, on a assisté à une renaissance de l'intérêt pour les matériaux en terre, alimentée par des préoccupations environnementales croissantes. Ce matériau est aujourd'hui reconnu comme un matériau de construction moderne. Les RE consistent en un mélange d'argile, de limon, de sable, de gravier et parfois de cailloux de quelques millimètres de diamètre. Lorsque l'argile est le seul liant, le matériau est appelé pisé non stabilisé (URE) ; lorsque le ciment est utilisé pour améliorer les qualités des pisés, telles que la résistance ou la durabilité, le matériau est appelé le pisé stabilisé au ciment (CSRE). Dans cette étude, l'URE est traitée comme un cas particulier de CSRE avec une teneur en ciment de 0%.

L'objectif de cette étude est de décrire globalement et de prévoir les comportements généraux chemo-thermo-hydro-mécaniques (CTHM) d'un mur CSRE (URE) typique dans les conditions in-situ.

Les auteurs ont effectué une revue de la littérature afin d'acquérir une compréhension complète des caractéristiques techniques fondamentales des CSRE (URE) et des facteurs influençant les propriétés des matériaux étudiés. Sur une étude approfondie de la littérature, il a été constaté que les caractéristiques des matériaux CSRE (URE) varient considérablement par rapport ces études expérimentales, ce qui rend leur application dans

des conditions in situ plus difficile. L'absence d'une perspective globale sur toutes sortes de matériaux CSRE (URE) empêche le développement d'une norme internationalement reconnue pour les matériaux CSRE (URE). Par conséquent, pour estimer le comportement CTHM à long terme des matériaux CSRE (URE), les effets combinés de la teneur en eau initiale, de la densité sèche initiale, de la distribution de pores initiale, de la teneur en ciment initiale, des conditions de durcissement et de la durée de durcissement doivent être évalués simultanément tout au long de la phase de conception.

Par conséquent, dans cette étude, un cadre numérique basé sur la méthode d'éléments finis applicable aux matériaux URE et CSRE est proposé pour expliquer les comportements CTHM liés de ces matériaux. Pour valider le cadre théorique proposé, plusieurs résultats expérimentaux pour les matériaux URE et CSRE issus de la littérature existante sont recréés et comparés aux résultats expérimentaux.

Le modèle numérique proposé est ensuite étendu pour étudier les comportements structurels des constructions CSRE (URE) dans des conditions in-situ. Les comportements structurels à long terme des murs URE sont d'abord étudiés en considérant les effets de différentes conditions climatiques sur les murs. Ensuite, les effets de l'humidité ascendante provenant du sol sont également étudiés pour les caractéristiques à long terme des murs URE. Enfin, les caractéristiques CTHM à long terme du mur CSRE sous les interactions de l'environnement et du sol souterrain sont étudiées.

Mots clés : Pisé non stabilisé (URE) ; Pisé stabilisé au ciment (CSRE) ; Couplage chimico-thermo-hydro-mécanique (CTHM) ; Effets climatiques ; Remontée d'humidité ; Flux d'eau ; Résistance thermique ; Résistance à la compression ; Simulations numériques.

Xiang ZHANG

Modeling the chemo-thermo-hydro-mechanical coupling (CTHM) of rammed earth structures

Abstract

Rammed earth (RE) is an ancient building technique that may be found at numerous heritage sites across the world. This material is compacted with the soil using a pneumatic or manual rammer in a formwork. In recent years, there has been a renaissance of interest in earth materials, fueled by rising environmental concerns. This material is today recognized as a modern construction material that can make aesthetically pleasing and comfortable structures. RE raw materials consist of a mixture of clay, silt, sand, gravel, and occasionally pebbles measuring a few millimeters in diameter. When clay is the only binder, the material is referred to as unstabilized rammed earth (URE); when cement is used to improve RE qualities, such as strength or durability, the material is referred to as cement stabilized rammed earth (CSRE). In this study, URE is treated as a special instance of CSRE with 0% cement content.

The objective of this study is to globally describe and forecast the general chemo-thermo-hydro-mechanical (CTHM) behaviors of a typical CSRE (URE) wall under in-situ conditions.

The authors conduct literature reviews in order to acquire a comprehensive understanding of the fundamental engineering characteristics of CSRE (URE) and the factors influencing the properties of the researched materials. On the basis of the literature review, it has been found that the characteristics of CSRE (URE) materials vary significantly across experimental studies, making their application under in-situ

conditions more challenging. The absence of a global perspective on all sorts of CSRE (URE) materials impedes the development of an internationally recognized standard for CSRE (URE) materials. Consequently, to estimate the long-term CTHM behavior of CSRE (URE) materials, the combined effects of initial water content, initial dry density, initial grain size distribution, initial cement content, curing conditions, and curing duration should be assessed simultaneously throughout the design phase.

Therefore, in this study, a novel finite element framework applicable to both URE and CSRE materials is proposed to explain the linked CTHM behaviors of these materials. To validate the proposed theoretical framework, several experimental results for URE and CSRE materials from the existing literature are recreated and compared with the experimental results.

The proposed numerical model is then extended to study the structural behaviors of CSRE (URE) constructions under in-situ conditions. The long-term structural behaviors of URE walls are first studied by considering the effects of different environment types on the walls. After that, apart from the effects from the environment, the effects of rising damp from the ground are also studied for the long-term characteristics of the URE walls. Eventually, the long-term CTHM characteristics of the CSRE wall under the interactions of the environment and underground soil are studied.

Keywords: Unstabilised rammed earth (URE); Cement stabilized rammed earth (CSRE); Chemo-thermo-hydro-mechanical (CTHM) coupling; Climate effects; Rising damp; Water flow; Thermal resistance; Compressive strength; Numerical simulations